

**University of  
Sheffield**

**A Nanoparticle Approach to the Inhibition of  
Protein-Protein Binding**

**Abdullatif Hamdan Alanazi**

Submitted to the University of Sheffield

In fulfilment of the requirements for the degree of

Doctor of Philosophy

Supervisor: Dr. Lance J Twyman

Department of Chemistry

September 2024



## Acknowledgments

I would like to extend my deepest gratitude to my supervisor, Dr. Lance Twyman, whose unwavering support, insightful guidance, and thoughtful suggestions have been invaluable throughout this journey. His expertise and encouragement have played a pivotal role in the successful completion of this thesis. I am also profoundly thankful for the warm, collaborative atmosphere fostered by the Twyman research group, where I have felt truly welcomed as part of the family. In particular, I would like to express my appreciation to Dr. Abdelfatah Blau and Mrs Manar Alshammari for their continuous support and camaraderie. My sincere thanks also go to Dr. Ahmed Iraqi's group, especially Saif Alruwaili, for their generous assistance and contributions.

This thesis is dedicated to my beloved parents and family, who have been my unwavering source of inspiration and strength. Your belief in me has been the foundation of my resilience, perseverance, and determination. Thank you for instilling in me the values of hard work and dedication. Your unconditional love, support, and sacrifices have made this accomplishment possible, and I hope this work serves as a small token of my deep appreciation for everything you have done.

I am deeply thankful to all the staff in the Chemistry Department at the University of Sheffield. So many of you have contributed to my journey in ways large and small, and while I may not be able to thank each of you personally, please know that I am sincerely grateful for all your help and encouragement.

Finally, I would like to express my heartfelt gratitude to my beloved country, Saudi Arabia, and to my sponsor, King Abdulaziz Military Academy. Without your generous financial support, this PhD would not have been possible. Your investment in my education has allowed me to pursue my academic ambitions, and for that, I am forever grateful.

## Abbreviations:

<b>PPI</b> .....	Protein protein interactions
<b>DCC</b> .....	Dynamic combinatorial chemistry
<b>DCLs</b> .....	Dynamic combinatorial libraries
<b>MNP or MNPs</b> .....	Magnetic Nanoparticles
<b>PAMAM</b> .....	Poly(amido amine)
<b>PAMAM-OH</b> .....	Neutral Hydroxyl Terminated PAMAM
<b>PAMAM-COOH</b> .....	Acid Terminated PAMAM
<b>NaOH</b> .....	Sodium Hydroxide
<b>DCM</b> .....	Dichloromethane
<b>DMSO</b> .....	Dimethyl sulfoxide
<b>EDA</b> .....	Ethylenediamine
<b>MA</b> .....	Methyl Acrylate
<b>EDC</b> .....	1-Ethyl-3-(3-dimethylaminopropyl) carbodiimide
<b>DMAP</b> .....	4-Dimethylaminopyridine
<b>GO</b> .....	Graphene Oxide
<b>BTNA</b> .....	N-benzoyltyrosine-p-nitroanilide
<b>Chy</b> .....	$\alpha$ -chymotrypsin
<b>IR/FTIR</b> .....	Infra-Red/Fourier Transfer Infra-Red Spectrometry
<b>UV/Vis</b> .....	Spectrometry Ultraviolet/Visible Spectrometry
<b><sup>1</sup>H NMR</b> .....	Nuclear Magnetic Resonance Spectrometry
<b><sup>13</sup>C NMR</b> .....	Nuclear Magnetic Resonance Spectrometry
<b>ES-TOF MS</b> .....	Electron Spray Time-Of-Flight Mass Spectrometry
<b>MALDI-TOF MS</b> .....	Matrix Assisted Laser Desorption Ionisation Time of Flight
<b>K<sub>2</sub>CO<sub>3</sub></b> .....	Potassium Carbonate
<b>ε</b> .....	Extinction coefficient

**Nm**.....Nanometre  
**L-Tyr**..... L-Tyrosine methyl ester  
**L-Ph**.....L-phenylAlanine  
**L-Val**.....L-valine Methyl ester  
**L-Glu**.....L-glutamic  
**NHS**.....N-Hydroxysuccinimide

## **Author's Declaration**

I, Abdullatif Hamdan Alanazi, confirm that the Thesis is my own work. I am aware of the University's Guidance on the Use of Unfair Means ([www.sheffield.ac.uk/ssid/unfair-means](http://www.sheffield.ac.uk/ssid/unfair-means)). This work has never before been submitted for an award at this university, or any other, university.

## **Abstract:**

This study explores the functionalization of generation 2.5 Polyamidoamine (PAMAM) dendrimers with various amino acids, including Tyrosine, Phenylalanine, Alanine and Valine, and evaluates their ability to stabilize iron oxide magnetic nanoparticles ( $\text{Fe}_3\text{O}_4$  MNPs) and bind to cytochrome-c. The primary goal was to enhance the binding affinity and selectivity of MNPs using amino acid-functionalized dendrimers for potential applications in protein interaction inhibition. The functionalization of dendrimers was confirmed through  $^1\text{H}$  NMR,  $^{13}\text{C}$  NMR, IR and mass spectroscopy, and the resulting functionalized MNPs were characterized by dynamic light scattering (DLS) and TEM, showing greatly improved stability compared to unfunctionalized systems. The binding affinities of these functionalized MNPs were tested against cytochrome-c, revealing that Tyrosine-functionalized PAMAM dendrimers exhibited the highest binding affinity (53%) due to the presence of aromatic rings and hydroxyl groups, which facilitated  $\pi$ - $\pi$  stacking and hydrogen bonding. Valine-functionalized systems also showed strong binding (38%) driven by hydrophobic interactions, while phenylalanine-functionalized MNPs demonstrated moderate binding (26%) due to the absence of hydroxyl groups and limited hydrogen bonding capacity. Alanine-functionalized MNPs exhibited intermediate binding (29%) due to the presence of an additional carboxylic acid group, which contributed to strengthening the binding interactions. This extra carboxyl group increased the overall binding affinity by providing additional sites for electrostatic interactions, hydrogen bonding, and other non-covalent forces, thereby enhancing both the stability and specificity of the binding. The unfunctionalized PAMAM G3.5 dendrimer system served as a control, showing only minimal binding (12%). These findings highlight the potential of amino acid-functionalized dendrimers to enhance MNP stability and selectivity for protein binding,

offering a promising strategy for inhibiting protein-protein interactions in disease-related applications.

In the third chapter, we explore the functionalization of graphene oxide (GO) with monomeric and oligomeric glutamic acid to enhance its potential for enzyme inhibition, particularly targeting  $\alpha$ -chymotrypsin. GO was synthesized via the modified Tour method, ensuring improved safety and efficiency over traditional methods. The functionalization process aimed to increase the surface carboxylic acid groups of GO through the attachment of glutamic acid, enabling stronger electrostatic interactions and improved protein binding capabilities. Two approaches were employed: monomeric glutamic acid functionalization, involving the use of diester-protected glutamic acid, and oligomeric functionalization, where unprotected glutamic acid facilitated the formation of glutamic acid chains on the GO surface.

Comprehensive characterization was performed using Fourier-transform infrared spectroscopy (FT-IR), scanning electron microscopy (SEM), Raman spectroscopy, X-ray photoelectron spectroscopy (XPS), and X-ray diffraction (XRD) to confirm the successful attachment of glutamic acid and examine structural changes. Results showed that oligomeric functionalization led to higher uniformity and amide bond formation, enhancing protein interaction. This functionalized GO exhibited promising potential as a platform for enzyme inhibition, showing selectivity and binding efficiency towards  $\alpha$ -chymotrypsin, with implications for therapeutic and biochemical applications.



## Contents

Chapter 1 .....	14
Introduction.....	14
Introduction: .....	15
Introduction to Protein-Protein Interfaces:.....	15
Recognizing protein-protein interfaces:.....	17
Hot spots and interfacial area: .....	21
Small molecule inhibitor:.....	23
$\alpha$ -Helix Mimetics: .....	28
Supramolecular protein scaffold: .....	33
Dynamic Combinatorial libraries: .....	36
Dendrimers.....	39
Structure of Dendrimers: .....	39
Dendrimers Synthesis Methods.....	40
Properties of Dendrimers .....	42
Biocompatibility .....	43
Solubility .....	44
Distribution:.....	44
References: .....	46
Chapter 2 .....	57
Magnetic-nanoparticles.....	57
Introduction: .....	58
Iron oxides: .....	58
Nanoparticles:.....	61
Magnetic Nanoparticles (MNPs): .....	62
The nanoscale, nanoscience, and nanotechnology: .....	63
Natural nanoparticles: .....	66
Nanoparticle movement - Brownian motion: .....	67
Magnetism: .....	67
Magnetic nanoparticles in nature:.....	68
Superparamagnetism: .....	69
Particles' aggregation: .....	71

Importance in Biological Systems:.....	76
Nanoparticle characterisation: .....	77
Techniques for Analyzing Crystal Structures: .....	78
Techniques for Analyzing Particle Surfaces: .....	82
Techniques for Analyzing Chemical Properties: .....	86
Aims and Objectives:.....	93
<b>Chapter 3:</b>	
Results and Discussion: .....	100
Synthesis of PAMAM dendrimers: .....	101
Mechanism of PAMAM Dendrimers' Reaction: .....	104
Purification of dendrimers: .....	113
Synthesis of carboxylic PAMAM dendrimer (COOH):.....	115
Synthesis of Iron Oxide Nanoparticles (Fe <sub>3</sub> O <sub>4</sub> MNPs): .....	120
Stabilization of MNPs using OH terminated PAMAM dendrimers: .....	125
Stabilization of MNPs using COOH-PAMAM dendrimers: .....	129
Preparation for Cytochrome-c (Cyt-c) binding assay: .....	134
Assay to determine binding between dendrimer stabilized MNPS and Cytochrome c: .....	136
Functionalization of MNPs with COOH PAMAM dendrimers and various amino acids: .....	141
Synthesis of the tyrosine functionalized PAMAM dendrimer: .....	144
Binding of functionalized Magnetic Nanoparticles to Cytochrome C: .....	154
Conclusion: .....	158
Future work:.....	161
References: .....	163
<b>Chapter 4</b> .....	172
Functionalization of GO with oligo amino acids and its applications as enzyme inhibitors. ....	172
.....	172
Introduction:.....	174
The newly developed carbon-derived materials: .....	174
Synthesis method for graphene oxide: .....	176
The evaluation of GO for its ability to bind proteins:.....	179
Aims and Objectives: .....	182
Results and Discussion: .....	187
Unfunctionalized Graphene Oxide Synthesis: .....	188
Chemical Functionalisation of GO:.....	196

Synthesis of Graphene Oxide Functionalized with Oligomeric and monomeric Glutamic Acid:	199
Characterization of the Monomeric and Oligomeric GO Systems:	202
Assay to measure relative binding between GO and glutamic acid functionalized systems using $\alpha$ -chymotrypsin:	209
Exploring selectivity by functionalizing GO with various amino acids:	217
Assay to measure relative binding between amino acid functionalized GO and $\alpha$ -chymotrypsin:	220
Conclusion:	224
References	228
Chapter 5	234
Conclusion	234
Future focuses	234
Chapter 6	246
Experimental Part: Materials and method	246
Solvents and Instrumentals:	247
Instrumentation:	247
Infrared (FTIR) spectroscopy	247
Nuclear Magnetic Resonance Spectroscopy (NMR)	247
Mass Spectroscopy (MS)	247
The Raman spectroscopy	248
X-ray photoelectron spectroscopy (XPS)	248
Thermal conductivity analysis (TGA)	248
X-ray diffraction (XRD) patterns	248
Elemental Analysis	249
Scanning electron microscope	249
Experiments:	249
Synthesis of PAMAM dendrimers:	249
Synthesis of the methyl ester of PAMAM G 0.5 (4 OMe).	249
Synthesis of the methyl ester of PAMAM G 1.0 (4NH <sub>2</sub> )	250
Synthesis of the methyl ester of PAMAM G 1.5 (8OMe).	250
Synthesis of the methyl ester of PAMAM G 2.0 (8NH <sub>2</sub> )	251
Synthesis of the methyl ester of PAMAM G 2.5 (16OMe).	251
Synthesis of the methyl ester of PAMAM G 3.0 (16NH <sub>2</sub> ).	252
Synthesis of the methyl ester of PAMAM G 3.5 (32OMe).	252

Synthesis of hydroxylate PAMAM dendrimers:.....	253
Synthesis of PAMAM dendrimer with 24 OH terminal groups.....	253
Synthesis of PAMAM dendrimer with 48 OH terminal groups.....	254
Synthesis of PAMAM carboxylate terminated PAMAM dendrimers from methyl ester	
PAMAM dendrimer: .....	254
Generation 0.5 carboxylate PAMAM dendrimer (8 COOH).....	255
Generation 1.5 carboxylate PAMAM dendrimer (16 COOH).....	255
Generation 2.5 carboxylate PAMAM dendrimer (32 COOH).....	255
Generation 3.5 carboxylate PAMAM dendrimer:.....	255
Synthesis of functionalized PAMAM dendrimers with Amino acid: .....	256
Functionalization of PAMAM dendrimer with phenylalanine methyl ester.....	256
Functionalization of Pamam dendrimer with alanine methyl ester.....	256
Functionalization of Pamam dendrimer with valine methyl ester .....	257
Functionalization of Pamam dendrimer with tyrosine methyl ester .....	257
General method for the Hydrolysis of dendrimers.....	257
Hydrolysis of PAMAM with Valine methyl ester .....	257
Hydrolysis of PAMAM with phenylalanine methyl ester.....	258
Hydrolysis of PAMAM with Tyrosine methyl ester .....	258
Synthesis of Fe <sub>3</sub> O <sub>4</sub> NPs.....	258
Stabilization of Fe <sub>3</sub> O <sub>4</sub> NPs using dendrimers .....	259
Preparation for Cytochrome c (Cc) binding assay .....	259
The interactions between cytochrome c and PAMAM dendrimers.....	259
Preparation of cytochrome- c solution:.....	259
Preparation of Phosphate buffer solution:.....	259
Preparation of MNPs-Polymer Solution: .....	260
Assay of Cytochrome-c Activity .....	260
Synthesis of Graphene Oxide (GO) .....	261
Functionalized Graphene Oxide:.....	261
Graphene oxide functionalized with methyl ester of tyrosine (Tyr-OCH <sub>3</sub> ).....	261
Synthesis of Tyr-mono-deprotected Graphene Oxide.....	262
Graphene Oxide – Valine -OCH <sub>3</sub> .....	262
Graphene Oxide modified with Valine through mono-deprotection .....	263
Graphene Oxide – PhenylAalanine -OCH <sub>3</sub> .....	263
Graphene Oxide – Phenylalanine (Mono-Deprotection) .....	263
Graphene Oxide – Glu -OCH <sub>3</sub> .....	264
Graphene Oxide – Glutamic (Mono-Deprotection) .....	264

Graphene Oxide- Glutamic (Oligo) .....	265
Inhibition of $\alpha$ -chymotrypsin using graphene oxide (GO):.....	265
Experimental Procedure:.....	265
Assessment of chymotrypsin activity using Graphene Oxide.....	265

# Chapter 1

## Introduction

## Introduction:

### Introduction to Protein-Protein Interfaces:

Proteins interact in various ways to form complexes that are essential to biological processes, typically classified as either homocomplexes or heterocomplexes. Homocomplexes consist of identical proteins that come together, forming stable and long-lasting structures due to strong intrinsic interactions. These complexes are critical for processes requiring consistent and sustained activity, such as maintaining cellular structures or facilitating metabolic functions. In contrast, heterocomplexes involve different proteins and are more dynamic, often forming and breaking down in response to external stimuli like changes in pH, temperature, or signaling molecules. While heterocomplexes can also be stable, their formation is typically more flexible, allowing them to adapt to changing environmental activities.<sup>1</sup> A distinctive feature of heterocomplexes is that they often include at least one protein capable of functioning independently, without requiring the complex for its biological activity. These protein complexes are crucial for numerous biological functions, including immune responses, signal transduction, cytoskeletal remodeling, viral self-assembly, and cell regulation. However, improper protein interactions can lead to diseases, such as HIV-1 protease malfunction in HIV infection, aberrant amyloid-beta and tau protein interactions in Alzheimer's disease, and abnormal protein complexes contributing to inflammation in rheumatoid arthritis.<sup>2</sup> Moreover, protein-protein interactions are a major target for therapeutic interventions, particularly in cancer. For example, in cancers driven by prolonged c-Myc activation, inhibitors targeting c-Myc complexes are being explored as potential treatments. c-Myc is an oncogene, and its overactivity is linked to several cancers. By disrupting these specific protein-protein

interactions, cancer growth may be hindered. Similarly, targeting interactions involved in plaque formation has implications for treating neurodegenerative diseases like Alzheimer's. Disrupting or preventing the interactions that lead to the aggregation of proteins like amyloid-beta may slow or prevent the progression of these diseases.<sup>3</sup> In summary, understanding and manipulating protein-protein interactions, both homocomplexes and heterocomplexes, hold significant potential for treating a wide range of diseases, from viral infections to neurodegeneration and cancer.<sup>3</sup> The ability to specifically target these interactions with inhibitors or other therapies represents a powerful approach in modern medicine. (See figure 1.1 for a visual representation of how disrupting specific protein interactions can influence disease treatment).

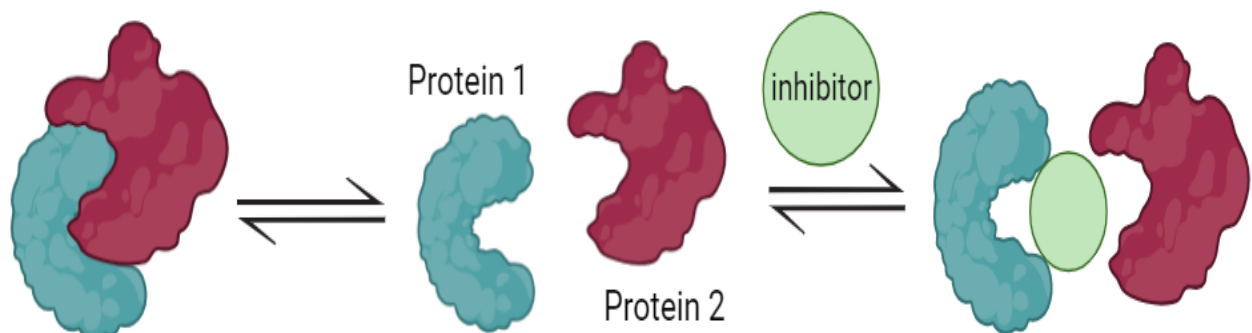


Figure 1.1: Encapsulates the essential strategy of using targeted inhibitors to regulate protein interactions, a key method in controlling biological developments and preventing disease. This concept is critical for advancing drug design and therapeutic interventions that aim to disrupt harmful protein interactions while preserving normal cellular functions.



## Recognizing protein-protein interfaces:

Proteins are made up of long chains of amino acids, with the primary structure being defined by the specific sequence of these amino acids.<sup>4</sup> These sequences can be composed of various combinations of the 20 amino acids found in nature, resulting in an immense diversity of primary structures. Each unique sequence dictates how the protein folds into its secondary and tertiary structures, which ultimately determine the protein's final form and function. Proteins can also form quaternary structures when multiple polypeptide chains (subunits) come together, adding another level of structural diversity. The folding and complex formation of proteins enable them to perform a wide range of biological functions.<sup>5</sup> For example, proteins can act as enzymes, hormones, transporters, or structural components in cells. The tertiary structure defines how the protein folds into a three-dimensional shape, whereas the quaternary structure involves interactions between multiple polypeptide chains or subunits. Protein-protein interactions are essential for forming protein complexes, where two or more proteins interact, often through non-covalent bonds like hydrogen bonding, van der Waals forces, or electrostatic interactions. These interactions are critical for biological processes such as signal transduction, immune response, and molecular transport. As represented in figure 1.2, these protein-protein complexes are responsible for forming active compounds that carry out specific cellular functions.<sup>6</sup> The ability of proteins to interact and form complexes is fundamental to their roles in regulating cellular activities, metabolism, and communication within and between cells. Moreover, the versatility of these interactions allows for the dynamic regulation of cellular processes. Proteins can associate or dissociate based on environmental conditions or cellular signals, allowing the formation of transient complexes that respond to biological needs. This flexibility is a hallmark of protein function and highlights the complexity of protein

biology. The range of protein-protein complexes is vast, and they are crucial in pathways such as DNA replication, transcription, and cell cycle regulation.<sup>7</sup>

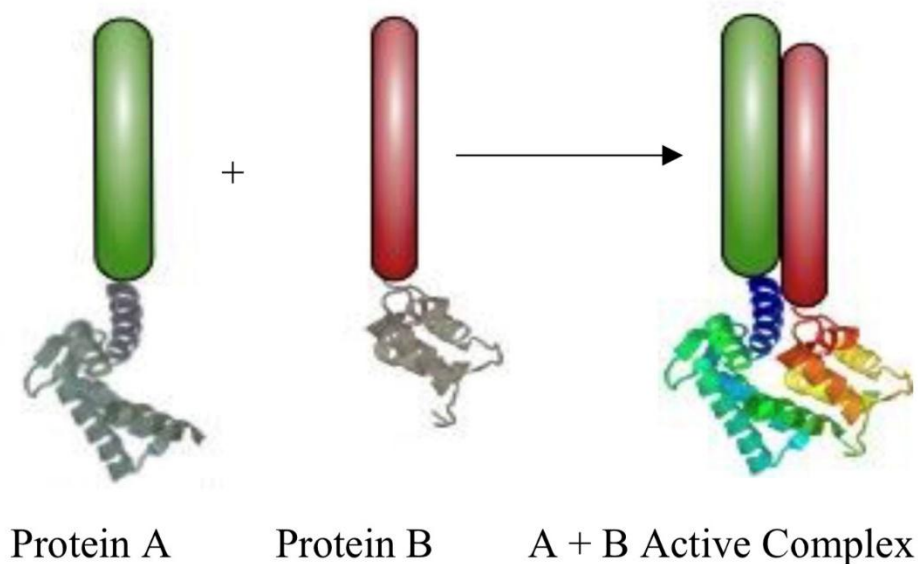


Figure 1.2: Demonstrates the formation and structure of a combined active complex, a key concept in understanding the interaction between multiple molecular components that work together to achieve a specific function.

These forces provide a collective strength, which they don't have individually, caused by cooperative binding that provides stability to molecule-molecule interactions.<sup>8</sup> A variety of biochemical and biological methods are based on cooperative binding. A growth in apparent affinity suggests positive support, meaning the likelihood of binding a second molecule rises due to an important enhancement in the ligand's relative affinity for the second binding site.<sup>9</sup> The results of cooperative binding are shown in figure 1.3. The initial bond between the ligand

and the original binding site forms at affinity described by  $K_1$ . Afterward, the second interaction happens much faster and is stronger, due to the higher relative concentration of the second ligand compared to other molecules. Since  $K_1$  is much lower than  $K_2$ , the effect is non-additive, whereas cooperative binding leads to a more clearly additive result.

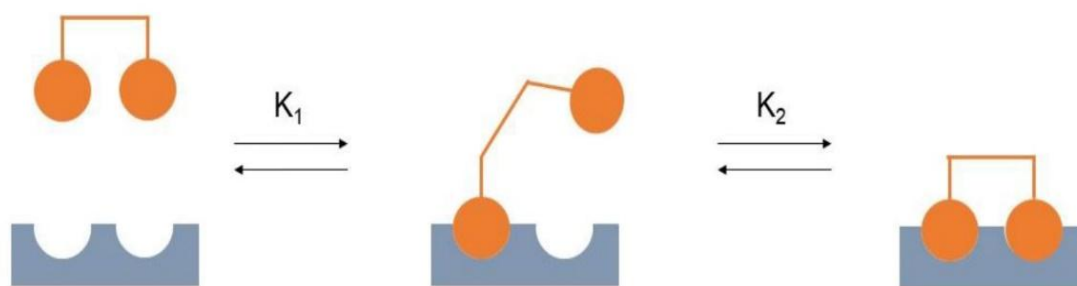


Figure 1.3: Illustrates a scenario in which the first binding constant ( $K_1$ ) is notably smaller than the second binding constant ( $K_2$ ), highlighting a form of positive cooperativity. the  $K_1$  and  $K_2$  values refer to binding constants (a type of equilibrium constant).

It is found that during binding interactions, certain amino acids are much denser than other regions of the protein molecule.<sup>10</sup> Due to hydrophobic properties of these amino acids, binding interactions between proteins are more likely to be improved. Also, large aromatic amino acids are often favoured at binding interfaces, with binding surfaces being the most likely areas of the protein where amino acids such as tyrosine are found.<sup>10,11</sup> Table 1.1 lists potential target proteins for evaluating the binding capacity of polymers, as well as their ability to distinguish between

different protein surfaces within the same enzyme group. The disruption of protein interactions by synthetic inhibitors relies on the formation of stable synthetic subunit complexes that prevent protein subunits from interacting with each other.

Enzyme type	Protein	Amino acid residue	Inhibitor	Cleavage site
Serine Protease	Elastase	240	$\alpha$ -anititrypsin	Ala, Gly
	$\alpha$ -chymotrypsin	241	Aprotinin	Phe, Tyr, Trp
	Trypsin	233	p-aminobenzamidine	Arg, Lys
	Kallikrein	619	Aprotinin	Arg
	Thrombin	308	Argatroban	Arg
Zinc protease	Carboxypeptidase A	307	Benzomercaptopropanoic acid	Phe, Trp, Leu
Aspartate protease	Cathepsin D	346	Pepstatin A	Phe-Phe

Table 1.1: Enzymes classified by their typical inhibitors and cleavage sites. Adapted summary from Gilles et al., Biomacromolecules, 18(6), pages 1772–1784, 2017.<sup>12</sup>

## Hot spots and interfacial area:

Before applying approaches to manipulate or study protein-protein interactions, it is crucial to understand the recognition sites and binding mechanisms involved in these complexes. Several key factors must be considered when examining protein-protein interfaces, including the size, shape, and structure of the interacting proteins, the specific properties of the amino acid residues at the interface, and any conformational changes that occur upon complex formation.<sup>13</sup> Additionally, the complementarity between interacting surfaces and the types of forces that drive the interaction, such as hydrophobic interactions, hydrogen bonds, and electrostatic forces, play critical roles in the binding process.<sup>14</sup> When protein-protein complexes form, the large interfacial regions become inaccessible to the solvent, which tend to be predominantly hydrophobic, though they are often surrounded by polar groups. The interfacial surface area between interacting proteins typically ranges from 500 to 5000 Å<sup>2</sup>.<sup>14</sup> For example, the interface between cytochrome c and cytochrome c peroxidase is approximately 1150 Å<sup>2</sup>, while the interface between chymotrypsin and its protein analogue spans about 2200 Å<sup>2</sup> (figure 1.4). Initially, it was thought that the free energy of binding between proteins was primarily driven by hydrophobic interactions between contact amino acid residues. However, research has shown that the binding energy is a result of a combination of various intermolecular interactions across the interface, which, although individually weak, collectively contribute to the overall strength and specificity of the protein-protein interaction. Understanding these interactions in detail is essential for deciphering how protein complexes function in biological systems.<sup>14</sup>

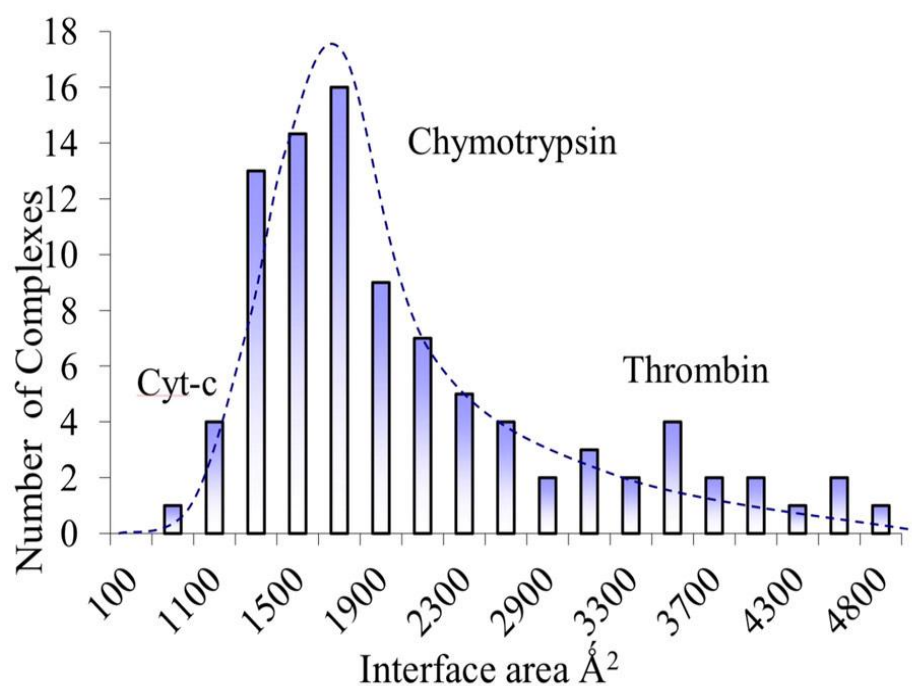


Figure 1.4: This figure provides a detailed illustration of how interfacial areas are distributed in typical protein-protein complexes. It highlights the specific regions where proteins interact with one another, showcasing the varying sizes and patterns of these interfacial areas. <sup>15</sup>

Furthermore, the regulation of protein binding can be influenced by two primary mechanisms. The first involves aiming for the inner active site of a protein, which is often buried and inaccessible to bulk solvent, making it a more challenging but effective target for disrupting protein interactions. The second mechanism focuses on the external surface of the protein, which remains accessible to solvent and can be targeted to prevent binding or disrupt existing complexes.<sup>16</sup> These mechanisms play a critical role in therapeutic strategies aimed at modulating protein-protein interactions, as understanding and targeting hot spots can lead to

the development of inhibitors that block key binding events essential for the formation of functional protein complexes.<sup>17</sup>

## Small molecule inhibitor:

The design of small molecules as potential inhibitors has become a key area of research, especially in the effort to target protein-protein interactions.<sup>18</sup> These inhibitors are typically designed to interact with specific regions of a protein, such as the active site or allosteric sites, to modulate its function.<sup>19</sup> The driving principle behind the design of small molecule inhibitors is their ability to interfere with key biochemical processes by binding to these critical sites, thereby preventing or altering protein interactions that are essential for cellular function. Small molecules exert their inhibitory effects primarily through several types of non-covalent interactions that are typically observed in protein active sites.<sup>20</sup> These involve electrostatic interactions, hydrogen bonding, and the formation of salt bridges, all of which contribute to the specificity and strength of binding between the small molecule and its target. Given the nature of these interactions, small molecules with appropriate physicochemical properties, such as hydrophilicity and the presence of hydrogen bond donor groups, are often favored in drug development.<sup>21</sup> These properties enable small molecules to effectively engage with polar residues and functional groups within the active site, enhancing their binding affinity and selectivity.<sup>22</sup>

The rational design of small molecule inhibitors often involves a detailed understanding of the three-dimensional structure of the target protein and the specific interactions that occur at the binding site. Advances in techniques such as X-ray crystallography, NMR spectroscopy, and

computational modeling have provided insights into the structural features of active sites and the dynamics of protein-ligand interactions. This knowledge allows for the optimization of small molecule inhibitors to maximize their efficacy, specificity, and pharmacokinetic properties.<sup>23</sup>

In addition to targeting active sites, small molecule inhibitors can also be designed to disrupt protein-protein interfaces, particularly at hot spots—regions that are critical for maintaining the stability and functionality of protein complexes. In these cases, small molecules must be carefully engineered to mimic the natural interactions between proteins or to introduce new interactions that destabilize the complex.<sup>24</sup> The challenge lies in the typically large and flat nature of protein-protein interfaces, which makes it difficult for small molecules to achieve high-affinity binding. However, recent advances in fragment-based drug discovery and molecular docking techniques have shown promise in overcoming these challenges, enabling the development of small molecule inhibitors that can effectively target protein-protein interactions.<sup>25</sup>

Designing synthetic agents tailored to target protein-protein interactions presents significant challenges. One major hurdle for small molecule inhibitors is the requirement for a large surface area (700-1500 Å<sup>2</sup>) for effective recognition. Additionally, selective targeting is challenging because protein interaction surfaces often have shallow depressions that lack unique defining features.<sup>26</sup> The discontinuous nature of the binding regions between two proteins adds to the complexity, making replication with simple synthetic peptides problematic. Protein-protein interfaces are more intricate than those between enzymes and ligands, as both proteins may present a combination of projections and pockets, rather than the traditional ligand-enzyme dynamic of filling a single pocket.<sup>27</sup>



Moreover, the *in vivo* efficacy of small molecules being developed as potential drugs must be thoroughly tested. These molecules must exhibit both high specificity for the target protein and minimal toxicity, while also ensuring adequate bioavailability. A relevant example is Maraviroc (figure 1.5), an HIV-1 treatment that blocks the CCR5 receptor on immune cells, preventing the virus from entering and infecting these cells. Maraviroc, typically used alongside other antiretroviral drugs, highlights the importance of balancing efficacy, safety, and bioavailability in the development of protein interaction inhibitors.<sup>28</sup>

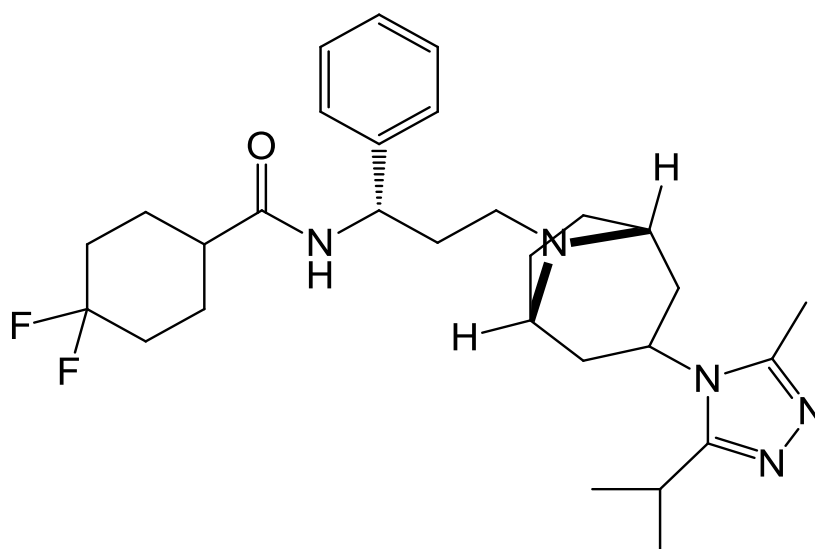


Figure 1.5: Shows the chemical structure of the inhibitor "Maraviroc," a chemokine CCR5 receptor antagonist developed to target viral reverse transcriptase or protease enzymes in the treatment of HIV.

The chemical structures of specific inhibitors, like Nutlins, are notably distinct from those in other established drug classes. Nutlin-3, a key member of this group, was chemically optimized

and developed, as illustrated in Figure 1.6. This compound exhibits a strong capacity to disrupt hDM2-p53 interactions, with an  $IC_{50}$  value of 90 nM. Furthermore, Nutlin-3 has demonstrated efficacy in *in vivo* models, showing significant activity against xenograft tumors.<sup>29</sup>

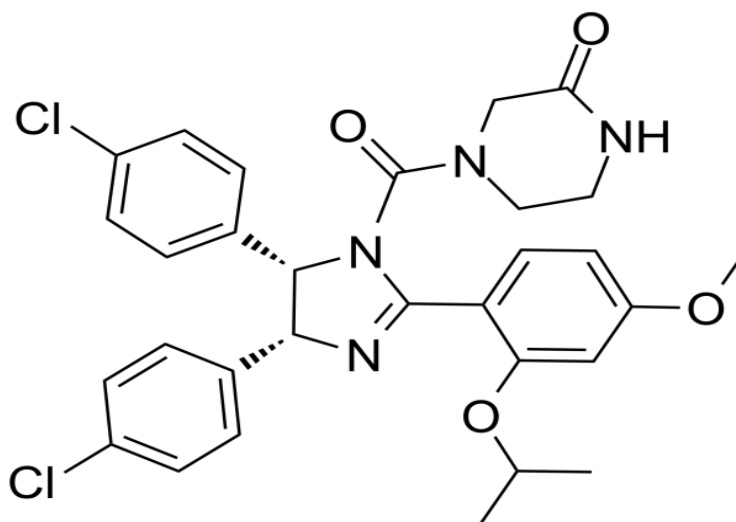


Figure 1.6: The chemical structure of cis-imidazoline Nutlin, illustrating its chemical configuration and key functional groups.

Inducible nitric oxide synthase (iNOS) is a critical protein target due to its role in producing nitric oxide, an essential molecule in signal transduction, via its dimeric enzyme structure. The inducible form of iNOS is associated with tissue damage in various autoimmune diseases, making selective iNOS inhibitors promising candidates for therapeutic interventions. McMillan and colleagues employed combinatorial chemistry to develop such an iNOS inhibitor, as shown in figure 1.7. X-ray crystallography revealed that the inhibitor disrupts both

the substrate binding site and the dimerization interface of iNOS, thereby preventing the formation of the active enzyme dimer. In *in vivo* studies in rat models further demonstrated the inhibitor's efficacy, with an ED<sub>50</sub> value below 2 mg/kg, underscoring its potential as a therapeutic agent.<sup>30</sup>

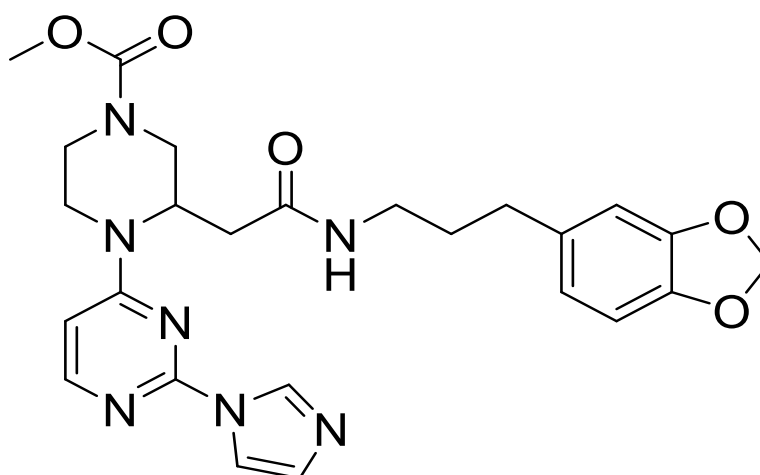


Figure 1.7: The chemical structure of iNOS inhibitor 86, illustrating its molecular framework and key functional groups. This diagram provides a detailed view of the compound's structure, highlighting specific elements and arrangements that contribute to its ability to inhibit inducible nitric oxide synthase (iNOS).

Tumor necrosis factor alpha (TNF- $\alpha$ ), a member of the cytokine family, plays a pivotal role in systemic inflammation, making it a critical target for therapeutic intervention. Biologic agents such as Remicade, Humira and Enbrel — antibodies that neutralize TNF- $\alpha$  — have been developed to directly inhibit TNF- $\alpha$  and have shown significant efficacy in the treatment of rheumatoid arthritis. However, despite the success of these biologics, there is continued strong

interest in developing small molecule inhibitors for the reason that they are economical and simple to administer. Figure 1.8 illustrates a potent small molecule TNF- $\alpha$  inhibitor. The mechanism of action of this inhibitor involves the disruption of the active TNF- $\alpha$  trimer by displacing a subunit, leading to the formation of an inactive dimer, thereby suppressing its biological activity.<sup>31</sup>

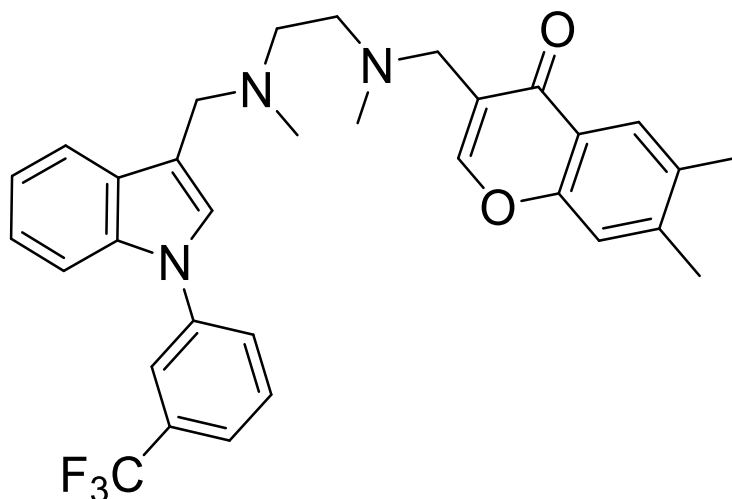


Figure 1.8: Shows the chemical structure of a TNF- $\alpha$  inhibitor and highlights the specific regions of the protein that are essential for its inflammatory effects and provides insights into potential binding sites for therapeutic interventions.

### $\alpha$ -Helix Mimetics:

In recent years, peptide-based therapeutics have garnered considerable interest for their potential in treating a wide range of diseases. Peptides with well-defined and stable secondary structures, such as  $\alpha$ -helices and  $\beta$ -turns, have demonstrated promise in enhancing both biological activity and therapeutic effectiveness.<sup>32</sup> A key focus of current research is the design

of peptides that display conformational stability, meaning they maintain their three-dimensional structure under physiological conditions. Achieving this stability typically requires peptides composed of more than 15 amino acid residues, which are essential for preserving their specific secondary structural elements.<sup>33</sup>

A major advancement in peptide-based therapeutics involves the use of stable  $\beta$ -turns and  $\alpha$ -helices, which are constrained by hydrogen-bond surrogates. This innovative method replaces native hydrogen bonds within peptides with surrogate structures, locking them into specific conformations.<sup>34</sup> Similarly,  $\beta$ -sheet systems are being engineered for enhanced stability. These advanced peptide designs show significant therapeutic potential, particularly for targeting diseases like cancer and HIV. The increased stability of these peptides ensures resistance to degradation, improved binding affinity for target proteins, and prolonged therapeutic effects, making them highly valuable candidates for drug development.<sup>35</sup>

The recent emphasis on these stable secondary structures is driven by their ability to enhance drug delivery, increase specificity in targeting disease-related proteins, and address the limitations of traditional small molecules and biologics. Consequently, structured peptides are becoming powerful tools in modern medicine, with ongoing research exploring their applications in areas such as oncology, immunology, and antiviral therapies.<sup>36</sup>

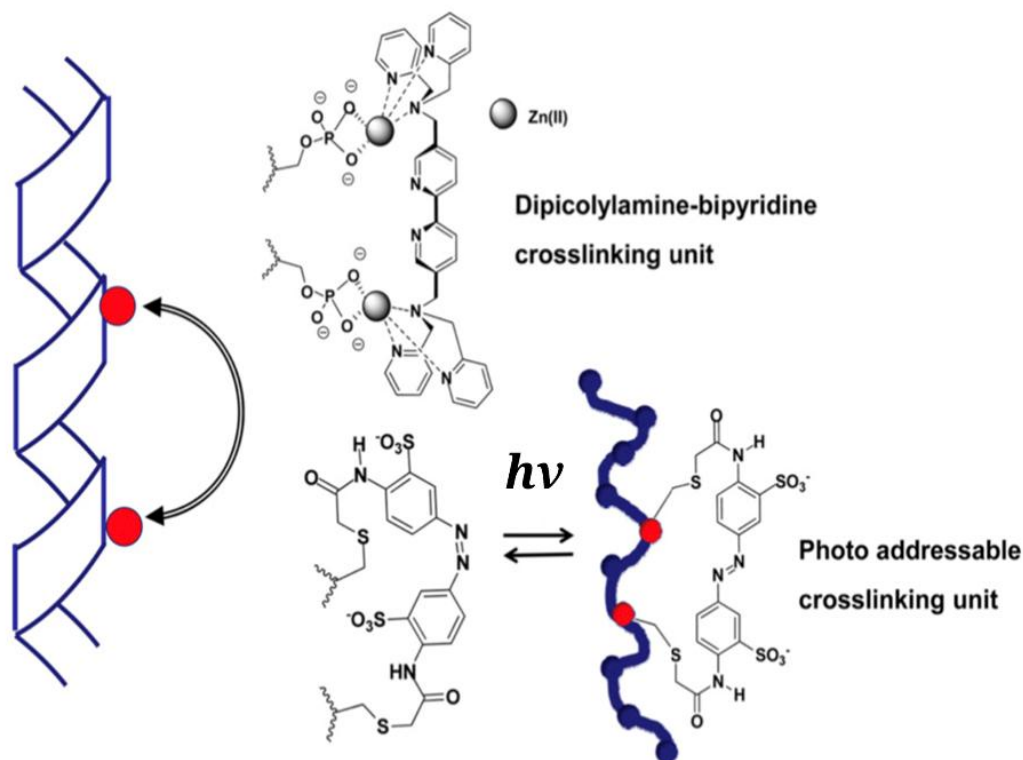


Figure 1.9: Demonstrates the molecular structures and cross-linking units of azobenzene and dipicolylamine-bipyridine, highlighting their roles in facilitating structural rigidity and stability in various molecular systems.

Peptide stabilization has been explored using azobenzene photoaddressable and dipicolylamine-bipyridine cross-linking units (figure 1.9). These  $\beta$ -peptides exhibit side chains along one face, similar to  $\alpha$ -helices, although not all of them share the same three-dimensional orientation. The primary advantage of these systems lies in their conformational stability, since they procedure well-defined secondary structures and are resistant to proteolytic degradation.<sup>37</sup>

In another approach, Breslow and colleagues utilized a range of  $\beta$ -cyclodextrin dimers ( $\beta$ -CD) to demonstrate selective disruption of protein aggregation (figure 1.10). Their study revealed that only  $\beta$ -CD compounds with depressions facing each other, separated by an appropriately spaced linker, were effective in disrupting protein aggregation. This finding suggests that the inhibitory effect is dependent on the specific properties of the linker.<sup>38</sup>

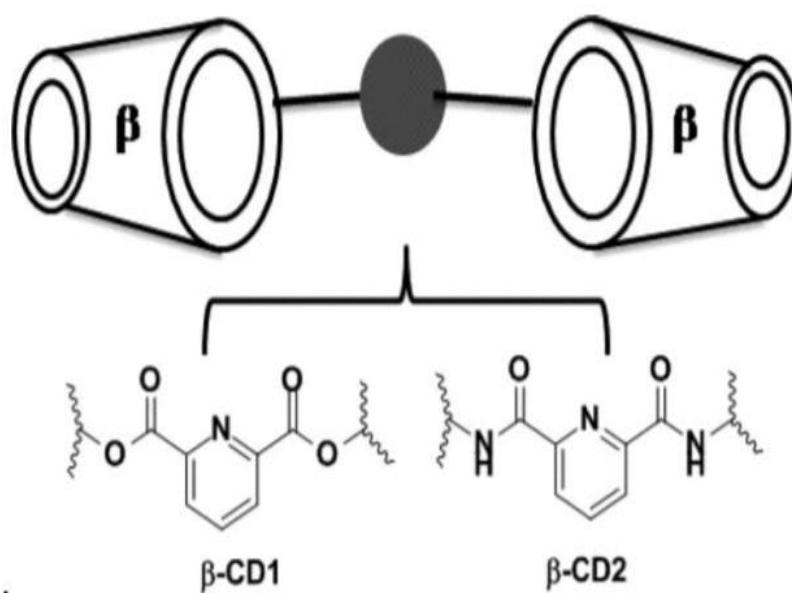


Figure 1.10: Depicts two  $\beta$ -cyclodextrin ( $\beta$ -CD) molecules oriented toward each other, with a linker separating them.

Terephthalamides and alkylidene cycloalkanes have also been proposed as scaffold-type  $\alpha$ -helix mimetics, showing potential for use as  $\alpha$ -helical mimics.<sup>39</sup> Reymond and colleagues utilized an  $\alpha$ -helical conformation in the development of peptide dendrimers. Additionally,

significant efforts have been directed toward the design of non-peptidic small molecule  $\alpha$ -helical mimics as inhibitors of protein-protein interactions.<sup>40</sup> In a notable study, Lee and colleagues introduced a new pyrrolopyrimidine-based receptor, illustrated in figure 1.11. The effectiveness of this scaffolding as an  $\alpha$ -helical mimic was reviewed based on its capacity to interrupt the interfaces between p53 and MDMX. The evaluation process included screening the scaffold against a library of 900 compounds and selecting primary amines with hydrophobic groups. These hydrophobic groups were essential in mimicking the side chains of three key amino acids, thereby improving selectivity. The scaffold was ultimately found to be conformationally rigid, highly water-soluble, and capable of permeating cells, making it a promising candidate for therapeutic development.<sup>41</sup>

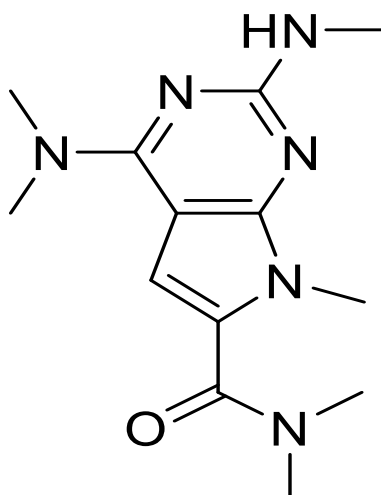


Figure 1.11: The chemical structure of the pyrrolopyrimidine-based  $\alpha$ -helix mimic is presented, highlighting its core framework and essential functional groups.



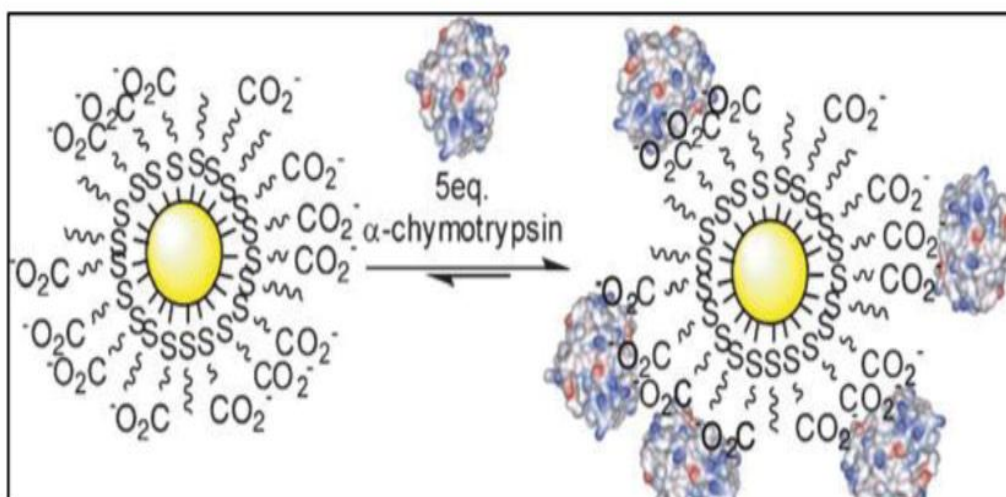
Developing small molecule inhibitors remains a significant challenge, prompting the exploration of alternative approaches that mimic the selective mechanisms of protein-protein interactions. One such strategy involves interfering with these interactions by targeting the protein surface near, rather than directly within, the active site.<sup>42</sup> Each protein has a unique peripheral surface, characterized by hydrophobic, hydrophilic, and charged regions. The interface between interacting proteins involves electrostatic interactions, as well as  $\pi$ - $\pi$  stacking interactions and hydrogen bonding.<sup>43</sup>

While many studied inhibitors function by binding within active site depressions to block interactions, much less is known about artificial molecules which bind to the exterior surface of proteins to interrupt their role. Investigating such molecules could yield novel therapeutic agents and provide valuable insights into the mechanisms of protein surface recognition and peripheral interactions.<sup>44</sup>

### Supramolecular protein scaffold:

Rotello utilized self-assembled systems for surface recognition by employing mixed-monolayer protected gold clusters (MMPCs) functionalized with terminal anionic groups. These MMPCs selectively bound to the positively charged surface of  $\alpha$ -chymotrypsin, resulting in the suppression of its enzymatic activity.<sup>45</sup>

This suppression occurred through a two-step mechanism: an initial fast, reversible inhibition followed by a slower, irreversible route involving gradual enzyme degradation (as depicted in scheme1.1).



Scheme 1.1: Illustrates the application of Mixed Monolayer Protected Clusters (MMPCs) in surface recognition, showcasing how these engineered nanoparticles interact with specific surfaces or biological targets.

The electrostatic interactions within the system proved to be highly effective, showing significant selectivity compared to elastase. The strong binding between the gold nanoparticle and  $\alpha$ -chymotrypsin was confirmed using circular dichroism spectroscopy, which revealed a  $K_i(\text{app})$  of 10 nM and a stoichiometry of five protein molecules per MMPC. Moreover, the inhibition mechanism demonstrated higher selectivity for  $\alpha$ -chymotrypsin over  $\beta$ -galactosidase.<sup>46</sup>

Graphene oxide (GO)-based inhibitors have also garnered significant attention. In GO, the surface carboxylate group acted as both a potent inhibitor and a synthetic receptor of  $\alpha$ -chymotrypsin, outperforming other synthetic inhibitors in terms of dose-dependent suppression of  $\alpha$ -chymotrypsin activity. In parallel, Wang and colleagues demonstrated that a composite

material at the nanoscale combining GO and iron oxide (IO) holds potential for developing novel therapies for Alzheimer's disease.<sup>47</sup>

Dendrimers are a promising class of protein inhibitors, featuring terminal groups that enhance their interface with hot spot residues. Their size and structure often lead to comparisons with artificial globular proteins. Two dendrimeric peptide mimics were proposed by Fassina, each composed of four copies of the tripeptide Arg-Thr-Tyr (using either L-amino acids or partial-retro-inverso D-amino acids), connected to a poly-lysine core with asymmetric characteristics. Among these, the mimic based on natural amino acids demonstrated the highest efficacy.<sup>48</sup> Twyman further provided evidence that dendrimers could inhibit chymotrypsin and cytochrome-c, indicating their potential for developing size-selective binding mechanisms. Figure 1.12 illustrates the PAMAM dendrimers utilized in these studies.<sup>49</sup>

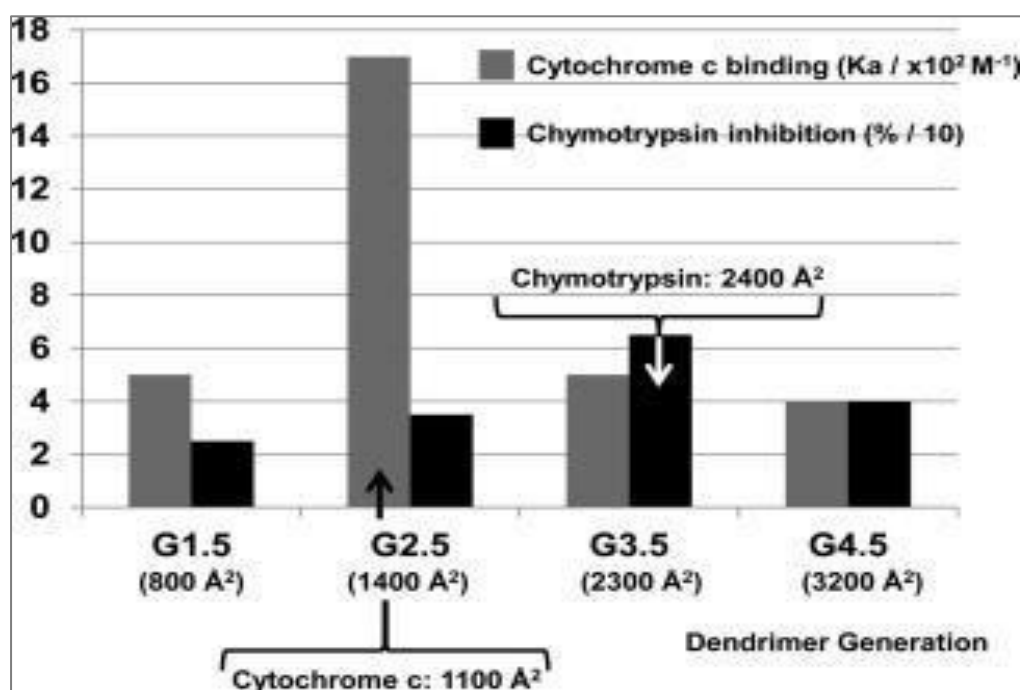


Figure 1.12: Presents the results of binding and inhibition studies involving poly(amidoamine).

In essence, for a specific protein, the dendrimer that has a surface area comparable to the protein's interfacial region achieves the most efficient binding. Inhibition of enzymatic activity occurs when a large ligand interacts with the enzyme's active site, effectively preventing access. Consequently, dendrimers with the greatest inhibition potency are those that bind most effectively.<sup>49</sup> Astruc's method to dendrimer-supported dynamic combinatorial chemistry (DCC) involves using dendrimers as soluble supporters. DCC is distinguished by its solution-phase chemistry, simple purification processes, routine characterization of intermediates, and high loading capacities. The results suggest that combinatorial libraries are efficiently generated using DCC. As a result, dynamic combinatorial libraries (DCLs), which improve access to molecular networks, show great promise for advancing the study and development of chemical complexity.<sup>50</sup>

## Dynamic Combinatorial libraries:

Dynamic Combinatorial Libraries (DCLs) refer to molecular assemblies that exist in a constant, reversible equilibrium, formed through either covalent or non-covalent interactions under thermodynamic control. These assemblies self-organize from individual building blocks into a variety of complexes, with the library's overall composition reflecting the relative stability of each component in the system.<sup>51</sup>

The stability of the components in a DCL is highly sensitive to external factors such as temperature, pH, or the presence of specific templates like proteins or other biomolecules.

When exposed to such templates, the DCL dynamically adapts, promoting the formation of the most stable and favorable complexes. This adaptive process allows the system to respond to external stimuli, often leading to the amplification of components that interact most effectively with the template.<sup>52</sup> Figure 1.13 demonstrates how a DCL's structure is altered when exposed to a template, such as a protein. Upon introduction of the protein, the library reorganizes to form specific complexes that bind efficiently to the template. This dynamic adaptation is especially useful in drug discovery and molecular recognition, as the DCL can evolve to generate high-affinity binders that are thermodynamically favored in the presence of a target molecule. Therefore, DCLs serve as a valuable tool for identifying molecules with optimal binding properties and stability, as their composition is shaped by the external conditions they encounter.

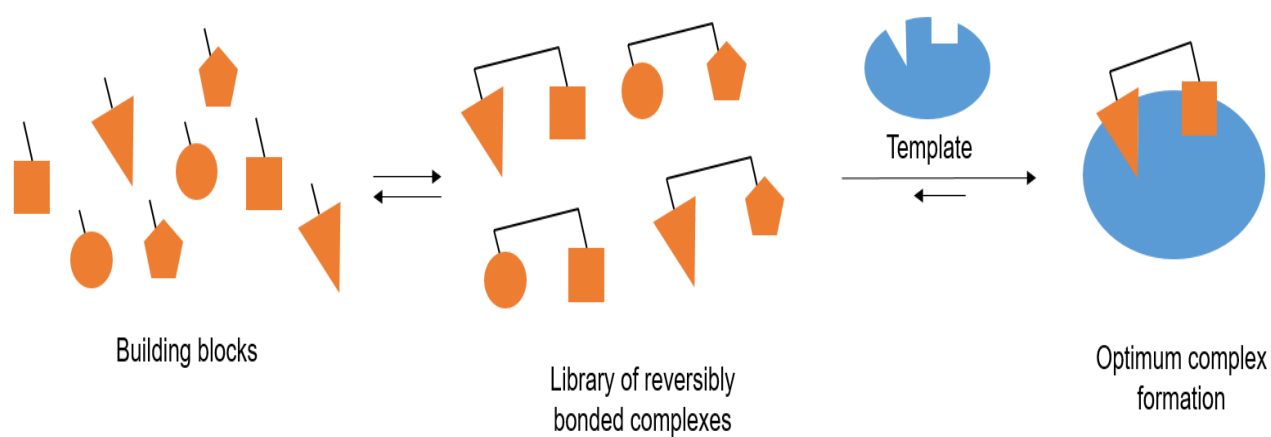


Figure 1.13: Explains the concept and behavior of Dynamic Combinatorial Libraries (DCLs), highlighting the dynamic assembly and reorganization of molecular components into various complexes.

Dynamic Combinatorial Libraries (DCLs) present a highly effective strategy for drug discovery and molecular design, enabling the dynamic self-assembly of molecules based on their interactions with a template molecule. In this process, introducing a template, such as a protein, into the reaction mixture steers the system towards forming the product with the strongest affinity for the template.<sup>53</sup> This process is driven by thermodynamic equilibrium, where the most stable and favorable complex emerges, guided by factors such as size, shape, and noncovalent interactions, including hydrogen bonding, van der Waals forces, and electrostatic interactions with the template.<sup>54</sup>

This approach is particularly valuable for optimizing dendrimer chain complexes, where the structure and branching of the dendrimer play a crucial role in effective binding to target proteins. By using proteins as templates, DCLs can explore a diverse range of dendrimer configurations, selecting the one that exhibits the highest affinity for the template. This selection process is not random; it is based on the ability of the molecular components to adapt and form the most stable complex in response to the protein template.<sup>55</sup>

One of the key advantages of DCLs is their efficiency and speed. Traditionally, drug discovery involves labor-intensive and time-consuming steps of testing various compounds, followed by structural refinement to optimize binding affinity. DCLs streamline this process by allowing the system to naturally evolve towards the optimal binding complex in a single step. As the DCL continuously adapts to the template, it rapidly identifies the most effective molecular candidates.<sup>56</sup>

In medicinal chemistry, this dynamic selection capability significantly accelerates drug discovery. Rather than manually screening vast libraries of compounds, DCLs automatically focus on molecules with the strongest interactions with the target, reducing the time and resources needed to identify and optimize drug candidates. As a result, this technique holds great promise for the development of new therapeutic agents, offering a faster and more efficient pathway to drug discovery.<sup>57</sup>

## Dendrimers

Dendrimers are highly branched, three-dimensional macromolecules characterized by a well-defined, symmetric structure with multiple arms radiating from a central core. The stepwise synthesis of dendrimers results in these highly branched molecules, with well-defined peripheral groups.<sup>58</sup> This process leads to the production of dendrimers with uniform branching, which are relatively straightforward to synthesize. In contrast, polymerization synthesis can yield polymers with irregular branching and less defined structures. Recent research has increasingly focused on the synthesis of dendrimers through both chemical and biological methods, given their significant potential in various biological and medicinal applications.<sup>59</sup>

### Structure of Dendrimers:

Dendrimers are defined by their highly symmetric molecular architecture, which originates from a central atom or group of atoms known as the core. From this core, branches called "dendrons" extend outward, expanding through a series of controlled chemical reactions. Unlike many linear polymers, dendrimers can be synthesized with a high degree of precision,

resulting in globular macromolecules with numerous branches at the periphery (figure 1.14). This precise control over structure is one of the key distinguishing features of dendrimer chemistry.<sup>60</sup>

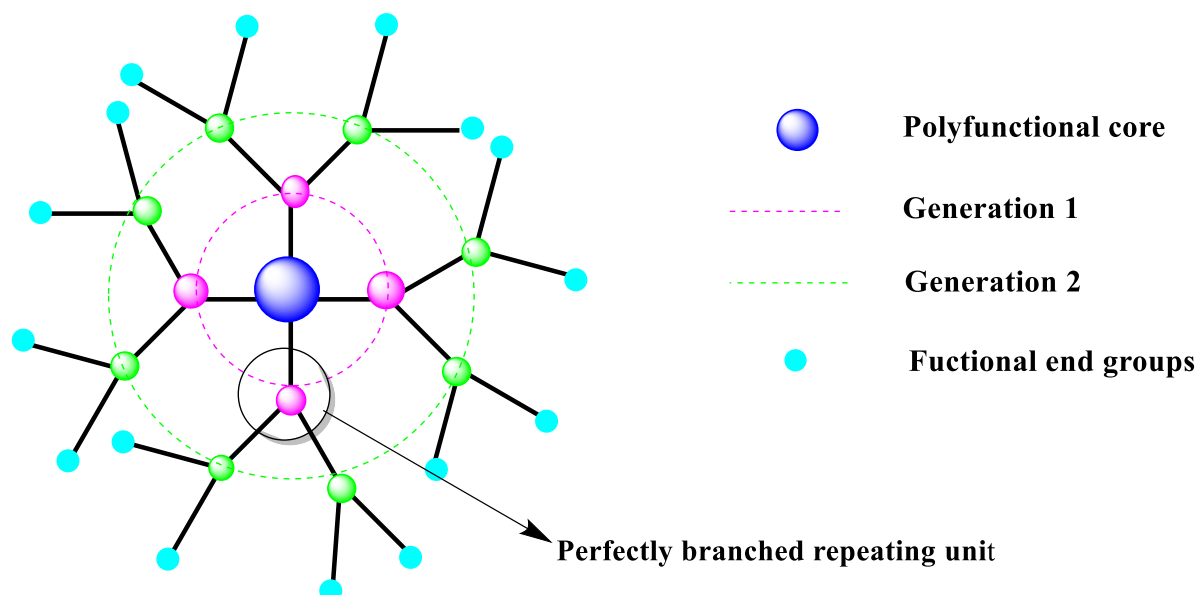


Figure 1.14: Provides a visual depiction of the basic structure of dendrimers. These macromolecules are extensively branched and resemble a tree-like form, originating from a central core. From this core, multiple generations of repeating units extend outward, creating a layered architecture. Each successive generation consists of an increasing number of branches, contributing to the dendrimer's complex and highly branched structure.

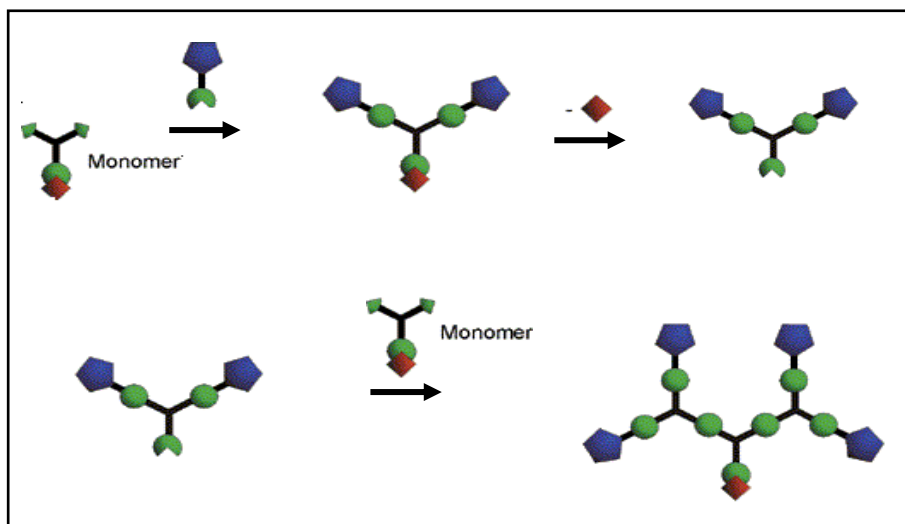
## Dendrimers Synthesis Methods

Dendrimers can be synthesized in a controlled manner, enabling the creation of structures with a variety of backbones and surface functional groups. The two primary methods for the synthesis of dendrimers are the convergent and divergent approaches. (figure 1.15).<sup>61</sup> Divergent synthesis, pioneered by Donald Tomalia, involves initiating growth from a



polyfunctional core, expanding radially outward to form the dendrimer. In contrast, Craig Hawker and Jean Fréchet introduced the convergent synthesis method, where dendrimers are assembled by building outward from the surface toward central focal points. While both techniques result in structurally equivalent dendrimers, each has its own distinct advantages and limitations.<sup>62</sup>

a)



b)

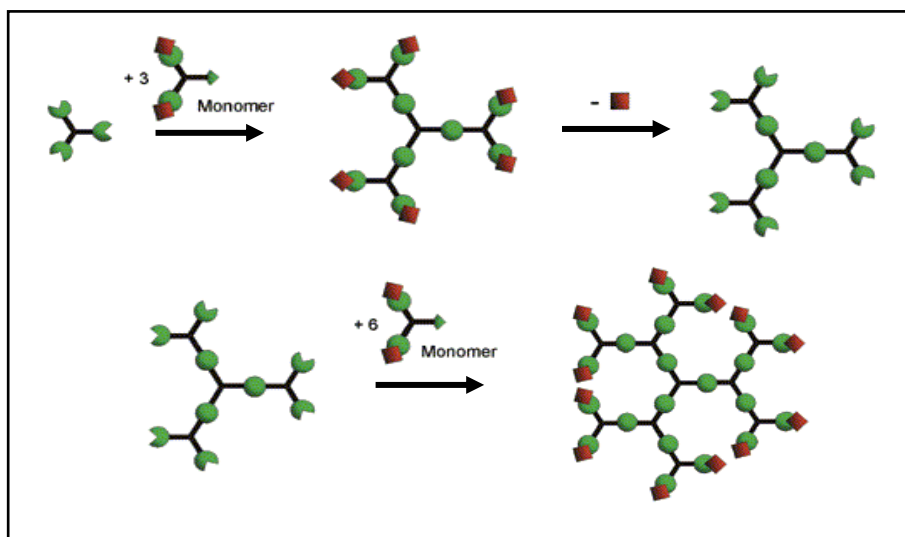


Figure 1.15: Illustrates the two primary approaches for dendrimer synthesis: (A) the convergent method and (B) the divergent method.

Divergent synthesis is commonly used for large-scale dendrimer production but can lead to defects such as missing arms or dimers due to the iterative reaction steps and steric hindrance at the periphery.<sup>63</sup> Synthesizing dendrimers via this method poses challenges, particularly during purification, as the complex branching and numerous functional groups make traditional purification methods labor-intensive. These issues are mitigated by the alternative convergent synthesis method.<sup>64</sup> In this approach, individual molecular building blocks, or "dendrons," are synthesized and purified separately to ensure structural purity. These purified dendrons are then "converged" with a polyfunctional core molecule, resulting in a dendrimer. This method simplifies purification and produces well-defined dendrimers with fewer impurities, offering a more controlled and efficient synthesis process.<sup>65</sup>

However, divergent synthesis encounters difficulties when generating high-generation (5G and 6G) dendrimers due to steric congestion around the core. Both divergent and convergent approaches have their restrictions, particularly because dendrimer dimensions, surface area, and backbone structure significantly influence their biological interactions. In the present research, PAMAM dendrimers will be synthesized using the divergent method, as it is adaptable and capable of producing modified and functionalized dendrimers.<sup>66</sup>

## Properties of Dendrimers

Unlike linear polymers, dendrimers possess a uniform and highly organized geometry. Their non-dispersive nature results from a precisely controlled polymerization process, ensuring consistency throughout synthesis. The unique spherical architecture and dimensions of

dendrimers closely mimic those of several key biological polymers. These structural features, combined with their biological properties, make dendrimers highly valuable in biomedical applications.<sup>67</sup>

## Biocompatibility

For polymer-based carriers in biomedical uses, ensuring they are non-toxic, and biodegradable is essential for safety. Dendrimers, a class of highly branched polymers, exhibit cytotoxicity that largely depends on their surface groups, which directly interact with cells. The surface charge plays a critical role in determining toxicity: positively charged dendrimers, such as PAMAM (polyamidoamine) dendrimers, can disrupt cell membranes, leading to cell lysis. This disruption is primarily due to the strong interactions between the cationic groups and negatively charged cell membranes.

In particular, PAMAM dendrimers with amine-terminated surfaces (positively charged) exhibit higher cytotoxicity compared to their anionic or neutral counterparts. Studies have shown that modifying the surface groups, such as introducing hydroxyl groups (PAMAM–OH), can significantly reduce cytotoxicity. These dendrimers demonstrate lower toxicity levels, making them more suitable for biomedical applications like drug delivery. Despite many *in vitro* studies on dendrimer cytotoxicity, *in vivo* research remains limited, although some studies have explored their biocompatibility and clearance pathways. For example, PAMAM dendrimers are commonly used in drug delivery systems due to their ability to encapsulate drugs and enhance solubility. However, balancing their high functionality with biocompatibility remains a challenge, and further *in vivo* studies are crucial to fully understand their potential in clinical applications.<sup>69, 70</sup>

## Solubility

Solubility plays a critical role in the effectiveness of dendrimers, particularly in biomedical applications, where it impacts drug delivery, biocompatibility, and overall efficacy. Functional groups on the dendrimer surface largely determine solubility. A common approach to improving solubility is through surface modification, such as conjugating polyethylene glycol (PEG), acetyl, or hydroxyl groups.<sup>71</sup> These modifications not only improve solubility in polar solvents like water but also reduce cytotoxicity and enhance drug-binding capabilities. Dendrimers' unique spherical architecture and internal cavities, particularly in higher generations, make them ideal for encapsulating hydrophobic drugs. This capacity allows them to increase the solubility of poorly water-soluble drugs by encapsulating them within their structure. For instance, PEGylation or the addition of hydroxyl groups increases dendrimer solubility and helps improve the bioavailability of encapsulated drugs, which is crucial for drug delivery systems. This ability to encapsulate, along with controlled release properties, makes dendrimers particularly valuable in enhancing the solubility and therapeutic performance of hydrophobic drugs in pharmaceutical applications.<sup>72</sup>

## Distribution:

The distribution of dendrimers is a key pharmacokinetic property that influences how effectively these polymeric carriers can deliver therapeutic agents throughout body tissues and fluids. Size and surface modifications, such as PEGylation or functionalization with targeting ligands, play significant roles in determining biodistribution. For instance, smaller dendrimers tend to be cleared rapidly through renal filtration, while larger dendrimers exhibit prolonged

circulation times. To achieve targeted delivery, dendrimers can be engineered to accumulate in specific tissues, particularly tumors, by exploiting the enhanced permeability and retention (EPR) effect.<sup>73</sup> For effective *in vivo* applications, dendrimers must demonstrate selective distribution patterns that allow them to reach targeted tissues without causing off-target toxicity. Research has shown that modifying dendrimer surfaces to create neutral or negatively charged surfaces can reduce nonspecific interactions with cells, further refining their distribution and enhancing drug delivery accuracy.<sup>74, 75</sup>

## References:

1. Jones, S. and Thornton, J.M., 1996. Principles of Protein-Protein Interactions. *Proceedings of The National Academy of Sciences*, 93(1), pp.13-20.
2. Bahadur, R.P. and Zacharias, M., 2008. The Interface of Protein-Protein Complexes: Analysis of Contacts and Prediction of Interactions. *Cellular and Molecular Life Sciences*, 65, pp.1059-1072.
3. Hirabayashi, J., Yamada, M., Kuno, A. and Tatenno, H., 2013. Lectin Microarrays: Concept, Principle and Applications. *Chemical Society Reviews*, 42(10), pp.4443-4458.
4. Eisenhaber, F., Persson, B. and Argos, P., 1995. Protein Structure Prediction: Recognition of Primary, Secondary, and Tertiary Structural Features from Amino Acid Sequence. *Critical Reviews in Biochemistry and Molecular Biology*, 30(1), pp.1-94.
5. Vendruscolo, M., Zurdo, J., MacPhee, C.E. and Dobson, C.M., 2003. Protein Folding and Misfolding: A Paradigm of Self-Assembly and Regulation in Complex Biological Systems. *Philosophical Transactions of the Royal Society of London. Series A: Mathematical, Physical and Engineering Sciences*, 361(1807), pp.1205-1222.
6. Keskin, O., Gursoy, A., Ma, B. and Nussinov, R., 2008. Principles of Protein-Protein Interactions: What are the Preferred Ways for Proteins to Interact? *Chemical Reviews*, 108(4), pp.1225-1244.

7. Safari-Alighiarloo, N., Taghizadeh, M., Rezaei-Tavirani, M., Goliaei, B. and Peyvandi, A.A., 2014. Protein-Protein Interaction Networks (PPI) and Complex Diseases. *Gastroenterology and Hepatology from Bed to Bench*, 7(1), p.17.
8. Skaug, M.J., 2011. *Single Molecule Dynamics in Lipid Membranes*. University of California, Davis.
9. Vega, S., Abian, O. and Velazquez-Campoy, A., 2019. Handling Complexity in Biological Interactions: Allostery and Cooperativity in Proteins. *Journal of Thermal Analysis and Calorimetry*, 138(5), pp.3229-3248.
10. Stites, W.E., 1997. Protein– Protein Interactions: Interface Structure, Binding Thermodynamics, and Mutational Analysis. *Chemical Reviews*, 97(5), pp.1233-1250.
11. Baker, C.M. and Grant, G.H., 2007. Role of Aromatic Amino Acids in Protein– Nucleic Acid Recognition. *Biopolymers: Original Research on Biomolecules*, 85(5-6), pp.456-470.
12. Gilles, P., Wenck, K., Stratmann, I., Kirsch, M., Smolin, D.A., Schaller, T., de Groot, H., Kraft, A. and Schrader, T., 2017. High-Affinity Copolymers Inhibit Digestive Enzymes by Surface Recognition. *Biomacromolecules*, 18(6), pp.1772-1784.
13. Jones, S. and Thornton, J.M., 1997. Analysis of Protein-Protein Interaction Sites Using Surface Patches. *Journal of Molecular Biology*, 272(1), pp.133-143.
14. Janin, J., 1999. Geometric Features in Protein–Protein and Protein–DNA Recognition. *Perspectives in Structural Biology: A Volume in Honour of GN Ramachandran*, p.226.
15. Conte, L.L., Chothia, C. and Janin, J., 1999. The Atomic Structure of Protein-Protein Recognition Sites. *Journal of Molecular Biology*, 285(5), pp.2177-2198.

16. Zhou, H.X. and Pang, X., 2018. Electrostatic Interactions in Protein Structure, Folding, Binding, and Condensation. *Chemical Reviews*, 118(4), pp.1691-1741.
17. Zinzalla, G. and Thurston, D.E., 2009. Targeting Protein–Protein Interactions for Therapeutic Intervention: A Challenge for The Future. *Future Medicinal Chemistry*, 1(1), pp.65-93.
18. Higuero, A.P., Jubb, H. and Blundell, T.L., 2016. Protein–Protein Interactions as Druggable Targets: Recent Technological Advances. *Cell Communication and Signaling*, 14(1), p.8.
19. Fischer, G., Rossmann, M. and Hyvönen, M., 2015. Alternative Modulation of Protein–Protein Interactions by Small Molecules. *Current Opinion in Biotechnology*, 35, pp.78-85.
20. Arkin, M.R., Tang, Y. and Wells, J.A., 2014. Small-Molecule Inhibitors of Protein-Protein Interactions: Progressing Toward the Reality. *Chemistry & biology*, 21(9), pp.1102-1114.
21. Gohlke, H. and Klebe, G., 2002. Approaches to the Description and Prediction of the Binding Affinity of Small-Molecule Ligands to Macromolecular Receptors. *Angewandte Chemie International Edition*, 41(15), pp.2644-2676.
22. Poreba, M., Szalek, A., Kasperkiewicz, P., Rut, W., Salvesen, G.S. and Drag, M., 2015. Small Molecule Active Site Directed Tools for Studying Human Caspases. *Chemical Reviews*, 115(22), pp.12546-12629.
23. Wu, K., Karapetyan, E., Schloss, J., Vadgama, J. and Wu, Y., 2023. Advancements in Small Molecule Drug Design: A Structural Perspective. *Drug Discovery Today*, p.103730.



24. Toogood, P.L., 2002. Inhibition of Protein– Protein Association by Small Molecules: Approaches and Progress. *Journal of Medicinal Chemistry*, 45(8), pp.1543-1558.
25. Jin, L., Wang, W. and Fang, G., 2014. Targeting Protein-Protein Interaction by Small Molecules. *Annual Review of Pharmacology and Toxicology*, 54(1), pp.435-456.
26. Mannhold, R., Kubinyi, H. and Folkers, G., 2013. *Protein-Protein Interactions in Drug Discovery*. John Wiley & Sons.
27. Winter, A., Higuero, A.P., Marsh, M., Sigurdardottir, A., Pitt, W.R. and Blundell, T.L., 2012. Biophysical and Computational Fragment-Based Approaches to Targeting Protein–Protein Interactions: Applications in Structure-Guided Drug Discovery. *Quarterly Reviews of Biophysics*, 45(4), pp.383–426.
28. Yavuz, B., Morgan, J.L., Showalter, L., Horng, K.R., Dandekar, S., Herrera, C., LiWang, P. and Kaplan, D.L., 2018. Pharmaceutical Approaches to HIV Treatment and Prevention. *Advanced Therapeutics*, 1(6), p.1800054.
29. Zhang, Q., Zeng, S.X. and Lu, H., 2014. Targeting P53-MDM2-MDMX Loop for Cancer Therapy. *Mutant P53 and MDM2 in Cancer*, pp.281–319.
30. McMillan, J.M., 1999. Galactosamine Decreases Nitric Oxide Formation in Cultured Rat Hepatocytes: Mechanism of Suppression. *Journal of Biochemical and Molecular Toxicology*, 13(3-4), pp.143–148.

31. Esposito, E. and Cuzzocrea, S., 2009. TNF-Alpha as a Therapeutic Target in Inflammatory Diseases, Ischemia-Reperfusion Injury and Trauma. *Current Medicinal Chemistry*, 16(24), pp.3152–3167.
32. Li, T., Lu, X.M., Zhang, M.R., Hu, K. and Li, Z., 2022. Peptide-Based Nanomaterials: Self-Assembly, Properties and Applications. *Bioactive Materials*, 11, pp.268–282.
33. Madden, D.R., 1995. The Three-Dimensional Structure of Peptide-MHC Complexes. *Annual Review of Immunology*, 13(1), pp.587–622.
34. Lamers, C., 2022. Overcoming the Shortcomings of Peptide-Based Therapeutics. *Future Drug Discovery*, 4(2), p.FDD75.
35. Tsomaia, N., 2015. Peptide Therapeutics: Targeting the Undruggable Space. *European Journal of Medicinal Chemistry*, 94, pp.459–470.
36. Mulder, K.C., Lima, L.A., Miranda, V.J., Dias, S.C. and Franco, O.L., 2013. Current Scenario of Peptide-Based Drugs: The Key Roles of Cationic Antitumor and Antiviral Peptides. *Frontiers in Microbiology*, 4, p.321.

37. Mignani, S., El Kazzouli, S., Bousmina, M.M. and Majoral, J.P., 2014. Dendrimer Space Exploration: An Assessment of Dendrimers/Dendritic Scaffolding as Inhibitors of Protein–Protein Interactions, a Potential New Area of Pharmaceutical Development. *Chemical Reviews*, 114(2), pp.1327–1342.
38. Leung, D.K., Yang, Z. and Breslow, R., 2000. Selective Disruption of Protein Aggregation by Cyclodextrin Dimers. *Proceedings of the National Academy of Sciences of the United States of America*, 97(10), pp.5050–5053.
39. Rae, J.M. and Jachimska, B., 2021. Analysis of Dendrimer–Protein Interactions and Their Implications on Potential Applications of Dendrimers in Nanomedicine. *Nanoscale*, 13(5), pp.2703–2713.
40. Cai, X., Javor, S., Gan, B.H., Köhler, T. and Reymond, J.L., 2021. The Antibacterial Activity of Peptide Dendrimers and Polymyxin B Increases Sharply Above pH 7.4. *Chemical Communications*, 57(46), pp.5654–5657.
41. Lee, J.H., Zhang, Q., Jo, S., Chai, S.C., Oh, M., Im, W., Lu, H. and Lim, H.S., 2011. Novel Pyrrolopyrimidine-Based  $\alpha$ -Helix Mimetics: Cell-Permeable Inhibitors of Protein–Protein Interactions. *Journal of the American Chemical Society*, 133(4), pp.676–679.

42. Scott, D.E., Bayly, A.R., Abell, C. and Skidmore, J., 2016. Small Molecules, Big Targets: Drug Discovery Faces the Protein–Protein Interaction Challenge. *Nature Reviews Drug Discovery*, 15(8), pp.533–550.
43. Caporale, A., Adorinni, S., Lamba, D. and Saviano, M., 2021. Peptide–Protein Interactions: From Drug Design to Supramolecular Biomaterials. *Molecules*, 26(5), p.1219.
44. Honarparvar, B., Govender, T., Maguire, G.E., Soliman, M.E. and Kruger, H.G., 2014. Integrated Approach to Structure-Based Enzymatic Drug Design: Molecular Modeling, Spectroscopy, and Experimental Bioactivity. *Chemical Reviews*, 114(1), pp.493–537.
45. Jordan, B.J., Subramani, C. and Rotello, V.M., 2010. Functional Nanoparticles as Catalysts and Sensors. In: *John Wiley & Sons Inc.*, pp.301–331.
46. Mignani, S., El Kazzouli, S., Bousmina, M.M. and Majoral, J.P., 2014. Dendrimer Space Exploration: An Assessment of Dendrimers/Dendritic Scaffolding as Inhibitors of Protein–Protein Interactions, a Potential New Area of Pharmaceutical Development. *Chemical Reviews*, 114(2), pp.1327–1342.
47. Wang, Y., Di, S., Yu, J., Wang, L. and Li, Z., 2023. Recent Advances of Graphene–Biomacromolecule Nanocomposites in Medical Applications. *Journal of Materials Chemistry B*, 11(3), pp.500–518.

48. Moiani, D., Salvalaglio, M., Cavallotti, C., Bujacz, A., Redzyna, I., Bujacz, G., Dinon, F., Pengo, P. and Fassina, G., 2009. *The Journal of Physical Chemistry B*, 113(50), pp.16268–16275.
49. Chiba, F., Hu, T.C., Twyman, L.J. and Wagstaff, M., 2010. Dendritic Macromolecules as Inhibitors to Protein-Protein Binding. In: *Macromolecular Symposia*, 287(1), pp.37–41. Weinheim: Wiley-VCH Verlag.
50. Astruc, D. and Chardac, F., 2001. Dendritic Catalysts and Dendrimers in Catalysis. *Chemical Reviews*, 101(9), pp.2991–3024.
51. Lafuente Fabra, M., 2018. Study and Applications of Dynamic Chemical Networks of Pseudopeptidic Compounds.
52. Moulin, E., Cormos, G. and Giuseppone, N., 2012. Dynamic Combinatorial Chemistry as a Tool for the Design of Functional Materials and Devices. *Chemical Society Reviews*, 41(3), pp.1031–1049.
53. Li, J., Nowak, P. and Otto, S., 2013. Dynamic Combinatorial Libraries: From Exploring Molecular Recognition to Systems Chemistry. *Journal of the American Chemical Society*, 135(25), pp.9222–9239.
54. Jaegle, M., Nawrotsky, E., Wong, E.L., Arkona, C. and Rademann, J., 2016. Protein-Templated Fragment Ligation Methods: Emerging Technologies in Fragment-Based Drug Discovery. In: *Fragment-Based Drug Discovery Lessons and Outlook*, pp.293–326.

55. Raynal, M., Ballester, P., Vidal-Ferran, A. and Van Leeuwen, P.W., 2014. Supramolecular Catalysis. Part 2: Artificial Enzyme Mimics. *Chemical Society Reviews*, 43(5), pp.1734–1787.
56. Adamski, P.R., 2023. Integration of Compartmentalization and Metabolism in Systems of Synthetic Replicators.
57. Komáromy, D., Nowak, P. and Otto, S., 2017. Dynamic Combinatorial Libraries. In: *Dynamic Covalent Chemistry: Principles, Reactions, and Applications*, pp.31–119.
58. Inoue, K., 2000. Functional Dendrimers, Hyperbranched and Star Polymers. *Progress in Polymer Science*, 25(4), pp.453–571.
59. Medina, S.H. and El-Sayed, M.E., 2009. Dendrimers as Carriers for Delivery of Chemotherapeutic Agents. *Chemical Reviews*, 109(7), pp.3141–3157.
60. Das, N., Sharma, P.A., Seth, A., Maheshwari, R., Tekade, M., Shrivastava, S.K. and Tekade, R.K., 2018. An Overview of Dendrimers and Their Biomedical Applications. In: *Dendrimers for Drug Delivery*, pp.135–206.
61. Singh, S.K., Lohiya, G.K., Limburkar, P.P., Dharbale, N.B. and Mourya, V.K., 2009. Dendrimer: A Versatile Polymer in Drug Delivery. *Asian Journal of Pharmaceutics (AJP)*, 3(3).
62. Tomalia, D.A., 2005. Dendrimeric Supramolecular and Supramacromolecular Assemblies. In: *Supramolecular Polymers*, pp.201–270. CRC Press.

63. Thakur, A. and Sharma, A., 2021. Synthesis of Dendrimers. In: *Dendrimers in Nanomedicine*, pp.89–122. CRC Press.
64. Campagna, S., Ceroni, P. and Puntoriero, F. eds., 2011. *Designing Dendrimers*. John Wiley & Sons.
65. Nazemi, A. and Gillies, E.R., 2014. Dendrimer Bioconjugates: Synthesis and Applications. In: *Chemistry of Bioconjugates: Synthesis, Characterization, and Biomedical Applications*, pp.146–183.
66. Kalovidouris, S.A., 2002. Constructing Carbohydrate-Based Multivalent Scaffolds for Studying Carbohydrate–Protein Interactions. University of California, Los Angeles.
67. Kharwade, R., More, S., Warokar, A., Agrawal, P. and Mahajan, N., 2020. Starburst PAMAM Dendrimers: Synthetic Approaches, Surface Modifications, and Biomedical Applications. *Arabian Journal of Chemistry*, 13(7), pp.6009–6039.
68. Yellepeddi, V.K., Kumar, A. and Palakurthi, S., 2009. Surface Modified Poly (Amido) Amine Dendrimers as Diverse Nanomolecules for Biomedical Applications. *Expert Opinion on Drug Delivery*, 6(8), pp.835–850.
69. Alfei, S. and Schito, A.M., 2020. From Nanobiotechnology, Positively Charged Biomimetic Dendrimers as Novel Antibacterial Agents: A Review. *Nanomaterials*, 10(10), p.2022.
70. Borowska, K., Wolowiec, S., Rubaj, A., Glowniak, K., Sieniawska, E. and Radej, S., 2014. Bioapplications of Poly(Amidoamine) (PAMAM) Dendrimers in Nanomedicine. *Journal of Nanoparticle Research*, 16(9), p.2342.

71. Araújo, R.V. de, Santos, S. da S., Igne Ferreira, E. and Giarolla, J., 2018. New Advances in General Biomedical Applications of PAMAM Dendrimers. *Molecules*, 23(11), p.2849.
72. Jain, N.K. and Gupta, U., 2008. Application of Dendrimer–Drug Complexation in the Enhancement of Drug Solubility and Bioavailability. *Expert Opinion on Drug Metabolism & Toxicology*, 4(8), pp.1035–1052.
73. Wang, J., Li, B., Qiu, L., Qiao, X. and Yang, H., 2022. Dendrimer-Based Drug Delivery Systems: History, Challenges, and Latest Developments. *Journal of Biological Engineering*.
74. Sehrawat, A., Basak, A. and Höfner, G., 2023. GPR119 Agonists as Potential Therapeutics for Type 2 Diabetes: Challenges and Prospects. *Journal of Pharmacy and Pharmacology*.
75. Zhang, F., Mastorakos, P., Mishra, M.K., Mangraviti, A., Hwang, L., Zhou, J., Hanes, J., Brem, H., Olivi, A., Tyler, B. and Kannan, R.M., 2015. Uniform Brain Tumor Distribution and Tumor Associated Macrophage Targeting of Systemically Administered Dendrimers. *Biomaterials*, 52, pp.507–516.



## Chapter 2

# Magnetic Nanoparticles

## Introduction:

### Iron oxides:

Iron, though present in extremely small quantities in its elemental form on the Earth's surface, becomes far more abundant when combined with other elements, forming a wide variety of ores. These ores are widely distributed across the globe. Significant deposits can be found in virtually every region, highlighting their extensive presence. Among the most common and economically valuable iron ores are iron oxides, including magnetite ( $\text{Fe}_3\text{O}_4$ ) and hematite ( $\text{Fe}_2\text{O}_3$ ). These particular ores have played a critical role in the development of industrial iron and steel production due to their rich iron content. Mt. Whaleback in Western Australia is one of the largest and most famous examples of such deposits, consisting primarily of magnetite. It has been actively mined for its high-quality iron ore, contributing significantly to Australia's standing as a major iron producer on the global stage (Silver, 1993).

However, Mt. Whaleback's extensive magnetite deposits have historically posed unique challenges. In the 1960s, it was discovered that the high iron content in the region, specifically magnetite, caused significant disruptions to magnetic navigation systems used by airplanes. The magnetic field generated by the large concentration of iron was strong enough to interfere with aircraft navigation from a considerable distance, rendering the area hazardous for air travel until these effects were better understood and mitigated. This magnetic anomaly underscores the unique physical properties of iron ores like magnetite, which are not only valuable for their metal content but also for their magnetic characteristics (Silver, 1993).

In total, there are sixteen different types of iron oxides that have been identified, all of which vary in their chemical composition and geological formation. These iron oxides can be classified into three main categories: oxides, hydroxides, and oxide-hydroxides. Each type exhibits distinct physical and chemical properties that make them useful for different industrial and scientific applications. For example, magnetite is particularly notable for its magnetic properties, which are leveraged in various technological applications beyond metallurgy, while hematite is prized for its role in the steelmaking process due to its high iron content and ease of processing. The different types of iron oxides, including their detailed chemical structures and physical characteristics, are listed in table 2.1, providing a comprehensive understanding of the various forms in which iron occurs naturally. These variations in iron oxide composition also play a crucial role in determining how iron ores are processed and utilized in different industries, highlighting the versatility and importance of iron as a material.

Name	Chemical Formula	Colour	Magnetic behaviour at RT
Goethite	$\alpha\text{-FeOOH}$	Yellow-brown	Antiferromagnetic
Lepidocrocite	$\beta\text{-FeOOH}$	Orange	Paramagnetic
Akaganeite	$\gamma\text{-FeOOH}$	Brown to bright yellow	Paramagnetic
	$\delta\text{-FeOOH}$	Red-brown	Ferrimagnetic
Feroxyhyte	$\delta\text{-Fe}^{3+}\text{O}(\text{OH})$	Red-brown	Superparamagnetic
	High Pressure $\delta\text{-Fe}^{3+}\text{O}(\text{OH})$		
Ferrihydrite	$\text{Fe}_5(\text{OH})_8 \cdot 4\text{H}_2\text{O}$	Reddish brown	Superparamagnetic
Bernalite	$\text{Fe}(\text{OH})_3$	Greenish	Weakly ferromagnetic
	$\text{Fe}(\text{OH})_2$ Iron (II) hydroxide	White	
Schwertmannite	$\text{Fe}_{16}\text{O}_{16}(\text{OH})_y(\text{SO}_4) \cdot n\text{H}_2\text{O}$	Yellow	Paramagnetic
Haematite	$\alpha\text{-Fe}_2\text{O}_3$	Red	Weakly ferromagnetic
Magnetite	$\text{Fe}_3\text{O}_4$	Black	Ferromagnetic
Maghemite	$\gamma\text{-Fe}_2\text{O}_3$	Dark Brown	Ferromagnetic
	$\beta\text{-Fe}_2\text{O}_3$		
	$\varepsilon\text{-Fe}_2\text{O}_3$		
Wustite	$\text{FeO}$	Black	Paramagnetic

Table 2.1: Provides a comprehensive list of the sixteen known iron oxides, as documented by Cornell and Schwertmann in 1996.<sup>2</sup> These iron oxides, which include various phases and polymorphs, differ in their chemical composition, crystallographic structure, and physical properties.

## Nanoparticles:

In addition to their geological importance, iron oxides play a key role in modern nanotechnology due to their magnetic properties, which are exploited in various applications involving magnetic nanoparticles (MNPs). Exploration of nanoparticles and their potential applications have sparked a lot of interest in the last few years, it is phrased as “the problem of manipulating and controlling things on a small scale” by the physicist and Nobel winner Richard Feynman<sup>3</sup>. Despite being recognised as a novel technology, the utilisation of nanoparticles extends to drug delivery, catalysis, food production, cosmetics and the various advanced fields of nanomaterials tailored with specialised features. Some Roman glassworks that date back more than two millennia were coloured with nanoparticle-coloured glasses. (Barber and Freestone, 1990; Wagner et al., 2000)<sup>4&5</sup>. Over a century and a half ago, Faraday introduced his gold sols to the Royal Society in London, (documented Faraday, 1857)<sup>6</sup>. Another example of using of nanoparticles can be the development of photography during the 19th century as containing nanoparticles.<sup>7</sup>

## Magnetic Nanoparticles (MNPs):

Magnetic nanoparticles (MNPs) have emerged as a versatile and powerful tool in various scientific and technological fields due to their unique magnetic properties at the nanoscale. Typically composed of iron oxides, such as magnetite ( $\text{Fe}_3\text{O}_4$ ) or maghemite ( $\gamma\text{-Fe}_2\text{O}_3$ ), MNPs exhibit superparamagnetic behavior when their size is reduced to a critical threshold, usually between 1 to 100 nanometers.<sup>9</sup> This allows them to become magnetized in the presence of an external magnetic field and to lose their magnetism once the field is removed, making them particularly useful in applications where controlled magnetic responses are required. The development of MNPs has been driven by the ability to manipulate their properties by altering their size, shape, composition, and surface chemistry. This tunability allows researchers to optimize their behavior for specific applications, including in medicine, environmental science, catalysis, and data storage. Among these, biomedical applications have been one of the most actively explored areas due to the biocompatibility and controllability of MNPs.<sup>10</sup>

The core-shell structure is one of the most common forms of MNPs, where a magnetic core is surrounded by a protective shell. The shell can be composed of organic molecules, polymers, or inorganic materials, which enhance the stability and functionality of the nanoparticles. The surface of the shell can be functionalized with various ligands to target specific cells or molecules in biomedical applications.<sup>11,12</sup>

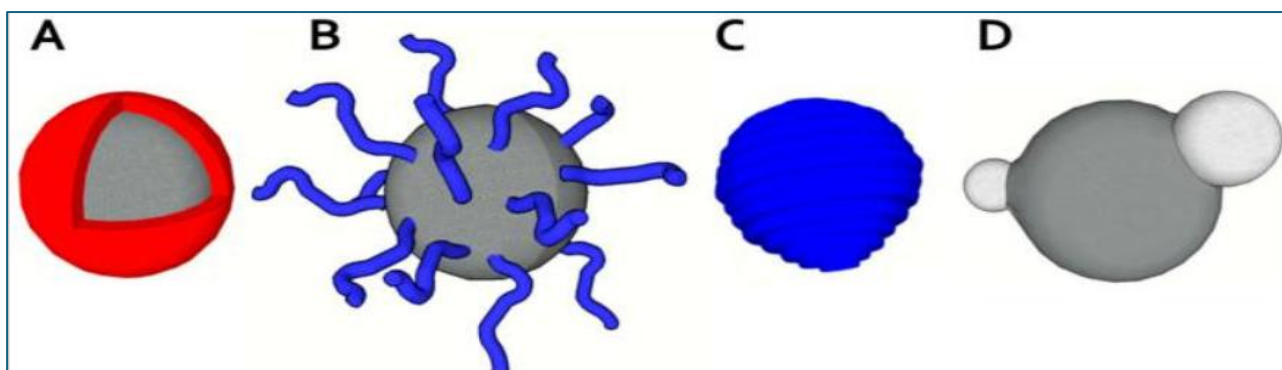


Figure 2.1: Schematic representations of various magnetic nanoparticle structures and their coating strategies: (A) Core-shell structure with a magnetic core surrounded by a protective shell; (B) Magnetic nanoparticle coated with a polymer via end-grafting; (C) Completely encapsulated magnetic particle with a full polymer coating; (D) Heterodimer configuration consisting of two distinct magnetic components. (Adapted with permission from reference 12, National Library of Medicine).

### The nanoscale, nanoscience, and nanotechnology:

The general definition of Nanotechnology is having one dimension between 1 and 100nm, however there exist applications where the dimension of interest falls below 1 nm or larger than 100 nm. Figure 2.2 (A & B) provides a comprehensive depiction of the relative scale of various objects, incorporating both natural and synthetic materials for comparison. This visual representation highlights the vast range of sizes, from the smallest nanoparticles and molecules to much larger biological and man-made structures. Additionally, the figure includes the electromagnetic radiation spectrum, which serves to contextualize these objects within the broader framework of different wavelengths of light. By integrating these elements, the figure offers a detailed perspective on how these diverse entities relate to one another in terms of size and their interactions with electromagnetic radiation. This comparative scale helps to illustrate the remarkable

diversity in the dimensions of both natural phenomena and human-engineered materials, emphasizing the unique properties and applications that arise at different scales.<sup>7</sup>

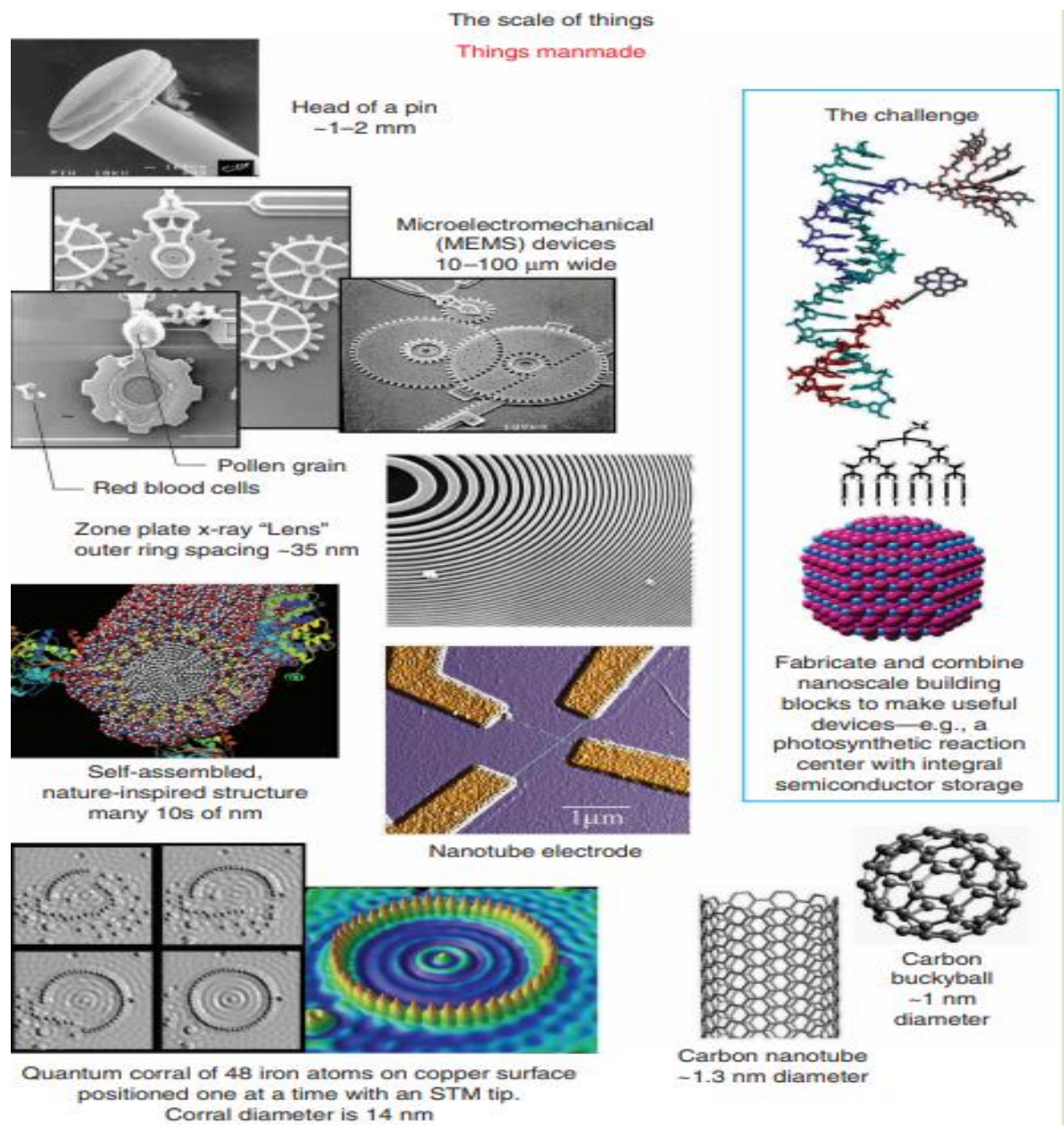


Figure 2.2 (A): Offers a comparative visual representation of nanoscale and man-made objects, as provided by The Richard E. Smalley Institute at Rice University. This figure highlights the dramatic differences in size between objects at the nanoscale and more familiar macroscopic objects created by humans.



## The scale of things

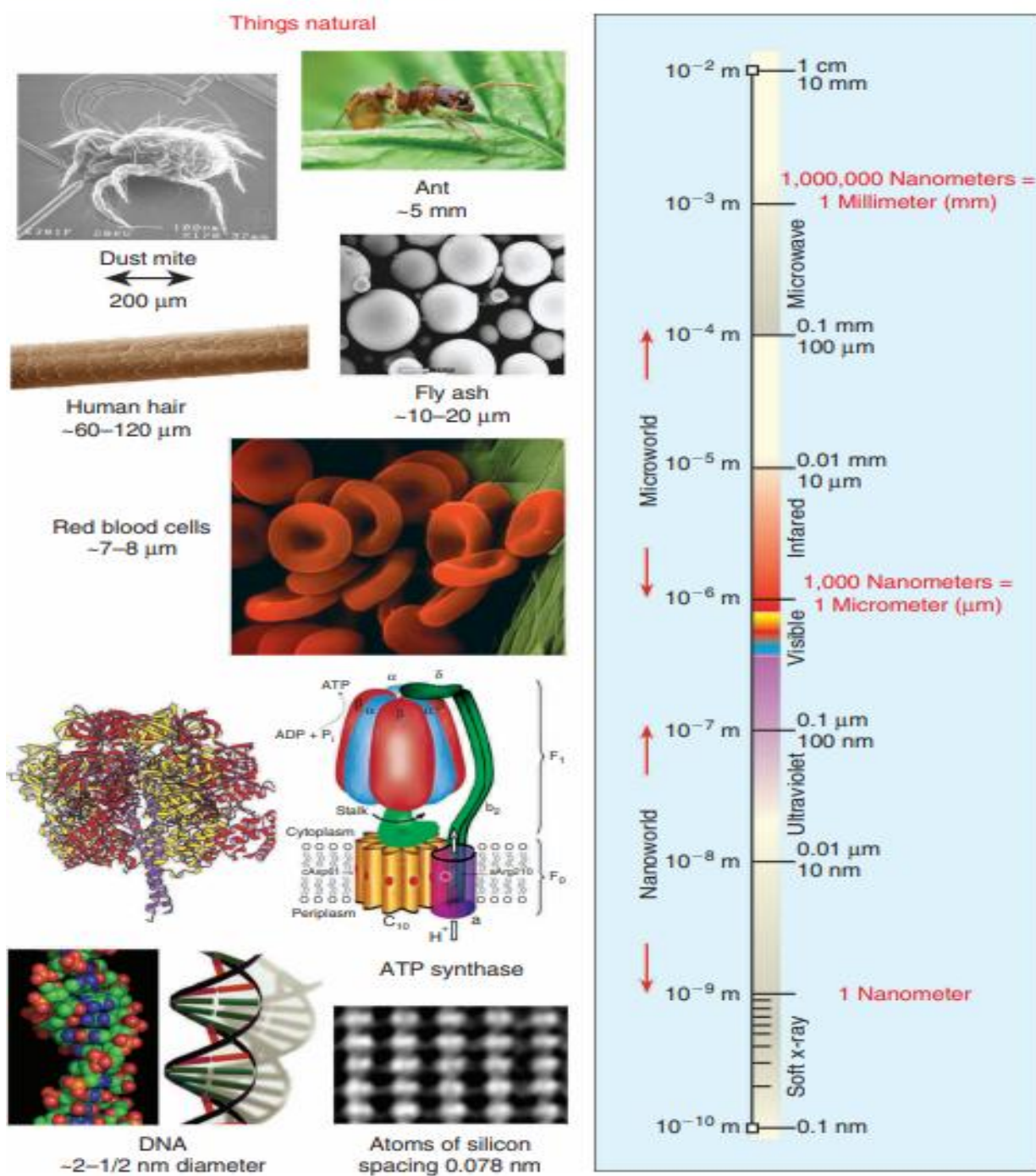


Figure 2.2 (B): Provides a comparison of nanoscale objects and naturally occurring structures, as illustrated by The Richard E. Smalley Institute at Rice University. This figure visually contrasts the scale of nanomaterials with various biological and natural entities, highlighting the incredible diversity in size that exists within nature.

Since the nanoscale is the transitional region between atoms and bulk materials, where notable departures from the bulk material's behaviour can be witnessed, it is of great interest.

### Natural nanoparticles:

Nanoparticles can significantly impact natural activities and can appear in the environment naturally. To give an example, the radiative balance of the Earth's atmosphere can be directly and indirectly changed by atmospheric aerosols (Wang et al., 2010).<sup>13</sup> Natural nanoparticles comprising sea salt, sulphates and miscellaneous organic chemicals were found in an Irish location. These particles most likely originated in plankton that was close to the surface of sea (O'Dowd et al., 2004).<sup>14</sup> Furthermore, magnetic iron nanoparticles were discovered in a tap water sample through studies; these are probably the result of corrosion and may act as sites for the adsorption of pollutants such as lead, copper, and arsenic. The flowing water samples contained ferromagnetic particles larger than 100 nm in multiple domains, as well as clusters of very fine superparamagnetic subdomain particles, with sizes ranging from 3.2 to 5.6 nm. In stagnant water samples, besides the small superparamagnetic subdomain particles, there were also larger subdomain particles averaging between 59 and 67 nm. Both large and small subdomain particles were captured by the fine charcoal in household filters (Senftle et al., 2007; Barkatt et al., 2009).<sup>15,16</sup>

Measurements of the atmosphere in urban areas, secluded islands, woods, and far-off troposphere have consistently shown times when concentrations of up to 106 nanoparticles/cm<sup>3</sup> occur (Smith, 2009),<sup>17</sup> these particles, especially when they originate from polluting processes, may be harmful to human health (Bang and Murr, 2002).<sup>18</sup>

## Nanoparticle movement - Brownian motion:

Brownian motion is a phenomenon seemingly a random movement of particles suspended in a fluid. It was discovered by botanist Robert Brown, who noticed the motion in pollen grains (Brown, 1828).<sup>19</sup> Since then, Einstein (1905),<sup>20</sup> Perrin (1909 & 1913),<sup>21,22</sup> and Smoluchowski (1906, 1916a, b),<sup>23,24,25</sup> among others, have made significant contributions to our knowledge of this phenomenon. There are numerous examples of Brownian motion, with suspended nanoparticles being one of them, exhibiting similar movement characteristics. The smaller the suspended particles, the faster their motion. This movement remains stable and continuous as long as the particles stay suspended in the fluid. It is largely unaffected by external factors such as electric fields, light, gravity, or other outside influences. However, temperature plays a significant role, which is expected, as the motion also relies on the viscosity of the medium.

## Magnetism:

The motion of electrons around atoms is a source of magnetism and each atom retains a tiny permanent magnet moment. In addition, an atom's electron can create its own orbital magnetic moment as it spins on its own axis and make an extra source of magnetism (see figure 2.3 below). In the majority of materials, these magnetic moments offset each other, resulting in the absence of any overall magnetization.

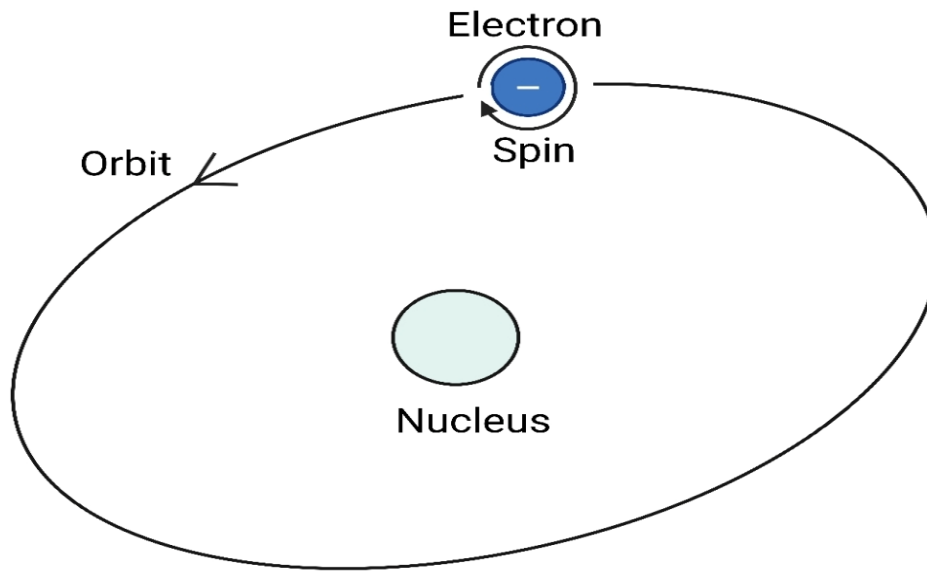


Figure 2.3: Illustrates the orbit of a spinning electron around the nucleus of an atom, as described by the Magnetic Materials Group at the University of Birmingham. This figure represents a fundamental concept in atomic physics, where electrons, negatively charged particles, move around the positively charged nucleus in defined orbitals.

### Magnetic nanoparticles in nature:

Magnetic nanoparticles are ubiquitous and can be found in some of the most unexpected places. For instance, every human brain contains over  $10^8$  magnetic nanoparticles of magnetite or maghemite per gram of tissue, and these particles are associated with various biological effects.<sup>27</sup> Additionally, magnetic nanoparticles are present in bacteria, where they assist in geomagnetic navigation, and they have been discovered in eukaryotic algae. These particles are also found in the bodies of higher animals,<sup>28,29,30</sup> including homing pigeons.<sup>31</sup> Moreover, magnetic nanoparticles are present as ferrihydrite-like mineral cores in the iron storage protein ferritin within migratory birds, ants, bees, salmon, tuna, sharks, rays, salamanders, newts, mice,

and cetaceans.<sup>32</sup> In nearly every plant and animal cell, including those of humans, these particles can be found in various forms, such as key-stone crystals in hornet comb cells<sup>33</sup> or bacterial micro-fossils.<sup>28,34</sup> They may also precipitate onto bacterial cell walls,<sup>35,36</sup> further demonstrating their wide distribution.

Magnetic nanoparticles also have important medical applications, particularly as contrast agents for magnetic resonance imaging (MRI).<sup>37,38,39</sup> These versatile particles are not only fundamental to various biological systems but also offer significant potential in medical diagnostics and other technological applications.

### Superparamagnetism:

Superparamagnetism is a phenomenon in which magnetic materials display paramagnetic-like behavior, even when the temperature is beneath the Curie or Néel temperature. In suitably minor nanoparticles (approximately 1-10 nm), magnetisation can randomly flip direction under the effect of temperature. The average time between these flips is known as the Neel relaxation time. When the measurement time for the magnetization of these nanoparticles is much longer than the Neel relaxation time and there is no external magnetic field, their magnetisation appears to average out to zero, placing them in a superparamagnetic state. In this condition, the nanoparticles can be magnetized by an external magnetic field, much like a paramagnet does (see figure 2.4). Even if the temperature is lower than the Curie or Neel temperature (meaning the thermal energy is not strong enough to break the coupling forces between adjacent atoms), it is still enough to alter the magnetisation direction of the whole crystallite. These fluctuations in the direction of magnetization can cause the overall magnetic field to average out to zero. As a result, the material behaves similarly to a paramagnet. However, unlike in paramagnetism

where each atom responds independently to an external magnetic field, in this case, the magnetic moment of the entire crystallite aligns with the external field.<sup>40</sup>

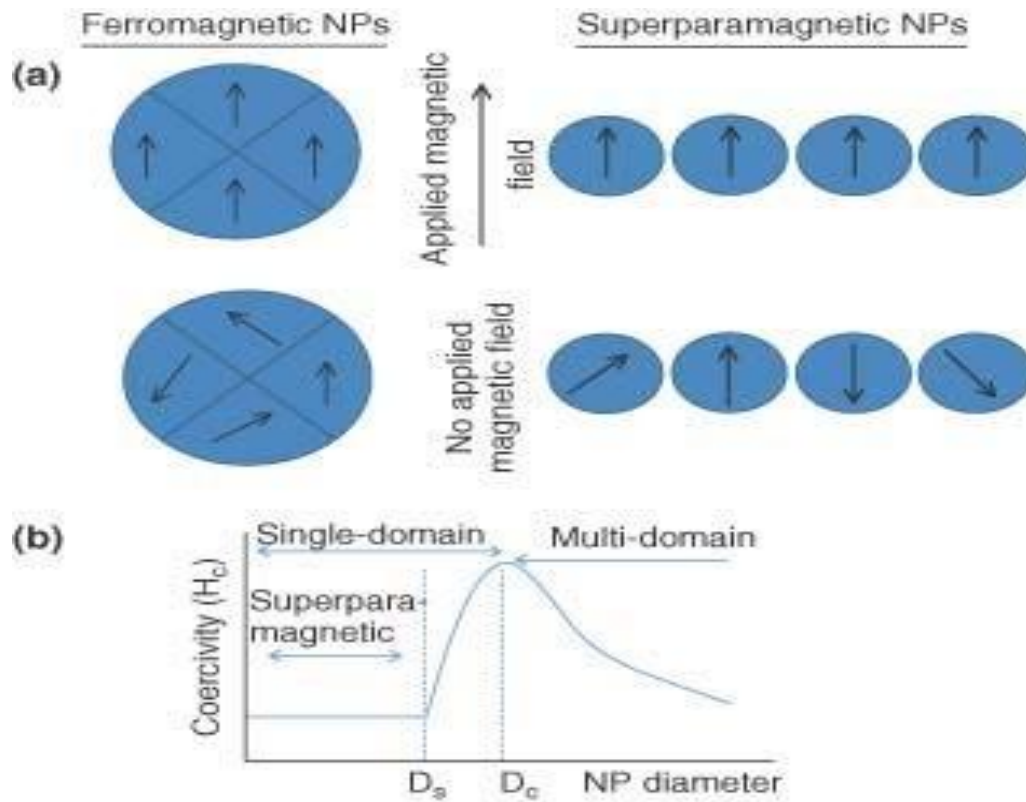


Figure 2.4: Illustration of superparamagnetism and the effect of particle size on magnetic behavior. As particle size decreases, magnetic materials transition from multi-domain to single-domain, and below a critical size ( $D_c$ ), they exhibit superparamagnetism.  $D_c$  is the critical diameter at which coercivity reaches a maximum before dropping to zero, indicating the onset of superparamagnetic behavior due to thermal fluctuations. This transition is size-dependent and distinct from the Curie temperature ( $T_c$ ), which is the temperature above which a material loses its magnetization altogether.

## Particles' aggregation:

Aggregation of the particles can happen due to the occurrence of a net attractive attraction among particles. These forces exhibit differences not only in form but also in range of action, exerting a substantial influence only within certain distances. Israelachvili (1991) provided a comprehensive overview of all intermolecular and surface interactions.<sup>41</sup>

## Van der Waals interactions:

The attractive forces that van der Waals first hypothesized to explain the non-ideal behavior of gases consist of three distinct types of intermolecular interactions.<sup>42</sup> These include dipole-dipole interactions, also known as Keesom or orientation forces, which occur when molecules align in such a way that their dipoles attract each other, resulting in a net attractive force. Another type is dipole-induced dipole interactions, often referred to as Debye or induction forces, where a molecule with a permanent dipole induces a dipole in a neighboring non-polar molecule, creating an attractive force. Lastly, LDF interactions, explained by London in 1930 and commonly known as London dispersion forces, arise from temporary fluctuations in electron distribution within one molecule, inducing a dipole in another molecule, and resulting in mutual attraction.<sup>43</sup>

For instance, hydrocarbons like octane demonstrate interactions driven primarily by LDFs due to their non-polar nature. Despite lacking permanent dipoles, hydrocarbons maintain cohesive forces due to the interactions between their non-polar tails (typically long chains of carbon and hydrogen atoms). These London forces, though weak, increase as molecular size grows, as seen in the liquid or solid states of larger alkanes. Interactions between the non-polar tails of amphiphilic molecules, such as fatty acids or surfactants, can also lead to the formation of

micelles or bilayers, driven by the exclusion of water molecules and the minimization of unfavorable interactions between water and the non-polar segments. This hydrophobic effect, while not a force in itself, is often coupled with London dispersion forces to stabilize the structures formed by such molecules. Similarly, in biological membranes, the hydrophobic interactions between lipid tails, along with London dispersion forces, contribute to the stability and integrity of the membrane structure.<sup>44</sup>

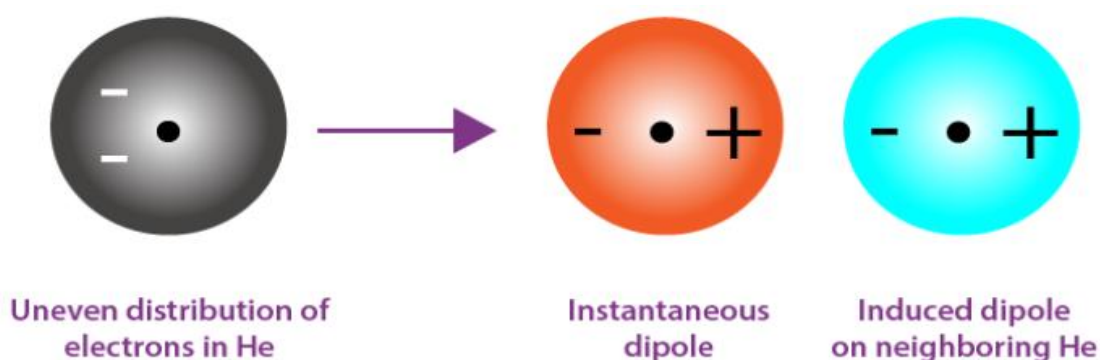


Figure 2.5: Illustrates the concept of London dispersion forces or induced dipole-induced dipole interactions, which are a type of van der Waals force.

### Electrostatic interactions:

Electrostatic interactions, a key type of intermolecular force, arise from the attraction between oppositely charged particles, specifically between positive and negative charges. These forces play a fundamental role in shaping molecular behavior, influencing both the structure and interactions of molecules. Ionic interactions, a specific form of electrostatic interaction, occur between positively charged (cationic) and negatively charged (anionic) species. These interactions tend to be quite strong in a vacuum but are significantly weaker in aqueous environments due to the effects of solvation. For example, the interaction between a negatively charged carboxylate group ( $-\text{COO}^-$ ) and a positively charged amino group ( $-\text{NH}_3^+$ ) in proteins is essential for maintaining protein structure.<sup>45</sup>



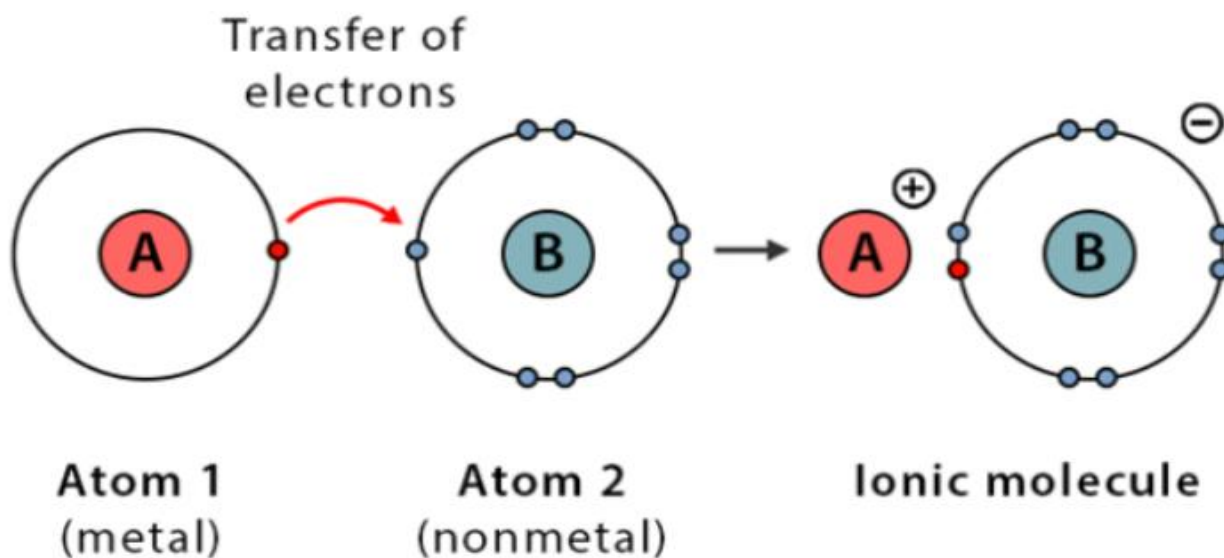


Figure 2.6: Illustrates an ionic interaction, where Atom 1 (the metal) loses an electron, becoming a positively charged ion (cation), and Atom 2 (the non-metal) gains that electron, becoming a negatively charged ion (anion). The resulting electrostatic attraction between the oppositely charged ions forms an ionic molecule. Ionic bonds are commonly found in compounds like sodium chloride (NaCl), where sodium (Na) donates an electron to chlorine (Cl), creating a stable ionic bond.

### Hydrogen Bonds:

Hydrogen bonds form when a hydrogen atom, which is covalently bonded to a highly electronegative atom such as nitrogen, oxygen, or fluorine, interacts with another electronegative atom in a nearby molecule or within the same molecule. This interaction results from the partial positive charge on the hydrogen and the partial negative charge on the electronegative atom, creating a weak but significant attractive force. These bonds are stronger than most other non-covalent interactions and are critical in stabilizing the structures of proteins (such as alpha-helices and beta-sheets) and DNA (holding base pairs together). For example:

water molecules hydrogen bond with each other, leading to water's high boiling point and surface tension.<sup>46</sup>

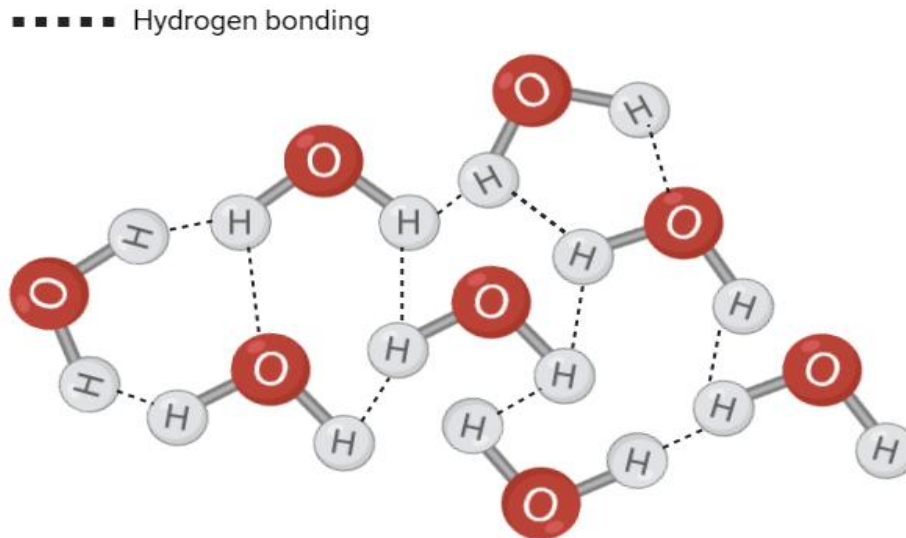


Figure 2.7: Displays a network of hydrogen bonding between water molecules.

### Hydrophobic Interactions:

Hydrophobic interactions are non-covalent forces that arise when non-polar molecules or molecular groups in an aqueous environment aggregate to minimize their exposure to water. Since water is polar and tends to form hydrogen bonds with other polar molecules, it energetically disfavours the presence of non-polar substances within its structure. As a result, water molecules effectively "exclude" non-polar substances, pushing them together. This exclusion leads to the aggregation of hydrophobic molecules, which reduces their contact with water and is energetically more favourable for the system. When non-polar molecules or molecular groups are introduced into water, water molecules form a highly ordered structure around them. This ordering of water molecules increases the system's entropy cost, which is thermodynamically unfavourable. By clustering together, non-polar molecules reduce the

surface area in contact with water, thereby minimizing this ordering effect. This reduction in the number of water molecules forced into a structured arrangement around the hydrophobic regions lowers the overall free energy of the system, driving the aggregation of non-polar substances.

For example, in protein folding, hydrophobic interactions are crucial. Non-polar amino acid side chains (such as leucine, isoleucine, valine, and phenylalanine) aggregate in the protein's core, away from the aqueous environment. This folding process is driven by the need to bury the hydrophobic residues inside the protein structure while exposing polar and charged residues to the surrounding water. The formation of a hydrophobic core is essential for maintaining the protein's three-dimensional structure and functional integrity. Another example is protein-protein interactions and molecular recognition. Hydrophobic interactions play a key role in these processes as well. When proteins interact with each other or with small molecules (ligands), regions with hydrophobic amino acid residues often form binding pockets. In these pockets, hydrophobic residues from both the protein and the ligand come together, stabilizing the complex through hydrophobic interactions. This is particularly important in enzyme-substrate binding, receptor-ligand interactions, and the assembly of protein complexes.<sup>47</sup>

#### $\pi$ - $\pi$ Stacking:

$\pi$ - $\pi$  Stacking refers to non-covalent interactions that happen between aromatic rings, such as benzene, due to the overlap of their  $\pi$ -electron clouds. These interactions are characterized by attractive forces between the delocalized electrons in the  $\pi$ -orbitals of adjacent aromatic rings. Although  $\pi$ - $\pi$  stacking is relatively weak compared to covalent bonds, it plays a critical role in stabilizing the structure of many biomolecules and synthetic systems. The interaction arises from a combination of electrostatic attraction, dispersion forces, and quantum mechanical effects between the  $\pi$ -electrons. These interactions can occur in several geometric

arrangements, including face-to-face (parallel stacking), where two aromatic rings align directly over one another, and edge-to-face (T-shaped stacking), where one aromatic ring interacts with the edge of another.

For instance, in DNA and RNA,  $\pi$ - $\pi$  stacking is crucial for maintaining the structural stability of nucleic acid strands. Base pairs in the DNA double helix stack on top of each other via  $\pi$ - $\pi$  interactions, contributing significantly to the stabilization of the helical structure. These stacked interactions, particularly between purine and pyrimidine bases (adenine, guanine, cytosine, and thymine), help prevent the unwinding of the DNA double helix, maintaining its compact and stable form. This stacking is also essential during processes like DNA replication and transcription, ensuring the strands remain properly aligned. In proteins,  $\pi$ - $\pi$  stacking interactions also occur between aromatic amino acids, such as phenylalanine, tyrosine, and tryptophan, which are often found within protein structures. These interactions are particularly important in protein folding, stability, and molecular recognition. Aromatic side chains can engage in  $\pi$ - $\pi$  stacking with each other, stabilizing the protein's overall three-dimensional conformation. Moreover, these interactions play a key role in molecular recognition, where proteins bind small molecules, often involving the stacking of aromatic rings with ligand molecules.<sup>48</sup>

### Importance in Biological Systems:

Non-covalent interactions are fundamental to the stability and function of biological systems, playing a critical role in maintaining the intricate structures of biomolecules. These interactions, which include hydrogen bonds, hydrophobic forces, van der Waals forces, and electrostatic interactions, are vital in numerous biological processes. For

instance, in protein folding, the three-dimensional conformation of a protein is predominantly stabilized by non-covalent interactions. Hydrogen bonds form between the amino acid backbones, while hydrophobic interactions drive the packing of nonpolar side chains away from the aqueous environment. Van der Waals forces further stabilize these folded structures by facilitating close contact between atoms. This precise folding is essential for the protein's function, as even small disruptions can lead to loss of activity or disease.

Similarly, the structure of DNA relies heavily on non-covalent interactions. The iconic double helix is stabilized by hydrogen bonds between the nitrogenous bases, specifically between adenine and thymine (A-T), and guanine and cytosine (G-C). Additionally,  $\pi$ - $\pi$  stacking interactions between the aromatic rings of adjacent nucleotide bases further enhance the stability and rigidity of the DNA structure. These interactions ensure that DNA can store genetic information efficiently while remaining stable enough to undergo replication and transcription processes.

In enzymatic activity, non-covalent interactions also play a pivotal role. Enzymes rely on these interactions for substrate recognition and binding. The active site of an enzyme is often complementary in shape and charge to its substrate, allowing specific binding through hydrogen bonds, ionic interactions, and hydrophobic effects. This specificity ensures that enzymes catalyze only their intended reactions, maintaining the fidelity of biological processes. Non-covalent interactions, though weaker than covalent bonds, provide the flexibility needed for dynamic processes like enzyme-substrate binding, protein folding, and molecular recognition, making them indispensable to biological systems.<sup>49</sup>

## Nanoparticle characterization:

Scientists have developed numerous systems for characterizing nanoparticles, with advanced techniques playing a key role in progressing the field of nanotechnology. Some common approaches include measuring particle size using dynamic light scattering (DLS) and small-angle X-ray scattering (SAXS), which can also provide surface information. In addition, researchers have used electron microscopes such as TEM and SEM for both sizing and directly visualizing the nanoparticles' structures and structures. Atomic force microscopy (AFM) and scanning tunneling microscopy (STM) are powerful tools that can allow topological and surface structure characterisation with atomic scale resolution. Furthermore, numerous chemical techniques are employed to analyse crystal structures, particle surfaces (which may host adsorbed molecules), and chemical properties of particles.<sup>7,50</sup> These techniques provide detailed insights into the physical and chemical characteristics of materials at various scales. Some of the most commonly used techniques include:

## Techniques for Analyzing Crystal Structures:

### X-ray Diffraction (XRD):

It is a vital tool in characterizing both nano magnetic particles and PAMAM dendrimer-functionalized systems, particularly in studying their crystallinity, particle size, and structural modifications. Additionally, XRD can be applied in studying protein binding on these materials, helping to understand how structural properties influence the binding efficiency and interactions between dendrimers, magnetic particles, and proteins. XRD works by directing X-rays onto a material, where the X-rays are diffracted by the crystal lattice. By measuring the angles and intensities of these diffracted beams, a diffraction pattern is produced, which can be analyzed to reveal information about the material's atomic structure.<sup>52</sup> There are two main types

of X-ray diffraction (XRD) methods: powder X-ray diffraction (PXRD) and single crystal X-ray diffraction (SCXRD). PXRD involves analyzing a sample composed of numerous microcrystals oriented randomly. This method produces a one-dimensional diffraction pattern (intensity vs.  $2\theta$ ), which is useful for phase identification, crystallinity assessment, and lattice parameter determination. It is a rapid technique that requires only a small amount of material, making it highly suitable for routine analysis.

In contrast, SCXRD is used when a single, well-formed crystal is available. This technique enables complete three-dimensional structural elucidation, allowing researchers to determine the precise atomic arrangement within the crystal. It provides detailed information such as bond lengths, bond angles, and space group symmetries. Although it is more time-consuming and depends on the availability of high-quality crystals, SCXRD offers unparalleled precision and is regarded as the gold standard for structural characterization.

### Electron Diffraction (ED):

Electron diffraction (ED) is a crucial technique for analyzing the structure of materials at the nanoscale, including magnetic nanoparticles and PAMAM dendrimers. In the context of nanomagnetic particles, electron diffraction can reveal information about the crystalline structure, which is essential for understanding and manipulating their magnetic properties for various applications such as targeted drug delivery or magnetic resonance imaging. For PAMAM dendrimers, particularly when functionalized with bioactive molecules like proteins, electron diffraction can provide insights into the surface characteristics and the binding efficacy of these functional groups. This is important in the biomedical field, where PAMAM dendrimers are often used as carriers for drug delivery systems. The detailed structural

information obtained from ED can help in understanding how these dendrimers interact with proteins, which is critical for optimizing their design for specific therapeutic targets.

Research has explored the synthesis and characterization of different generations of PAMAM dendrimer-coated magnetic nanoparticles, highlighting the versatility and potential of combining dendrimers with nanomagnetic particles for enhanced biomedical applications. The characterization typically involves assessing the size, surface chemistry, and magnetic properties, which are crucial for their functionality as drug delivery systems or in diagnostic applications.<sup>53</sup>

There are several advantages of electron diffraction (ED) over X-ray diffraction (XRD). While XRD is essential for crystalline analysis, electron diffraction offers unique benefits, particularly in nanoscale applications. ED uses a beam of electrons instead of X-rays, resulting in a much stronger interaction with matter. This makes it especially effective for analyzing extremely small or thin samples, such as nanoparticles or films.

Compared to XRD, ED can resolve structures at much smaller scales, making it ideal for characterizing nanoparticles, thin films, and surface features. It is commonly integrated with Transmission Electron Microscopy (TEM), enabling researchers to simultaneously visualize morphology and obtain crystallographic data at atomic resolution. ED is highly sensitive and capable of providing structural information even when conventional XRD cannot, due to limited sample size or crystallinity. However, electron diffraction requires more complex instrumentation and sample preparation, making it more specialized than conventional XRD techniques.



## Neutron Diffraction:

Neutron diffraction is a powerful technique used in materials science and solid-state chemistry to probe the atomic structure and properties of materials. Unlike electron diffraction, which interacts with the electron cloud surrounding atoms, neutron diffraction involves the interaction of neutrons with the nuclei. This gives it unique advantages, particularly in studying materials that are difficult to analyze using other radiographic techniques due to the similar scattering power of light atoms.

Neutron diffraction offers several advantages for the study of materials, particularly in areas where other techniques like X-ray diffraction may be limited. First, it excels in structural analysis, especially in identifying the positions of light atoms such as hydrogen, which are often difficult to detect using X-ray diffraction due to their low electron density. Neutron diffraction overcomes this limitation, providing detailed information about the arrangement of these atoms within a molecule or crystal lattice. Second, neutron diffraction is highly effective in investigating magnetic properties. Because neutrons possess a magnetic moment, they can interact with magnetic fields within materials, enabling the study of the alignment and interactions of magnetic domains. This makes neutron diffraction an essential tool for the analysis of magnetic materials. Lastly, neutron diffraction is invaluable for studying complex materials, such as proteins, enzymes, and large biological molecules, in their natural environments. This capability is critical for understanding biological processes at a molecular level and plays a significant role in pharmaceutical development, as it allows researchers to study these molecules in conditions that closely mimic those in living organisms.<sup>54</sup>

## Techniques for Analyzing Particle Surfaces:

### Scanning Electron Microscopy (SEM)

It is a highly versatile technique commonly used in materials science to examine the surface structures and compositions of various materials at high magnification and resolution. SEM functions by scanning a focused beam of electrons across the surface of a sample, where the electrons interact with the sample's atoms, generating signals that can be detected and transformed into highly detailed images. The primary components of an SEM include an electron gun, which produces the electron beam; condenser and objective lenses that focus the beam onto the sample; and detectors that capture the emitted signals, such as secondary and backscattered electrons. These components are housed in a vacuum chamber to prevent interference from air molecules. As the electron beam is raster-scanned across the sample, the emitted electrons are collected to form an image of the sample's surface. SEM is invaluable for analyzing a wide range of materials, including metals, ceramics, biological specimens, and nanomaterials. It allows researchers to observe microstructures, surface fractures, and topographical details with a level of clarity not achievable through conventional light microscopy. In forensic science, SEM is used to analyze minute details, such as dust particles or fibre structures on clothing, providing critical insights for investigations. While SEM offers the significant advantage of producing high-resolution images of surface topography and composition, it does come with limitations. SEM systems are expensive and require a controlled environment free from vibrations and electromagnetic interference. Additionally, samples must be able to withstand the vacuum environment and be conductive or coated to become conductive for accurate analysis.<sup>55</sup>

### Transmission Electron Microscopy (TEM):

Transmission Electron Microscopy (TEM) is an advanced and indispensable technique for understanding the atomic and molecular structure of materials. By transmitting a beam of electrons through an ultra-thin specimen, TEM captures interactions that produce highly detailed images or diffraction patterns, offering insight into the material's structure, chemical composition, and electronic states. In materials science, TEM is particularly valuable for providing high-resolution images at the atomic scale, making it a critical tool for analyzing nanomaterials such as nanocrystals and nanorods. This level of detail enables researchers to study crystal structures, defects, and interfaces with precision. Beyond materials science, TEM is also widely used in biology to examine cell ultrastructures and investigate the subcellular localization of proteins. The technique is enhanced by several advanced modalities, including High-Resolution TEM (HRTEM), which overcomes lens aberrations to image atomic-scale features; Selected Area Electron Diffraction (SAED), which provides crystallographic information with greater sensitivity than traditional X-ray diffraction; and Analytical TEM, which incorporates tools such as Energy Dispersive X-ray Spectroscopy (EDX) and Electron Energy Loss Spectroscopy (EELS) for chemical composition analysis. Despite its extensive capabilities, TEM requires very thin samples and operates under high-vacuum conditions, which can limit its applicability to certain materials or environments. Nevertheless, TEM remains a cornerstone in both nanotechnology and materials science due to its ability to uncover intricate physical and chemical properties at the atomic level.<sup>56</sup>

### Atomic Force Microscopy (AFM):

Atomic Force Microscopy (AFM) is a powerful imaging technique known for its ability to provide high-resolution, three-dimensional images of surfaces at the nanoscale. One of its key

strengths is its versatility, as AFM can be employed in various environments, including air, vacuum, and liquid, making it suitable for a wide range of materials such as biological specimens, polymers, and inorganic compounds. The principle of AFM involves scanning a tiny cantilever with a sharp tip across the surface of the sample. As the tip interacts with the surface, the resulting deflections in the cantilever are detected by a laser beam reflected off the cantilever's top. These deflections are then translated into topographical maps with atomic-scale resolution, providing detailed surface information.

AFM has wide-ranging applications in numerous scientific fields. In materials science, it is used to analyze surface roughness, patterns, and properties of materials at micro - nanoscale levels. In biology and medicine, AFM allows for the study of cell membranes, proteins, DNA, and other biomolecules in their natural environments without the need for invasive sample preparation. In nanotechnology, AFM is crucial for manipulating and characterizing nanoscale materials, nanodevices, and circuits, enabling precise control and measurement at the atomic level. AFM offers several distinct advantages. It is a non-destructive technique, meaning that samples do not need to be coated or placed in a vacuum, allowing observations of materials in their natural state. AFM also provides higher resolution than optical microscopes, making it possible to image features down to the atomic scale. Additionally, AFM's versatility enables it to measure various forces—such as mechanical, electrical, and magnetic—on both rigid and soft materials. However, AFM does have some limitations. Scanning speed can be slower compared to other microscopy techniques, and the technique is generally limited to smaller sample areas, sometimes requiring extensive sample preparation to achieve optimal results. Despite these limitations, AFM remains an essential tool in fields requiring nanoscale precision and analysis.<sup>57</sup>

## X-ray Photoelectron Spectroscopy (XPS):

X-ray Photoelectron Spectroscopy (XPS), also known as Electron Spectroscopy for Chemical Analysis (ESCA), is a surface-sensitive analytical technique used to determine the elemental composition and chemical states of the surface of a material. XPS works by irradiating a sample with X-rays, which causes the emission of photoelectrons from the material's surface. By measuring the kinetic energy and the number of emitted electrons, researchers can infer the elements present on the surface, as well as the chemical states of these elements. XPS is widely used across multiple fields due to its ability to provide detailed surface chemical analysis. In materials science, XPS is employed to characterize surface chemistry, analyze corrosion, measure layer thickness, and study interfaces between different materials. In catalysis, XPS helps identify the surface composition and electronic states of catalysts, which are critical for understanding their catalytic behavior. The semiconductor industry uses XPS to analyze thin films, detect surface contamination, and examine device interfaces. In biomedical research, XPS is instrumental in studying surface modifications of biomaterials and their interactions with biological environments. XPS offers several advantages. It is a quantitative technique that provides both qualitative and quantitative information about the surface layers of a sample. It exhibits elemental and chemical sensitivity, detecting nearly all elements (except hydrogen and helium) and identifying their chemical and electronic states. XPS also enables depth profiling, allowing researchers to analyze the composition of surface layers at different depths by varying the angle of analysis. However, XPS has some limitations. It is primarily limited to surface analysis, meaning it only provides information about the surface layers and may not reflect the bulk properties of the material. XPS also requires a high vacuum environment, which restricts its use with certain samples, such as liquids or volatile substances. Additionally, the X-ray beam can damage or alter the properties of sensitive materials, posing a challenge when

analyzing delicate samples. Despite these limitations, XPS remains a crucial tool in fields requiring precise surface characterization.<sup>59</sup>

## Techniques for Analyzing Chemical Properties:

### Fourier Transform Infrared Spectroscopy (FTIR):

Fourier Transform Infrared Spectroscopy (FTIR) is a versatile and powerful analytical technique used to identify the molecular composition and structure of materials through their infrared absorption spectra. FTIR analyzes how a material absorbs infrared light, revealing the types of chemical bonds and functional groups present within a sample. This makes FTIR an essential tool in fields such as materials science, pharmaceuticals, and environmental science. The technique provides critical data on molecular structures, interactions, and chemical compositions, aiding in a wide range of research and industrial applications. FTIR operates by passing a beam of infrared light through or reflecting it off a sample. As the light interacts with the sample, certain wavelengths of infrared light are absorbed by the material, causing the chemical bonds within the sample to vibrate at characteristic frequencies. These frequencies depend on the chemical structure and functional groups present in the material. The light that passes through (or is reflected from) the sample is collected and analyzed. The key component of FTIR is its ability to measure these absorption patterns using a Fourier Transform. Instead of measuring each frequency individually, as in traditional dispersive infrared spectroscopy, FTIR collects a full spectrum of infrared light at once as an interferogram. This interferogram is a complex signal that contains information about all the different frequencies absorbed by the sample. The Fourier Transform is then applied to convert this raw data into a usable absorption spectrum, showing distinct peaks corresponding to the vibrational frequencies of

the chemical bonds in the sample. The resulting FTIR spectrum plots the intensity of absorption against the frequency (or wavelength) of the infrared light. Each peak in the spectrum corresponds to a specific molecular vibration, which can be related to particular functional groups or bonds in the material. One of FTIR's significant strengths lies in its ability to analyze a wide range of materials—gases, liquids, and solids—while offering both quantitative and qualitative data. This versatility makes it ideal for applications such as quality control, forensic analysis, and even archaeological research, where determining the chemical makeup of artifacts is crucial to understanding their composition and preservation. Recent advancements, such as micro-FTIR and nano-FTIR, have further expanded the technique's utility. These innovations enable high-resolution analysis of extremely small sample areas, which is especially valuable in cutting-edge fields like nanotechnology and cellular biology. By allowing for detailed examination of microscopic regions, these advancements have broadened FTIR's applicability, making it an indispensable tool for modern scientific research and industrial applications.<sup>60</sup>

### Raman Spectroscopy:

Raman Spectroscopy is a powerful, non-destructive analytical technique used to gain detailed molecular information by measuring the inelastic scattering of light, known as Raman scattering. When a sample is irradiated with a laser beam, most photons are elastically scattered (Rayleigh scattering), meaning they bounce back with the same energy. However, a small fraction of the light interacts with molecular vibrations, resulting in a shift in energy. These energy shifts correspond to specific vibrational modes within the molecule and form the basis of the Raman spectrum. The Raman spectrum acts as a molecular fingerprint, revealing information about molecular structure, chemical bonding, and crystal phases. Each peak in a Raman spectrum corresponds to a specific vibrational mode of a bond or group of atoms within the molecule. While both Raman and FTIR spectroscopy provide information about molecular

vibrations and chemical bonds, they operate on fundamentally different principles and are sensitive to different types of vibrational modes. FTIR measures how molecules absorb infrared light, which excites dipole-active vibrational modes (those that involve a change in dipole moment). Raman Spectroscopy, on the other hand, detects vibrational modes that result in a change in polarizability of the molecule (how easily its electron cloud is distorted). As a result, FTIR and Raman are complementary techniques—some vibrational modes may be visible in one and not in the other. For instance, symmetric non-polar bonds (like C=C or C–C stretches) are often strong in Raman but weak or inactive in FTIR.

Due to its versatility and non-invasive nature, Raman spectroscopy is widely used across many fields. In material science, it is used to characterize crystal structures, identify phases, and analyze stress within materials. In the biological and medical sciences, it aids in diagnosing diseases, studying bone composition, and analyzing cellular structures. Within the chemical industry, it assists in the identification of chemicals and the monitoring of chemical reactions, while in pharmaceuticals, it plays a key role in drug development and quality control. In environmental science, Raman spectroscopy is employed for detecting pollutants and studying atmospheric chemistry. There are several advantages to using Raman spectroscopy. It is non-destructive and often requires minimal or no sample preparation. It works well with solid, liquid, and gas samples and provides highly specific molecular fingerprints for compound identification. Additionally, it can analyze samples through glass or water, which is useful for biological or sealed systems. Recent advancements, such as portable Raman spectrometers and surface-enhanced Raman spectroscopy (SERS), have greatly expanded the technique's sensitivity and made it suitable for in-field applications and even single-molecule detection under the right conditions. However, Raman spectroscopy does have some limitations. Fluorescence interference can overwhelm the Raman signals in certain samples, making accurate data collection difficult. It also generally has lower sensitivity than FTIR for some



types of compounds, particularly those without strong polarizability changes. To overcome this, enhancement techniques such as SERS are often employed to improve signal strength and sensitivity.

In summary, Raman spectroscopy is a complementary technique to FTIR, offering unique insight into molecular vibrations through light scattering instead of absorption. Its precision, flexibility, and non-invasive nature make it a valuable tool in both laboratory and field-based scientific research and industrial applications.<sup>61</sup>

### Nuclear Magnetic Resonance (NMR) Spectroscopy:

Nuclear Magnetic Resonance (NMR) Spectroscopy is a fundamental analytical technique extensively used across chemistry, biology, and materials science to study molecular properties and structures. NMR operates based on the magnetic properties of atomic nuclei, which, when placed in a magnetic field and exposed to radiofrequency pulses, resonate at frequencies characteristic of their chemical environment. The resulting spectral data provide invaluable insights into molecular structures, dynamics, and interactions, making NMR a critical tool for a wide range of scientific inquiries.

NMR is particularly effective for the identification of organic compounds, as well as for the study of complex biological molecules such as proteins and is also used to explore molecular motions. Its ability to precisely elucidate molecular structures renders it indispensable in research and development, especially in areas involving chemical synthesis and biomolecular studies. The key applications of NMR include chemical structure elucidation, where it helps determine the exact molecular structure of compounds, studying biomolecular complexes to understand the structure and function of large biological macromolecules, and material analysis, where it aids in investigating the molecular properties and behavior of materials.

Recent technological advancements have significantly enhanced the capabilities of NMR spectroscopy. Innovations such as high-field magnets and advanced pulse sequences have greatly improved the sensitivity and resolution of NMR measurements. Additionally, the introduction of cryoprobes and automation has made NMR more efficient and accessible for routine laboratory use, enabling faster and more precise analyses. These developments have cemented NMR's role as an indispensable tool for both fundamental research and practical applications across multiple scientific disciplines.<sup>62</sup>

### Mass Spectrometry (MS):

Mass Spectrometry (MS) is a vital analytical technique used to measure the mass-to-charge ratio of ions, providing essential data on the molecular weights and structures of compounds. The process works by ionizing chemical compounds to create charged molecules or molecular fragments, which are then analyzed based on their mass-to-charge ratios using specialized detectors. MS is widely employed across various fields due to its precision and versatility, playing a crucial role in areas such as proteomics, where it is used to identify and quantify proteins in biological samples, shedding light on biological processes and disease mechanisms. In metabolomics, MS helps analyze small molecule metabolites, offering insights into cellular functions and metabolic pathways. It is also invaluable in environmental science, where it is used to detect and study pollutants in water, soil, and air. In the pharmaceutical industry, MS is used to analyze drug purity and composition, as well as to monitor degradation processes. Additionally, in forensic science, it assists in identifying unknown compounds, such as poisons, making it an essential tool for law enforcement and forensic investigations.

Several key techniques enhance the utility of Mass Spectrometry. Electrospray Ionization (ESI) produces ions using an electrically charged liquid, while Matrix-Assisted Laser Desorption/Ionization (MALDI) employs a laser to ionize compounds within a matrix. Time-

of-Flight (TOF) measures the time ions take to travel through a vacuum tube to determine their mass-to-charge ratios, and Tandem Mass Spectrometry (MS/MS) involves multiple rounds of mass spectrometry to provide detailed analysis of complex samples.

Mass Spectrometry offers several significant advantages. It is highly sensitive and specific, capable of detecting substances at very low concentrations, and it has a wide range of applications, from analyzing small organic molecules to large biomolecules like nucleic acids and proteins. MS is also proficient in quantitative analysis, allowing for the precise measurement of compound concentrations within complex mixtures. However, there are some limitations, including the need for extensive sample preparation in some cases and the complexity of the data, which requires sophisticated software and skilled interpretation. The continued evolution of Mass Spectrometry has led to advancements in accuracy, speed, and the range of applications, particularly in scientific research and diagnostics. Innovations such as high-resolution mass spectrometry and improvements in ionization techniques have significantly expanded its capabilities, enabling more precise analysis of complex biological and environmental samples. For a deeper understanding of Mass Spectrometry techniques and their applications, comprehensive literature is available on platforms such as ScienceDirect and SpringerLink, providing detailed research findings on this essential tool in modern science.<sup>63</sup>

#### Dynamic Light Scattering (DLS):

Dynamic Light Scattering (DLS) is a sophisticated analytical technique employed to determine the size distribution of particles within solutions or suspensions. Also referred to as photon correlation spectroscopy (PCS) or quasi-elastic light scattering (QLS), DLS works by analyzing the fluctuations in light scattered by particles undergoing Brownian motion. The rate of these fluctuations correlates with the diffusion coefficient of the particles, which can be used

to calculate the particle sizes, typically ranging from a few nanometers to several microns, making DLS an essential tool in particle characterization across various fields.

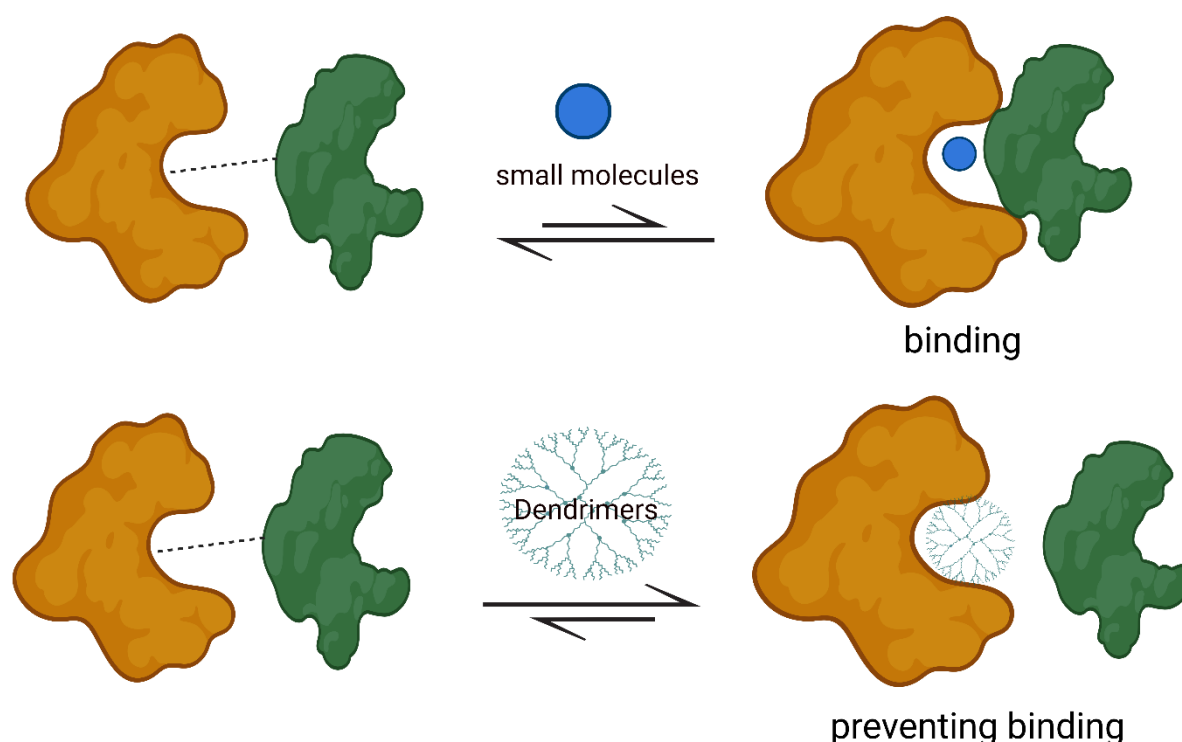
DLS finds applications in numerous scientific and industrial sectors. In pharmaceuticals, it is widely used for characterizing the size of drug particles in formulations, which is crucial for ensuring proper drug delivery and efficacy. In biotechnology, DLS is employed to measure the size of biological macromolecules such as proteins, viruses, and other complex biomolecules. In materials science, DLS helps in analyzing the properties of nanoparticles and colloids, providing valuable insights into their behavior and stability. Additionally, in environmental science, DLS is used to study particulate matter in environmental samples, contributing to research on pollution and environmental monitoring.

DLS offers several advantages. It is non-invasive, meaning it does not require altering or consuming the sample, allowing for repeated measurements. The technique is rapid and accurate, providing quick and reliable size distribution measurements. Its versatility allows it to be applied to a wide range of sample types, including opaque or viscous liquids, making it a highly adaptable method for particle sizing. Despite its strengths, DLS does have some limitations. It is sensitive to sample quality, meaning particle aggregation or the presence of contaminants can skew results. Additionally, DLS is most effective for small particles and may have reduced accuracy when analyzing larger aggregates or complex mixtures. Recent advancements in DLS technology have enhanced its resolution, allowing for the detection of smaller particles with greater precision. Improvements in software algorithms have also improved data analysis and user experience, making the technique more accessible and reliable. These advancements have expanded the utility of DLS, making it an indispensable tool in fields that require accurate and precise particle sizing, such as pharmaceuticals, biotechnology, and environmental science.<sup>64</sup>

## Aims and Objectives:

The core objective of this work is to inhibit uncontrolled protein-protein interactions, which are well-documented contributors to diseases like Alzheimer's disease (AD), Parkinson's disease (PD), Creutzfeldt-Jakob disease (CJD), and various cancers. These aberrant interactions disrupt cellular functions and contribute to disease pathogenesis. By inhibiting such interactions, it may be possible to prevent or mitigate disease progression. Small molecules, traditionally used as inhibitors, often face challenges due to their inability to bind strongly to the large interfacial areas of target proteins, limiting their efficacy in inhibiting interactions. This limits their ability to effectively bind and inhibit interactions at the required sites. To overcome these limitations, larger molecules including dendrimers, present a promising alternative. This is due to their highly branched and symmetric structures. Their large, adaptable surface area allows for more extensive interactions with target proteins, improving binding affinity and inhibitory effects. Additionally, their controlled size enables precise targeting of protein binding sites, offering an advantage over small molecules. These features make dendrimers particularly well-suited to fill the binding sites, or "hot spots," on target proteins. By occupying these hot spots, dendrimers can effectively inhibit protein-protein interactions. The advantages of dendrimers as potential protein-protein interaction inhibitors are manifold. Firstly, their highly branched architecture provides a larger and more adaptable surface area for binding to a protein's interfacial area compared to small molecules. This allows for more extensive and stronger interactions with the target proteins, thereby enhancing their inhibitory effects. Secondly, the controlled size and symmetrical structure of dendrimers ensure that they can be precisely tailored to fit specific binding sites on the proteins. This precision enables dendrimers to target interactions more accurately, increasing their efficacy as inhibitors. In summary, dendrimers' structural advantages make them ideal inhibitors of protein-protein interactions, as they effectively occupy binding sites and inhibit unwanted

interactions. This capability is crucial for the development of new therapeutic agents aimed at treating diseases associated with aberrant protein-protein interactions. Scheme 2.1 below provides a visual representation of how dendrimers inhibit protein interactions, highlighting their role as promising candidates in the fight against these complex diseases.



Scheme 2.1: Provides a schematic representation of how dendrimers can inhibit protein-protein interactions (PPI), a critical process in many biological functions. The figure visually demonstrates how dendrimers, which are highly branched, tree-like macromolecules, can interfere with or block the interaction between proteins, thereby preventing certain biological processes or disease mechanisms. This figure was created by using [BioRender](#).

Moreover, the terminal groups of dendrimers can be functionalized to modify or enhance their binding affinity for specific proteins. This functionalization allows for the introduction of various targeting groups that increase the specificity and strength of interactions with desired protein targets. For example, our group functionalised dendrimers with three amino acids (phenylalanine, tyrosine, and valine). The outcomes show that dendrimers functionalized with phenylalanine and tyrosine enhance binding. Yet, the valine-functionalized dendrimers contribute fewer secondary interactions, resulting in weaker binding.<sup>65</sup>

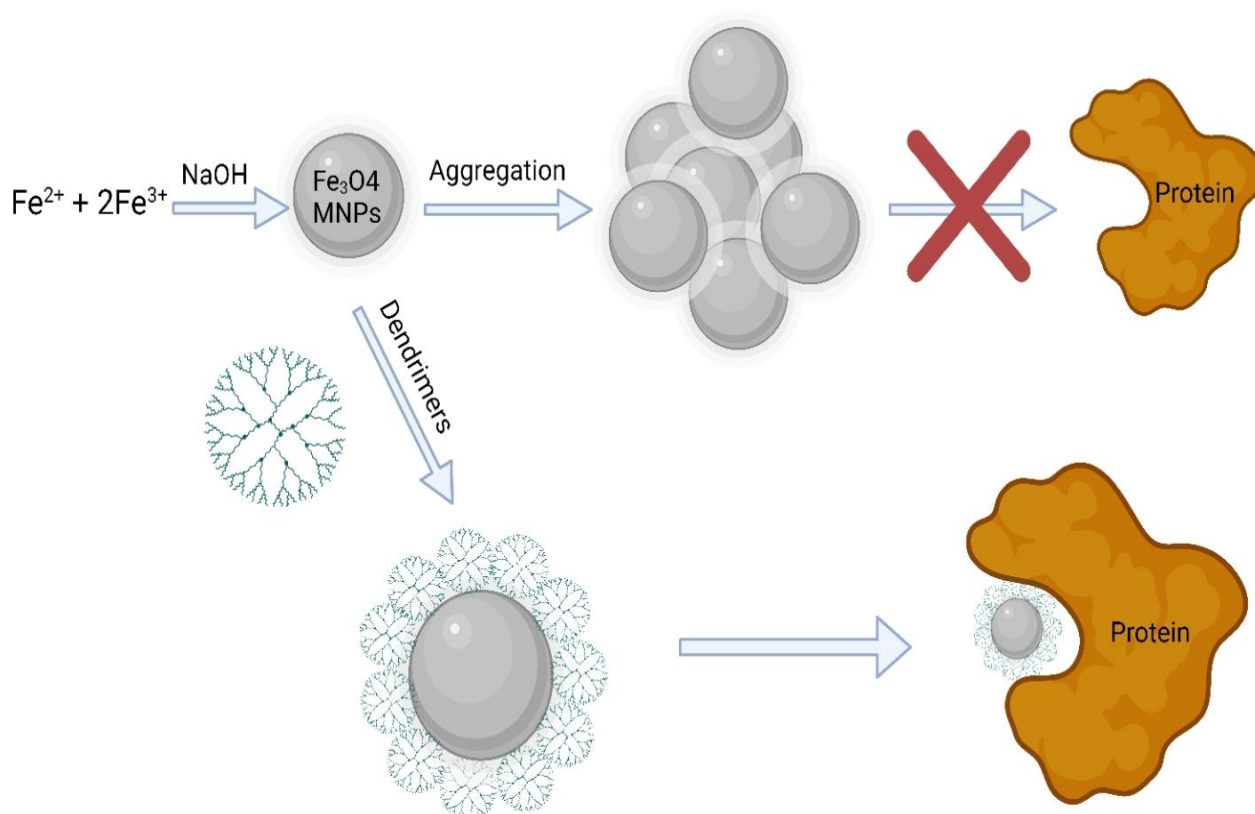
However, covalently attaching these targeting groups poses significant challenges. One primary difficulty lies in the precise attachment of amino acid residues to specific locations on the 3D structure, making efficient binding challenging to achieve. To address these challenges, a dynamic, non-covalent approach can be employed. For example, targeting groups could be connected to the dendrimer via a series of hydrogen bonds. By utilizing molecules capable of forming hydrogen bonds with dendrimers, we can create dendrimer-complexes without the need for covalent modifications. This would allow any targeting groups to move across the 3D surface and maximize interactions through a combination of non-covalent interactions., such as charge/charge interactions, aromatic/ $\pi$ - $\pi$  interactions, hydrogen bonding, and hydrophobic interactions, offer a versatile and potentially simpler alternative. With respect to protein binding, the primary non-covalent interaction we are focusing on are simple electrostatic interactions. Electrostatic interactions provide a strong initial binding forces due to the attraction between oppositely charged groups on the dendrimers and the target protein's surface. Selectivity will then come from secondary interactions supplied by the targeting group. In this case other non-covalent interactions contribute to the selectivity and specificity of the binding process, the important/strongest ones include hydrogen bonding, electrostatic interactions, Van der Waals forces, hydrophobic interactions,  $\pi$ - $\pi$  stacking and cation- $\pi$  interactions.

Non-covalent interactions are generally weaker than covalent bonds, but they are collectively important due to their number and ability to dynamically form and break, which is crucial for many biological processes. By combining these various non-covalent interactions in a dynamic way, we can achieve a high degree of control and flexibility in the formation of dendrimer-protein complexes. This approach not only simplifies the modification process but also allows for the fine-tuning of interactions to achieve the desired binding characteristics. Ultimately, leveraging non-covalent interactions offers a promising strategy for developing dendrimer-based systems with enhanced specificity and binding capabilities for a wide range of protein targets. Although the long-term aim of this work is to develop a dynamic approach to targeting, this work will primarily focus on the covalent modification of the dendrimers and the use of magnetic nanoparticles to facilitate separation and purification of proteins. Magnetic nanoparticles (MNPs) offer a promising solution to enhance selectivity, as their biocompatibility and surface-charged molecules enable them to bind to protein surfaces through electrostatic interactions. However, magnetic iron oxide nanoparticles tend to agglomerate easily under the influence of magnetic and van der Waals forces. Additionally, bare  $\text{Fe}_3\text{O}_4$  nanoparticles typically exhibit high chemical activity and are particularly prone to oxidation, which often results in a decline in their magnetic properties. In addition, magnetic nanoparticles themselves have a hydrophobic surface, so they will interact with each other to form larger clusters, and eventually form agglomerated larger-sized nanoparticles.<sup>51</sup> These problems have largely been overcome by stabilizing the particles with surface groups (including polymers and dendrimers). These stabilized magnetic nanoparticles have shown promise in the area of protein binding, but the applications are largely limited to non-selective binding. Selective or specific variations of these nanoparticles can be prepared by functionalization with biological molecules. However, this makes them extremely complicated, difficult to synthesize and restricted to the generation of small amounts (limited



to mg levels for research). To overcome this problem, we plan to synthesize MNP and stabilize them with PAMAM dendrimers. These dendrimers possess numerous terminal groups that can be functionalized with specific chemical groups to enhance protein binding affinity, which can result in selectivity. The proposed approach therefore involves combining magnetic particles with dendrimers to create a hybrid particle capable of specific protein binding (scheme 2.2).

For this work, magnetic particles derived from iron oxide  $\text{Fe}_3\text{O}_4$  were chosen for several key reasons. First, iron oxide is an economical and readily obtainable starting material, making it cost-effective and accessible for large-scale synthesis. The synthesis of iron oxide-based magnetic particles is also highly reproducible and sustainable, ensuring consistent results across different batches, which is critical for scalability. Additionally, iron oxide nanoparticles possess a nanoscale core with high magnetization properties, enabling efficient magnetic manipulation. Their biocompatibility and low toxicity further make them ideal candidates for biomedical applications. Moreover, iron oxide nanoparticles provide an efficient platform for functionalizing the particle surface with dendrimers or other molecules, enhancing binding specificity and versatility, making them highly adaptable for various applications.



Scheme 2.2: The schematic representation of inhibiting protein-protein interactions (PPI) by magnetic nanoparticles (MNPs) stabilized using PAMAM (Polyamidoamine) dendrimers illustrates the innovative approach of using nanotechnology to disrupt biological processes involving protein interactions. This diagram visually explains how MNPs, when coated or stabilized with PAMAM dendrimers, can effectively block or hinder PPIs. This figure was prepared by using [BioRender](#).

Iron magnetic nanoparticles (MNPs) will initially be stabilized using various generations of OH-terminated polyamidoamine (PAMAM) dendrimers. It is expected that this approach will stabilize the MNPs through oxygen lone pair interactions. If successful, these MNPs will possess a neutral surface and will not bind directly to protein surfaces. As a result, only functional groups added to the surface will be capable of binding, allowing for the independent comparison of various terminal groups without interference from non-specific interactions on the dendrimer surface. However, it is anticipated that stabilization may be ineffective due to

the relatively weak interaction between the nanoparticles and the OH groups. Consequently, the terminal ester groups of the PAMAM dendrimers will undergo hydrolysis to carboxylate groups, which should form stronger bonds with the iron in the nanoparticles, resulting in improved stabilization. This process is similar to the use of polyacrylic acid, which has been shown to provide effective stabilization.<sup>66</sup>

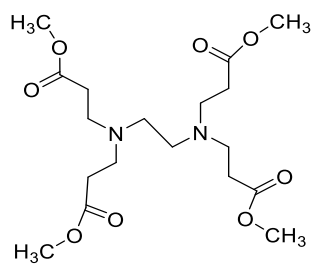
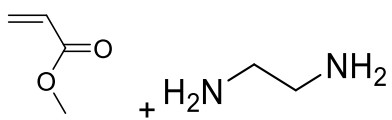
## Chapter 3

# Results and Discussion

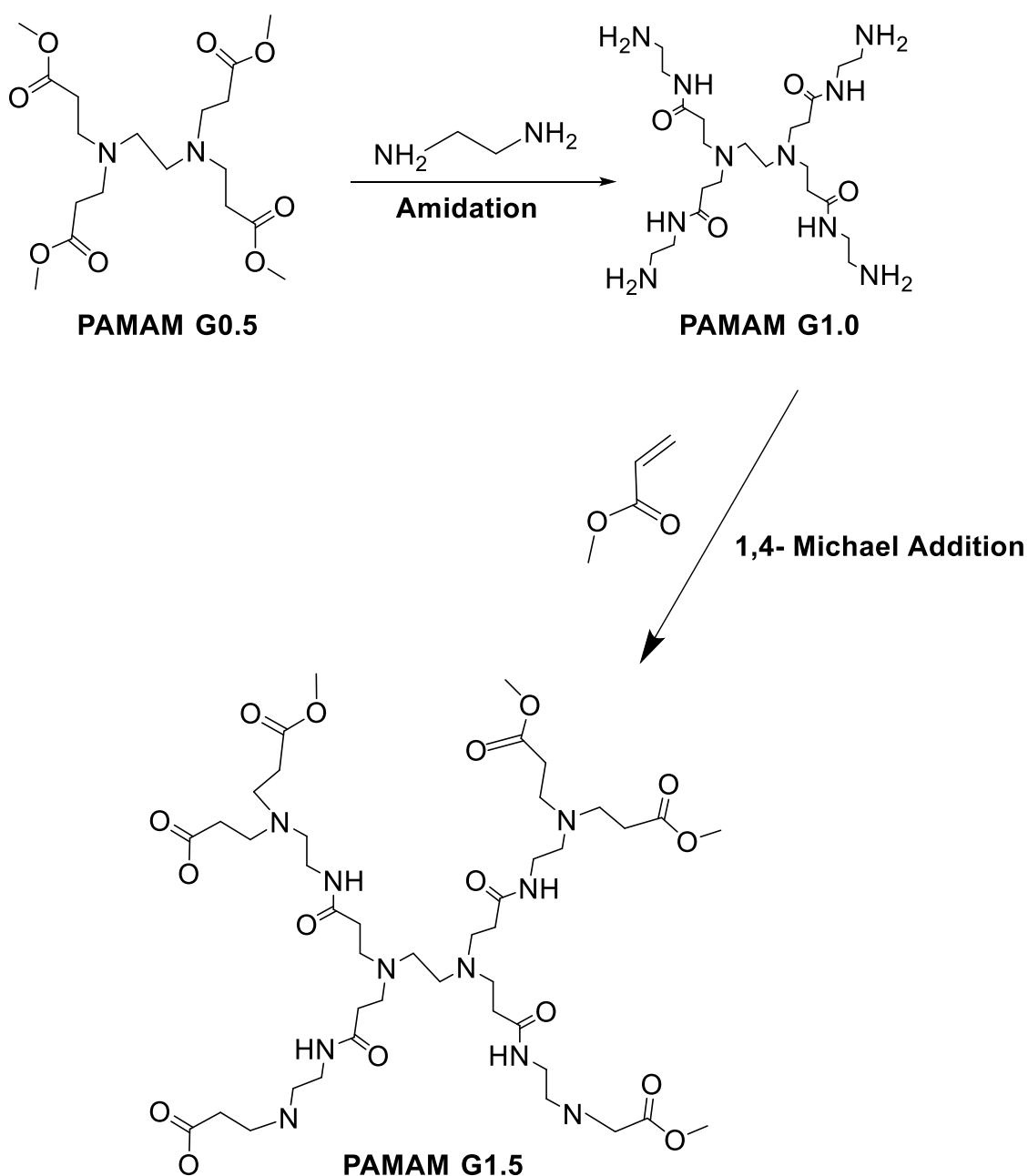
The objective of this study is to synthesize Iron Oxide Nanoparticles ( $\text{Fe}_3\text{O}_4$  MNPs). Due to their inherent instability, it is crucial to stabilize these nanoparticles effectively. To achieve this, we propose the use of PAMAM dendrimers as stabilizing agents. Specifically, we aim to synthesize neutral, hydroxyl-terminated PAMAM dendrimers. However, these neutral dendrimers exhibit limited binding affinity to Iron Oxide Nanoparticles because they are capped with hydroxyl groups, and do not carry a significant charge. This absence of charge leads to weak or nonexistent electrostatic interactions with the charged surface of the iron oxide nanoparticles, resulting in limited binding affinity. Therefore, it is necessary to functionalize these dendrimers, converting them into carboxyl-terminated PAMAM dendrimers, which possess a stronger binding capacity to the magnetic nanoparticles. This functionalization will enhance the stabilization and performance of the  $\text{Fe}_3\text{O}_4$  MNPs.

### Synthesis of PAMAM dendrimers:

The synthesis of PAMAM dendrimers began with the generation 0.5 (G 0.5) dendrimer, utilizing the divergent method due to its straightforward and simpler approach compared to the convergent method. As illustrated in Scheme 2.3, the synthesis involved reacting methyl acrylate with ethylenediamine (EDA) at room temperature. In this reaction, the nucleophilic EDA added to the unsaturated alkene group of methyl acrylate. EDA, containing two amine groups each with two hydrogen atoms, reacted with four molecules of methyl acrylate, resulting in the formation of the G 0.5 dendrimer. To ensure complete nucleophilic addition, methyl acrylate was used in slight excess. After the reaction, any excess solvent and unreacted methyl acrylate were removed using a rotary evaporator.



**PAMAM G0.5**



Scheme 2.3: Depicts the synthetic route for the creation of 0.5 and 1.0 generation dendrimers using the divergent method, a popular approach for constructing dendrimers layer by layer from a central core. This scheme visually illustrates the stepwise process involved in the synthesis, highlighting key chemical reactions and structural transformations at each stage of dendrimer growth.

## Mechanism of PAMAM Dendrimers' Reaction:

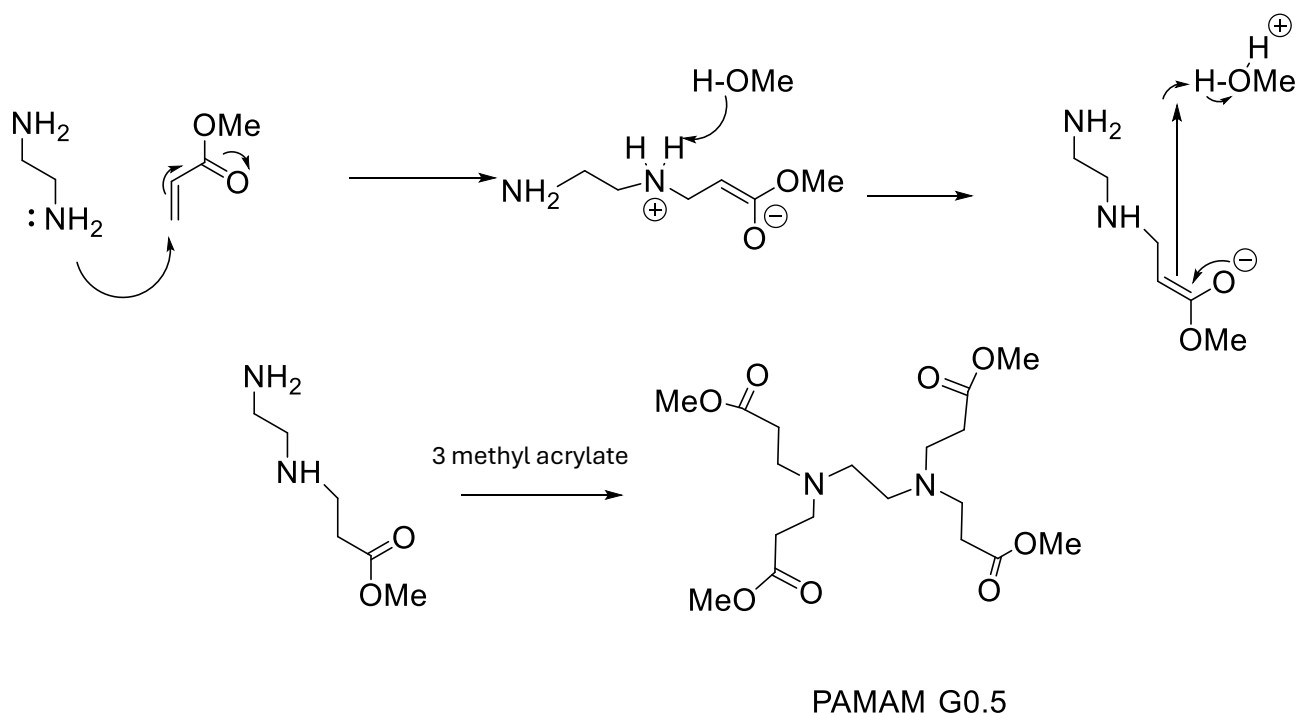
The procedure consists of two key reactions repeated in sequence: (1) a 1,4-Michael addition forming ester-terminated PAMAM dendrimers, and (2) an amination reaction at the amine termini of the dendrimers, as illustrated in Scheme 2.4. This approach allows for the systematic construction of dendrimer generations, enabling the assembly of a combinatorial library of various dendrimer sizes. Scheme 2.4 depicts the initial 1,4-Michael addition step for creating half-generation PAMAM dendrimers. Generation 0.5 (G 0.5) was synthesized in methanol using ethylene diamine (EDA) and methyl acrylate, with methyl acrylate used in excess to ensure complete Michael addition and prevent dendrimer degradation. In this reaction, the nucleophilic amine group in EDA attacks the electrophilic terminal  $\beta$ -carbon of methyl acrylate via 1,4-Michael addition. The reaction's completion was confirmed by  $^1\text{H}$  NMR analysis, which identified a methoxy peak (ester group) at 3.68 ppm and a singlet at 2.53 ppm, integrating 4H, attributed to the core EDA. The absence of a peak around 5-6 ppm indicated the complete removal of excess methyl acrylate. Additionally,  $^{13}\text{C}$  NMR and FTIR spectra showed ester C=O signals at 175 ppm and  $1729\text{ cm}^{-1}$ , respectively. Mass spectrometry corroborated the molecular mass with an ion at 404 ( $\text{MH}^+$ ), confirming the product.

The second step involves an amidation reaction to produce a full generation dendrimer, as shown in Scheme 2.5. In this step, the lone pair of nitrogen in EDA attacks the electrophilic carbon ester ( $\text{C}=\text{O}$ ), forming an intermediate. This intermediate is protonated by a second terminal amine, causing the methoxy group to leave and resulting in the formation of a full generation dendrimer. Generation 1.0 (G 1.0) was synthesized by reacting G 0.5 in methanol with an excess of EDA. The excess EDA was removed using an azeotropic mixture of toluene and methanol (9:1 ratio). The purified G 1.0 dendrimer was confirmed by  $^1\text{H}$  NMR spectroscopy, which showed the absence of the EDA peak at 2.66 ppm. The FTIR peak at  $1731\text{ cm}^{-1}$

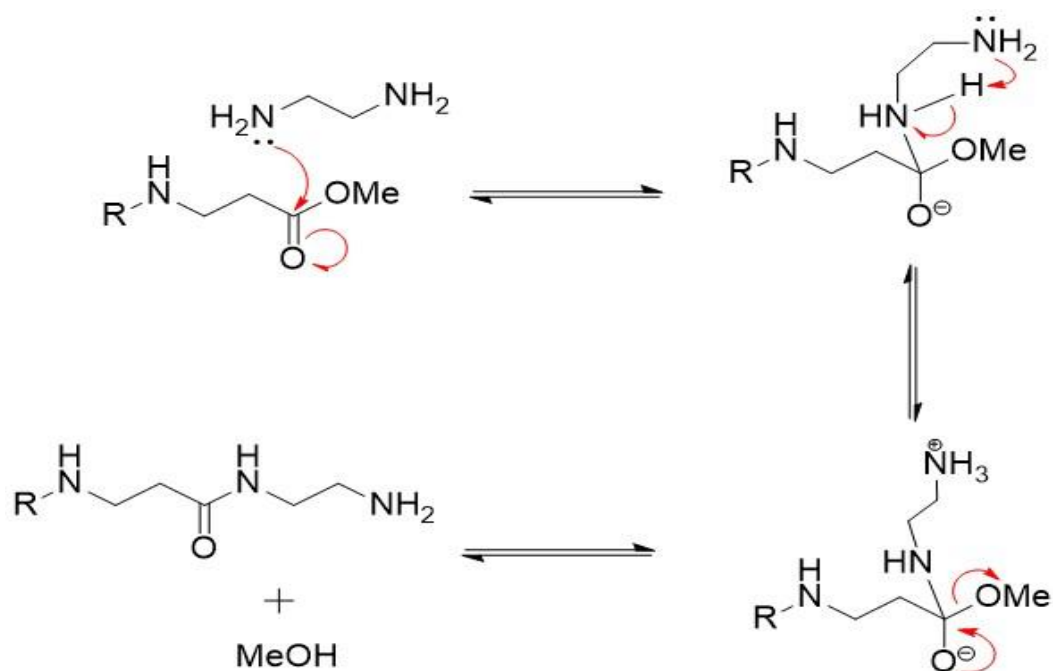


$\text{cm}^{-1}$  and the  $^1\text{H}$  NMR peak at 3.68 ppm, representing the C=O ester, were no longer visible.

The characterization of 0.5 to 4.0 generations PAMAM dendrimers is summarized in table 2.2.



Scheme 2.4: Illustrates the mechanism of the reaction for half-generation (G0.5) PAMAM (Polyamidoamine) dendrimers with ester termination. This scheme details the chemical processes involved in synthesizing a dendrimer with a 0.5 generation, where the dendrimer has partially developed branches that end in ester groups. The diagram typically breaks down the reaction steps, the intermediates formed, and the transformations leading to the final dendrimer structure.



Scheme 2.5: Details the mechanism of the amidation reaction used to synthesize full generation (G1.0) PAMAM (Polyamidoamine) dendrimers with amine-terminated branches. This schematic representation provides insight into the chemical process by which PAMAM dendrimers are constructed and functionalized, specifically focusing on the formation of the first full generation dendrimer with amine terminal group.

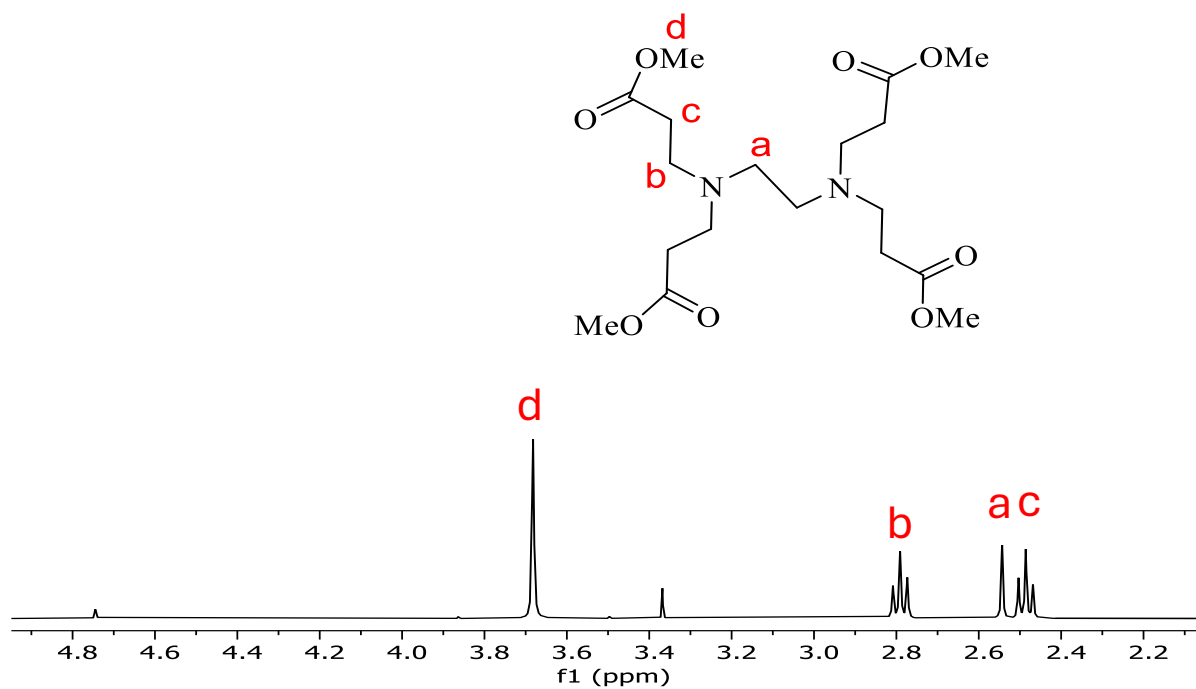


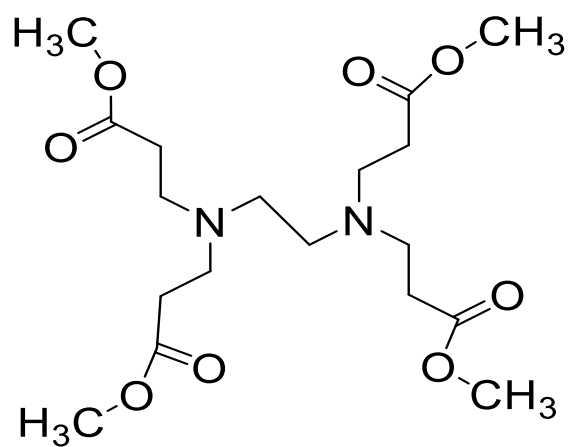
Figure 2.8: Presents the  $^1\text{H}$  NMR (proton nuclear magnetic resonance) spectra for half-generation PAMAM (Polyamidoamine) dendrimers. This figure provides a detailed analysis of the chemical environment and structure of PAMAM dendrimers at the 0.5 generation stage, offering insights into their molecular composition and functional groups.

Dendrimer generation	Molecular formula	Molecular weight (g/mol)	Terminal groups
0.5	C <sub>18</sub> H <sub>32</sub> N <sub>2</sub> O <sub>8</sub>	404.46	4 esters (CO <sub>2</sub> Me)
1.0	C <sub>22</sub> H <sub>48</sub> N <sub>10</sub> O <sub>4</sub>	516.69	4 amines (NH <sub>2</sub> )
1.5	C <sub>54</sub> H <sub>96</sub> N <sub>10</sub> O <sub>20</sub>	1205.41	8 esters (CO <sub>2</sub> Me)
2.0	C <sub>62</sub> H <sub>128</sub> N <sub>26</sub> O <sub>12</sub>	1429.87	8 amines (NH <sub>2</sub> )
2.5	C <sub>126</sub> H <sub>224</sub> N <sub>26</sub> O <sub>44</sub>	2808	16 esters (CO <sub>2</sub> Me)
3.0	C <sub>142</sub> H <sub>288</sub> N <sub>58</sub> O <sub>28</sub>	3257	16 amines (NH <sub>2</sub> )
3.5	C <sub>270</sub> H <sub>480</sub> N <sub>58</sub> O <sub>92</sub>	6011	32 esters (CO <sub>2</sub> Me)
4.0	C <sub>302</sub> H <sub>608</sub> N <sub>122</sub> O <sub>60</sub>	6908.93	32 amines (NH <sub>2</sub> )

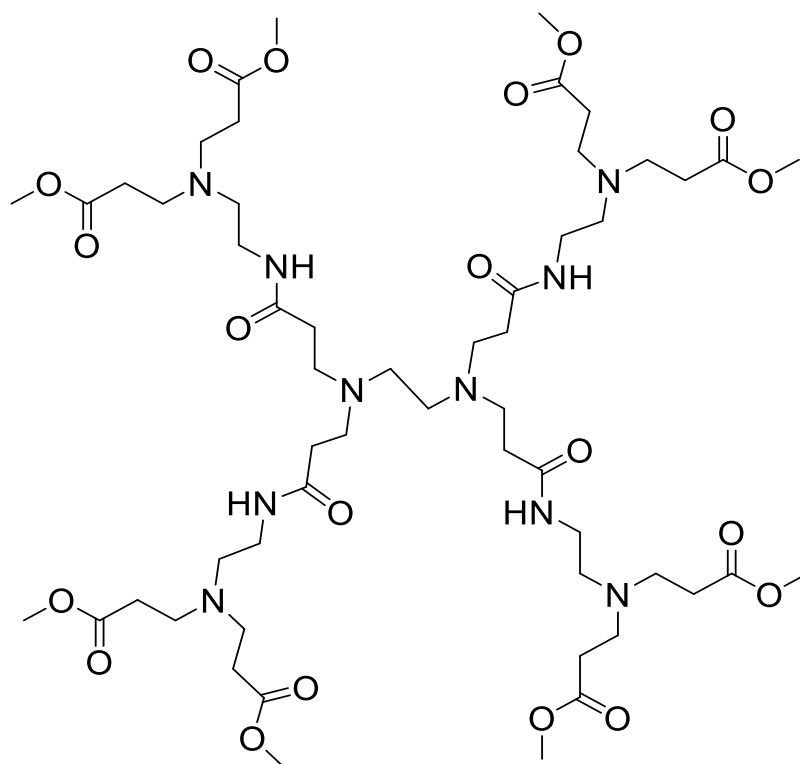
Table 2.2: Provides a comprehensive overview of PAMAM dendrimers across generations, from 0.5 to 4.0, focusing on the evolution of their structural and functional properties. By detailing the number of branching units, terminal functional groups, molecular weight, size, surface density, and applications, the table offers valuable insights into how dendrimers grow and change with each generation.

<b>Dendrimer Generation (G)</b>	<b>C=O (cm<sup>-1</sup>) ester</b>	<b>C=O (cm<sup>-1</sup>) Amide</b>
0.5	1733	-
1.0	-	1640
1.5	1734	1648
2.0	-	1639
2.5	1733	1644
3.0	-	1635
3.5	(734	1645

Table 2.3: Provides an extensive analysis of the infrared (IR) spectra for PAMAM (Polyamidoamine) dendrimers across various generations, ranging from 0.5 to 3.5. This table is crucial for understanding the chemical characteristics and structural changes in PAMAM dendrimers as they progress through different generations.

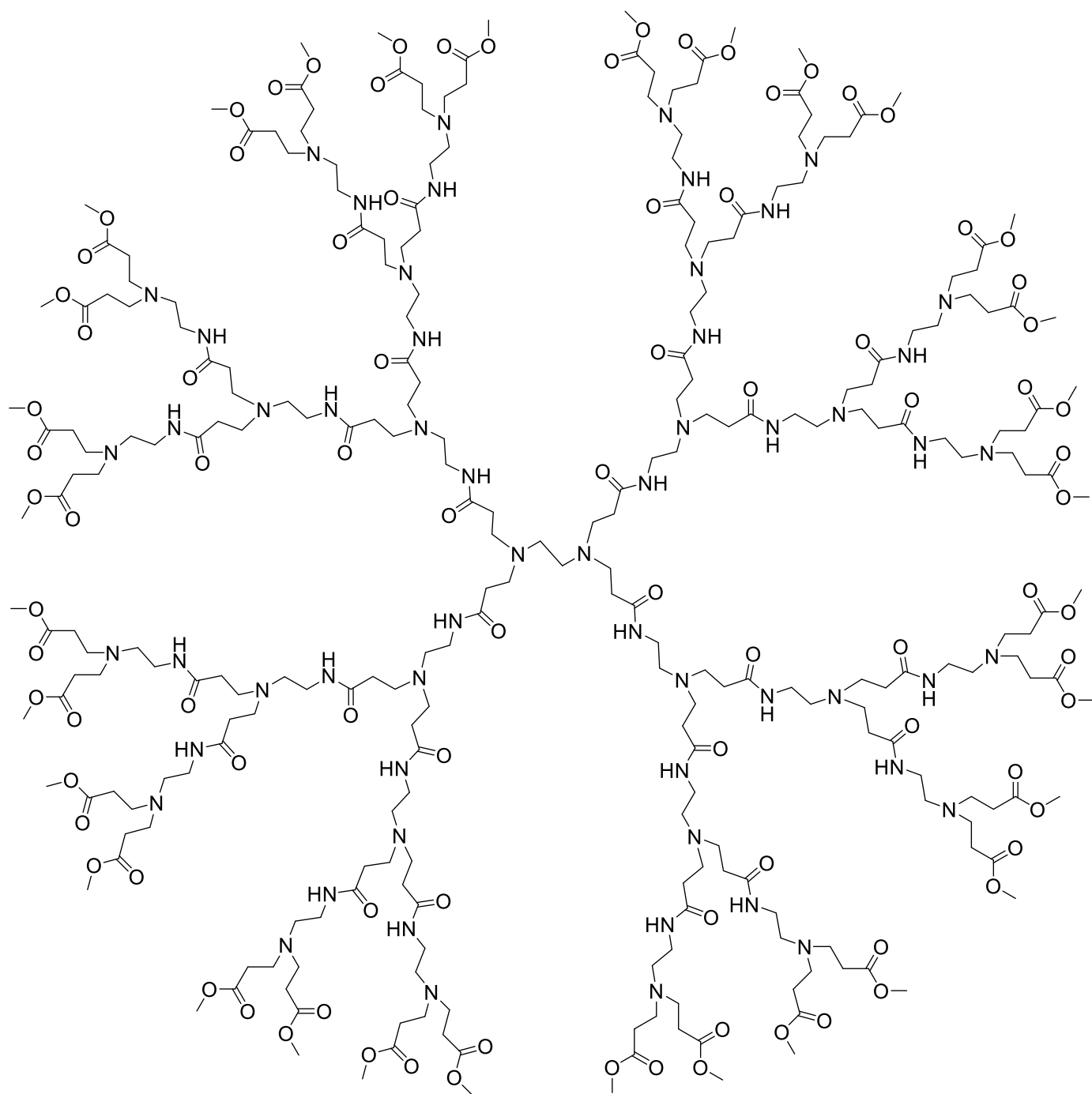


**Scheme Representation of PAMAM dendrimers generation 0.5**



**Schematic Representation of PAMAM dendrimers generation 1.5**





**Schematic Representation of PAMAM dendrimers generation 3.5**



## Purification of dendrimers:

To ensure the successful application of dendrimers across various fields, it is crucial that they are synthesized in a highly pure form. The synthesis of PAMAM dendrimers involves multiple generations, each requiring careful purification to remove excess reagents and prevent unwanted side reactions. The purification process can be divided into two main steps: removal of methyl acrylate (MA) and ethylenediamine (EDA), both of which are used in different stages of the synthesis. In the first half-generation, ester-terminated dendrimers are formed, and excess MA must be removed. This step is relatively straightforward because of MA's high volatility, allowing for efficient removal using a rotary evaporator. However, the challenge arises during the second half-generation, where amidation occurs, and EDA is used. EDA strongly interacts with amide and amine groups through hydrogen bonding, making it much harder to remove compared to MA. Any residual EDA can interfere with subsequent reactions, leading to the formation of by-products and increasing the molecular weight distribution, ultimately affecting the purity of the dendrimer. Due to the limitations of standard rotary evaporation at high temperatures (which risks reversing essential Michael addition reactions), a more effective purification method is necessary. One proven approach is using an azeotropic mixture of toluene and methanol in a 9:1 ratio. This mixture disrupts the hydrogen bonding of EDA with the dendrimer, allowing for its more complete removal when combined with prolonged rotary evaporation. The success of the purification is confirmed using  $^1\text{H}$  NMR spectroscopy, where the presence of residual EDA is detectable by its signal at approximately 2.7 ppm. An alternative method, developed by Tomalia et al.,<sup>67</sup> involves using n-butanol for purification. Although n-butanol has a high boiling point, which makes it more difficult to remove, it does not participate in any unwanted side reactions. This makes it a useful option for the synthesis of higher-generation dendrimers, where purification challenges become more

pronounced. However, for lower generations, the azeotropic toluene-methanol mixture, paired with a powerful vacuum pump, remains the more effective approach.

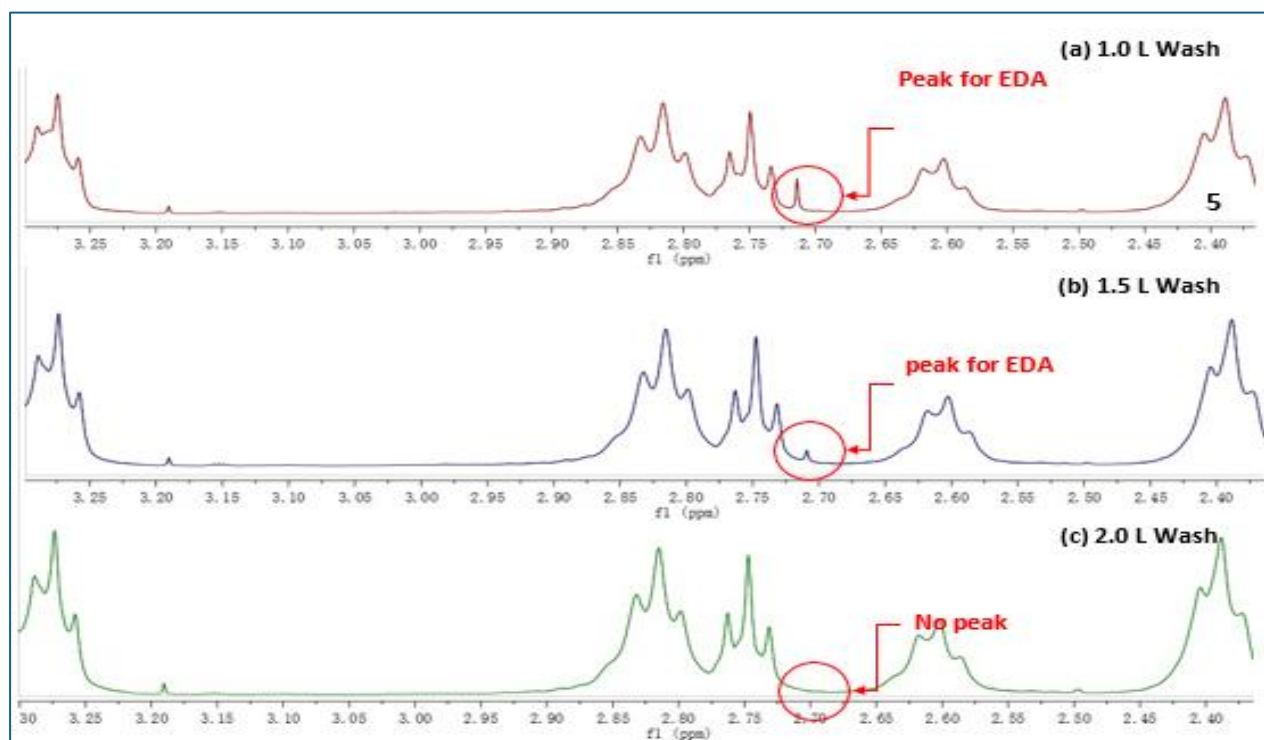


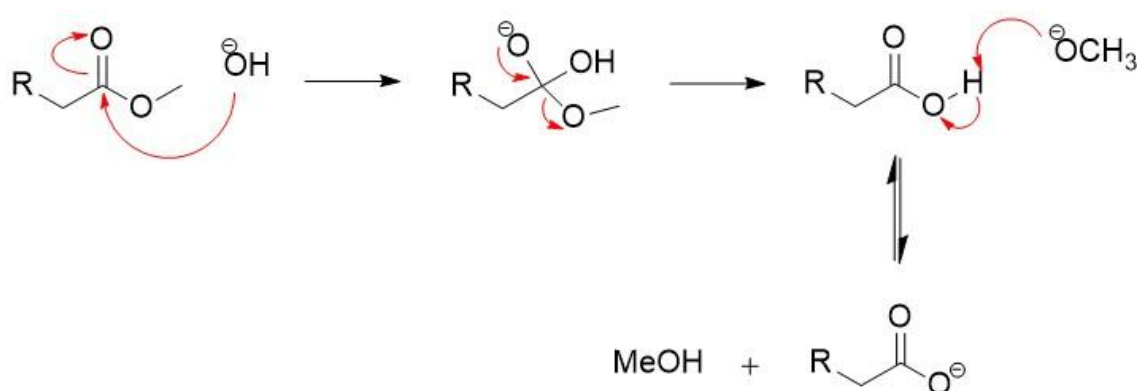
Figure 2.9: Shows a series of NMR spectra representing the results of washing Generation 3 PAMAM dendrimers with different volumes of azeotropic mixture in order to remove residual ethylenediamine (EDA), which is a byproduct or impurity that needs to be eliminated after dendrimer synthesis.

The series of spectra presented in figures (a), (b), and (c) illustrate the progressive removal of ethylenediamine (EDA) from the sample through increasing wash volumes. In Figure (a), after a 1.0 L wash, a distinct peak at around 2.7 ppm indicates a significant amount of residual EDA in the sample, suggesting that the purification process is incomplete. As shown in Figure (b), after washing with 1.5 L of solvent, the intensity of the EDA peak at 2.7 ppm decreases, indicating partial removal of the compound, though it is still present in the sample. Finally, in Figure (c), following a 2.0 L wash, the EDA peak has completely disappeared from the

spectrum, confirming the complete removal of EDA and successful purification of the dendrimer. These results highlight the effectiveness of increased wash volumes in eliminating EDA, a crucial step in ensuring the purity and functionality of dendrimers for further applications.

### Synthesis of carboxylic PAMAM dendrimer (COOH):

To test the ability of PAMAM dendrimers to bind with positively charged protein molecules, dendrimers with negatively charged terminal groups were selected. Specifically, the ester groups present in the half-generation PAMAM dendrimers were hydrolyzed using sodium hydroxide, converting them into carboxylate groups. This reaction yields the sodium salt form of the dendrimers (PAMAM-COONa), which were isolated and used for all subsequent characterizations. The negatively charged carboxylate groups are ideal for this purpose, as they can interact electrostatically with the positively charged proteins, promoting effective binding.



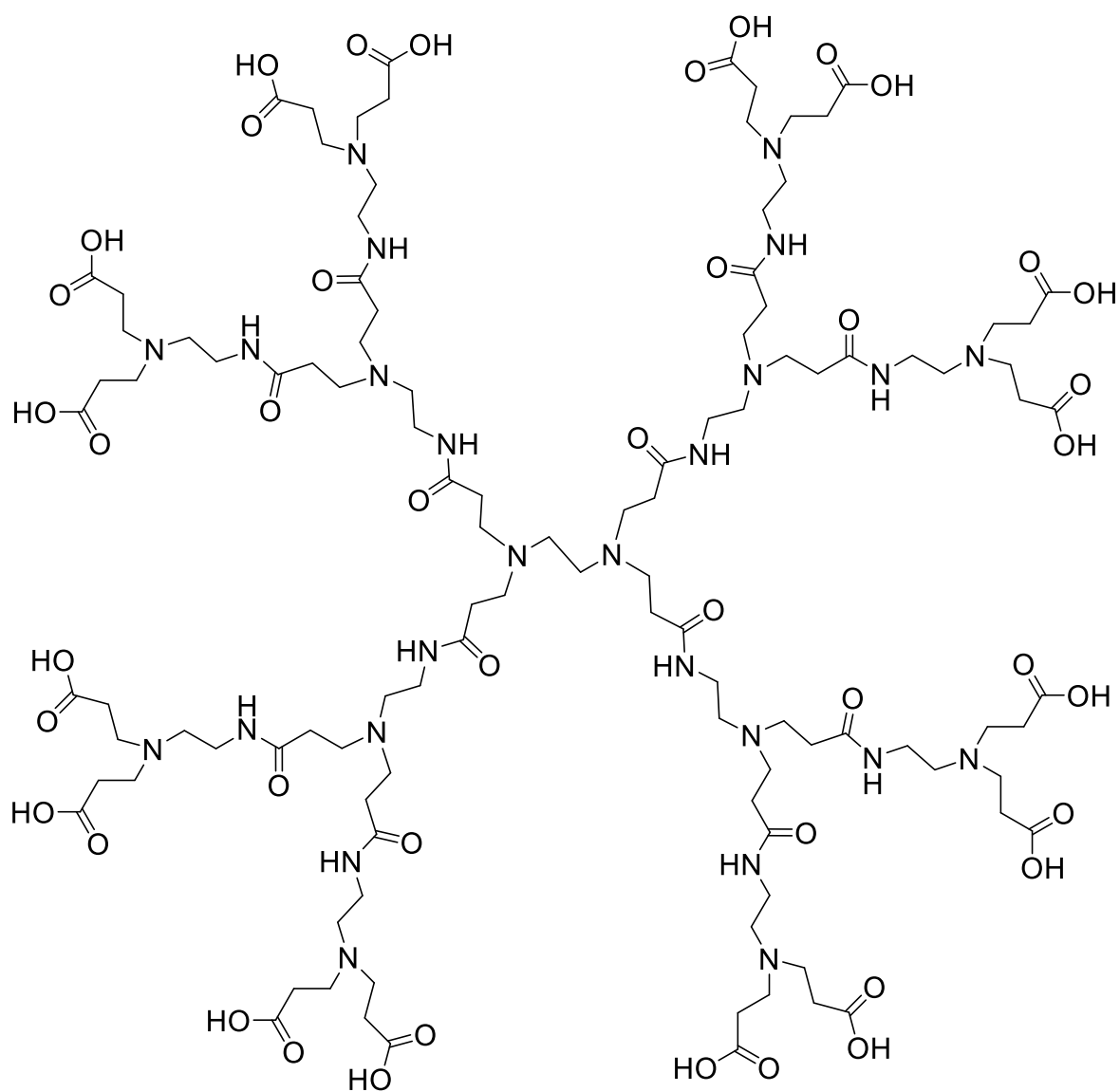
Scheme 2.6: Illustrates the formation of a tetrahedral intermediate, initiated by the attack of a hydroxide ion on the electrophilic carbon of the ester group (C=O). This is followed by the methoxy anion acting as a base, deprotonating the carboxylic acid.

The successful conversion to G1.5 COOH was verified using  $^1\text{H}$  NMR spectroscopy, where the disappearance of the methyl ester peak at 3.69 ppm confirmed the reaction, and new methylene protons appeared as a triplet at 2.26 ppm ( $\text{CH}_2\text{CO}$ ). To further validate the functional groups,  $^{13}\text{C}$  NMR spectroscopy showed peaks at 175.9 ppm ( $\text{C}=\text{O}$ ) and 182.3 ppm (carboxylate group  $\text{C}=\text{O}$ ). FTIR spectroscopy also confirmed key functional groups, with notable signals at  $3263\text{ cm}^{-1}$  (N-H stretch) and  $1645\text{ cm}^{-1}$  ( $\text{C}=\text{O}$  stretch). Completion of the reaction was additionally confirmed by mass spectrometry (MALDI-TOF MS), which detected a molecular ion peak at 1093 ( $\text{MH}^+$ ). The same synthetic process was applied to produce anionic dendrimers up to G3.5-COOH, with all generations characterized using the same methods as outlined in table 2.4.

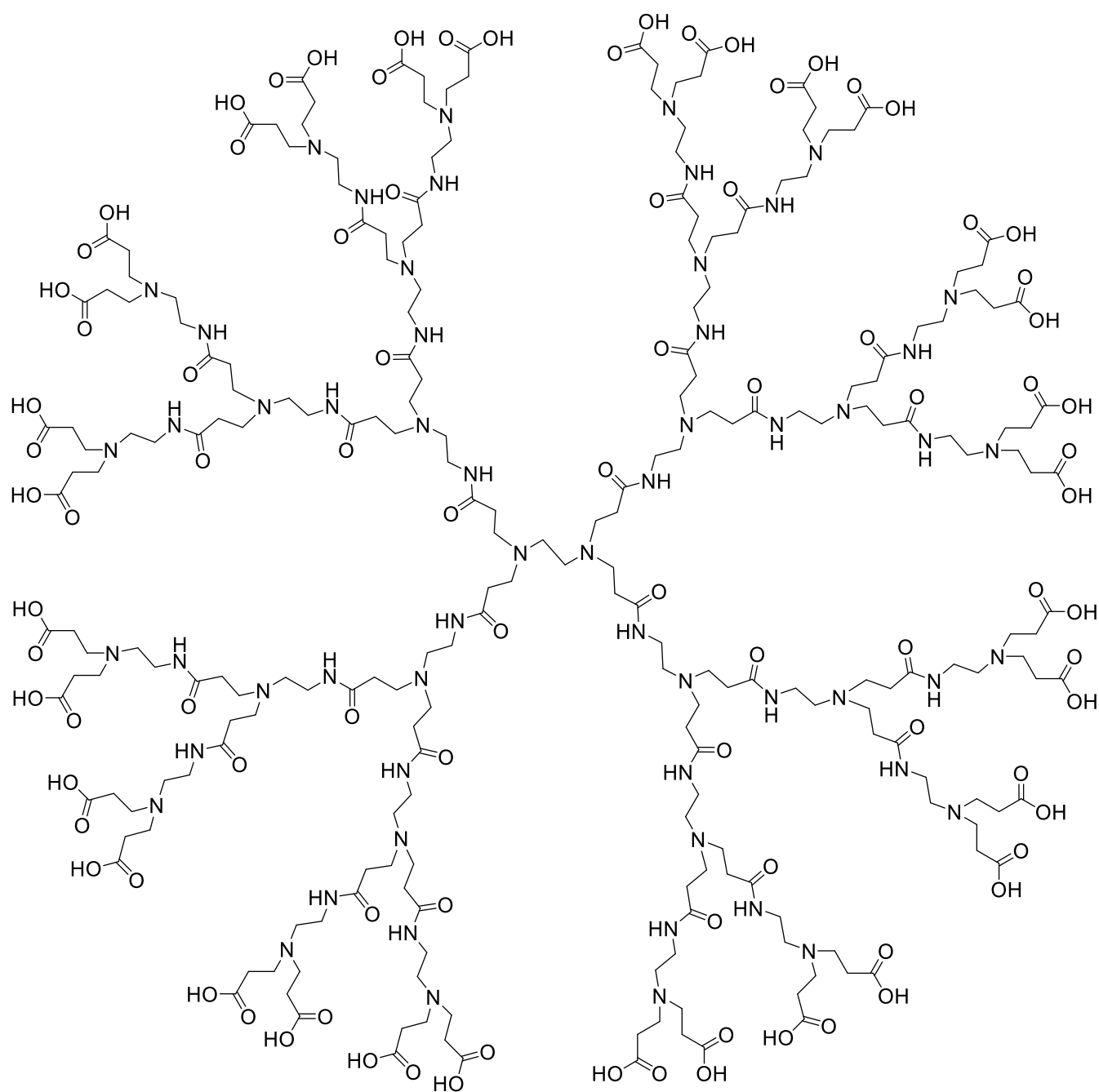
Acidic Dendrimer Generation	Chemical Formula	Expected Molecular weight (g/mol)	Number Of carboxylate surface groups	Addressable Area Å <sup>2</sup>	Obtained Mass ion ( $\text{MH}^+$ )
1.5	$\text{C}_{46}\text{H}_{80}\text{N}_{10}\text{O}_{20}$	1093	8	720	1093
2.5	$\text{C}_{110}\text{H}_{192}\text{N}_{26}\text{O}_{44}$	2583	16	1815	2583
3.5	$\text{C}_{238}\text{H}_{416}\text{N}_{58}\text{O}_{92}$	5563	32	2770	5563

Table 2.4: Presents the analysis of carboxylic PAMAM dendrimers (COOH) from generations 1.5 to 3.5, highlighting key characteristics such as molecular size, number of terminal carboxyl groups, binding Area and their structural properties. The analysis focuses on how the dendrimer generations differ in terms of their size, functionality, and potential applications.





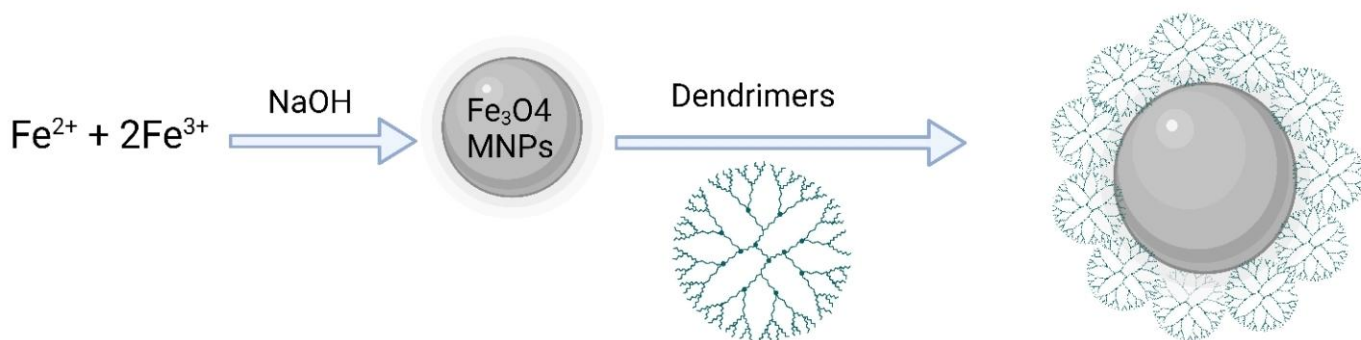
Schematic Representation of COOH PAMAM dendrimers generation 2.5



Schematic Representation of COOH PAMAM dendrimers generation 3.5

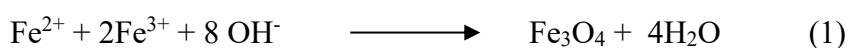
## Synthesis of Iron Oxide Nanoparticles (Fe<sub>3</sub>O<sub>4</sub> MNPs):

The main objective was to stabilize magnetic nanoparticles (MNPs) by employing different generations of PAMAM dendrimers, as described in scheme 2.6. Stabilization of MNPs is crucial for maintaining their stability, preventing agglomeration, and ensuring uniform distribution in a range of applications, such as magnetic resonance imaging (MRI), catalysis and drug delivery, by applying different generations of PAMAM dendrimers, which vary in size, surface functionality, and branching.



Scheme 2.6: Schematic representation of reactions used to functionalise the Fe<sub>3</sub>O<sub>4</sub> NPs onto the OH<sup>-</sup> terminated PAMAM dendrimers. This figure was prepared by using [BioRender](#).

The chemical reaction leading to the precipitation of Fe<sub>3</sub>O<sub>4</sub> (magnetite) is given by the following equation:



In this process, ferrous (Fe<sup>2+</sup>) and ferric (Fe<sup>3+</sup>) ions combine with hydroxide ions (OH<sup>-</sup>) in an aqueous solution. The hydroxide ions play a critical role by facilitating both oxidation and



hydrolysis, leading to the precipitation of magnetite ( $\text{Fe}_3\text{O}_4$ ), with water molecules being produced as byproducts.

The reactions involved in the formation of ferrous and ferric hydroxides are shown below:



Magnetite ( $\text{Fe}_3\text{O}_4$ ) is expected to fully precipitate within a pH range of 7.5 to 14, provided that the  $\text{Fe}^{2+}/\text{Fe}^{3+}$  molar ratio is maintained at 1:2 in a non-oxidizing environment. However, in the presence of oxidizing conditions,  $\text{Fe}_3\text{O}_4$  can undergo further oxidation, as illustrated in the following equations:

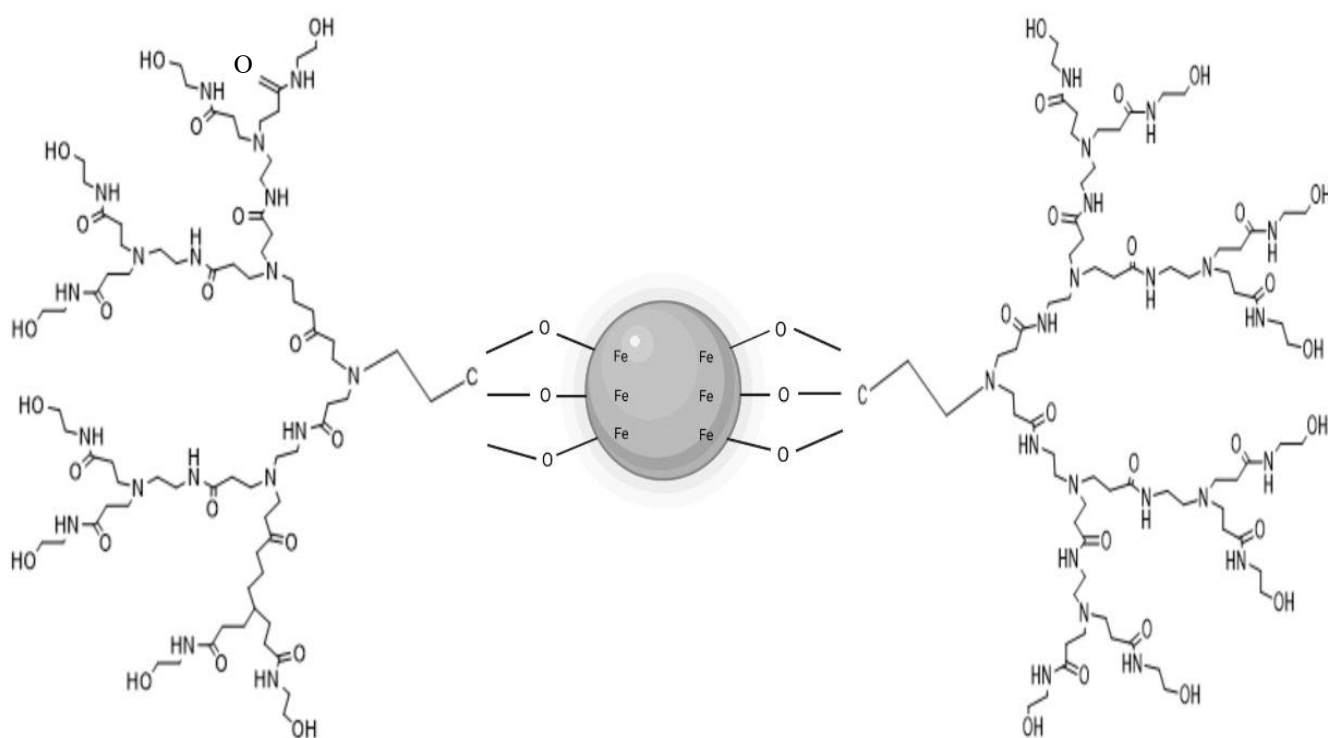


Figure 2.7: Schematic representation of the reactions used to functionalize  $\text{Fe}_3\text{O}_4$  nanoparticles onto COOH-terminated PAMAM dendrimers. For clarity, only two dendrimer arms are shown

to illustrate the binding process, although the full dendrimer structure possesses multiple functional groups available for attachment. This figure was prepared by using BioRender.

An aqueous dispersion of magnetic nanoparticles (MNPs) was prepared by adding a mixture of ferric and ferrous salts to a strong alkaline NaOH solution at room temperature. In this study, NaOH was chosen as the alkali source instead of ammonia because NaOH, being a strong base, fully dissociates in water, providing a stable and high pH necessary for many iron-related reactions. Ammonia, in contrast, is a weak base and does not offer as stable or strong a pH environment. To prevent oxidation during the synthesis, nitrogen gas was flowed through the reaction medium in a closed system to eliminate oxygen. MNPs with an average particle size of 6 nm were synthesized without the need for additional stabilizers. Typically, 5 mL of an iron solution containing 0.1 M  $\text{Fe}^{2+}$  and 0.2 M  $\text{Fe}^{3+}$  was added dropwise to 50 mL of NaOH solution (0.5 M), which had been preheated to 80 °C before the coprecipitation reaction. The mixture was stirred vigorously for 30 minutes at room temperature, and the suspension quickly turned black, indicating the formation of MNPs. The precipitated powders were collected using an external magnetic field, and the supernatant was removed by decantation. The particles were washed with deoxygenated Milli-Q water and separated by centrifugation at 2000 rpm. To neutralize the anionic charge on the particle surface, the MNPs were washed with 0.4 M HCl solution, after which the positively charged colloidal particles were again separated by centrifugation and washed with deoxygenated Milli-Q water. Iron can exist in multiple oxidation states, making redox reactions possible during synthesis. These redox reactions can lead to destabilization of the nanoparticles, and the formation of different iron species is closely linked to these redox processes.

Magnetite ( $\text{Fe}_3\text{O}_4$ ) can be synthesized through the controlled oxidation of  $\text{Fe}^{2+}$  in solution. This process typically involves maintaining specific conditions, such as pH and temperature, to ensure the proper balance between  $\text{Fe}^{2+}$  and  $\text{Fe}^{3+}$  ions, as outlined in the following equations:

The oxidation kinetics of  $\text{Fe}^{2+}$  are slow and difficult to control, making it more practical to form magnetite using a mixture of  $\text{Fe}^{2+}$  and  $\text{Fe}^{3+}$  in the starting solution. In this approach, steps are taken to prevent the oxidation of  $\text{Fe}^{2+}$  during the synthesis. As a result, stable  $\text{Fe}_3\text{O}_4$  magnetic nanoparticles (MNPs) were successfully produced. These nanoparticles demonstrated good stability, retaining their structural integrity and magnetic properties for over 30 days. Additionally, due to their strong magnetic properties, the  $\text{Fe}_3\text{O}_4$  MNPs could be easily manipulated using a magnet (as shown in figure 2.12).

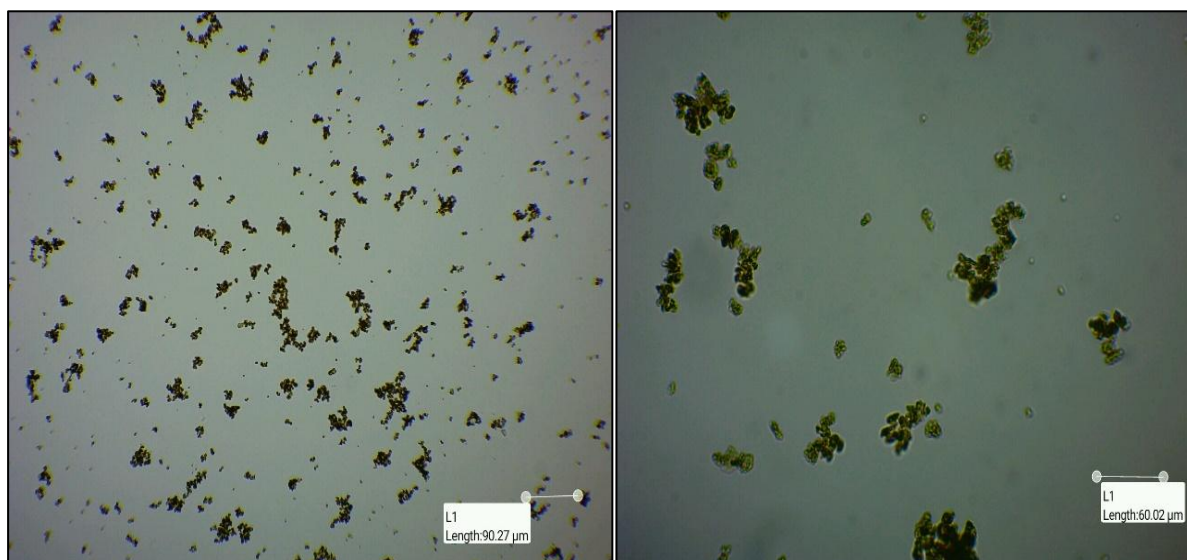


Figure 2.10: Microscope images of Magnetic Iron Oxide Nanoparticles ( $\text{Fe}_3\text{O}_4$  MNPs). These images provide a detailed visual representation of the nanoparticles, showcasing their shape, and overall morphology.

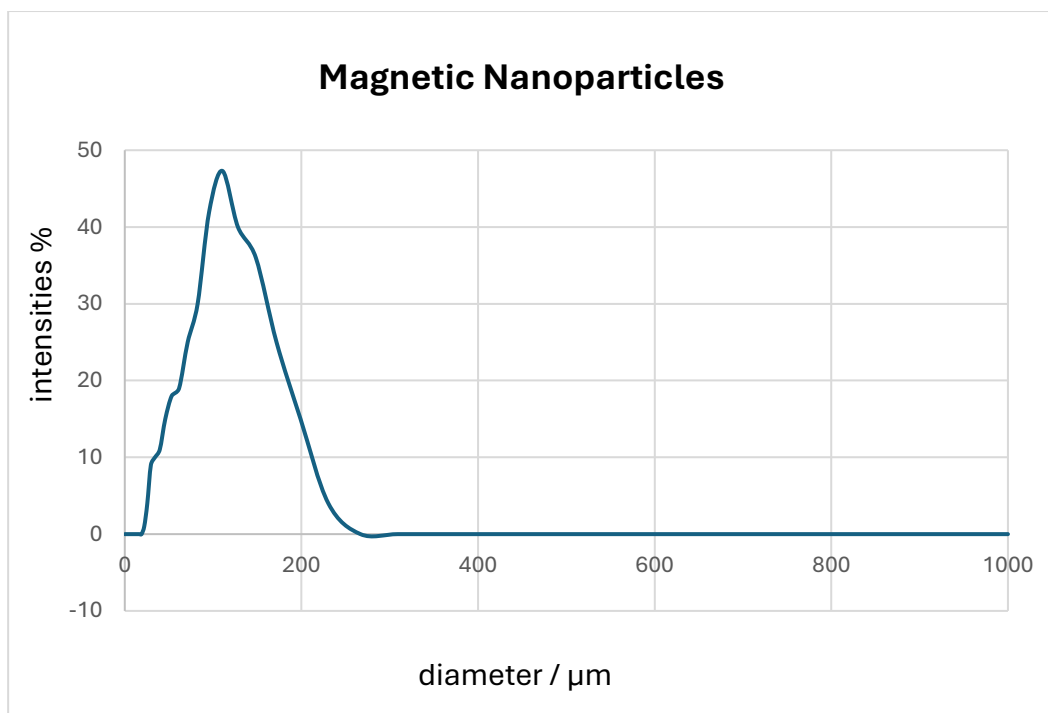


Figure 2.11: DLS data for iron magnetic nanoparticles (combined results from three separate sets of measurements). The intensity distribution reveals a broad peak, indicating a large particle size, which is attributed to aggregation. Magnetic nanoparticles tend to aggregate quickly, forming large clusters. Within approximately 30 minutes, these particles grow into micron-sized aggregates.

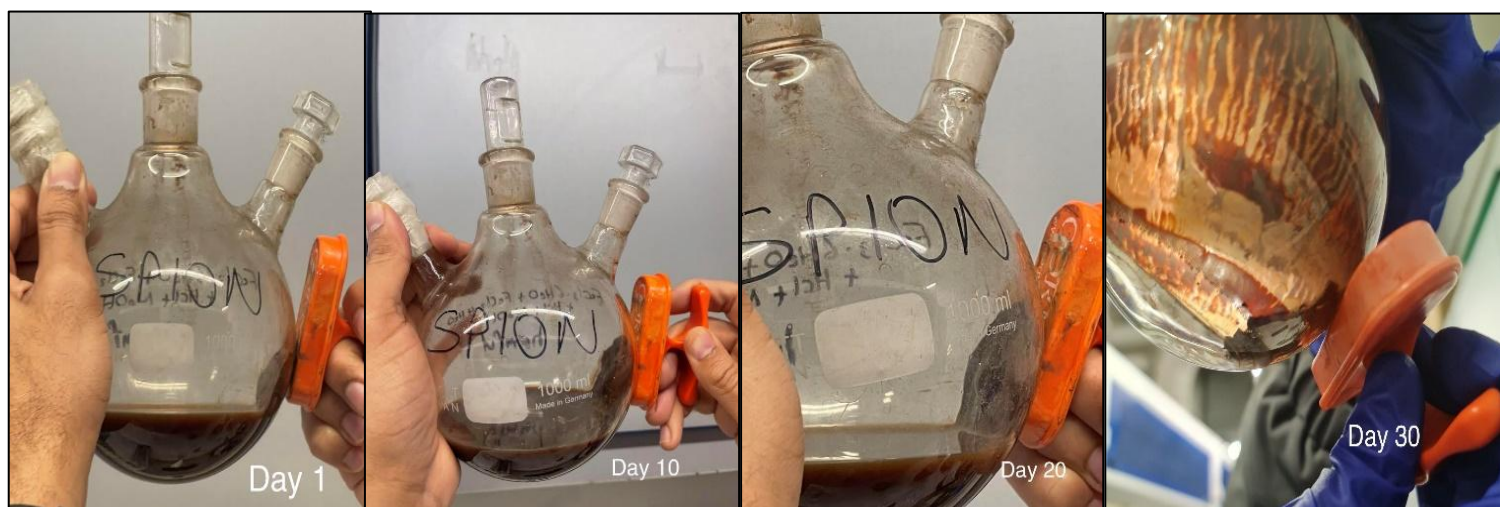


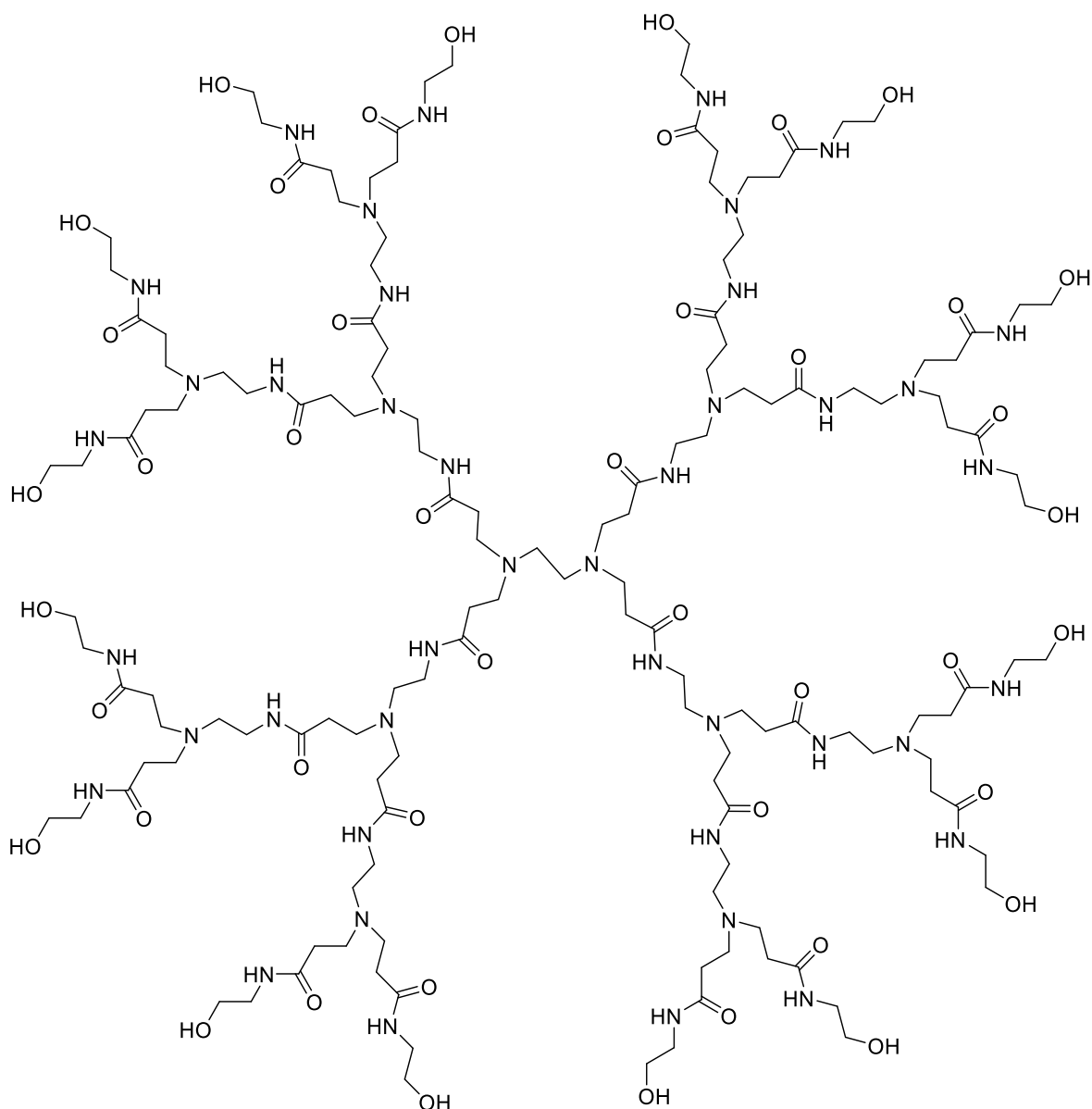
Figure 2.12: Illustrates the magnetic response of  $\text{Fe}_3\text{O}_4$  magnetic nanoparticles (MNPs) over time, demonstrating how these nanoparticles behave under the influence of an external magnetic field held at right of each picture. The images capture the dynamic interaction between the nanoparticles and the magnetic field, showcasing their ability to respond and align with the applied field.

### Stabilization of MNPs using OH terminated PAMAM dendrimers:

Amine-terminated polyamidoamine (PAMAM) dendrimers are generally not used to stabilize iron nanoparticles because they can promote the oxidation of  $\text{Fe}^{2+}$  to  $\text{Fe}^{3+}$ , leading to the formation of insoluble iron oxides or hydroxides. This oxidation can destabilize the nanoparticles, causing aggregation or precipitation, which is undesirable for many applications. In contrast, hydroxyl-terminated PAMAM dendrimers are preferred as they impart hydrophilicity, making them highly soluble in aqueous solutions. This improved solubility enhances the dispersion of iron nanoparticles, which in turn prevents aggregation and leads to more stable suspension. In this study, three generations of hydroxyl-terminated PAMAM dendrimers generations 1.5, 2.5, and 3.5 were tested to determine which was the most effective

at stabilizing magnetic nanoparticles (MNPs). It was initially hypothesized that the differences in stabilization efficiency among the generations would be minimal. However, generation 1.5 was found to be inadequate due to its limited number of terminal groups (8 groups) and smaller molecular size, resulting in a thinner coating on the nanoparticles and suboptimal stabilization. In contrast, generation 3.5, with its extensive branching and 32 terminal groups, provided a much thicker coating, but its large size led to difficulties with mixing and homogeneity in the nanoparticle suspension. Generation 2.5 dendrimers, with their intermediate size and branching, offered the best performance, achieving a balance that prevented nanoparticle aggregation effectively. The moderate number of terminal groups provided sufficient surface coverage, making G2.5 dendrimers the optimal choice for stabilizing the MNPs without the issues seen in G3.5. Thus, generation 2.5 hydroxyl-terminated PAMAM dendrimers were identified as the most effective stabilizers (Figure 2.13).

The procedure was as follows: an aqueous solution (515 mL) containing 5 mg of  $\text{Fe}_3\text{O}_4$  nanoparticles was mixed with 1 mL of functionalized G2.5 PAMAM dendrimers ( $1 \text{ mg mL}^{-1}$  in water) and shaken for 24 hours. The mixture was then centrifuged at 6000 rpm for 10 minutes to remove any unadsorbed dendrimers. The particles were re-dispersed in water and subjected to intense sonication for two hours. To purify the dendrimer-stabilized  $\text{Fe}_3\text{O}_4$  nanoparticles, five cycles of centrifugation and dispersion were carried out. Finally, the  $\text{Fe}_3\text{O}_4$  nanoparticles were dissolved in water, and the water was replaced with phosphate buffer to maintain a stable suspension.



Schematic representation of generation 2.5 with 16 terminals hydroxy groups PAMAM dendrimer

The microscope images show that while the particles initially appear stable, they become unstable over time, leading to significant aggregation. The particles collapse shortly after the stabilization process. Additionally, the magnetic nanoparticles displayed a minimal magnetic response when exposed to an external magnetic field. This weak response can be attributed to the insufficient number of hydroxyl (OH) groups on the OH-terminated PAMAM dendrimers

used for stabilization. The limited number of OH groups resulted in poor surface functionalization, which compromised the nanoparticles' ability to exhibit strong magnetic properties. As a result, the stabilization provided by these dendrimers was not effective in enhancing the magnetic response of the nanoparticles under the applied magnetic field.

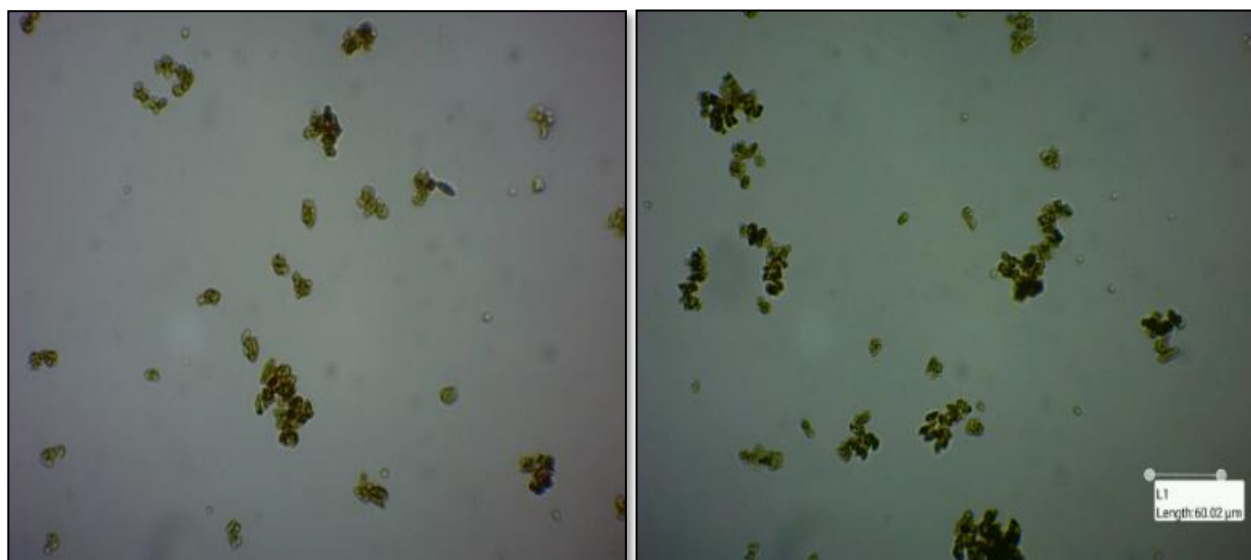


Figure 2.13: Microscope images that showcase the morphological and structural characteristics of  $\text{Fe}_3\text{O}_4$  nanoparticles (NPs) synthesized with two different generations of OH-terminated poly(amidoamine) (PAMAM) dendrimers: specifically, generations 2.5 (left) and 3.5 (right).



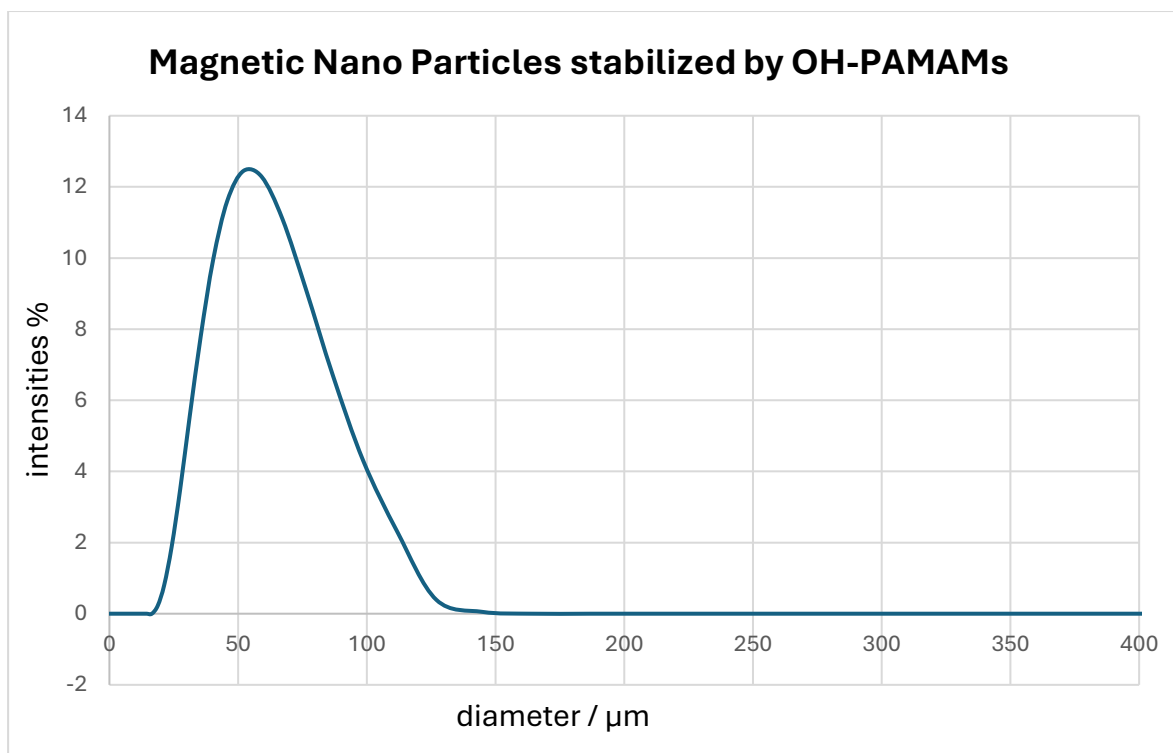


Figure 2.14: DLS data for magnetic nanoparticles (combined from three measurements) show a broad peak in the intensity distribution, indicating that the nanoparticles are not well-stabilized. This suggests that the use of PAMAM dendrimers did not improve their stability, as the larger particle size observed is likely due to aggregation.

### Stabilization of MNPs using COOH-PAMAM dendrimers:

Our goal was to enhance the stabilization of magnetic nanoparticles (MNPs) by incorporating an acid-terminated system, which introduces additional hydrogen-bonding groups. The presence of these groups maximizes the number of hydroxyl (-OH) groups, thereby improving the interactions between the MNPs and the dendrimers. This stronger interaction is crucial for ensuring the long-term stability and functionality of the nanoparticles in various applications, such as drug delivery, biosensing, and magnetic separation.

To address the issue of instability typically associated with MNPs, we specifically employed acidic dendrimers terminated with carboxyl (COOH) groups. The COOH-terminated dendrimers offer multiple advantages for stabilizing MNPs. First, the carboxyl groups provide additional binding sites that can interact with the surface of the nanoparticles, improving their dispersion and preventing aggregation. Second, the increased hydrogen-bonding potential enhances the strength of the interaction between the MNPs and the dendrimer coating, contributing to a more robust and stable system. The acidic dendrimers were used to overcome the instability that often arises in nanoparticle systems due to surface interactions, especially in solutions or biological environments. By ensuring stronger and more stable interactions between the dendrimers and the MNPs, we aimed to achieve better dispersion and reduce the likelihood of particle aggregation, which is a common issue that compromises nanoparticle performance. For consistency and to ensure comparability with our previous studies, we followed the same experimental protocol as outlined in earlier procedures. This involved the functionalization of the MNPs with the carboxyl-terminated dendrimers under controlled conditions to ensure uniform surface coverage. By maintaining the same protocol, we were able to directly assess the impact of the acid-terminated system on the stabilization of the MNPs compared to our previous results. In conclusion, the introduction of the acid-terminated system aimed to improve the overall stability of the MNPs by enhancing hydrogen bonding and surface interactions. This approach is expected to result in a more stable nanoparticle system, suitable for a range of practical applications where stability is critical.

The microscope figures display, just as our expectations, that the particles have shown abundance of strength and stability of MNPs, and very less of particle aggregation can be seen and they were sturdy after the stabilisation as they can stay suspended for hours. When magnetic field was presented to the mixture, they can be moved accordingly to the magnet which this is a prove of magnetically stabilization.

Generation	mw	Molecular Formula	No. of surface COOH group	Estimated binding Area (Å <sup>2</sup> )
0.5	1093.20	C <sub>46</sub> H <sub>80</sub> N <sub>10</sub> O <sub>20</sub>	8	250
1.5	2582.90	C <sub>110</sub> H <sub>192</sub> N <sub>26</sub> O <sub>44</sub>	16	720
2.5	5561.92	C <sub>238</sub> H <sub>416</sub> N <sub>58</sub> O <sub>92</sub>	32	1815
3.5	11527.16	C <sub>494</sub> H <sub>864</sub> N <sub>122</sub> O <sub>188</sub>	64	2770

Table 2.5: Provides a comprehensive analysis of carboxylic PAMAM dendrimers, correlating key properties such as generation, molecular weight, number of terminal amine groups, and the estimated surface area. These attributes are crucial in understanding the behavior and functionality of dendrimers for various applications, including drug delivery, gene therapy, and nanotechnology.

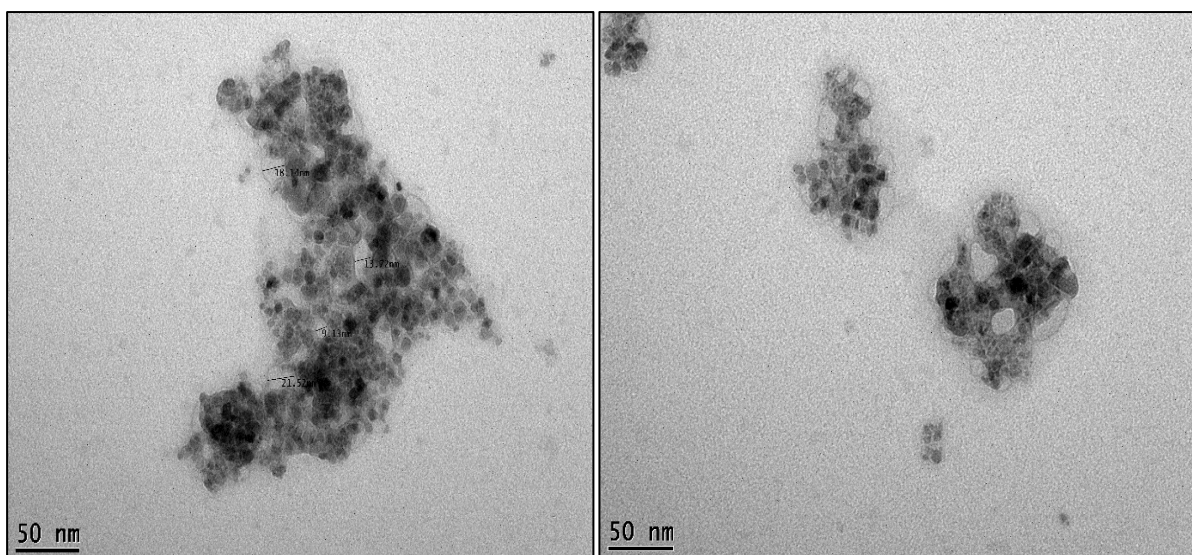


Figure 2.15: TEM images showcasing stabilized  $\text{Fe}_3\text{O}_4$  nanoparticles (NPs) that have been functionalized using 1.5 generation COOH-terminated dendrimers. This figure highlights the effectiveness of Generation 1.5 dendrimers in stabilizing the magnetic nanoparticles, providing insight into how the dendrimer interacts with the nanoparticle surface and prevents aggregation.

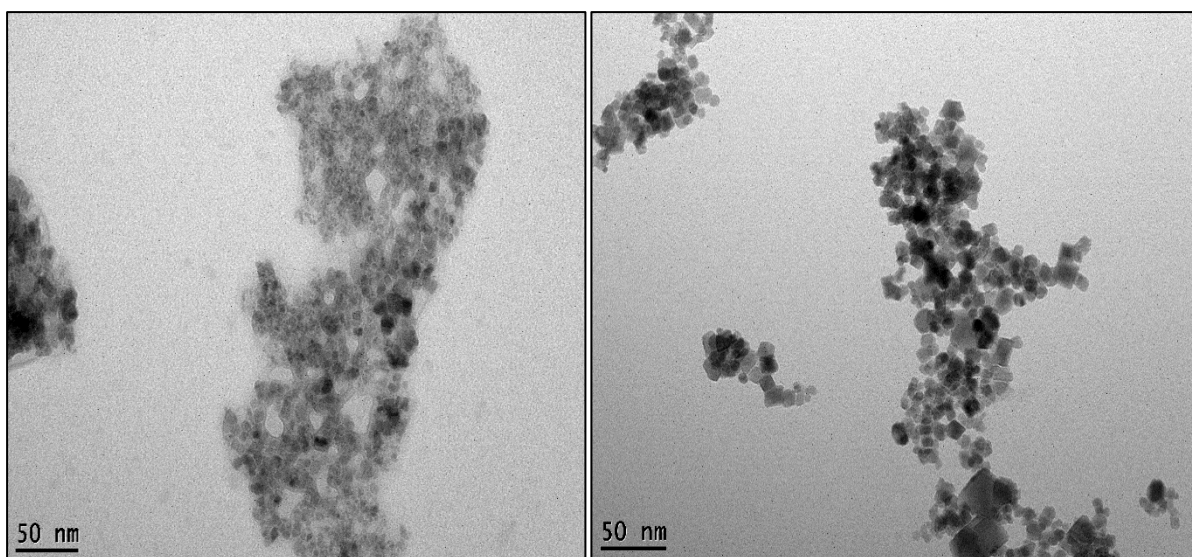


Figure 2.16: TEM demonstrates the successful stabilization of  $\text{Fe}_3\text{O}_4$  nanoparticles using Generation 2.5 COOH-terminated dendrimers. The microscope image reveals a well-dispersed nanoparticle system, free from aggregation, indicating that the dendrimer coating is effectively preventing magnetic interactions between the nanoparticles.

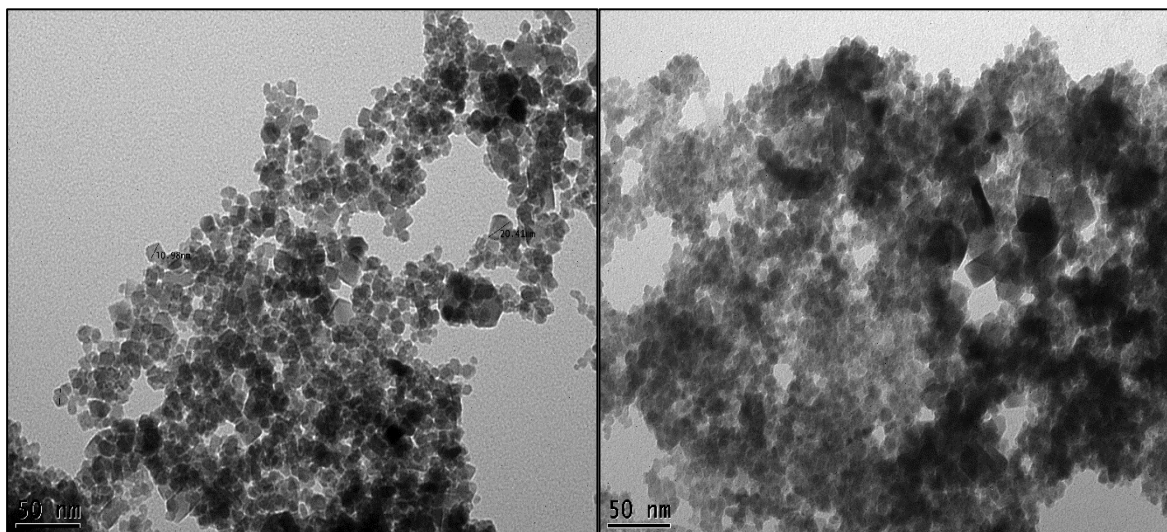


Figure 2.17: Shows TEM images of  $\text{Fe}_3\text{O}_4$  nanoparticles (NPs) stabilized using 2.5 generation COOH-terminated dendrimers.

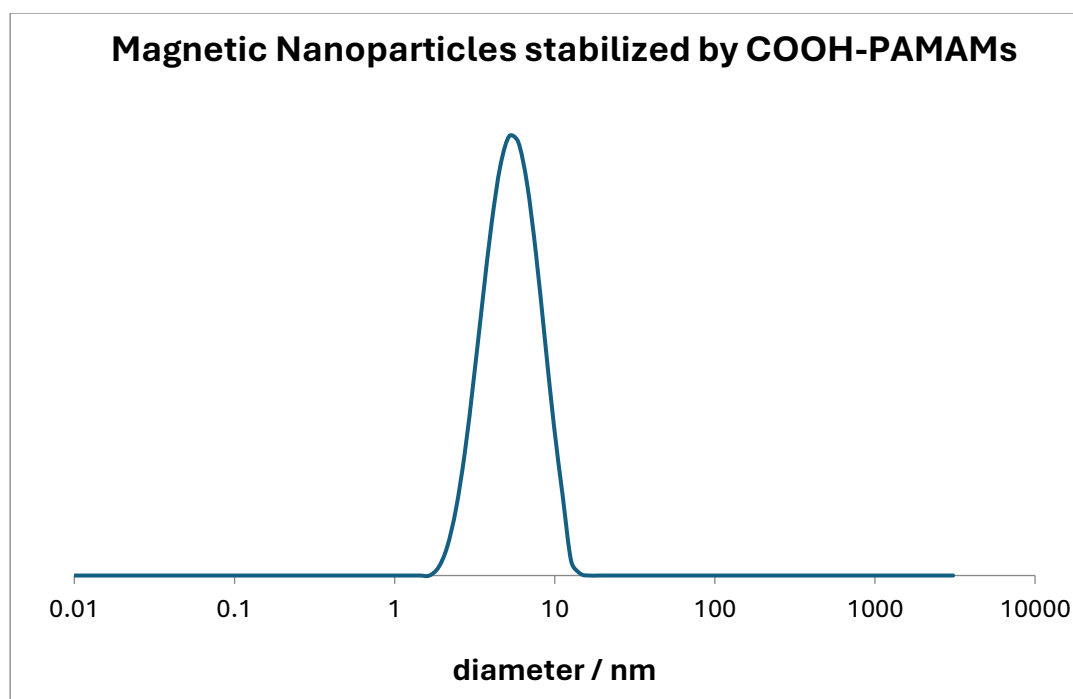


Figure 2.18: DLS data magnetic nanoparticles stabilized using COOH dendrimers generation 2.5 (combined from three measurements) exhibit a narrow peak in intensity distribution with average diameter of 8 nm. This indicates that the use of acidic PAMAM dendrimers helped to improve the stability of the nanoparticles.

### Preparation for Cytochrome-c (Cyt-c) binding assay:

Cytochrome-c was chosen as the target protein to evaluate dendrimer binding and the effectiveness of functionalized dendrimers. A non-covalent methodology was used to attach targeting groups to the protein's surface. Cytochrome-c was selected for several reasons: its structure is composed of three major and two minor helices folded into a globular shape, forming a heme pocket (figure 2.19). It consists of 104 amino acids and functions as an electron transporter, switching between ferrous ( $\text{Fe}^{2+}$ ) and ferric ( $\text{Fe}^{3+}$ ) oxidation states.

PAMAM dendrimers provide a suitable platform for binding cytochrome-c, as the protein's interfacial area, known as the hot spot, is typically around 1100 Å<sup>2</sup>. These binding surfaces have a high charge density, and interactions are primarily governed by polyvalent electrostatic forces. Non-covalent interactions at the protein's active site can be enhanced by targeting specific residues. Twyman's group recently discovered that a dendrimer with a porphyrin core can effectively bind to the surface of cytochrome-c.<sup>68</sup> Cytochrome-c is a small, highly conserved protein with a heme group and a region of concentrated positive charge near the entrance to its active site, making it an ideal target for dendrimer interactions.

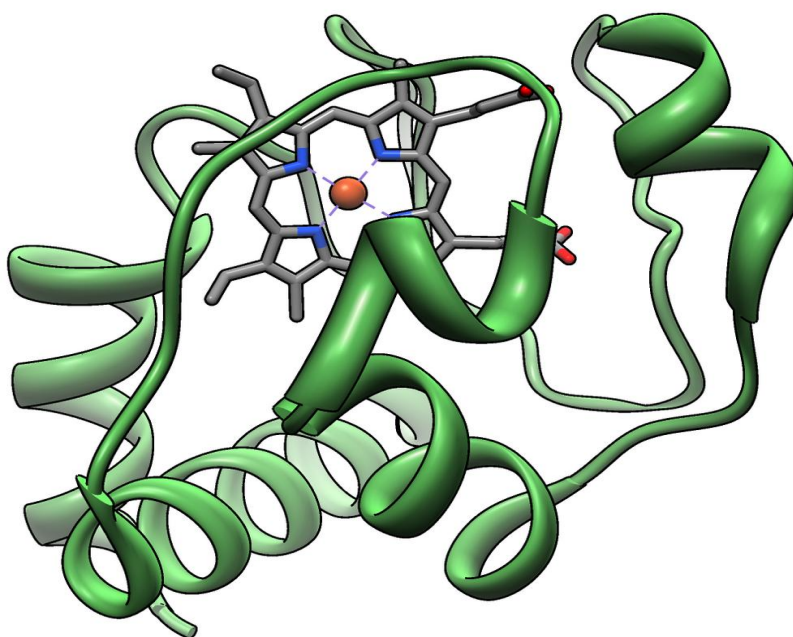


Figure 2.19: High-resolution 3D structure of Cytochrome c, represented in green, with a central heme molecule coordinating an iron atom, shown in orange, which is part of the horse heart Cytochrome c protein. This image offers a detailed visualization of the molecular architecture of Cytochrome c. (Protein Data Bank entry 1HRC).

### Assay to determine binding between dendrimer stabilized MNPS and Cytochrome c:

The experiment aimed to assess the ability of magnetic nanoparticles (MNPs) functionalized with acid-terminated Polyamidoamine (PAMAM) dendrimers to bind cytochrome P450 enzymes. The main objective was to compare the stabilization performance of three different generations of carboxyl-terminated PAMAM dendrimers generations 1.5, 2.5, and 3.5 and to identify the most effective generation for stabilizing the MNPs. While it was hypothesized that there would be only slight differences in stabilization efficiency across these generations, the results showed notable variations based on size. Previous studies involving dendrimers in solution (without magnetic nanoparticles) revealed a unique size-dependent effect on binding. In this case, binding was not typical of a simple electrostatic interaction, where affinity is directly related to the number of charges on each component. For dendrimers the charge count corresponds to the number of carboxylate groups, while for cytochrome-c, it matches the number of protonated amino acids on the protein's hot-spot surface. As such, it was predicted that the larger dendrimer would bind best, which was not the case. Instead, the dendrimer with a size that best matched the size of the protein hot spot, bound best. In the case of a MNP, where the dendrimers are tightly packed around the surface of the particle, we did not expect to see any effect with respect to dendrimer size. This is because the dendrimers are acting as a single connected unit, and not as individual dendrimers (as was the case in our previous solution-based study). The binding experiments were conducted as follows: A  $1 \times 10^{-6}$  M stock solution of cytochrome-c was prepared in buffer (pH 7.3, 0.1M), and a UV spectrum recorded. The absorption of cytochrome-c's porphyrin Soret band, at 410 nm, was noted and would be used as the baseline/control value. Concentrated solutions of dendrimer-stabilized magnetic nanoparticles (MNPs) were then prepared such that the final concentrations were 167 mg/mL of MNPs, and 33 mg/mL of dendrimer. Subsequently, 50 mL of each MNP solution was then added to 3 mL of the cytochrome-c stock solution. This mixture was gently agitated, and the



MNPs along with any bound protein were removed by magnetic separation. The remaining solution was analysed by UV, and the absorption of the remaining cytochrome-c's Soret band, at 410 nm, was measured and compared to the control sample. This process is illustrated schematically below in Figure 2.20.

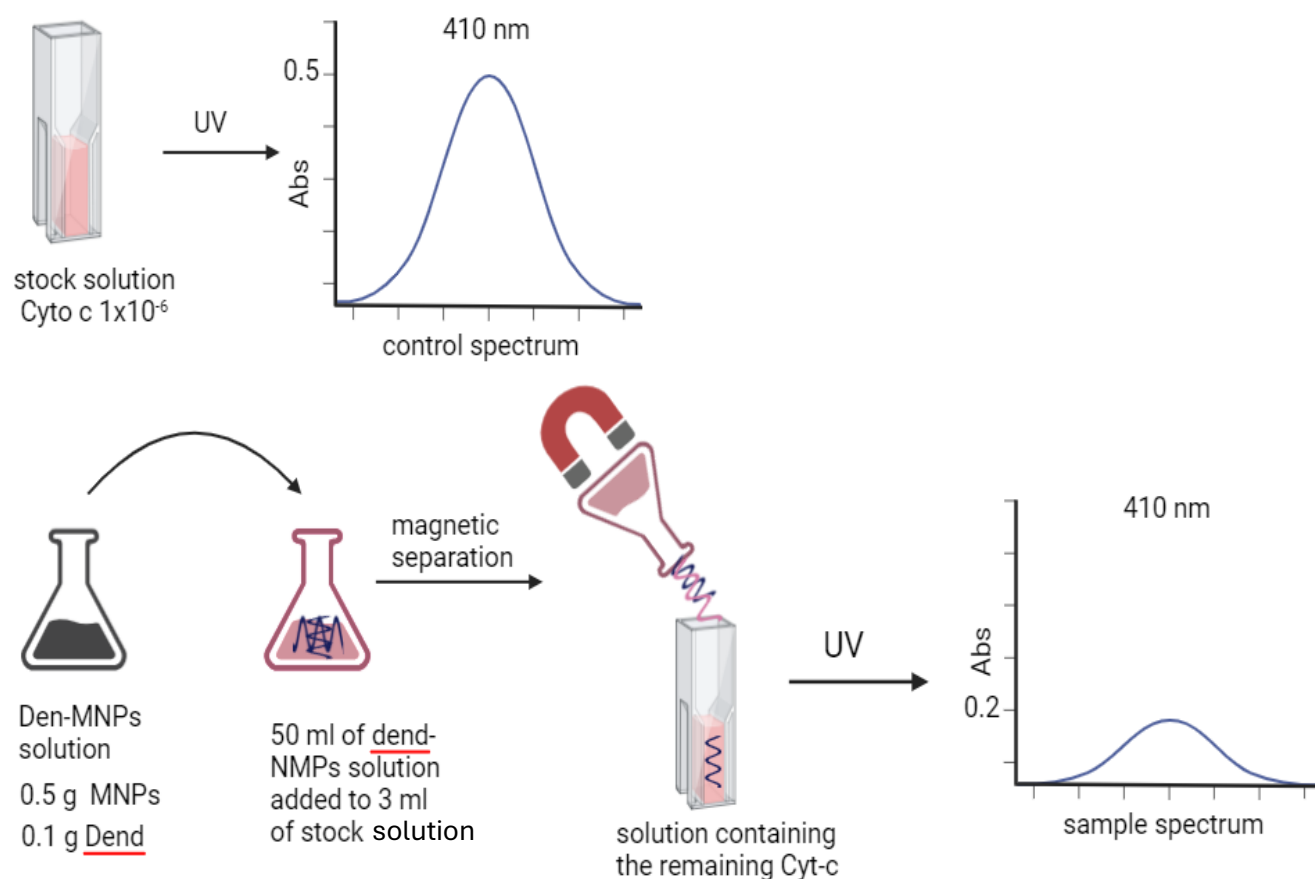


Figure 2.20: A schematic illustrating the experiment to determine binding between dendrimer-stabilized MNPs and Cytochrome c.

The amount of cytochrome-c remaining in solution (after magnetic separation) was calculated from the ratio of the MNP and stock solution absorptions, expressed as a percentage. The relative binding was then determined by subtracting this value from 100. The spectra obtained

for each dendrimer system and the binding data are shown below in figure 2.21 (A, B and C) and Table 2.6.

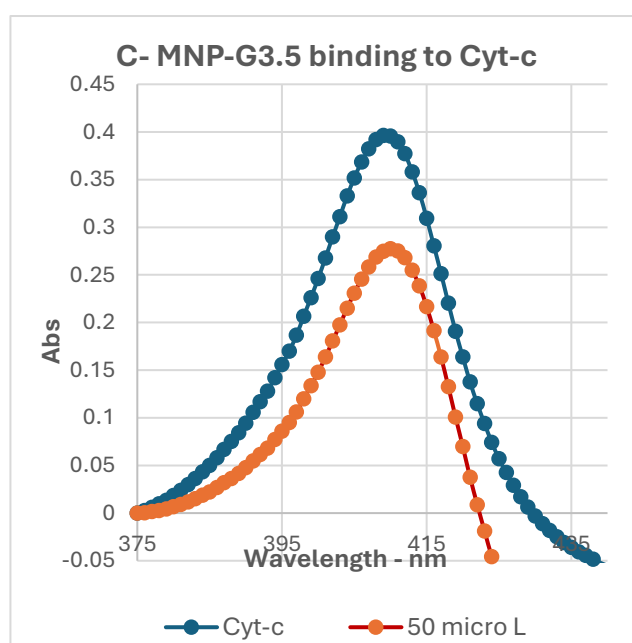
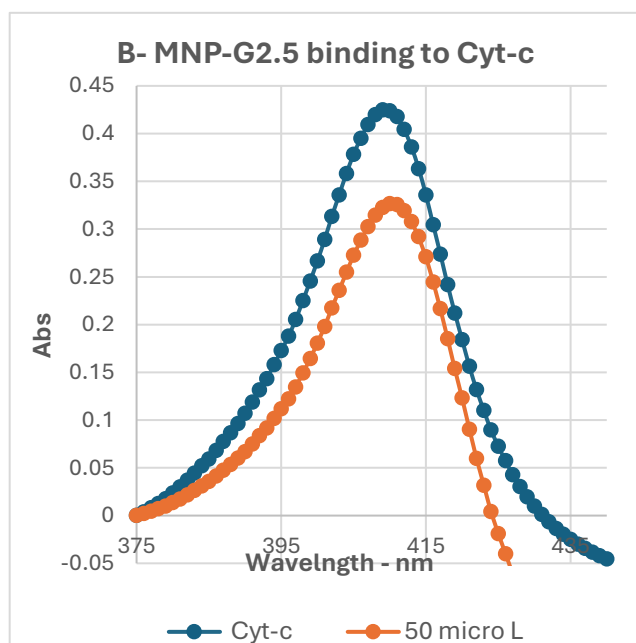
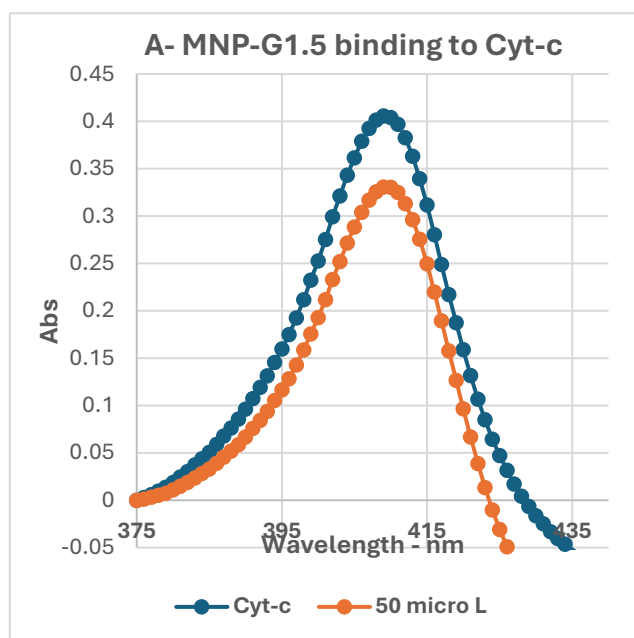
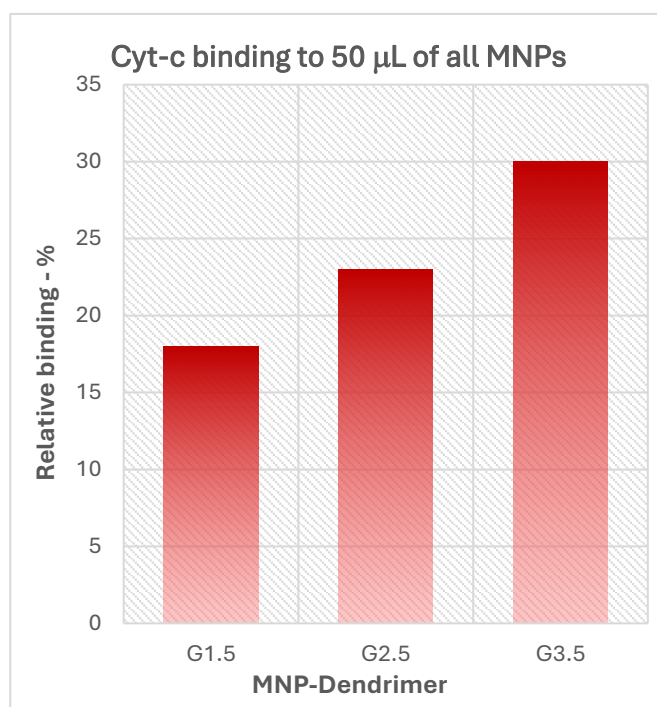


Figure 2.21: A, B and C: MNP binding for all dendrimer stabilized systems using 50 mL of the MNP solution. MNP solution used contained 0.5 g of MNP and 0.1 g of dendrimer in 3 mL of buffer (0.1 M) and Cytochrome-c concentration in the solution is  $1 \times 10^{-6}$  M.

Den-MNP	Rel Binding (%)
1.5	18
2.5	23
3.5	30

Table 2.6: Details MNP binding for all dendrimer stabilized nanoparticle systems.

Data shown is the average from 3 runs with estimated error  $\pm 8\%$ .



2.22: Relative binding for the system (MNP binding for all dendrimer generations 1.5, 2.5 and 3.5).

The results clearly demonstrate a generation-dependent binding, with larger dendrimer systems exhibiting the strongest binding affinity. Although this was unexpected, the data aligns with the traditional trend of simple electrostatic binding, where the dendrimer with the most carboxylate groups binds the strongest. This occurs despite the assumption that all dendrimers (G1.5 – 3.5) form a compact skin covering and stabilizing the MNP.

We suspect that the differences in binding are due to variations in how each dendrimer packs around the MNP. In all cases, the MNP surface is saturated with dendrimers. However, smaller dendrimers may pack around the MNP with a relatively high level of intermolecular interactions, resulting in fewer carboxylates being available for binding. Conversely, larger dendrimers may pack with fewer intermolecular interactions, allowing more terminal carboxylates to be presented to the protein. This phenomenon, related to different levels of dense shell/core packing, is well-known in dendrimer chemistry. For instance, our group has observed these effects in our work on drug delivery and catalytic studies.<sup>68</sup> Specifically, smaller dendrimers have an open structure with minimal dense packing. This allows neighbouring dendrimers to interlock through intermolecular hydrogen bonding between their arms. As a result, many terminal carboxylate groups become buried within neighbouring dendrimers and are unavailable for interaction with the protein's binding surface. In contrast, the larger G3.5 dendrimer has a more compact structure, densely packed with respect to its internal functionality and terminal groups. These larger dendrimers tend to adopt a harder, spherical structure, preventing them from interacting with each other in the same way as smaller dendrimers. Consequently, more terminal carboxylates are exposed and available on the surface.

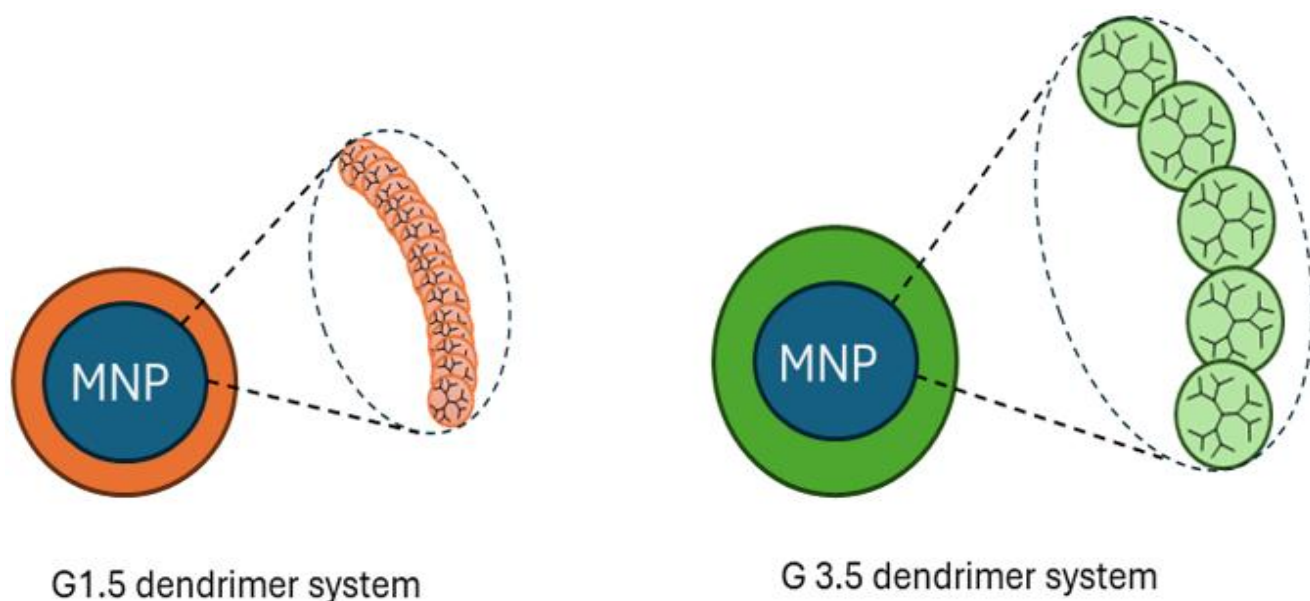
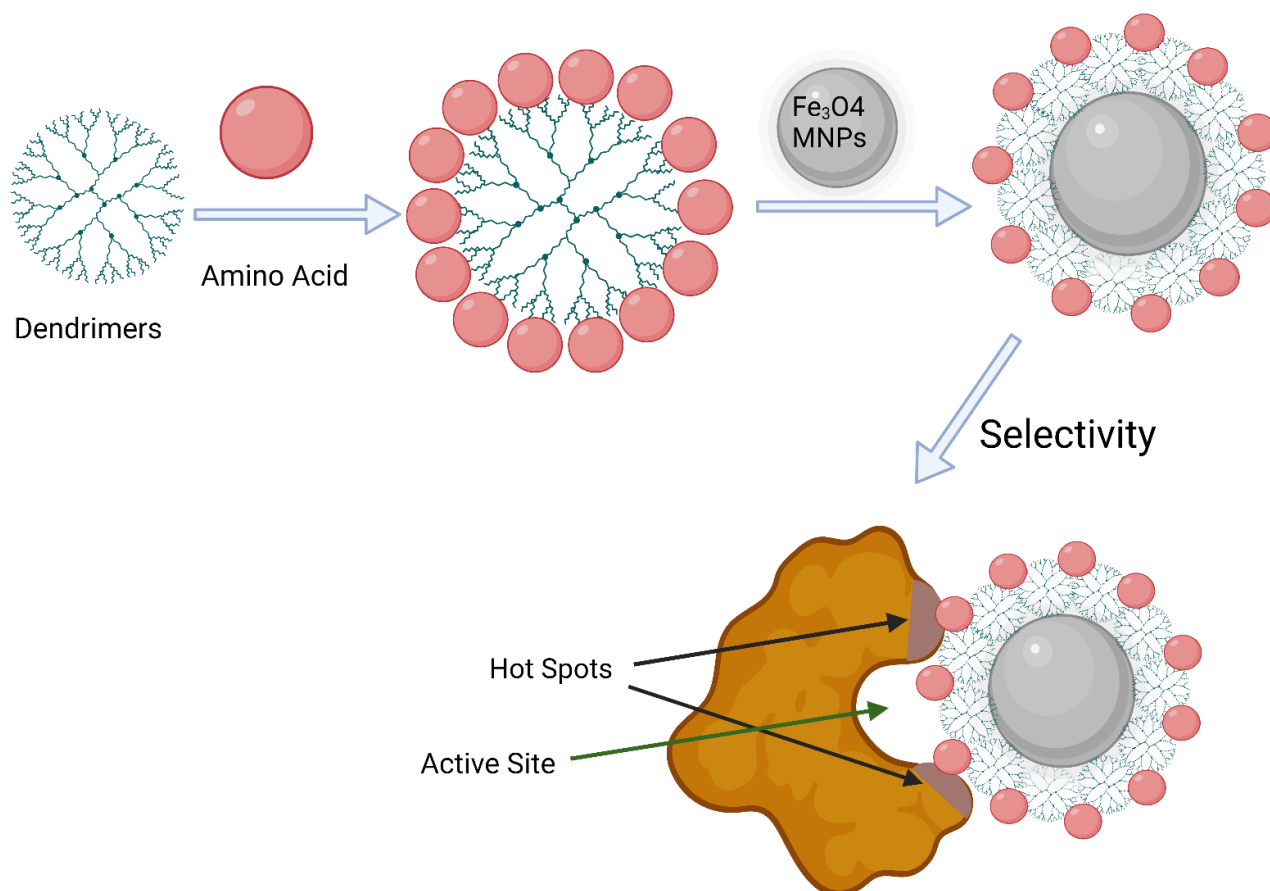


Figure 2.23: Schematic illustrating the impact of dendrimer dense packing on the availability of carboxylate groups on the MNP surface. The G1.5 dendrimer features an open structure, allowing dendrimers to penetrate and bind to the internal structure of neighbouring dendrimers. In contrast, the G3.5 dendrimer has a more densely packed, solid spherical structure, which limits penetration and results in a higher availability of terminal carboxylates.

### Functionalization of MNPs with COOH PAMAM dendrimers and various amino acids:

After establishing that an increase in the number of  $\text{CO}_2\text{H}$  groups enhances binding affinity, we aimed to further improve binding by exploring how different amino acid functional groups might influence binding affinity, particularly in terms of selectivity. Protein binding selectivity is affected by several factors, including the shape of the binding surface and the types of functional groups present on the amino acids. In previous experiments, we observed that magnetic nanoparticles functionalized with COOH-PAMAM showed a very strong binding

affinity for Cytochrome C, primarily due to increased electrostatic interactions. However, electrostatic binding alone does not ensure selectivity for other proteins (scheme 2.8).

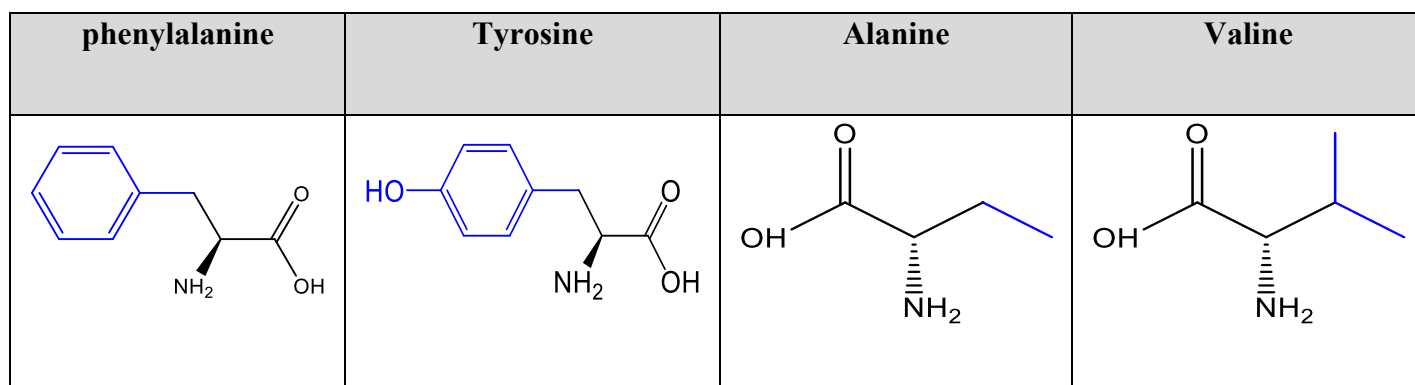


Scheme 2.8: Schematic representation of reactions used to functionalise the Fe<sub>3</sub>O<sub>4</sub> NPs onto the COOH- terminated PAMAM dendrimers with different amino acids. This figure was prepared by using BioRender.

To investigate this further, we simulated a protein's binding surface by incorporating various amino acids, each presenting different functional groups. For this protein-mimicking approach, we selected a range of amino acids with diverse functional groups, as outlined in scheme 2.9.

In addition to size, various non-covalent interactions play a crucial role in determining selectivity, including charge-charge interactions, hydrophobic effects, aromatic/ $\pi$ - $\pi$  interactions, and hydrogen bonding. These interactions are primarily contributed by a specific set of key amino acids. This was evidenced by a study that examined 2,325 protein-protein complexes. The study identified amino acids that contributed more than 2 kcal/mol to the binding energy, revealing that only three amino acids were frequently found in interfacial regions, each appearing with a frequency greater than 10%. These amino acids, which are capable of engaging in multiple types of interactions, include tryptophan (21%), arginine (14%), and tyrosine (13%). Therefore, factors such as multi/polyvalency, functionality, charge, and size are critical considerations in designing selective ligands for protein binding.<sup>64</sup> Tyrosine was included for its aromatic group, which facilitates additional  $\pi$ - $\pi$  interactions, and its phenolic OH group. When deprotonated to phenolate, the OH group introduces an extra negative charge and supports secondary hydrogen bonding. These features suggest that tyrosine could exhibit significant binding. We also included phenylalanine, which is similar to tyrosine but lacks the phenolic OH group, allowing us to assess the specific role of the OH group in binding affinity. Additionally, alanine was investigated as a replacement to introduce a carboxylic acid group, which could play a crucial role in enhancing binding interactions. This extra carboxyl group may enhance the overall binding affinity by increasing the number of potential sites for electrostatic interactions, hydrogen bonding, or other non-covalent forces, thereby improving the stability and specificity of the binding process. Lastly, valine was considered in the study due to its composition, which primarily consists of hydrophobic groups. Given that valine lacks functional groups capable of engaging in significant electrostatic interactions, hydrogen bonding, or  $\pi$ - $\pi$  stacking, it is expected to contribute minimally to the binding process. The absence of these functional groups suggests that valine's interaction with the binding surface would be driven primarily by hydrophobic interactions, which are generally

weaker and less specific than other types of molecular interactions. Consequently, valine's role in the binding process is likely to be limited, making it an interesting comparison point for understanding the importance of functional group diversity in enhancing binding affinity and selectivity. At this stage, our goal is to evaluate the relative binding affinities of individual amino acids.



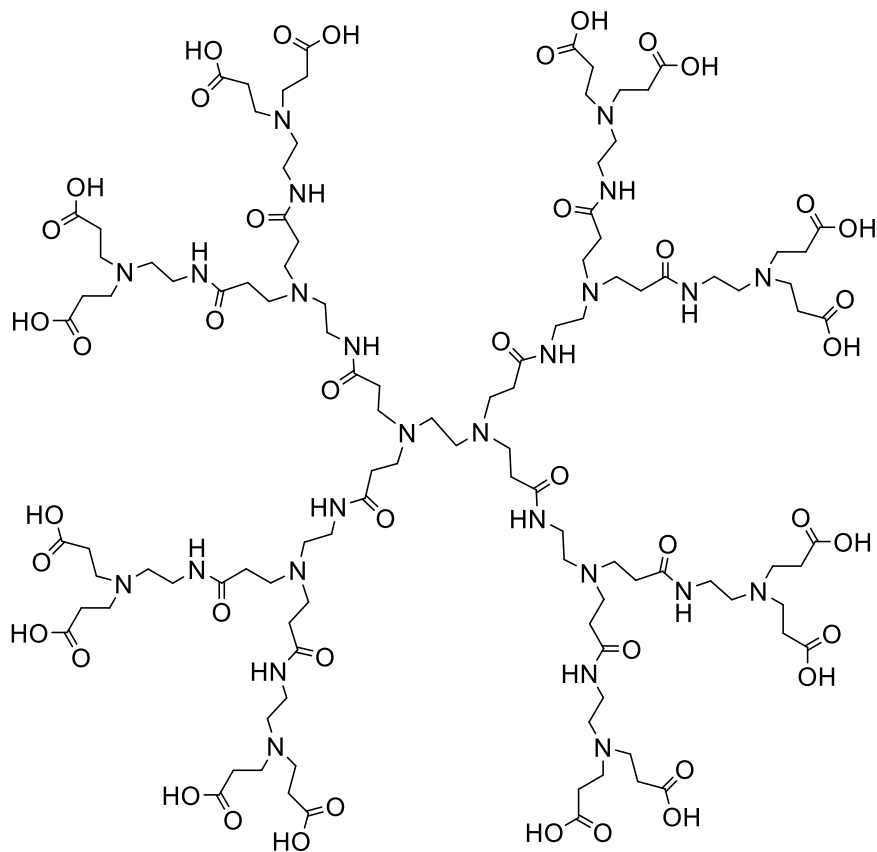
Scheme 2.9: Schematic representation of chosen amino acids bounded onto the COOH-terminated PAMAM dendrimers to functionalise the Fe<sub>3</sub>O<sub>4</sub> NPs.

### Synthesis of the tyrosine functionalized PAMAM dendrimer:

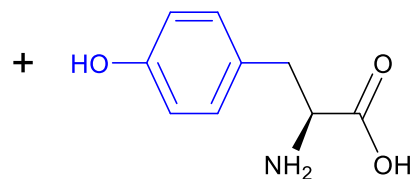
Starburst PAMAM dendrimer generation 2.5 was dissolved in water, along with the methyl ester hydrochloride of tyrosine. The pH of the solution was adjusted to 5.0 using hydrochloric acid. A mixture of coupling agent, 1-ethyl-3-(3-dimethylaminopropyl) carbodiimide hydrochloride (EDCI) and NHS (N-Hydroxysuccinimide) were dissolved in water and immediately added to the dendrimer solution. The mixture was stirred for 2 hours at room temperature, maintaining the pH at 5.0 throughout. The resulting product was subjected to dialysis to remove low-molecular-weight impurities, and subsequently freeze-dried to yield the crude tyrosine-protected dendrimer (illustrated in scheme 2.10). The ester groups were then



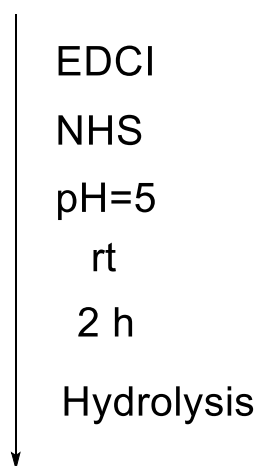
removed via base hydrolysis. The tyrosine functionalized dendrimer was dissolved in a mixture of methanol and distilled water. A stoichiometric amount of KOH was added, and the mixture heated at 30°C for 24 hours. The solvent was removed by rotary evaporation and the product purified by dialysis and freeze drying.

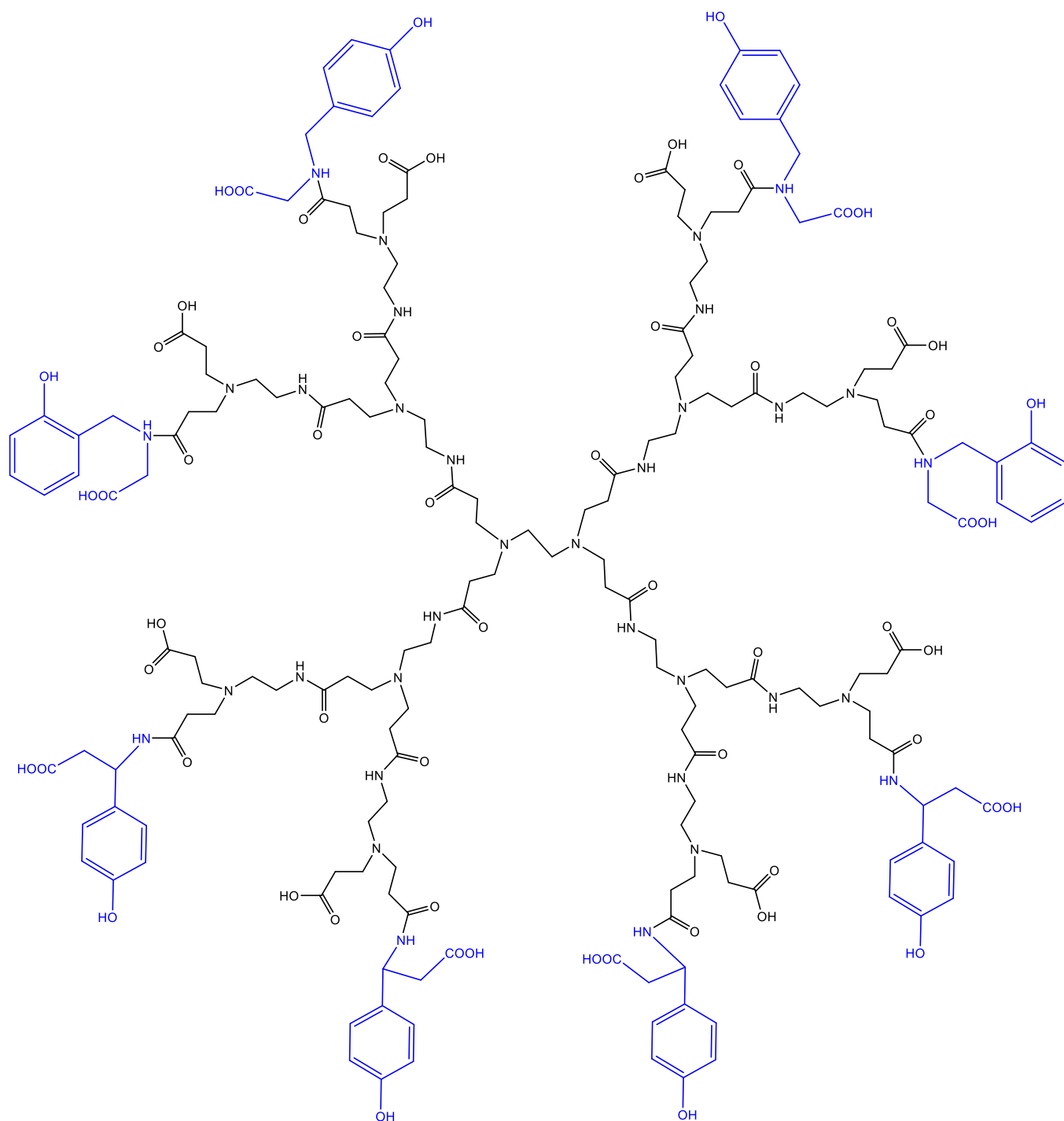


Carboxylic PAMAM G2.5



Tyrosine





Scheme 2.10: General method for the synthesis of tyrosine-functionalized PAMAM dendrimers of generation 2.5.

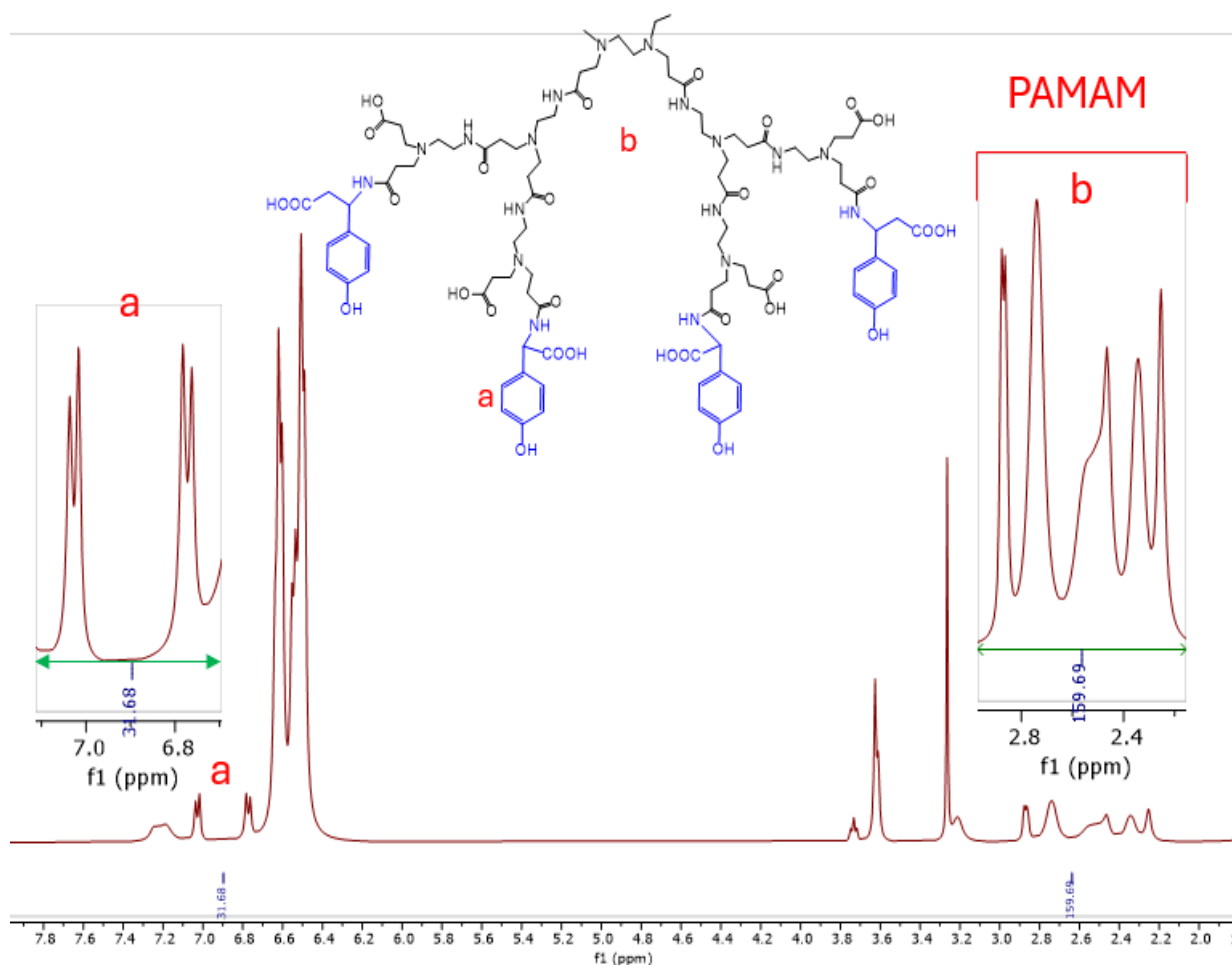


Figure 2.22: The  $^1\text{H}$  NMR spectrum of PAMAM dendrimers functionalized with tyrosine, highlighting the proton environment, and confirming the successful integration of tyrosine onto the polymer structure (only two arms shown for clarity). Loading calculated from the integral ratio of a & b.

In the analysis of the  $^1\text{H}$  NMR spectrum above, the chemical shift in the range of 2.2 to 2.9 ppm is particularly significant, as it corresponds to all the methylene protons of the PAMAM dendrimer's repeating units. This region of the NMR spectrum is characteristic of the PAMAM structure. Additionally, the presence of the smaller pair of doublets observed between 6.8 and 7.1 ppm is indicative of aromatic protons of the added tyrosine (the larger doublets correspond

to unreacted tyrosine). Based on the integration ratio of the Tyrosine peaks (with respect to the PAMAMs methylene protons between 2.2 and 2.9 ppm), we estimate that five tyrosine groups have been added to the surface of PAMAM. Although this is far from saturation, the coverage is likely spread across the dendrimer's surface. As such, some of the tyrosines will be available for protein binding after coordination to the MNP. The analysis also indicates the presence of considerable levels of unreacted tyrosine. However, this is not expected to pose a significant issue. Unreacted tyrosine is likely to engage in only single-point interactions with the magnetic nanoparticles (MNPs) and, therefore, is unlikely to contribute meaningfully to their stabilization. In contrast, the tyrosine-functionalized dendrimer is capable of establishing multiple interactions, resulting in multivalent or cooperative binding. Consequently, the overall interaction strength is expected to be significantly higher compared to monovalent tyrosine interactions. Furthermore, it is well-established that dendrimers form stable interactions that enhance MNP stabilization. Thus, any unreacted tyrosine will be effectively removed during the washing and magnetic separation steps, leaving behind a well-stabilized MNP-dendrimer complex.

The  $^{13}\text{C}$  NMR spectrum of the tyrosine-functionalized PAMAM dendrimers provide valuable insight into the chemical environment of the various functional groups. The methylene ( $-\text{CH}_2-$ ) groups of the PAMAM shifts around 35 ppm, indicative of their aliphatic nature. The amide carbonyl groups ( $-\text{C}=\text{O}$ ), which are critical to the dendrimer's structure, resonate prominently around 170 ppm. For the tyrosine functional groups, the spectrum shows distinct resonances. The aromatic carbons within the phenyl ring of tyrosine are observed near 132 ppm. Additionally, the carboxyl carbon ( $-\text{COOH}$ ) of the tyrosine side chain appears around 155 ppm, indicative of its carboxylic acid functionality. These shifts collectively confirm the successful functionalization of the dendrimers with tyrosine.

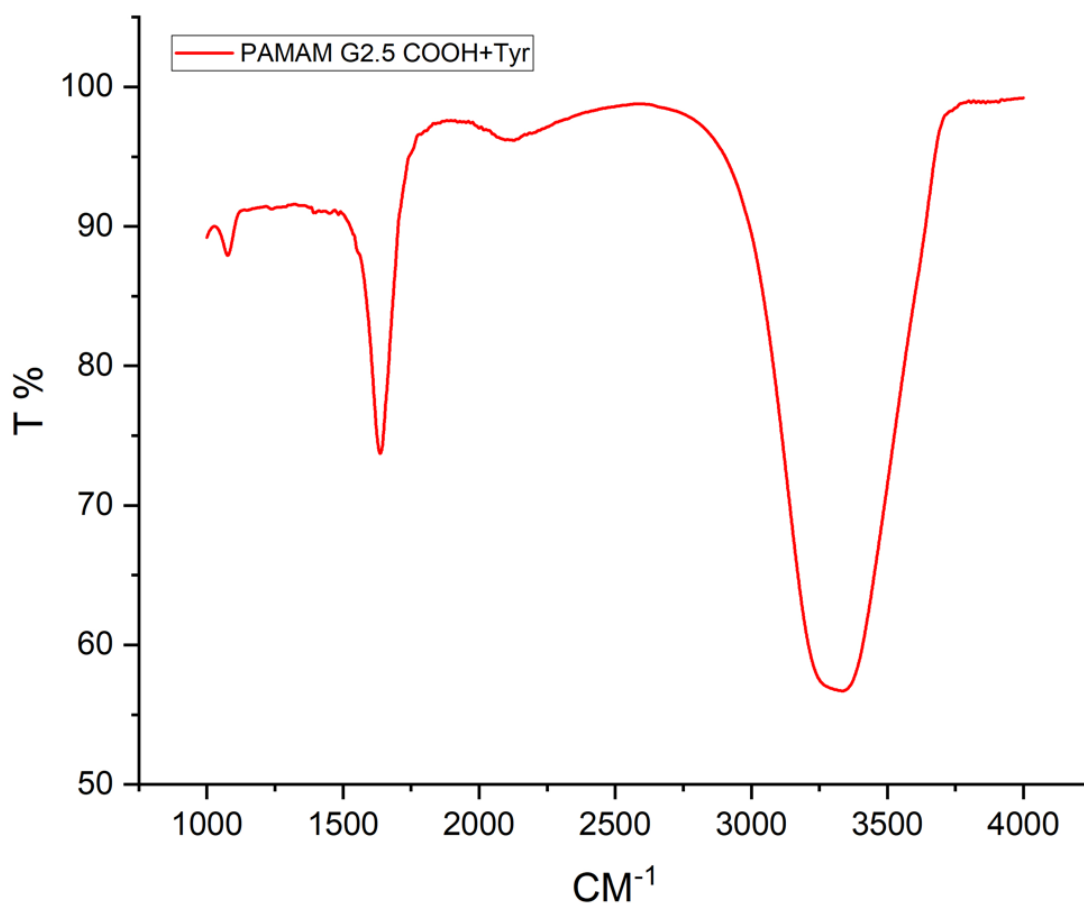


Figure 2.23: FTIR spectrum of COOH-PAMAM G2.5 functionalized with tyrosine.

The infrared spectrum (Figure 2.23) shows a broad peak between 3200 and 3500  $\text{cm}^{-1}$  and corresponds to the terminal carboxylic acid groups (of the dendrimer and amino acid). The peaks for the hydroxyl (O-H) groups in the phenolic ring and amine (N-H) groups in the amino acid structure are buried beneath. The carbonyl signals for the amide and carboxylic acid come around 1700  $\text{cm}^{-1}$ .

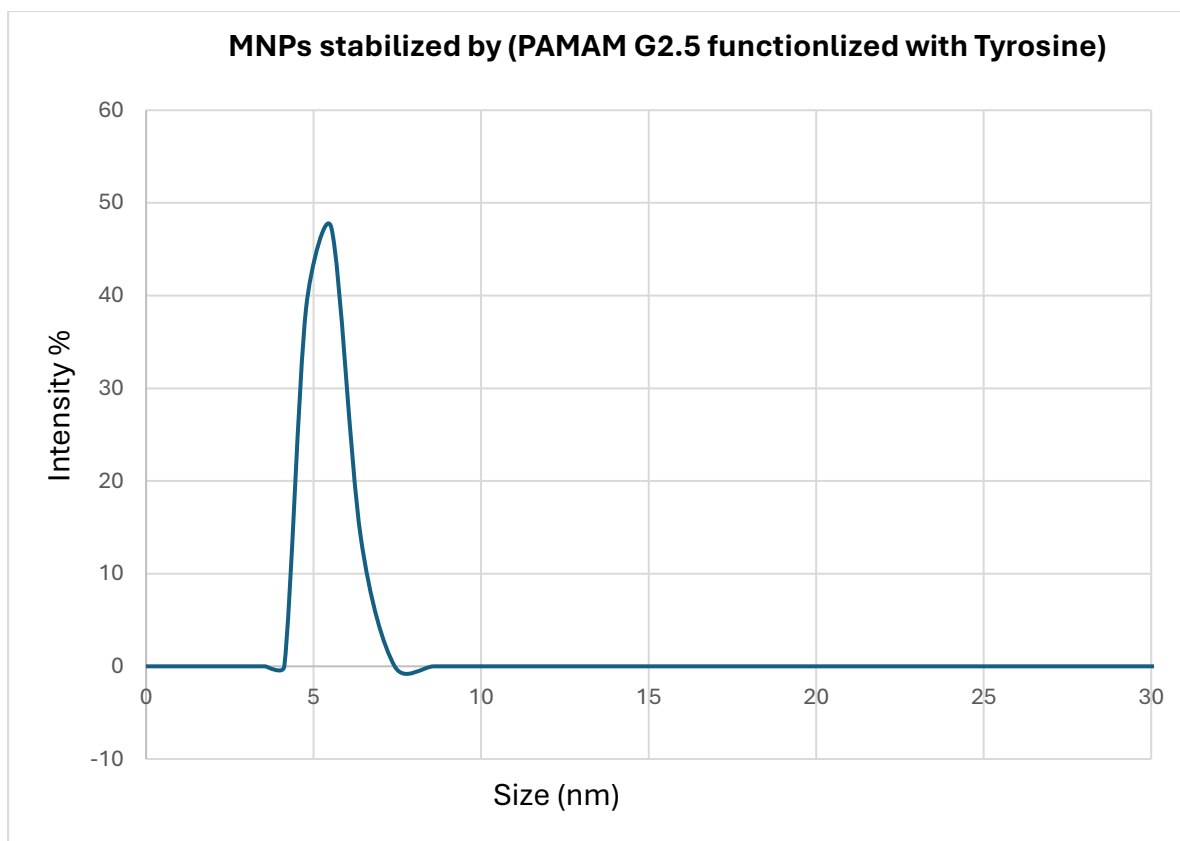
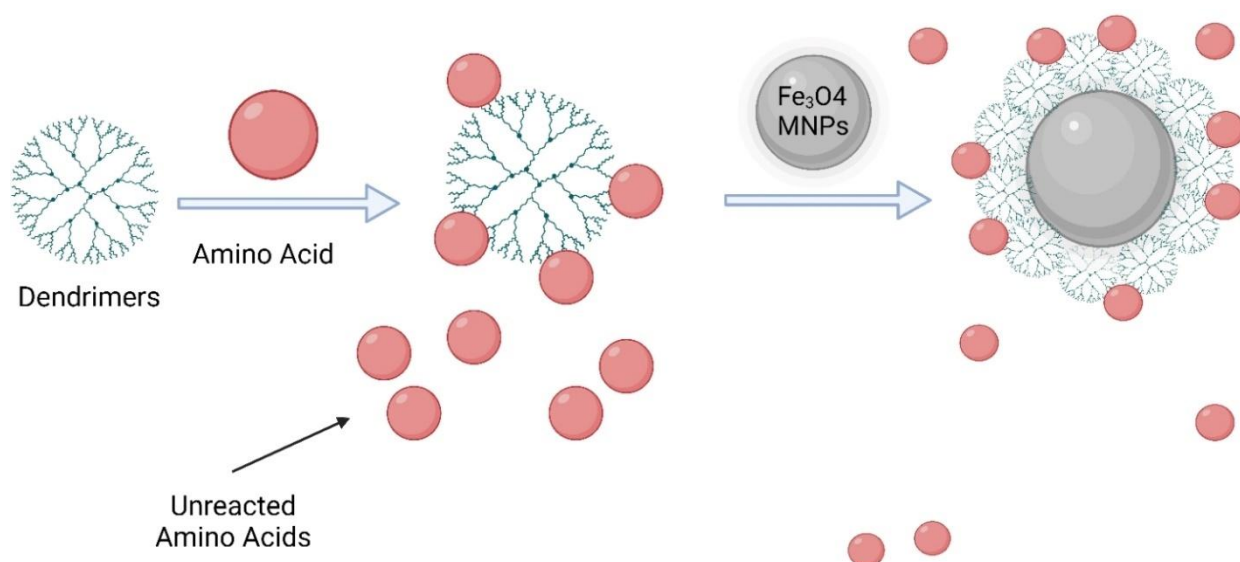


Figure 2.24: DLS data for magnetic nanoparticles stabilized using COOH dendrimers functionalized with tyrosine (combined from three measurements) exhibits a narrow peak in intensity distribution with average size of 6 nm.



Scheme 2.10: Schematic representation of reactions used to functionalise the Fe<sub>3</sub>O<sub>4</sub> NPs onto the COOH- terminated PAMAM dendrimers with tyrosine amino acids. This figure was prepared by using BioRender.

In summary, the observed chemical shifts and their integrals align with the expected tyrosine functionalised PAMAM dendrimer structure, affirming a successful reaction. Although significant starting materials remained, these will not compromise the synthesis and structure of the dendrimer stabilized MNP, as they are easily removed during the purification and magnetic separation of the final MNP. The same procedure was used to synthesis the valine, and phenylalanine functionalised PAMAM dendrimers and their corresponding stabilized MNP. The data for the PAMAM dendrimers is shown below in table 2.7.



Sample	Theoretical Molecular Weight for fully functionalised PAMAM	Number of amino acids added estimated by NMR	Theoretical Molecular Formula for fully functionalised PAMAM	Estimated binding Area (Å <sup>2</sup> )	Size of MNP by DLS (nm)
COOH PAMAM G3.5	11521	0	C <sub>494</sub> H <sub>864</sub> N <sub>122</sub> O <sub>188</sub>	2770	~14
COOH PAMAM G2.5-Tyr	7249	5-6	C <sub>328</sub> H <sub>606</sub> N <sub>67</sub> O <sub>110</sub>	3610	~10
COOH PAMAM G2.5-phe	7147	2-3	C <sub>328</sub> H <sub>600</sub> N <sub>67</sub> O <sub>104</sub>	3552	~12
COOH PAMAM G2.5-Val	6572	7-8	C <sub>292</sub> H <sub>506</sub> N <sub>67</sub> O <sub>101</sub>	3180	~9
COOH PAMAM G2.5-Ala	6107	4-5	C <sub>238</sub> H <sub>494</sub> N <sub>86</sub> O <sub>148</sub>	2975	~8

Table 2.7: Provides a detailed comparison of the properties of functionalized generation 2.5 COOH-PAMAM dendrimers with tyrosine, phenylalanine and valence, and unfunctionalized generation 3.5, highlighting key differences in terms of molecular structure, number of amino acids added, estimated binding area and size.

### Binding of functionalized Magnetic Nanoparticles to Cytochrome C:

The assay involved measuring the relative inhibition of cytochrome c enzymes using magnetic nanoparticles (MNPs) functionalized with carboxyl-terminated Polyamidoamine (PAMAM) dendrimers and various amino acids. The experimental process used was the same as discussed in the previous chapter (for the unfunctionalised MNP). Initially, an  $1 \times 10^{-6}$  mM solution of the protein was made up and a spectrum recorded using UV spectroscopy. The absorption of the protein's Soret band at 409 nm was recorded as the control. After which, the same solution of cytochrome-c was added to the solution of functionalized MNP to make up a 167 mg/mL solution of the MNP. The MNP was then removed using a magnet, and the UV spectrum of the solution reacquired and the absorption of the Soret band was compared to the control (the initial solution without MNPs). Relative binding could then be calculated from the ratio of the two absorptions. The spectra are displayed in figure 2.25 and the data presented in table 2.7.

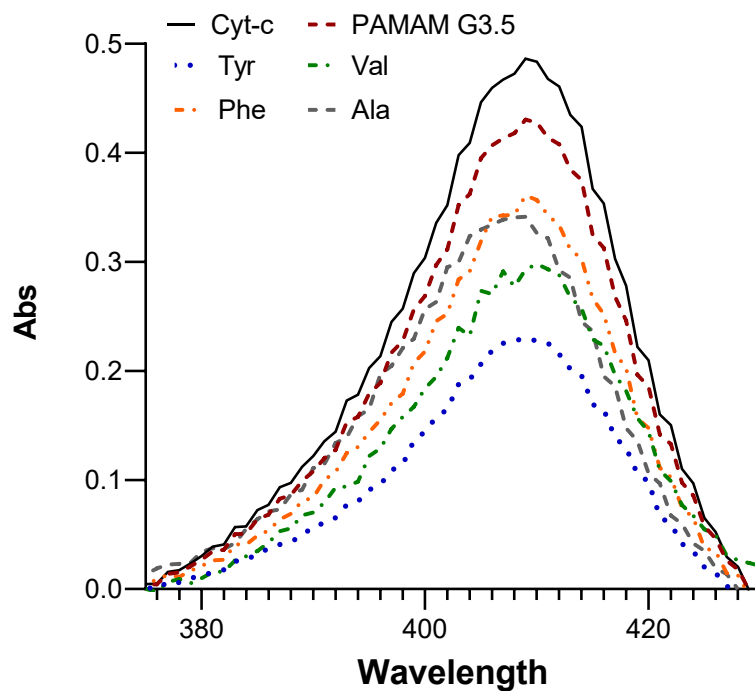


Figure 2.25: Binding of amino acid functionalized PAMAM stabilized MNP to cytochrome c.

MNP- stabilization species	Relative binding to Cyto-c (%)
PAMAM G3.5	12
Tyr-PAMAM G2.5	53
Phe-PAMAM G2.5	26
Val-PAMAM G2.5	38
Ala-PAMAM G2.5	29

Table 2.7: Details showing the percentage of binding between G 2.5 PAMAM and functionalized dendrimers with tyrosine, phenylalanine, alanine and valine. Data shown is the average from 3 runs with estimated error  $\pm 12\%$ .

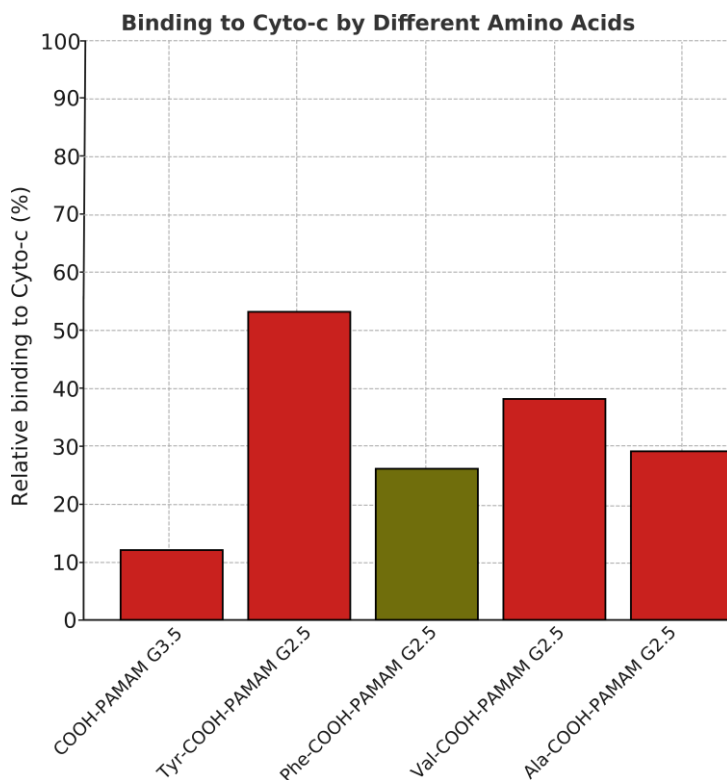


Figure 2.26: A graph representing the binding between Generation 2.5 PAMAM dendrimers and functionalized dendrimers with tyrosine, phenylalanine, alanine and valine.

We utilized five different mixtures to evaluate and compare the binding levels. These included cytochrome c with PAMAM 3.5 and MNPs with functionalized PAMAM 2.5, each conjugated with tyrosine, phenylalanine, alanine and valine. The MNPs stabilized with an unfunctionalized G3.5 dendrimer showed a modest 12% binding, serving as a reference point for further comparisons. A significant enhancement in binding affinity was noted when the MNPs were coupled with the tyrosine-functionalized PAMAM dendrimers, with the binding efficiency

surging to 53%. This substantial increase corroborates our theory regarding the pivotal role of tyrosine in protein binding, attributed to its capacity for multiple interactions with the cytochrome-c surface. Experiments with the valine and alanine-modified systems also demonstrated an increase in binding, with values ranging from almost 30% to 40%. Additionally, the use of MNPs stabilized by phenylalanine-functionalized PAMAM dendrimers resulted in an approximate 30% level of binding. While this figure represents an improvement over the baseline established by the unfunctionalized MNPs, it is lower than the binding efficiency observed with the valine and alanine systems, which were anticipated to be the least effective. The diminished binding in the phenylalanine system could be attributed to a reduced number of potential interactions with the protein surface or a lower degree of surface coverage, which in turn presents fewer phenylalanine for binding. In summary, the findings are encouraging and support our initial premise that selective binding is achievable when MNPs are functionalized with distinct amino acids.

## Conclusion:

The first stage of the research focused on the synthesis of PAMAM dendrimers and the functionalization of their terminal groups to create systems capable of stabilizing iron oxide nanoparticles. PAMAM dendrimers were synthesized using a stepwise approach, resulting in a library of dendrimers ranging from generation 0.5 to generation 4.0. The initial goal was to explore the use of hydroxyl-terminated dendrimers to stabilize  $\text{Fe}_3\text{O}_4$  MNPs. However, due to the limited interaction between neutral hydroxyl groups and the charged surface of iron oxide nanoparticles, these dendrimers provided only minimal stabilization. Hydroxyl-terminated PAMAM dendrimers, particularly at lower generations, lacked the electrostatic interaction strength necessary to prevent nanoparticle aggregation, leading to suboptimal results.

Initial results with hydroxyl-terminated dendrimers demonstrated poor stabilization, as the neutral charge of the hydroxyl groups resulted in weak interactions with the nanoparticle surface, leading to rapid aggregation over time. Dynamic light scattering (DLS) measurements indicated a broad size distribution, suggesting that the nanoparticles were prone to forming large aggregates. To address this issue, we utilized carboxyl-terminated PAMAM dendrimers, which significantly improved nanoparticle stability due to their ability to form stronger electrostatic bonds with the  $\text{Fe}_3\text{O}_4$  surface. Among the different generations tested, G2.5 carboxyl-terminated dendrimers emerged as the most effective stabilizers, providing the optimal balance between molecular size, surface coverage, and stabilization efficiency.

The generation 2.5 dendrimers had sufficient terminal groups to form a stable, uniform coating around the nanoparticles without the excessive branching seen in higher-generation dendrimers like G3.5, which sometimes led to challenges in achieving homogenous suspensions. The results showed that G2.5 PAMAM dendrimers effectively prevented nanoparticle aggregation,

maintained particle size stability, and exhibited favorable dispersion properties, making them ideal candidates for further functionalization and application in protein binding studies. After identifying G2.5 carboxyl-terminated dendrimers as optimal stabilizers, we explored their functionalization with specific amino acids to further enhance protein binding capabilities. The motivation behind this functionalization was to leverage non-covalent interactions, such as hydrogen bonding,  $\pi$ - $\pi$  stacking, and hydrophobic effects, to improve selectivity and affinity in binding to target proteins.

Four amino acids were chosen for functionalization: tyrosine, phenylalanine, alanine and valine, each offering unique functional properties. Tyrosine, with its aromatic ring and hydroxyl group, was expected to enhance binding via  $\pi$ - $\pi$  stacking and hydrogen bonding interactions. Phenylalanine, which shares the aromatic ring but lacks the hydroxyl group, was selected to assess the impact of this functional group on binding affinity. Alanine, Valine, a hydrophobic amino acid, was included to understand the role of hydrophobic interactions in protein binding.

The functionalization of PAMAM dendrimers with these amino acids was confirmed through NMR and FTIR analysis, which showed the successful attachment of the amino acids to the dendrimer structure. Tyrosine-functionalized dendrimers demonstrated the highest degree of functionalization, with an average of five tyrosine groups attached to each dendrimer. The incorporation of these functional groups significantly enhanced the potential for protein interactions. To evaluate the effectiveness of the functionalized dendrimers in binding to proteins, cytochrome-c was chosen as a model target protein. Cytochrome-c, with its well-defined structure and positively charged surface, provides an ideal test case for exploring how dendrimer-functionalized MNPs interact with protein surfaces. The assay involved measuring the binding affinity of dendrimer-functionalized MNPs to cytochrome-c by monitoring changes

in UV absorbance at the band. The results showed a clear generation- and amino acid-dependent effect on binding affinity. MNPs functionalized with tyrosine-modified PAMAM dendrimers exhibited the highest binding affinity, achieving a binding efficiency of 53%. This high affinity was attributed to the ability of tyrosine to engage in multiple non-covalent interactions, including  $\pi$ - $\pi$  stacking and hydrogen bonding, which allowed for a stronger and more specific interaction with the cytochrome-c surface. In contrast, Phenylalanine-functionalized dendrimers demonstrated a lower-than-expected binding efficiency of 26%, indicating a reduced number of potential interactions with the protein surface or a lower degree of surface coverage. This limited surface coverage likely resulted in fewer available phenylalanine groups for effective binding. Valine-functionalized dendrimers showed moderate binding at 38%, likely driven by hydrophobic interactions, though these interactions were weaker than the aromatic and hydrogen bonding interactions seen with tyrosine.

The data further demonstrated that while all functionalized dendrimers showed improved binding over the unfunctionalized G3.5 dendrimers, which exhibited minimal binding (~12%), the nature of the functional groups played a crucial role in determining the strength and selectivity of the interactions.



## Future work:

The enhanced purification and functionalization of PAMAM dendrimer-stabilized MNPs using a mixed amino acid system is a key area for future research, aimed at improving selectivity and increasing overall binding affinity. This suggests that the MNPs are being tailored to bind selectively to target molecules—likely proteins, or at least specific protein components. By optimizing the purification process and incorporating a strategic combination of amino acids, this approach holds significant potential to enhance interaction specificity, enabling more efficient and targeted binding in various applications.

For purifying MNP solutions, advanced techniques like ultrafiltration and centrifugation could be further developed. Future research should focus on optimizing these protocols to increase the purity of magnetic nanoparticle (MNP) solutions. Fine-tuning these methods could ensure that unbound proteins are thoroughly removed and MNP aggregates are minimized. Utilizing membranes with specific molecular weight cutoffs during ultrafiltration would enhance the removal of smaller proteins, such as cytochrome c, thereby improving binding accuracy in future studies. Another promising strategy is to explore dual purification methods. For example, combining ultrafiltration with size exclusion chromatography (SEC) could provide a more refined and selective approach for isolating MNPs and bound proteins. This dual approach would enable the selective retention of bound proteins while effectively eliminating unbound cytochrome c, improving the reproducibility of binding experiments.

In terms of functionalization with mixed amino acids for enhanced selectivity, designing a mixed amino acid system for functionalization is a key area of future work. The functionalization of PAMAM dendrimers with amino acids such as Tyrosine, Alanine, and Phenylalanine in combination could create a multifunctional surface that leverages both

hydrophobic and electrostatic interactions. Tyrosine can enhance binding via  $\pi$ - $\pi$  interactions and hydrogen bonding due to its aromatic ring and hydroxyl group. Alanine provides a small, non-polar side chain that influences hydrophobic interactions without adding steric hindrance. Phenylalanine which offers an additional aromatic ring for hydrophobic interactions and  $\pi$ - $\pi$  stacking but lacks hydroxyl groups for hydrogen bonding. Incorporating these amino acids in varying ratios could allow future studies to explore their synergistic effects on cytochrome c binding, potentially improving both selectivity and affinity.

In conclusion, future work on the purification and functionalization of PAMAM COOH G2.5 dendrimers for MNP systems offers multiple promising avenues. Enhanced purification methods, such as ultrafiltration, combined with innovative functionalization strategies involving mixed amino acids, can lead to increased selectivity and binding affinity to cytochrome c. These advances will provide deeper insights into binding mechanisms and pave the way for broader applications in biotechnology and nanomedicine.

## References:

1. Silver, J. (ed.), 1993. *Chemistry of Iron*. Glasgow, UK: Blackie Academic & Professional.
2. Cornell, R. & Schwertmann, U., 1996. *The Iron Oxides: Structure, Properties, Reactions, Occurrence and Uses*. Weinheim: VCH Verlagsgesellschaft.
3. Feynman, R., 1960. There's Plenty of Room at the Bottom. *Engineering and Science*, XXIII(5).
4. Barber, D.J. & Freestone, I., 1990. An Investigation of the Origin of the Color of the Lycurgus Cup by Analytical Transmission Electron-Microscopy. *Archaeometry*, 32(1), pp.33–45.
5. Wagner, S., Haslbeck, S., Stievano, L., Calogero, S., Pankhurst, Q. & Martinek, K.P., 2000. Before Striking Gold in Gold-Ruby Glass. *Nature*, 407(6805), pp.691–692.
6. Faraday, M., 1857. The Bakerian Lecture: Experimental Relations of Gold (and Other Metals) to Light. *Philosophical Transactions of the Royal Society London*, 147, pp.145–181.
7. Hornyak, G.L., Dutta, J., Tibbals, H.F. & Rao, A.K., 2008. *Introduction to Nanoscience*. Boca Raton: Taylor & Francis.
8. Harvell-Smith, S. & Thanh, N.T.K., 2022. Magnetic Particle Imaging: Tracer Development and the Biomedical Applications of a Radiation-Free, Sensitive, and Quantitative Imaging Modality. *Nanoscale*, 14(10), pp.3658–3697.

9. Obaidat, I.M., Nayek, C., Manna, K., Bhattacharjee, G., Al-Omari, I.A. & Gismelseed, A., Investigating Exchange Bias and Coercivity in  $\text{Fe}_3\text{O}_4$ - $\gamma$ - $\text{Fe}_2\text{O}_3$  Core-Shell Nanoparticles of Fixed Core Diameter and Variable Shell Thicknesses. *Nanomaterials*, 7(12), p.415.
10. Lim, K.Y., 2023. Experimental and Theoretical Study on Microalgae Harvesting Process by Using Continuous Flow Low Gradient Magnetic Separation (LGMS) Approach (Doctoral Dissertation, UTAR).
11. Yang, H.Y., Li, Y. & Lee, D.S., 2021. Functionalization of Magnetic Nanoparticles with Organic Ligands Toward Biomedical Applications. *Advanced NanoBiomed Research*, 1(5), p.2000043.
12. Kudr, J., Haddad, Y., Richtera, L., Heger, Z., Cernak, M., Adam, V. & Zitka, O., 2017. Magnetic Nanoparticles: From Design and Synthesis to Real-World Applications. *Nanomaterials*, 7(9), p.243.
13. Wang, L., Khalizov, A.F., Zheng, J., Xu, W., Ma, Y., Lal, V. and Zhang, R., 2010. Atmospheric Nanoparticles Formed from Heterogeneous Reactions of Organics. *Nature Geoscience*, 3(4), pp.238–242.
14. O'Dowd, C.D., Facchini, M.C., Cavalli, F., Ceburnis, D., Mircea, M., Decesari, S., Fuzzi, S., Yoon, Y.J. & Putaud, J.P., 2004. Biogenically Driven Organic Contribution to Marine Aerosol. *Nature*, 431(7009), pp.676–680.
15. Senftle, F.E., Thorpe, A.N., Grant, J.R. & Barkatt, A., 2007. Superparamagnetic Nanoparticles in Tap Water. *Water Research*, 41(13), pp.3005–3011.

16. Barkatt, A., Pulvirenti, A.L., Adel-Hadadi, M., Viragh, C., Senftle, F.E., Thorpe, A.N. & Grant, J.R., 2009. Composition and Particle Size of Superparamagnetic Corrosion Products in Tap Water. *Water Research*, 43(13), pp.3319–3325.
17. Smith, J.N., 2009. Atmospheric Nanoparticles: Formation and Physicochemical Properties. In: J.A. Schwarz, C.I. Contescu, & K. Putyera, eds., *Dekker Encyclopedia of Nanoscience and Nanotechnology*. 2nd ed. London: Taylor & Francis.
18. Bang, J. & Murr, L., 2002. Atmospheric Nanoparticles: Preliminary Studies and Potential Respiratory Health Risks for Emerging Nanotechnologies. *Journal of Materials Science and Letters*, 21, pp.361–366.
19. Brown, R., 1828. A Brief Account of Microscopical Observations Made on the Particles Contained in the Pollen of Plants. *London and Edinburgh Philosophical Magazine and Journal of Science*, 4, pp.161–173.
20. Einstein, A., 1905. Die von der Molekularkinetischen Theorie der Wärme Geforderte Bewegung von in Ruhenden Flüssigkeiten Suspendierten Teilchen. *Annalen der Physik*, 17, pp.549–560.
21. Perrin, J., 1909. Mouvement Brownien et Réalité Moléculaire. *Annales de Chimie et de Physique*, 8(18), pp.1–114.
22. Perrin, J., 1913. *Les Atomes*. Paris: Felix Alcan.
23. Smoluchowski, M., 1906. Zur Kinetischen Theorie der Brownschen Molekularbewegung und der Suspensionen. *Annalen der Physik*, 21, pp.756–780.

24. Smoluchowski, M., 1916a. Drei Vorträge über Diffusion, Brownsche Molekularbewegung und Koagulation von Kolloidteilchen. *Physikalische Zeitschrift*, 17, pp.557–571.
25. Smoluchowski, M., 1916b. Drei Vorträge über Diffusion, Brownsche Molekularbewegung und Koagulation von Kolloidteilchen. *Physikalische Zeitschrift*, 17, pp.587–599.
26. Mazo, R.M., 2002. *Brownian Motion: Fluctuations, Dynamics and Applications*. Oxford: Oxford University Press.
27. Kirschvink, J., Kobayashi-Kirschvink, A. & Woodford, B., 1992. Magnetite Biomineralization in the Human Brain. *Proceedings of the National Academy of Sciences of the United States of America*, 89(16), pp.7683–7687.
28. Kirschvink, J., Jones, D. & MacFadden, B., 1985. *Magnetite Biomineralization and Magnetoreception in Organisms: A New Biomagnetism*. New York: Plenum Press.
29. Kirschvink, J., 1989. Magnetite Biomineralization and Geomagnetic Sensitivity in Higher Animals: An Update and Recommendations for Future Study. *Bioelectromagnetics*, 10(3), pp.239–259.
30. Wiltschko, R. & Wiltschko, W., 1995. *Magnetic Orientation in Animals*. Berlin: Springer-Verlag.
31. Hanzlik, M., Heunemann, C., Holtkamp-Rotzler, E., Winklhofer, M., Petersen, N. & Fleissner, G., 2000. Superparamagnetic Magnetite in the Upper Beak Tissue of Homing Pigeons. *Biomaterials*, 13(4), pp.325–331.

32. Mann, S., Webb, J. & Williams, R., 1989. *Biomineralization: Chemical and Biochemical Perspectives*. Weinheim: VCH Publishers.
33. Stokroos, I., Litinetsky, L., van der Want, J. & Ishay, J., 2001. Magnetic Minerals: Keystone-Like Crystals in Cells of Hornet Combs. *Nature*, 411(6838), p.654.
34. Petersen, N., von Döbeneck, T. & Vali, H., 1986. Fossil Bacterial Magnetite in Deep-Sea Sediments from the South Atlantic Ocean. *Nature*, 320(6063), pp.611–615.
35. Fortin, D., Ferris, F. & Beveridge, T., 1997. Surface-Mediated Mineral Development by Bacteria. *Geomicrobiology: Interactions between Microbes and Minerals*, 35, pp.161–180.
36. Watson, J.H.P., Cressey, B.A., Roberts, A.P., Ellwood, D.C., Charnock, J.M. & Soper, A.K., 2000. Structural and Magnetic Studies on Heavy-Metal-Adsorbing Iron Sulphide Nanoparticles Produced by Sulphate-Reducing Bacteria. *Journal of Magnetism and Magnetic Materials*, 214(1-2), pp.13–30.
37. Grüttner, C. & Teller, J., 1999. New Types of Silica-Fortified Magnetic Nanoparticles as Tools for Molecular Biology Applications. *Journal of Magnetism and Magnetic Materials*, 194(1-3), pp.8–15.
38. Roch, A., Müller, R. & Gillis, P., 1999. Theory of Proton Relaxation Induced by Superparamagnetic Particles. *Journal of Chemical Physics*, 110(11), pp.5403–5411.
39. Bonnemain, B., 1998. Superparamagnetic Agents in Magnetic Resonance Imaging: Physicochemical Characteristics and Clinical Applications - A Review. *Journal of Drug Targeting*, 6(3), pp.167–174.

40. Ortega, D., 2012. Structure and Magnetism in Magnetic Nanoparticles. *Magnetic Nanoparticles: From Fabrication to Clinical Applications*, 3.
41. Israelachvili, J., 1991. *Intermolecular & Surface Forces*. London: Elsevier Academic Press.
42. Shaw, D., 1992. *Introduction to Colloid & Surface Chemistry*. Oxford: Butterworth-Heinemann.
43. London, F., 1930. Some Characteristics and Uses of Molecular Force. *Zeitschrift Für Physikalische Chemie-Abteilung B-Chemie Der Elementarprozesse Aufbau Der Materie*, 11(2/3), pp.222–251.
44. Atkins, P.W., De Paula, J. & Keeler, J., 2023. *Atkins' Physical Chemistry*. Oxford: Oxford University Press.
45. Lehninger, A.L., Nelson, D.L. & Cox, M.M., 2005. *Lehninger Principles of Biochemistry*. New York: Macmillan.
46. Voet, D., Voet, J.G. & Pratt, C.W., 2013. *Fundamentals of Biochemistry: Life at the Molecular Level*. 4th ed. Hoboken, NJ: Wiley.
47. Dill, K. & Bromberg, S., 2010. *Molecular Driving Forces: Statistical Thermodynamics in Biology, Chemistry, Physics, and Nanoscience*. New York: Garland Science.
48. Thakuria, R., Nath, N.K. & Saha, B.K., 2019. The Nature and Applications of  $\pi$ - $\pi$  Interactions: A Perspective. *Crystal Growth & Design*, 19(2), pp.523–528.
49. Kool, E.T., 2001. Hydrogen Bonding, Base Stacking, and Steric Effects in DNA Replication. *Annual Review of Biophysics and Biomolecular Structure*, 30(1), pp.1–22.



50. Gangadoo, S., Taylor-Robinson, A. & Chapman, J., 2015. Nanoparticle and Biomaterial Characterisation Techniques. *Materials Technology*, 30(sup5), pp.44–56.
51. Dinnebier, R.E. & Billinge, S.J. (eds.), 2008. *Powder Diffraction: Theory and Practice*. Cambridge: Royal Society of Chemistry.
52. Epp, J., 2016. X-Ray Diffraction (XRD) Techniques for Materials Characterization. In: *Materials Characterization Using Nondestructive Evaluation (NDE) Methods*, pp.81–124. Woodhead Publishing.
53. Tomalia, D.A., Reyna, L.A. and Svenson, S., 2007. Dendrimers as Multi-Purpose Nanodevices for Oncology Drug Delivery and Diagnostic Imaging. *Biochemical Society Transactions*, 35(Pt 1), pp.61–67.
54. Niimura, N. & Podjarny, A., 2011. *Neutron Protein Crystallography: Hydrogen, Protons, and Hydration in Bio-Macromolecules*. Oxford: Oxford University Press.
55. Goldstein, J.I., Newbury, D.E., Michael, J.R., Ritchie, N.W., Scott, J.H.J. & Joy, D.C., 2017. *Scanning Electron Microscopy and X-Ray Microanalysis*. Cham: Springer.
56. Harvey, D.J., 2019. Modern Analytical Techniques in Metabolomics Analysis. *Analyst*, 144, pp.3432–3448.
57. Nelms, B., 2005. *Inductively Coupled Plasma Mass Spectrometry Handbook*. Oxford: Blackwell Publishing.
58. Pecora, M., 1985. *Dynamic Light Scattering: Applications of Photon Correlation Spectroscopy*. New York: Springer.

59. Skoog, D.A., Holler, F.J. & Crouch, S.R., 2018. *Principles of Instrumental Analysis*. 7th ed. Boston: Cengage Learning.
60. Yang, C., 2008. *Encyclopedia of Microfluidics and Nanofluidics*. In: D. Li (ed.), New York: Springer.
61. Author(s), 2023. *Raman Spectroscopy: Advances and Applications*. 1st ed. Singapore: Springer.
62. Pecher, O., Carretero-González, J., Griffith, K.J. & Grey, C.P., 2017. Applications of Nuclear Magnetic Resonance in Battery Systems. *Chemistry of Materials*, 29, pp.213–242.
63. Wesdemiotis, C. & Wang, P., 2006. Thermochemistry Studies of Biomolecules. In: *Principles of Mass Spectrometry Applied to Biomolecules*. [Journal Name Missing].
64. Kaszuba, M., McKnight, D., Connah, M.T., McNeil-Watson, F.K. & Nobbmann, U., 2008. Measuring Sub-Nanometre Sizes Using Dynamic Light Scattering. *Journal of Nanoparticle Research*, 10, pp.823–829.
65. Chiba, F. & Twyman, L.J., 2017. Effect of Terminal-Group Functionality on the Ability of Dendrimers to Bind Proteins. *Bioconjugate Chemistry*, 28(8), pp.2046–2050.
66. Chiba, F., Hu, T.C., Twyman, L.J. & Wagstaff, M., 2008. Dendrimers as Size-Selective Inhibitors of Protein-Protein Binding. *Chemical Communications*, pp.4351–4353.
67. Bogan, A. & Thorn, K.S., 1998. *Journal of Molecular Biology*, 280(1).

68. Ellis, A., Wallace, M. & Twyman, L.J., 2013. Exploiting Dense Shell/Packing Principles to Invoke Stereoselectivity in a Reaction Accelerated by a Chiral Dendrimer. *Chemical Communications*, 49, pp.8063–8065.

## Chapter 4

Functionalization of GO  
with oligo amino acids and  
its  
applications as enzyme inhibitors  
by using  $\alpha$ -chymotrypsin.

**This chapter has been done in Cooperation with PhD student  
Dr.Abdelfatah Blau.**

**My contributions were:**

1. Unfunctionalized Graphene Oxide Synthesis.
2. Chemical functionalisation of GO with:
  1. Monomeric glutamic acid.
  2. Oligomeric glutamic Acid.
3. Characterisation of the monomeric and oligomeric GO systems.
4. Assay to measure inhibition and binding interactions between GO systems and  $\alpha$ -chymotrypsin.
5. Exploring selectivity by functionalizing GO with various amino acids.

## Introduction:

### The newly developed carbon-derived materials:

Graphene, made up of individual 2D sheets of  $sp^2$  hybridized carbon atoms, was first isolated in 2004.<sup>1</sup> This material was quickly utilized for various applications, including electronics, protein binding, and more recently, membrane technology. Geim and Novoselov were responsible for the groundbreaking discovery that graphene can be produced through the 'Scotch tape' method, where single sheets of graphene were meticulously exfoliated from bulk graphite.<sup>2</sup> Graphene oxide (GO) is an intermediate material formed during the synthesis of graphene through the oxidation of graphite, followed by a reduction step to eliminate oxygen-containing functional groups. Interestingly, GO has been discovered to have a variety of valuable applications, making it a significant material in its own regard.<sup>2</sup>

In its purest form, graphene is impermeable to all molecules, even the smallest ones like helium, due to its tightly packed carbon atom lattice (see figure 3.1).<sup>2</sup> In contrast, graphene oxide (GO), a derivative of graphene, shows significant promise for protein binding because of its diverse chemistry with various oxygen functional groups, which create distinct interactions with cations. The oxidation process used in the synthesis of GO, where graphite is the main raw material, generates an abundance of oxygen-rich functional groups. These properties make GO a promising high-performance substitute material for protein binding. Additionally, GO nanosheets can be arranged into a layered structure through filtration or coating techniques, forming rapid and selective 2D nanochannels that enhance molecular filtration.<sup>3</sup>

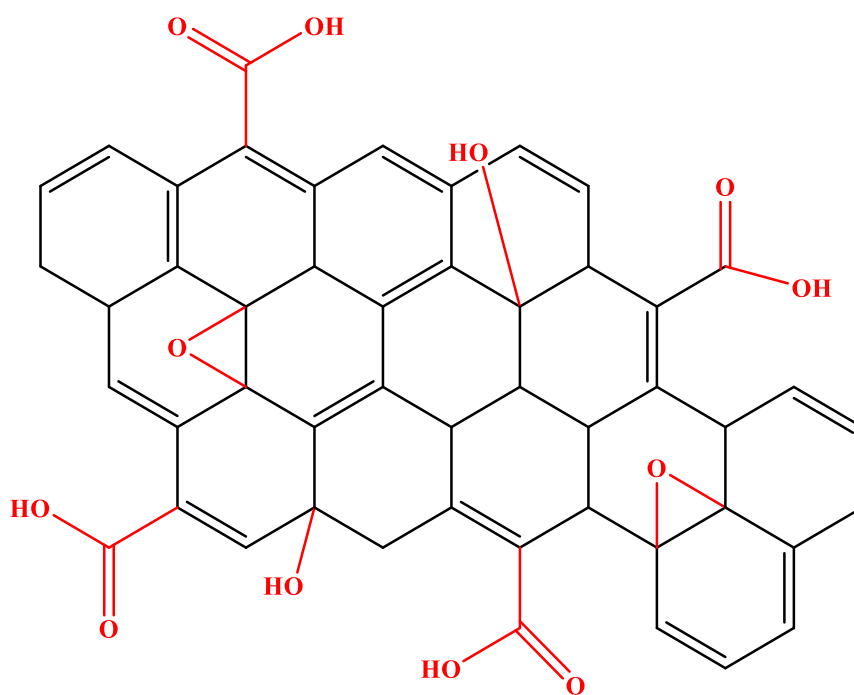


Figure 3.1: An illustration of the graphene oxide's structure.

Graphene oxide, previously known as graphite oxide, consists primarily of crumpled 2D carbon sheets decorated with various oxygenated functional groups present on both the basal planes and edges. Typically, its thickness measures around 1 nanometre, while its lateral dimensions range from a few nanometres to several microns. The origins of graphene oxide date back to an accidental discovery by Brodie. In 1859, while attempting to determine the molecular weight of graphite at the University of Oxford <sup>4</sup>, Brodie noticed that graphite exhibited distinct properties different from other forms of carbon like diamond or charcoal. He hypothesized that graphite represented a unique element and believed that oxidation was the most appropriate method to analyze its elemental composition. Despite Brodie's understanding of the molecular weights of hydrogen and oxygen, the analysis of graphite remained unresolved at that time.<sup>5</sup> Brodie's initial discovery was ruined by the use of hazardous chemicals. In 1898, Staudenmaier

made modifications to Brodie's method to improve the oxidation process of graphite.<sup>6</sup> A safer method was later developed by Hummer and Offeman in 1957, a century after Brodie's work.<sup>7</sup>

Today, graphene oxide (GO) is poised to facilitate a wide range of applications. Discovered almost 160 years ago, it has only recently gained significant attention from the scientific community over the past decade, mainly due to its role as a precursor to graphene. However, GO itself holds substantial scientific importance as a fundamental form of oxidized carbon, featuring a variety of intriguing properties that can be utilized across diverse applications.

### Synthesis method graphene oxide:

Methods like the modified Hummer's approach enable the large-scale production of GO. Over time, significant efforts have been made to streamline and improve these methods, making them safer, more practical, and increasing the yield of GO. In the upcoming sections, a brief chronological overview of GO synthesis methods will be provided, commencing with Brodie's, Staudenmaier's, Hummer's, modified Hummer's, and Tour's methodologies.

#### Brodie's method:

In the 19th century, as previously stated, Brodie was the first to synthesize graphene oxide (GO) during his exploration of graphite chemistry. In his research, noting graphite's low reactivity toward strong oxidizing agents, he utilized potassium chlorate ( $\text{KClO}_3$ ) and nitric acid ( $\text{HNO}_3$ ) for oxidation.  $\text{KClO}_3$  was added to a graphite slurry, combined with fuming  $\text{HNO}_3$ , resulted in a novel compound containing carbon, oxygen, and hydrogen. In the subsequent stage, the batch devoid of salts generated during the reaction underwent a process involving washing, drying at  $100^\circ\text{C}$ , and further exposure to an oxidizing environment. After three such sequential treatments, the substance's appearance changed to a light-yellow colour,



which persisted even with additional rounds of oxidation. When Brodie measured the weight of these substances, there was an increase compared to the original graphite, confirming successful oxidation had occurred.

In his experiment, Brodie emphasized the challenge of obtaining the final product through a single extended treatment. To preserve the substance's original properties, he had to repeat the oxidation process each time. Based on his elemental analysis, he proposed the molecular formula of the end product as  $C_{11}H_4O_5$  and named it graphitic acid. The resulting substances were characterized by their small size, limited thickness, and an imperfect structure reminiscent of a crystal. It's important to note that his observations and conclusions were influenced not only by theoretical considerations but also by the limitations of the characterization techniques available during his research, suggesting opportunities for further refinement and exploration.<sup>7</sup>

#### Hummer's method and modified Hummer's method:

Hummer and Offeman introduced an alternative method for synthesizing graphene oxide (GO). These chemists, affiliated with the Mellon Institution of Industrial Research, devised an oxidation process for graphite using a mixture of concentrated sulfuric acid ( $H_2SO_4$ ), sodium nitrate ( $NaNO_3$ ), and potassium permanganate ( $KMnO_4$ ) at  $45^\circ C$ .<sup>7</sup> They stated that the entire oxidation process could be completed in just 2 hours, resulting in a higher degree of oxidation in the final product compared to the Staudenmaier method. Yet, subsequent research revealed that the product from the Hummer's method was partially oxidized graphite. To improve the oxidation level, a pre-expansion process was found beneficial. This involved treating graphite with a mixture of  $H_2SO_4$ ,  $K_2S_2O_8$ , and  $P_2O_5$  at  $80^\circ C$  for a number of hours, a method initially developed by Kovtyukhova in 1999.<sup>8</sup>

Before undergoing oxidation using the Hummer's technique, the pre-treated mixture underwent steps including dilution, filtration, washing, and drying. Later studies indicated that by expanding or reducing the size of graphite flakes, some complex pre-treatments could be simplified or omitted. Various alterations to the Hummer's method were explored, such as expanding potassium permanganate quantities, precise additions of phosphoric acid, eliminating sodium nitrate, and extending reaction times. These adjustments aim to enhance oxidation levels and improve the production of graphene oxide (GO). Typically, GO produced using modified approaches consists of thin flakes about 1 nm thick and averaging approximately 1  $\mu\text{m}$  in lateral dimension. These adaptations have significantly enhanced both the extent of oxidation and the production yield of GO compared to the initial outcomes achieved with Brodie's method. However, the procedure for isolating and purifying GO applying the modified Hummer's approach still involves complexities and consumes time.

Another variation of Hummer's method, known as the Tour method, was pioneered in 2010 by the Tour Group at Rice University. This novel approach eliminated the use of sodium nitrate and escalated the quantity of potassium permanganate instead. Additionally, they introduced phosphoric acid into the reaction mixture. By conducting the reaction with a 9:1 ratio of sulfuric acid ( $\text{H}_2\text{SO}_4$ ) to phosphoric acid ( $\text{H}_3\text{PO}_4$ ) and six equivalents of  $\text{KMnO}_4$ , the group not only enhanced the overall reaction efficiency but also demonstrated that the addition of extra  $\text{KMnO}_4$  resulted in a higher yield of hydrophilic oxidized GO materials.<sup>9</sup> The key benefit of this method is the removal of sodium nitrate, which prevents the release of toxic gases like  $\text{NO}_2$ , resulting in a more eco-friendly development.

## The evaluation of GO for its ability to bind proteins:

Synthetic protein ligands have the potential to inhibit unwanted protein aggregations associated with several diseases such as diabetes, Alzheimer, and thromboembolism.<sup>10</sup> The ability of a synthetic inhibitor to bind to a protein is mainly attributed to exact interactions involving functional groups and charges positioned at accurate locations on a three-dimensional surface.<sup>11</sup>

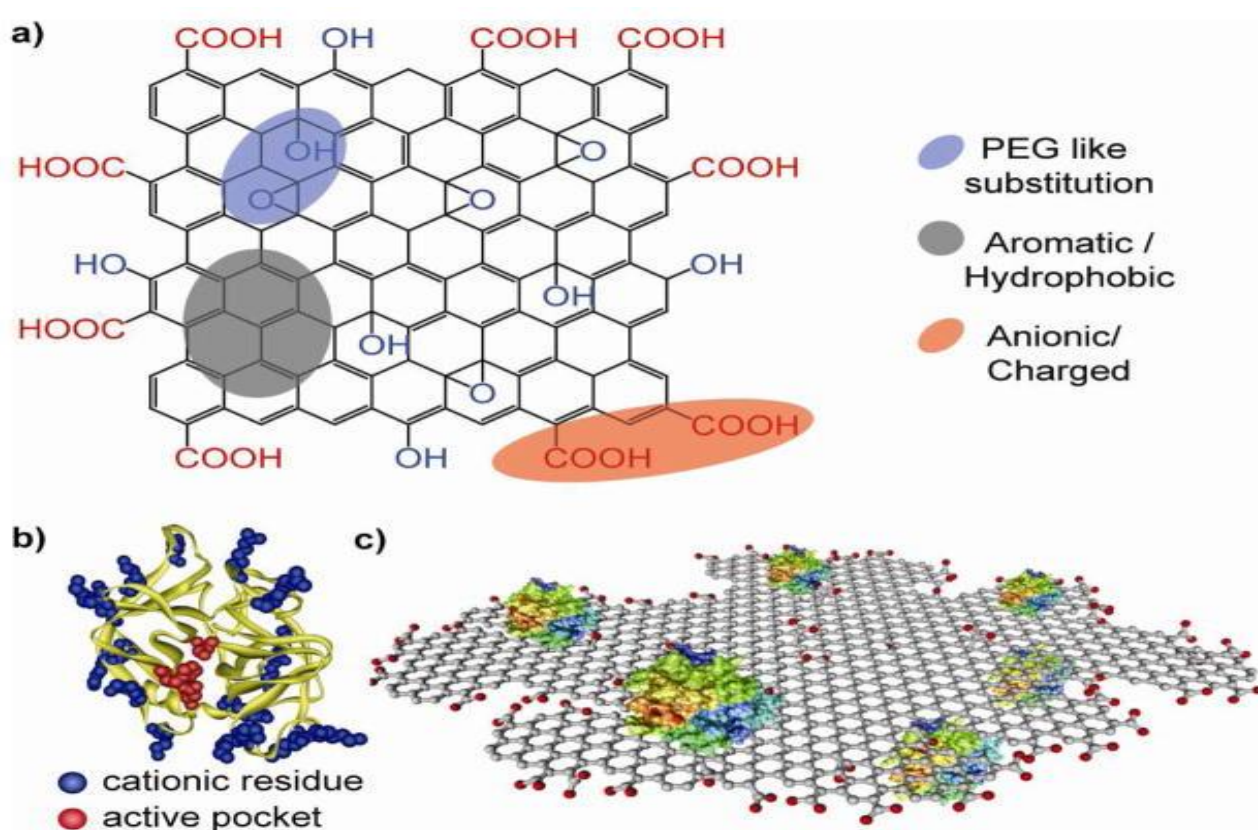
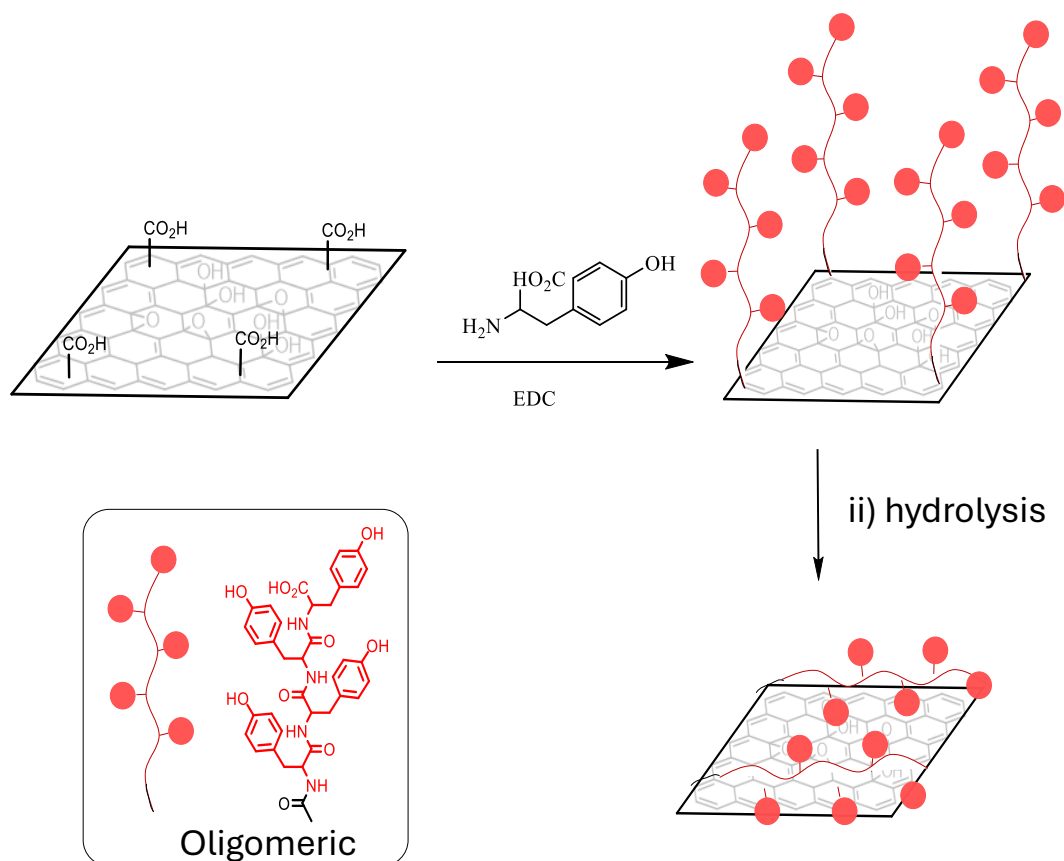


Figure 3.2: The diagram depicts (a) the structure of graphene oxide (GO) and (b)  $\alpha$ -chymotrypsin along with (c) a schematic representation illustrating the interaction between graphene oxide and the protein. It illustrates how graphene oxide binds to  $\alpha$ -chymotrypsin, affecting both  $\alpha$ -chymotrypsin activity and its secondary structure. These studies offer valuable insights into the potential of GO as a protein binder, warranting further investigation. Reproduced with permission from ref. 41. Copyright 2011, American Chemical Society.

This example involves unfunctionalized graphene oxide (GO), where the interaction strength is primarily determined by electrostatic interactions. Consequently, unfunctionalized GO binds to all proteins that attain a cationic surface.<sup>12</sup> In biological systems, proteins utilize the functional groups supplied by amino acids strategically positioned on their three-dimensional surfaces for selective binding with other biomolecules, including proteins.<sup>14</sup> Certain amino acids play crucial roles in protein-protein interactions.<sup>13</sup> For instance, tyrosine, though relatively rare, is often located within binding domains and is recognized for its crucial role in protein identification and selectivity.<sup>15</sup> While some studies have explored the functionalization of GO with amino acids, research specifically focused on selective protein binding remains limited.<sup>16</sup> The predominant method to add the amino acids involves using a coupling agent and an excess of unprotected amino acids, leading to oligomeric addition of amino acids on the GO surface. This approach offers simplicity, flexibility and enhanced functionality, with the potential to establish high-affinity and strong binding interactions.<sup>16</sup>

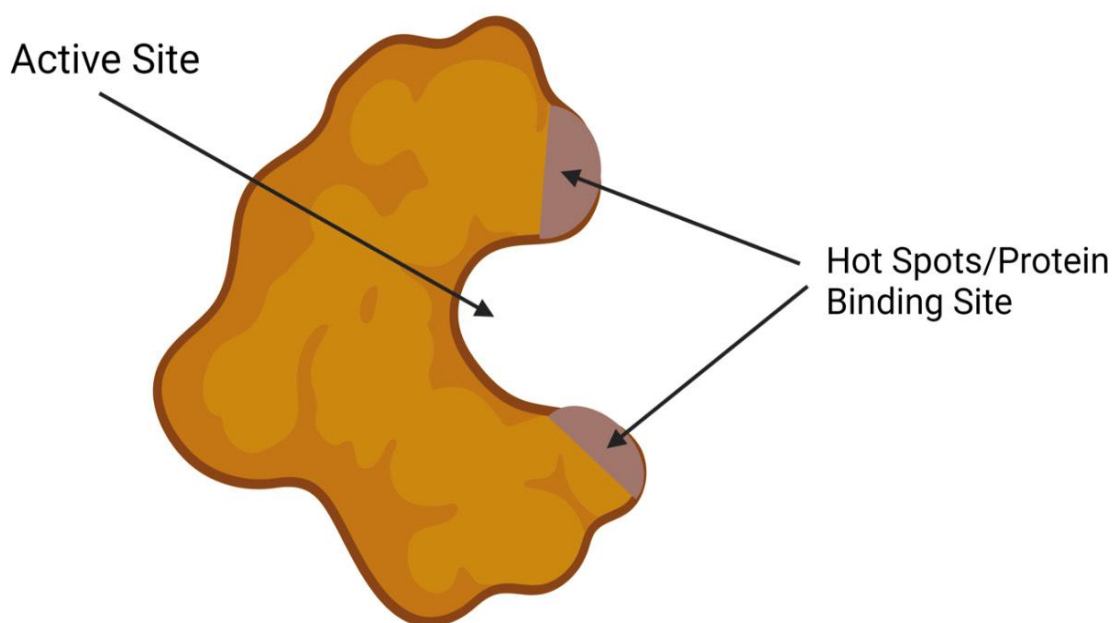
In a previous study, our group proposed using GO functionalized with oligomeric tyrosine, aiming to achieve stronger protein binding when compared to GO functionalized with a simple monomeric layer of tyrosine, as depicted in scheme 3.1. This proposal was based on the assumption that oligomeric systems would have the potential to bind cooperatively to the protein. However, the aromatic groups of tyrosine tend to strongly adsorb to the GO surface via  $\pi$ - $\pi$  interactions, which actually reduced protein binding. This was due to the cooperative nature of oligomeric interactions between tyrosine and the aromatic surface of GO, which can dominate the proposed GO-protein interactions, affecting overall binding outcomes.<sup>17</sup>



Scheme 3.1: An illustration of the first stage of functionalization, which entails coating with an oligomeric layer of amino acids. The oligomeric structure was formed by mixing EDC and unprotected tyrosine with a suspension of GO in water, followed by stirring at 70°C for 24 hours. The same study showed that GO functionalized with a monomeric layer of tyrosine could bind to the protein more strongly than the oligomeric or unfunctionalized GO. Despite the fact that monomeric system can still form  $\pi$ - $\pi$  interactions with the GO surface, these are monomeric. As such, this interaction is relatively weak and can be overcome as all of the tyrosines can interact with the protein, via a surface to protein cooperative interaction.<sup>18 & 19</sup>

## Aims and Objectives:

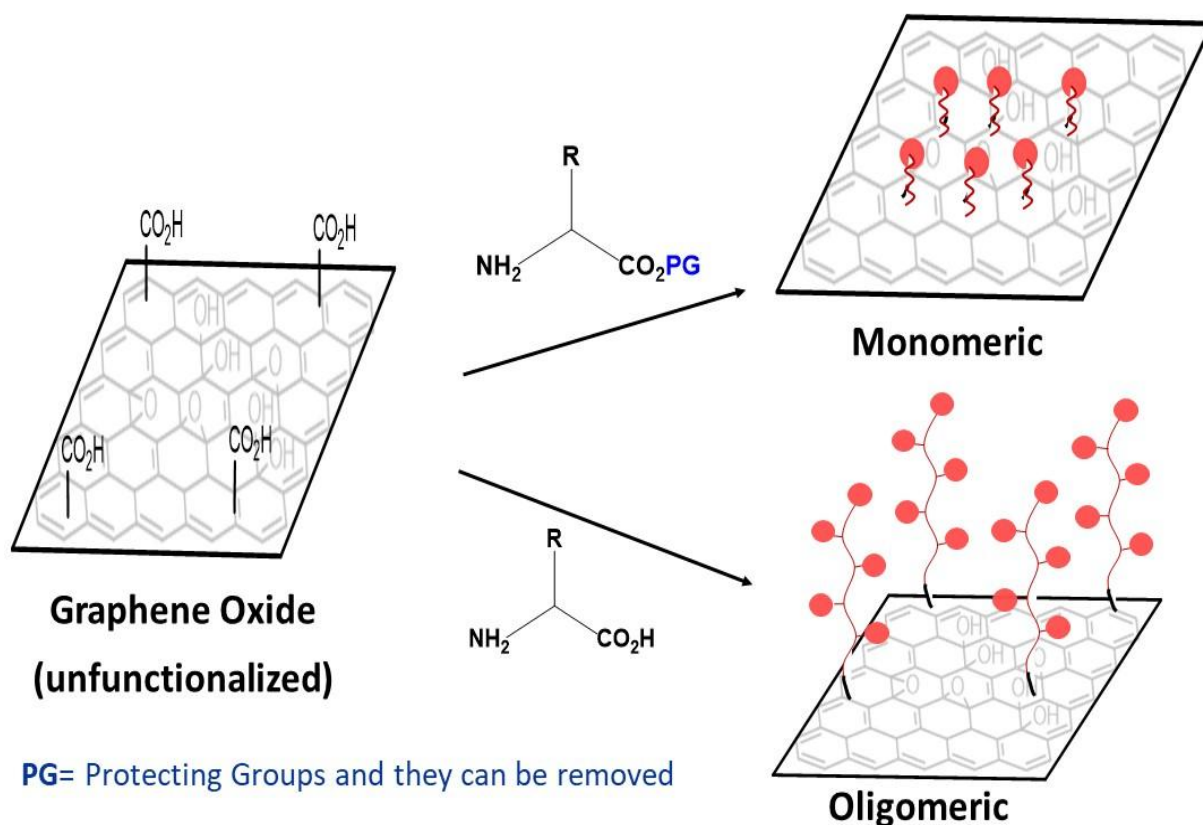
The primary aim of this project was to investigate different functionalized graphene oxides (GO) for their potential to improve binding. At the outset, the objective was to re-examine the idea that oligomeric functionalization could lead to enhanced binding.<sup>13</sup> Next, a range of amino acids will be studied in order to determine which ones are effective or ineffective in binding. If this proves successful, combining both approaches could lead to a method for creating GO-based ligands that are specific to different proteins. We will indirectly assess the kinetics of binding by determining the rates of enzyme hydrolysis with and without various GO ligands present. This method has been used before, targeting chymotrypsin as the protein/enzyme. Since the active site entrance is at the centre of the enzyme's binding site, the strength of binding will be directly related to the efficiency of inhibition (scheme 3.2).



Scheme 3.2: Indicating the active site and identifying the key hot spots where binding occurs. This figure was prepared by using [BioRender](#).

A brief description of this method can be found in the introduction above, and it is based on the technique described by Andrew several years ago. The initial goal was to functionalize GO with an oligomeric amino acid.<sup>14</sup> Even though our group's previous experiments with oligo tyrosine did not improve binding, we believe glutamic acid may be more successful. Unlike tyrosine, glutamic acid cannot form  $\pi$ - $\pi$  interactions with the GO surface, allowing the oligomeric chains to extend freely and present more carboxylic acid groups on the surface, thereby increasing binding affinity. Glutamic acid's inability to participate in  $\pi$ - $\pi$  interactions with the GO surface is due to its lack of an aromatic ring in its molecular structure, which can be problematic in protein binding.  $\pi$ - $\pi$  interactions are crucial for significantly enhancing binding affinity between molecules and surfaces. Without this capability, glutamic acid may result in weaker binding affinity, reduced selectivity, less stable protein conformations, and an overall less efficient binding process when compared to aromatic amino acids that can engage in these interactions.

Additionally, we synthesized a monomeric glutamic acid functionalized GO surface using a protection, addition, and deprotection method. While the main function of the monomeric glutamic acid system is to serve as a control for comparison with the glutamic acid oligomer, it is probable that it will be a stronger ligand than unfunctionalized GO. This results from glutamic acid's structure, which includes two carboxylic acid groups. When glutamic acid is introduced to GO, it removes a carboxylate from GO (as it couples), but as each molecule contributes two carboxylic groups, it doubles the carboxylates on the surface. This leads to an increase in carboxylates, increasing the electrostatic interactions.<sup>15</sup> Scheme 3.3 illustrates the idea in the scheme.

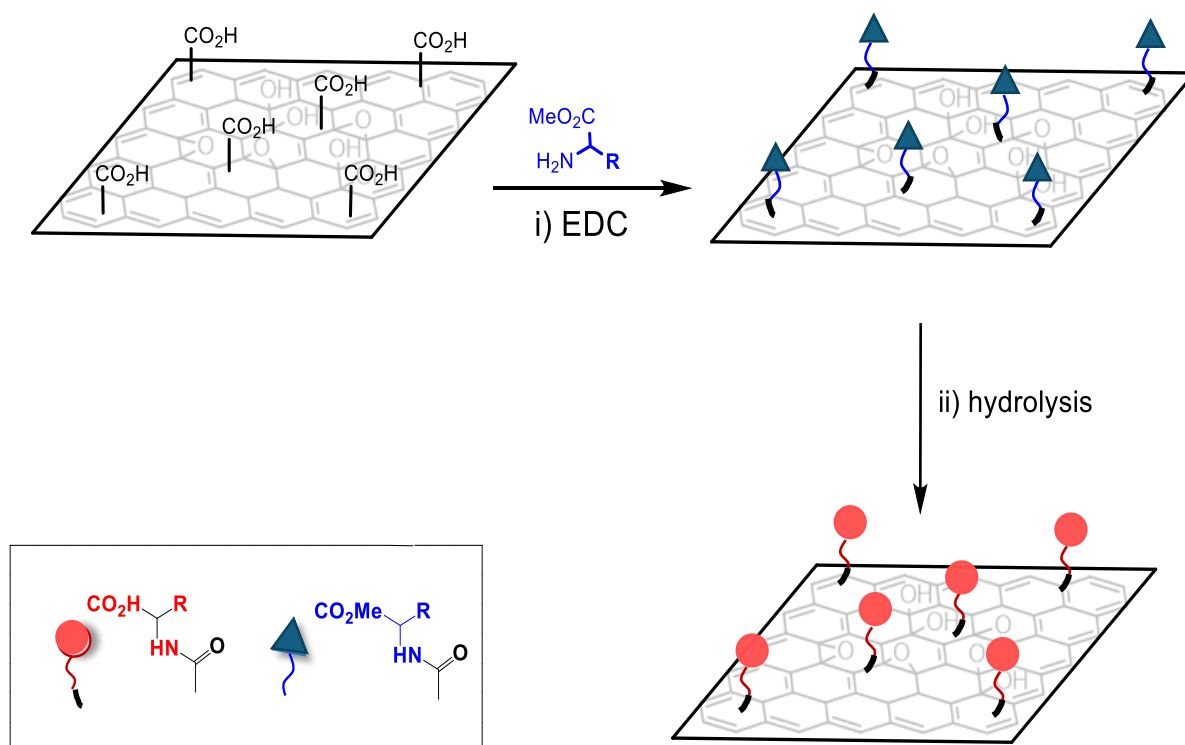


Scheme 3.3: The diagram depicts two different methods for modifying graphene oxide (GO) with glutamic acid. In the first method, glutamic acid is covalently attached to GO, and subsequent hydrolysis of the methyl ester produces carboxylic acid groups. This results in GO with a thin layer of glutamic acid, including a fixed spacer. In contrast, the second method simplifies the synthesis by directly reacting unprotected tyrosine (containing both  $\text{-NH}_2$  and  $\text{COOH}$  groups) with GO. This creates a thicker layer of glutamic acid on the GO surface, forming an oligomeric system.

After confirming the effectiveness of the approach by evaluating the number of charge–charge interactions, the next step was to investigate how specific amino acid functionalities influence protein binding. Since it was already established that charge plays a dominant role in these interactions, the study focused on two main objectives: first, to demonstrate that enhanced binding could be achieved using both mono- and oligo-glutamic acid; and second, to explore



the potential for selective binding. The goal was to determine whether the functional groups of different amino acids could positively or negatively impact binding. If successful, this approach could lead to the development of a selective method for creating GO-based ligands that exhibit specificity toward certain proteins, offering more targeted and efficient binding capabilities.<sup>16</sup> In these experiments, every amino acid would be applied as monomers using C-protected amino acids, resulting in a layer of monomeric amino acids after deprotection. The chosen amino acids were selected based on their known significance (or insignificance) in protein–protein binding.<sup>35</sup> Once synthesized, all products will be analyzed via elemental analysis (EA), thermogravimetric analysis (TGA), FT-IR and Raman spectroscopy. Moreover, systems including X-ray diffraction (XRD), X-ray photoelectron spectroscopy (XPS), and scanning electron microscopy (SEM) will be utilized to analyze and characterize the properties of graphene.



Scheme 3.4: The monomeric system was synthesized using the same initial procedure, but with the use of the methoxy ester of glutamic acid. After isolation, the functionalized GO was suspended again in water, and the ester group was hydrolyzed using sodium hydroxide.

## Results and Discussion:

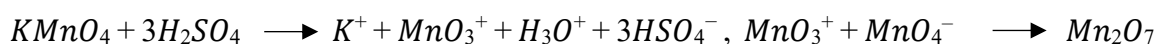
Graphene oxide (GO) can be synthesized using a variety of well-established methods. These methods ensure consistent production of GO, making it accessible for numerous applications. However, a significant drawback emerges when GO is dispersed in liquid media, as this complicates the analysis of its bulk structure, rendering techniques such as liquid-phase NMR and other conventional methods less effective or even impractical. As a result, researchers must turn to solid-phase analytical techniques to assess the structure and properties of GO accurately. Among these techniques, Fourier-transform infrared spectroscopy (FT-IR) is used to recognize functional groups and bonding structures. X-ray photoelectron spectroscopy (XPS) provides detailed information on the elemental composition and chemical states of the elements within GO. Elemental analysis offers quantitative data on the elemental composition, confirming the presence and ratios of carbon, oxygen, and other elements. Elemental analysis also provides information about the relative loading of each amino acid, which must be similar. This is key, as it allows us to compare systems directly (this has not always been done in the literature).

Additionally, various microscopic methods, including scanning electron microscopy (SEM) and transmission electron microscopy (TEM), are employed to visualize the morphology and structural details of GO at the nanoscale. These solid-phase techniques collectively provide a comprehensive understanding of GO's structure and properties, which is crucial for optimizing its performance in various applications.<sup>3</sup>

## Unfunctionalized Graphene Oxide Synthesis:

Brodie, Staudenmaier, and Hummers investigated various methods to produce graphene oxide (GO) from graphite oxidation by removing sodium nitrate ( $\text{NaNO}_3$ ) from the reaction. This modification enhances safety by eliminating the production of toxic nitrogen dioxide ( $\text{NO}_2$ ) gas, a hazardous byproduct in the original Hummers' method. The generation of toxic gases poses significant safety risks in laboratory environments. The Tour method's exclusion of  $\text{NaNO}_3$  reduces these risks associated with handling and disposing of toxic gases, making the synthesis of graphene oxide safer for researchers and laboratory personnel. Moreover, this modification simplifies the synthesis process, enhancing user-friendliness while maintaining the ability to produce high-quality graphene oxide effectively. Therefore, the Tour method is considered an advancement in both safety and practicality compared to the original Hummers' method.

For our work, graphene oxide was synthesized using the Tour method, outlined in figure 3.3. The process involved adding graphite powder to a 9:1 mixture of cool concentrated  $\text{H}_2\text{SO}_4/\text{H}_3\text{PO}_4$ , and solid  $\text{KMnO}_4$  was introduced gradually to mitigate potential hazards from exothermic reactions. Besides the graphite source, the selection of oxidation reagents significantly influences the degree of oxidation of the graphene flakes.  $\text{KMnO}_4$  and  $\text{H}_2\text{SO}_4$  are commonly used oxidation agents in graphene oxide synthesis.  $\text{KMnO}_4$  contains the permanganate ion, a well-known oxidation reagent whose reactivity requires an acidic environment, typically achieved through the formation of di manganese heptoxide when  $\text{KMnO}_4$  reacts with a strong acid.



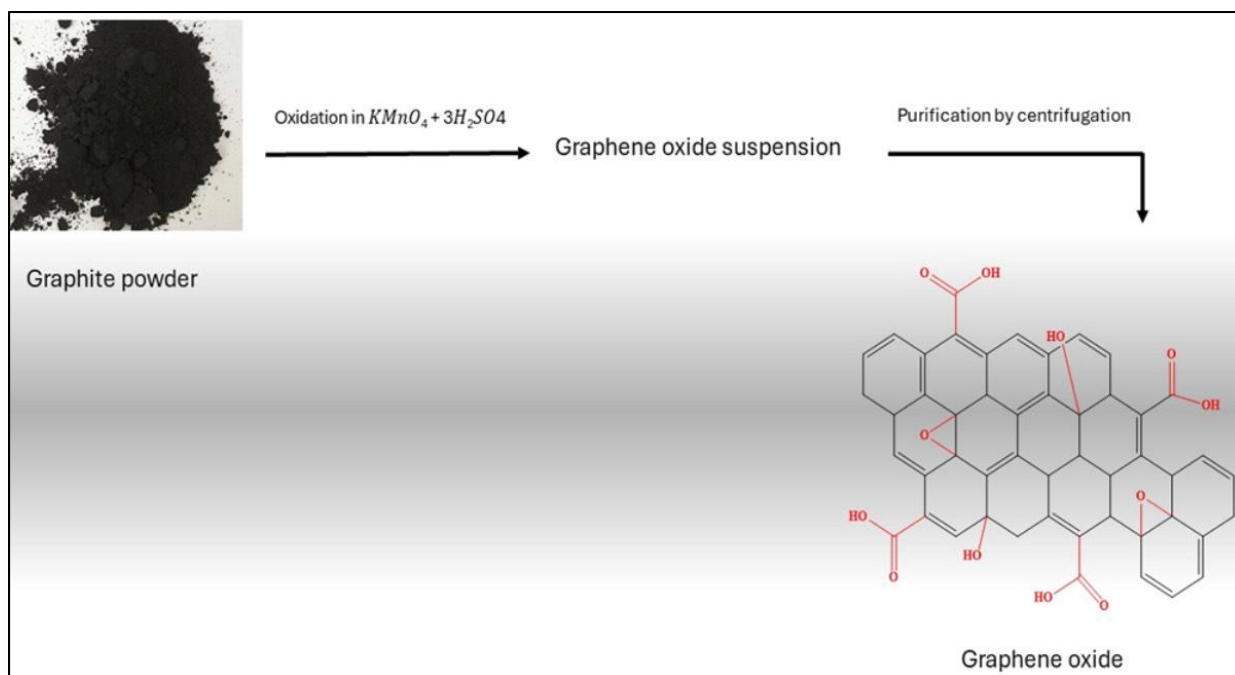


Figure 3.3: The diagram depicts the step-by-step process for synthesizing graphene oxide (GO) through the modified Tour method. These key stages encompass the creation of a graphite oxide suspension, oxidation facilitated by potassium permanganate, subsequent dilution with deionized water, purification via centrifugation and washing, and the final phases of exfoliation and stabilization.

The structural of graphene oxide (GO) was confirmed by comparing its characterization data with previously published findings. Initially, Fourier-transform infrared spectroscopy (FT-IR) was employed. In the FT-IR analysis, several distinctive peaks were identified, indicating the presence of oxygen-containing functional groups. Notably, a broad band observed at  $3350\text{ cm}^{-1}$  confirmed the presence of hydroxyl groups (OH). Additionally, peaks were observed at  $1732\text{ cm}^{-1}$  (indicative of carbonyl and carboxyl  $C=O$ ),  $1228\text{ cm}^{-1}$  (epoxy  $C-O$ ),  $1622\text{ cm}^{-1}$  (aromatic  $C=C$ ), and  $1041\text{ cm}^{-1}$  (related to skeletal  $C=O$  or  $C-C$ ), corresponding to carboxylic and epoxy groups. These observations aligned closely with

spectra reported in earlier studies,<sup>36</sup> validating the GO structure (figure 3.4).

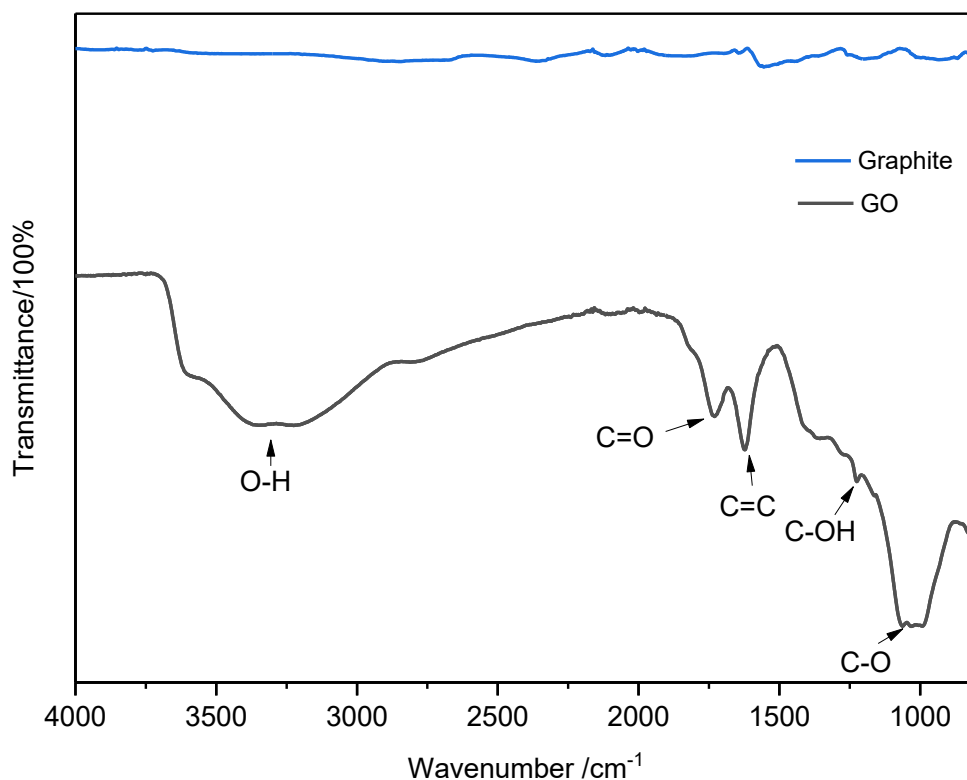


Figure 3.4: Confirms the presence of oxygen-containing functional groups in the sample.

A broad peak at 3350 cm<sup>-1</sup> indicates hydroxyl groups (OH) are present. Additionally, peaks at 1732 cm<sup>-1</sup> (carbonyl and carboxyl C=O), 1228 cm<sup>-1</sup> (epoxy C-O), and 1622 cm<sup>-1</sup> (aromatic C=C) were observed.

Further investigations were carried out using Raman spectroscopy and scanning electron microscopy (SEM) to provide additional insights and detailed characterization of the GO's structural and morphological properties. Raman technique allows for detailed analysis of the molecular bonding and arrangement of carbon atoms, providing insights into the material's

composition and properties at the nanoscale level. Peaks at  $1355\text{ cm}^{-1}$  and  $1593\text{ cm}^{-1}$  confirm notably the structural characteristics of graphene oxide (GO). In line with the D and G-bands, graphite displays a single, strong peak at  $1575\text{ cm}^{-1}$ . The structure of GO was verified by the presence of two prominent peaks at  $1355\text{ cm}^{-1}$  and  $1593\text{ cm}^{-1}$ , which correspond to the D and G-bands. In contrast, graphite exhibited a single sharp peak at  $1575\text{ cm}^{-1}$ .

The ID/IG intensity ratio of graphene oxide (GO) is 0.80, indicating that the attachment of oxygen-containing functional groups has introduced defects into the graphene structure. This ratio reflects the relative intensities of the D-band (around  $1350\text{ cm}^{-1}$ ), associated with defects and disorder in the graphene lattice, and the G-band (around  $1580\text{ cm}^{-1}$ ), which is related to the  $\text{sp}^2$ -hybridized carbon structure. The increase in the ID/IG ratio suggests that the  $\text{sp}^2$ -hybridized carbon structure has been altered, converting some carbon atoms to  $\text{sp}^3$ -hybridized carbon due to the introduction of oxygen-containing groups. Additionally, the  $\text{I}_{2\text{D}}/\text{IG}$  ratio provides insight into the formation of multilayer GO sheets, consisting of fewer than five layers. This is further supported by the wider and symmetrical 2D band observed in the range of  $2500\text{-}3200\text{ cm}^{-1}$  (Figure 3.5).

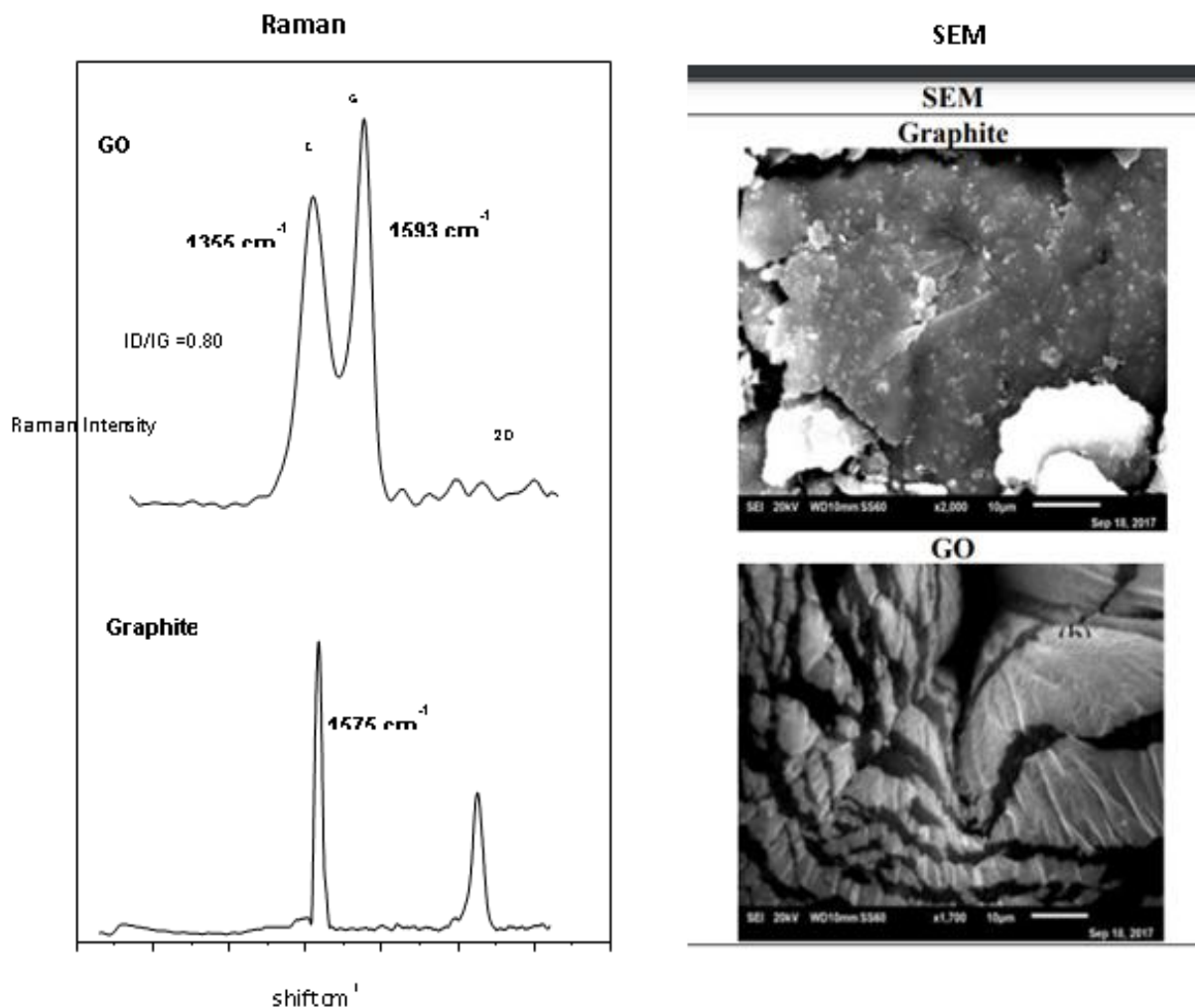


Figure 3.5: Presents a detailed comparison between Raman spectra (left) and Scanning Electron Microscopy (SEM) images for graphite and graphene oxide (right). The figure offers insights into the structural and morphological differences between these two materials by illustrating both their Raman scattering characteristics and their surface morphologies.

Additional examination of the oxygen functional groups in graphene oxide (GO) was conducted using X-ray photoelectron spectroscopy (XPS) using a ThermoFisher K-Alpha spectrophotometer. The XPS scans utilized a monochromatic Al-K $\alpha$  X-ray source with an



energy of 1486.69 eV. It measures the kinetic energy and the number of electrons emitted from a material when it is exposed to X-ray radiation in a high vacuum environment. This technique provides exceptional information about the elemental composition, empirical formula, chemical state, and electronic state of the elements present in the material.

As shown in the figure 3.6 below explains the C1s X-ray photoelectron spectroscopy (XPS) spectrum of graphene oxide (GO) typically reveals four distinct peaks, each corresponding to the electron binding energies of carbon atoms in different chemical environments. The first peak, at approximately 284.44 eV, represents carbon atoms involved in C–C (graphitic) bonds. The second peak, at 285.3 eV, corresponds to carbon atoms bonded to oxygen in C–O groups, such as ethers, alcohols, or epoxides. The third peak, around 287.76 eV, is associated with carbon atoms in C=O (carbonyl) groups, while the fourth peak, at 288.1 eV, corresponds to carbon atoms in O=C–OH (carboxyl) groups. These peaks reflect the varying electron affinities and bonding environments of the carbon atoms in GO.

In the O 1s spectrum, the binding energies were observed at 531.0 eV for C=O groups, 532.59 eV for C-OH groups, and 534.80 eV for O-C=O groups. These spectral features provide detailed information about the composition and distribution of oxygen-containing functional groups on the surface of GO, crucial for understanding its chemical properties and potential applications.

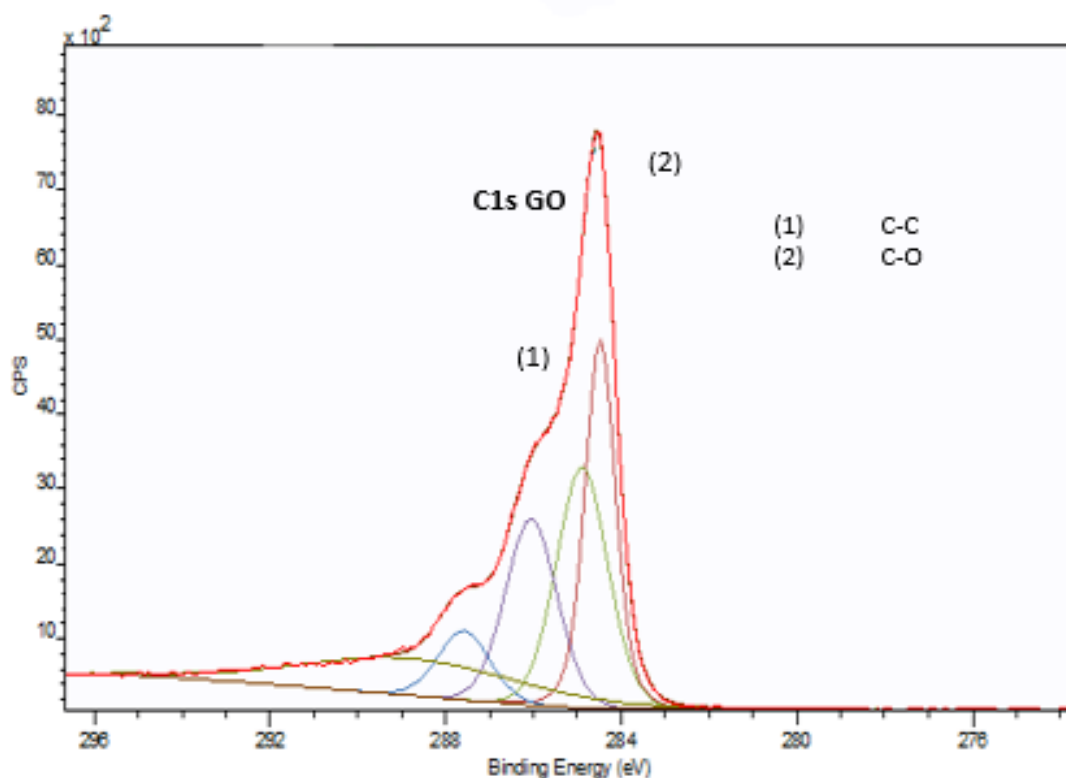


Figure 3.6: Deconvolution and identification involve separating and characterizing carbon and oxygen functional groups in the C1s and O1s X-ray photoelectron spectroscopy (XPS) spectra of graphene oxide (GO). This process aims to discern and analyze the specific types and distributions of these functional groups present on the GO surface, providing insights into its chemical composition and structure.

Oxygen-containing functional groups in graphene oxide (GO) were also examined using powder X-ray diffraction (XRD) analysis. XRD analysis employed Cu-K $\alpha$  radiation as the source, scanning over a  $2\theta$  range from  $5^\circ$  to  $100^\circ$ . The XRD equipment operated at 40 kV and 40 mA. The figure 3.7 presented depicts a typical XRD spectrum from the GO sample prepared for this research. Significant differences were observed when comparing the XRD patterns of graphite powder and GO. Graphite powder exhibited a sharp diffraction peak at  $2\theta = 26.7^\circ$ ,<sup>37</sup>

corresponding to an interlayer spacing of 0.33 nm. In contrast, GO showed a peak around  $2\theta$  18.59°, indicating an expanded interlayer spacing of 0.83 nm. This increased spacing in GO results from the introduction of oxygen functional groups during its synthesis, where graphite undergoes oxidation to form GO. Additionally, the absence of a peak in  $2\theta = 25\sim 30^\circ$  range suggests the complete conversion of graphite into graphene oxide.<sup>19</sup>

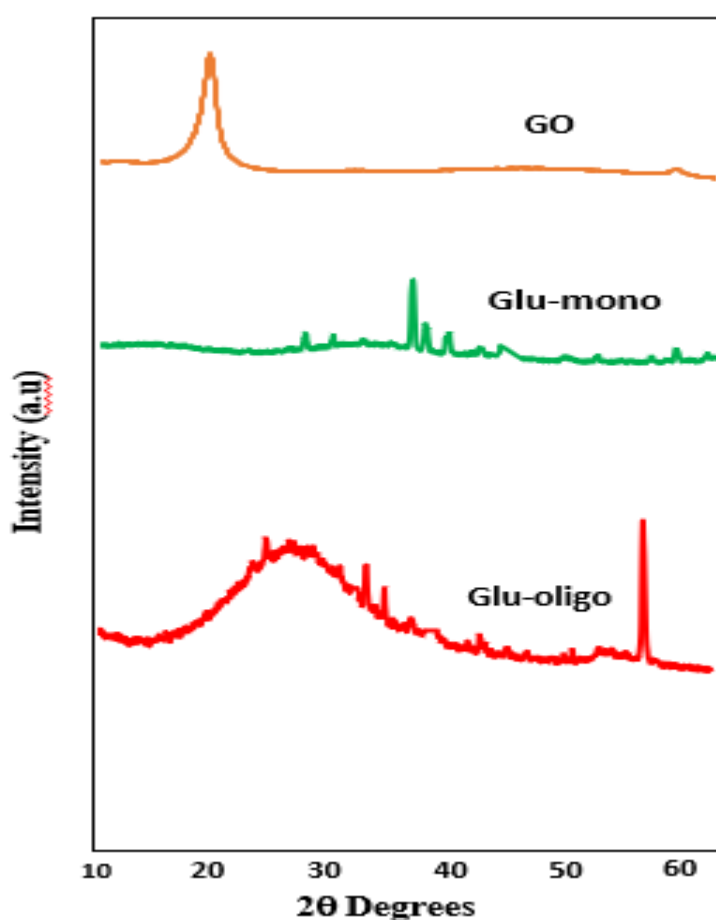


Figure 3.7: Illustrates XRD patterns showing the functionalization of GO-Glu (Mono) and GO-Glu (Oligo), displaying the d-spacing.

## Chemical Functionalisation of GO:

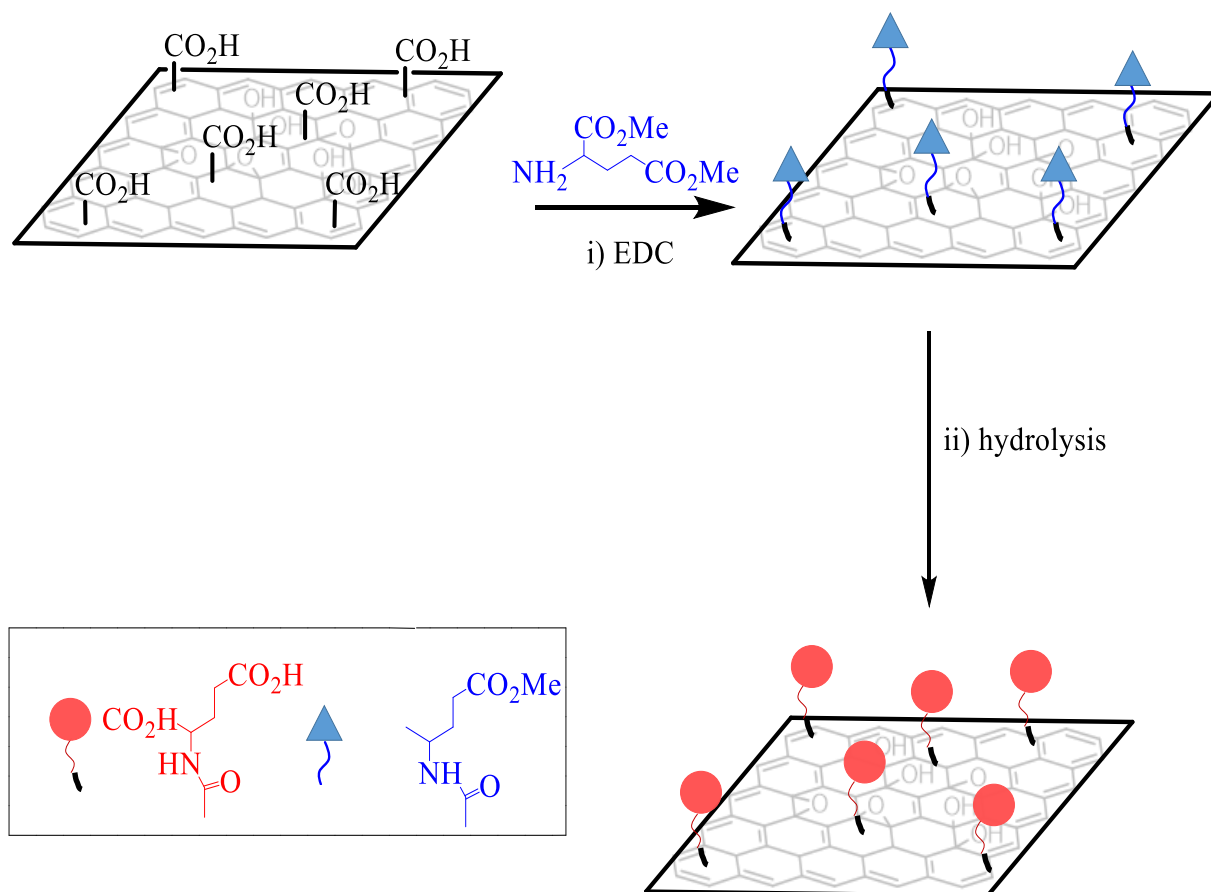
The aim of this study was focused on studying functionalized graphene oxides. This was achieved by reacting graphene oxide (GO) with a layer of diverse amino acids. As previously highlighted, it was critical to verify the well-defined structural properties of the synthesized materials and ensure the successful attachment of amino acids onto GO. In addition, it would be critical that the amino loadings of the various graphene oxide systems were similar, which would allow us to make meaningful comparisons. This would be achieved through various characterization techniques to assess the chemical composition, morphology, and functional groups present on the modified GO surface. Confirmation of successful functionalization was pivotal to understanding how these modifications influence the properties and potential applications of GO-based materials.

## Synthesis of graphene oxide functionalized with monomeric glutamic acid:

The initial goal was to create a monomeric glutamic acid system, which would double the carboxylic acid groups on the surface. These groups can alter their charge states based on the solution's pH, shifting between neutral ( $\text{COOH}$ ) and negatively charged ( $\text{COO}^-$ ) forms as the carboxyl group either protonates or deprotonates. This pH-dependent behaviour results in varying charge densities within the molecule. Furthermore, the presence of two carboxylic acid groups in the glutamic acid system enhances the dominant charge-charge interactions and increase the binding affinity. To achieve the desired functionalization, we added a single layer of diester-protected glutamic acid to the graphene oxide (GO) material. The functionalized GO was then dispersed in water, and the ester groups were hydrolyzed using potassium hydroxide at room temperature under constant stirring. After sufficient reaction time, the product was

washed and filtered to remove excess reagents, resulting in the targeted GO-Glu mono system, as illustrated in scheme 3.5.

The reaction conditions, including the NaOH concentration (e.g., 1 M) and the reaction duration 2–4 hours, were carefully controlled to ensure complete hydrolysis of the ester groups. The C=O peak for the diester-protected system appeared between approximately  $1600\text{ cm}^{-1}$  and  $1750\text{ cm}^{-1}$  in the FTIR spectrum, corresponding to the carbonyl groups of the esters. Initially, no peaks corresponding to the OH stretching of carboxylic acids in either GO or glutamic acid were observed between  $3000\text{ cm}^{-1}$  and  $3500\text{ cm}^{-1}$ . However, after deprotection, the OH peak became visible in this region, and the carbonyl peak simplified, no longer extending into the ester region ( $1750\text{ cm}^{-1}$ ), confirming the successful removal of ester groups. In terms of yield, the mass of the recovered GO-Glu mono system was greater than the initial mass of GO used, indicating successful attachment of the glutamic acid molecules. The overall yield was calculated to be 96.7% (based on experimental data), reflecting both the efficiency of the functionalization process and the amount of glutamic acid added. Further purification ensured that unreacted glutamic acid was removed, and the final product's purity was confirmed by FTIR analysis. These results confirm the successful addition of the protected glutamic acid and its subsequent hydrolysis to remove the ester protecting groups.<sup>25</sup>



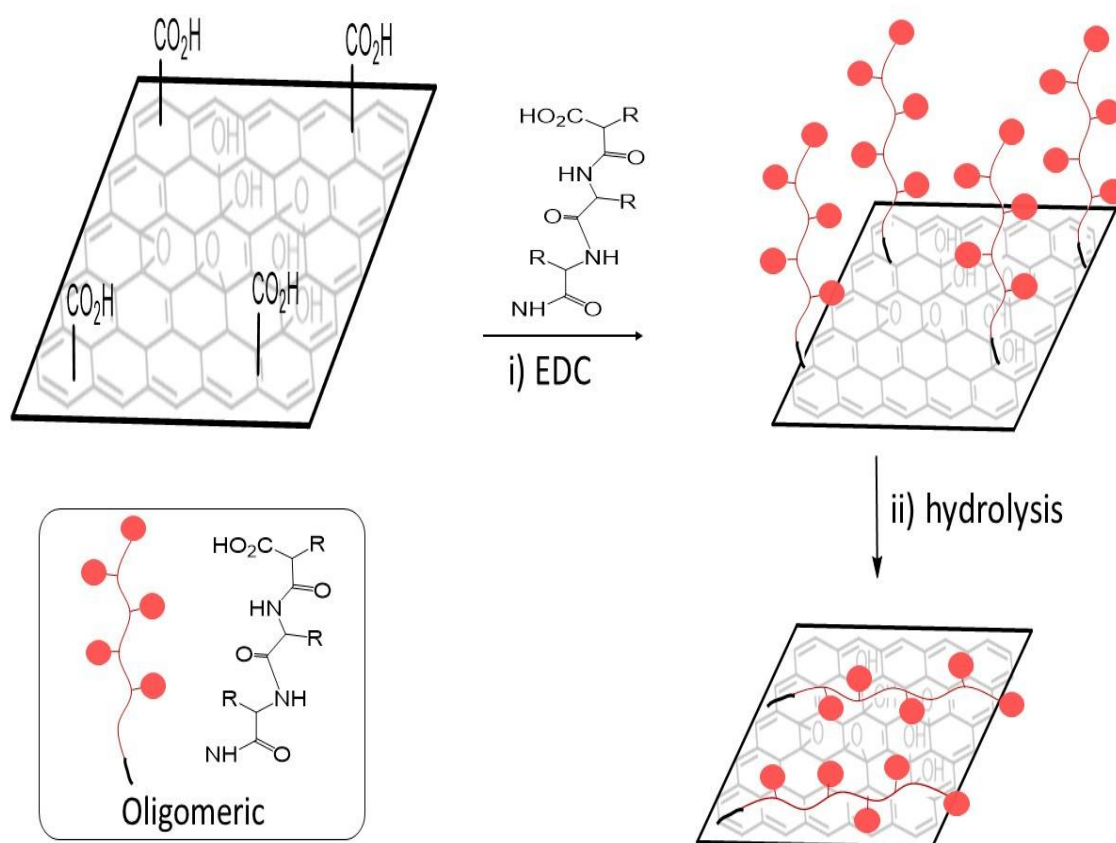
Scheme 3.5: Synthesis of a monomeric functionalized GO using a diester-protected glutamic acid. The functionalized graphene oxide (GO) material was then dispersed in water, and the ester groups removed using sodium hydroxide to create the required GO-Glu monomeric system.

## Synthesis of Graphene Oxide Functionalized with Oligomeric and Monomeric Glutamic Acid:

Graphene oxide (GO) has been widely studied as a potential ligand for protein binding. The carboxyl (-COOH) and hydroxyl (-OH) functional groups present on graphene oxide (GO) facilitate the binding of proteins via a range of interactions, including hydrogen bonding, hydrophobic effects, and electrostatic forces. These functional groups act as binding sites for complementary regions on the protein's surface, enabling their attachment to the GO surface.<sup>28,29</sup> Glutamic acid, an amino acid has two carboxylic acid groups, when added to GO, an increase the number of available carboxylate groups occurs. This, in turn, enhances the potential for ionic interactions with proteins.<sup>30</sup> Nevertheless, if added directly, the amine units of free or bound glutamic acid can react with the carboxylate groups of other glutamic acids (free in solution or attached to the GO surface), and a surface containing a glutamic acid oligomer is formed. One strategy to mitigate this issue involves protecting the carboxylic acid groups of glutamic acid before its attachment to GO. This protection entails temporarily adding a protective group to the carboxylic acid functionalities. Once glutamic acid is bound to GO, these protective groups can be removed, or deprotected, to expose the carboxylic acid groups again, possibly improving the binding to the protein. In order to synthesise a monomeric glutamic acid surface, we must use a diester protected glutamic acid. Once the protected glutamic acid is bound to GO, the protecting groups can be removed.<sup>17</sup>

The oligomeric functionalized GO was easier to prepare and could be synthesized in a single reaction. To produce an oligomeric functionalized GO, non-protected glutamic acid (-NH<sub>2</sub> and CO<sub>2</sub>H) was employed. The aim was to react the amine groups with the carboxylic acid groups on GO, followed by subsequent reaction with the new carboxylic acid groups of additional unprotected glutamic acid(s). The mass of the final product (0.29

g) shows a substantial increase compared to the initial mass of GO (0.25 g). This increase in mass confirms the successful addition of a significant amount of L-glutamic acid to the GO surface. The large increase in mass is consistent with the incorporation of multiple glutamic acid molecules, as indicated by the high yield. This substantial mass gain reflects effective functionalization and the attachment of a considerable number of glutamic acid units, demonstrating the success of the chemical modification.



Scheme 3.6: Formation of an oligomeric layer on the surface of GO and probable surface binding of GO.



FT-IR spectroscopy was utilized initially for qualitative rather than quantitative purposes, specifically to verify the successful introduction of amino acids onto the surface of graphene oxide (GO). This method confirms the existence of particular functional groups, serving as a qualitative assessment. Nevertheless, it does not quantify the exact concentration or amount of the introduced amino acids, which would require a quantitative analysis.<sup>26</sup>

The FT-IR spectra revealed vibrational stretching frequencies for the –OH and –NH functional groups within the range of 3210-3550  $\text{cm}^{-1}$ . Additionally, a peak observed in the 2300-2950  $\text{cm}^{-1}$  region corresponds to the vibrational modes of the C=O hydrophobic portion of glutamic acid, which is incorporated into the functionalized graphene oxide (GO) structure.

Elemental analysis using SEM-EDX was performed to assess the compound's composition. Due to the varied surface and bulk chemical compositions, and the fact that SEM-EDX only probes the top layer of the sample, the results were expected to show some variation. However, the data obtained were insufficient for full characterization. Despite this limitation, the comparisons between methodologies remained consistent. The detection of nitrogen in the analysis suggests that it originates from the amino acid, confirming the successful incorporation of glutamic acid into the functionalized GO.

The XRD pattern (figure 3.7 above) of the reactant L-glu indicated high crystallinity, with a diffraction peak at around 16-18° suggesting a layered structure in GO. In the L-Glu/GO pattern, the peak for GO was no longer visible, and new peaks appeared at 28.4°, 40.6°, and 45.2° for  $2\theta$ , differing from those of the starting glutamic acid material. These findings confirm the success of the reaction.<sup>26</sup>

## Characterization of the Monomeric and Oligomeric GO Systems:

The relative flexibility of oligomeric and monomeric GO-Glu structures on the GO surface was extensively studied. It was important to analyze their elemental composition and amine concentration to assess their impact on protein binding. The carbon content increased from 51% for GO to 61% for the monomeric and oligomeric systems, respectively, in line with the anticipated enhancement in carbon content. But, SEM-EDX analysis revealed that the carbon content increased from approximately 40% in GO to 45% and 48% in the monomeric and oligomeric systems, correspondingly, when comparing with glutamic acid. This rise in carbon content is expected because the addition of glutamic acid introduces more carbon relative to oxygen and nitrogen. Therefore, it is anticipated that the oligomeric system would exhibit a higher carbon content compared to the monomeric system, which in turn has more carbon than unfunctionalized GO. This relationship between carbon concentration and functionalization level aligns with previous studies.<sup>17</sup>

In the context of protein binding, assessing the surface density of amino acids is crucial, especially when conducting comparative analyses between different samples. It is imperative that these samples possess comparable amino acid densities to ensure valid comparisons. SEM-DEX is a surface technique and is an exceptionally valuable method for approximating amino acid density on surfaces, which can be estimated from the relative elemental distributions. Consequently, the carbon-to nitrogen ratio serves as a reliable metric for estimating the relative density of amino acids. A reduce of ratio indicates a higher proportion of nitrogen compared to carbon. SEM-EDX mapping indicated the presence of carbon and oxygen on the GO surface, with nitrogen also visible in images of both monomeric and oligomeric samples. Furthermore, SEM-EDX analysis provided the carbon-to-nitrogen ratios for the monomer and oligomer, detailed in table 3.1.

SEM-EDX				
Compound	C (mass %)	N (mass %)	O (mass%)	C/N
GO	5	0	4	-
GO-Glutamic (Mono)	51	15	27	3.4
GO-Glutamic (Oligo)	61	13	26	4.7

Table 3.1: SEM-EDX data for glutamic acid (oligo/mono) functionalized graphene oxide.

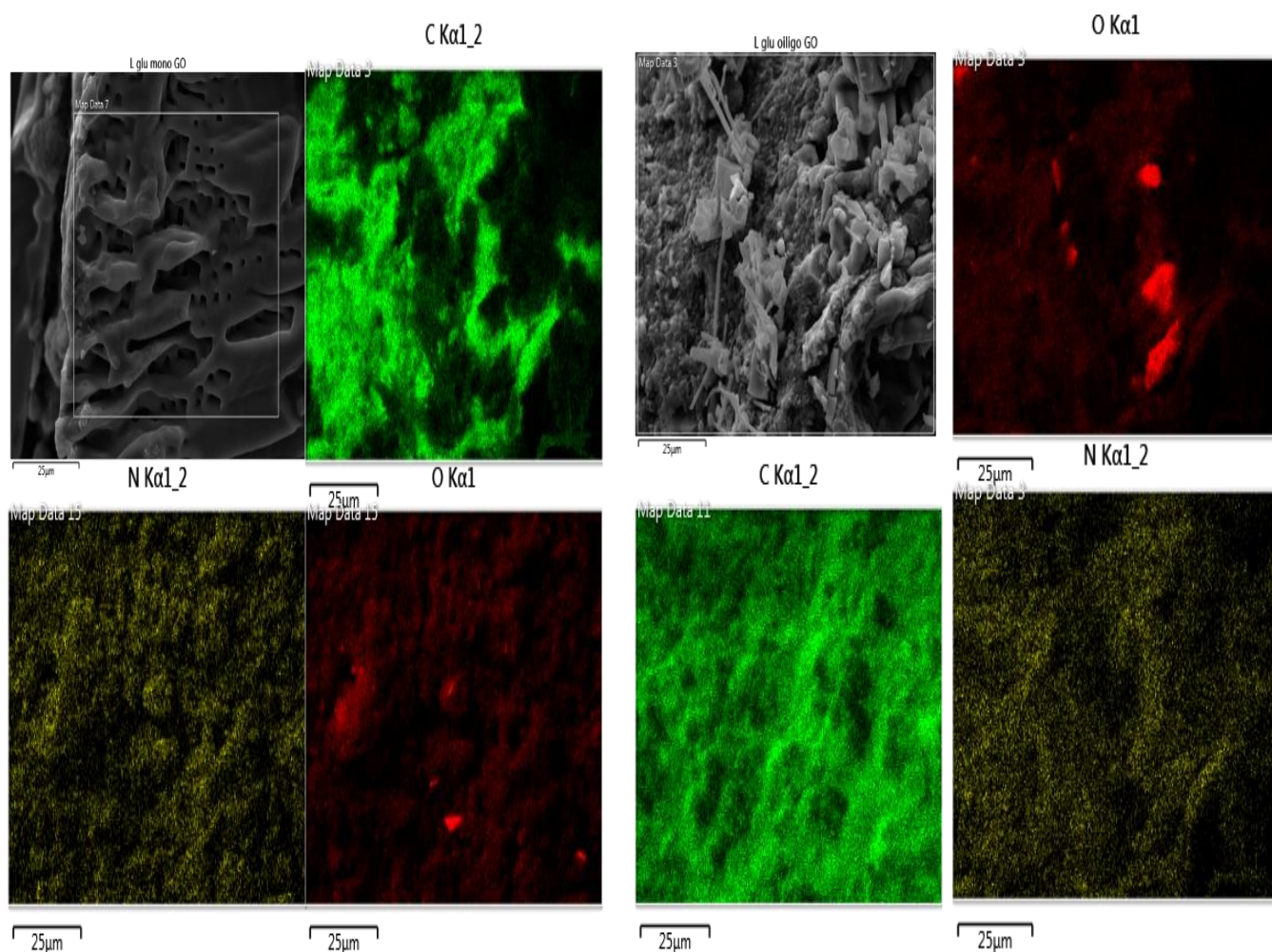


Figure 3.8: SEM-EDX element mapping of GO-Glu a) Mono and (b) Oligo of all elementals (25  $\mu\text{m}$  is the scale bar).

X-ray photoelectron spectroscopy (XPS) was used to analyze surface materials and identify functional groups, as well as determine alterations in the carbon-to-heteroatoms (N and O) ratio resulting from functionalization. This technique delivers precise data regarding the elemental composition and chemical states present on the surface. XPS primarily investigates the top few nanometers of a sample, which restricts its ability to provide insights into the bulk composition.

Moreover, it may not be suitable for extremely thin or highly insulating materials. However, this is not a problem, as we are only interested in the GO surface, which is the only part of the sample that interacts with the proteins.

Based on the XPS data (Figure 3.9 below), the Glu oligomer exhibited prominent peaks in its C 1s spectra at 284.5 and 286.5 eV, corresponding to electron emission from C–C and C–O bonds, respectively. Additional peaks were observed at 532.38 eV (electrons from C=O bonds), 531.28 eV (electrons from C–O bonds), and 399 eV (electrons from C–N bonds), indicating the presence of these functional groups.

Deconvolution of the N 1s and O 1s spectra revealed distinct signals such as C–N–C, N–H, and O–H. The intensity of these peaks indicated that the amine peak ratio in the oligomer was 1:0.33, whereas in the monomeric system this ratio was 1:1.35. This suggests a higher proportion of amide linkages in the monomeric structure. This discrepancy can be attributed to differences in the synthetic processes employed.

In both the oligomeric and monomeric production methods, the N-terminus of the amino acid reacts with carboxylate groups on the surface, forming amide bonds. In the oligomeric approach using unprotected Glu, the N-terminus can also react with the C-terminus of another amino acid or a growing oligomer chain, contributing to further amide bond formation.

The oligomeric system demonstrates greater uniformity compared to the monomeric system. In the oligomeric approach, additional amide bonds are formed. This enhanced uniformity contributes to a more pronounced amide peak in the analysis. Conversely, the monomeric system lacks this level of uniformity, leading to a less distinct amide peak in the spectral analysis.<sup>23</sup>

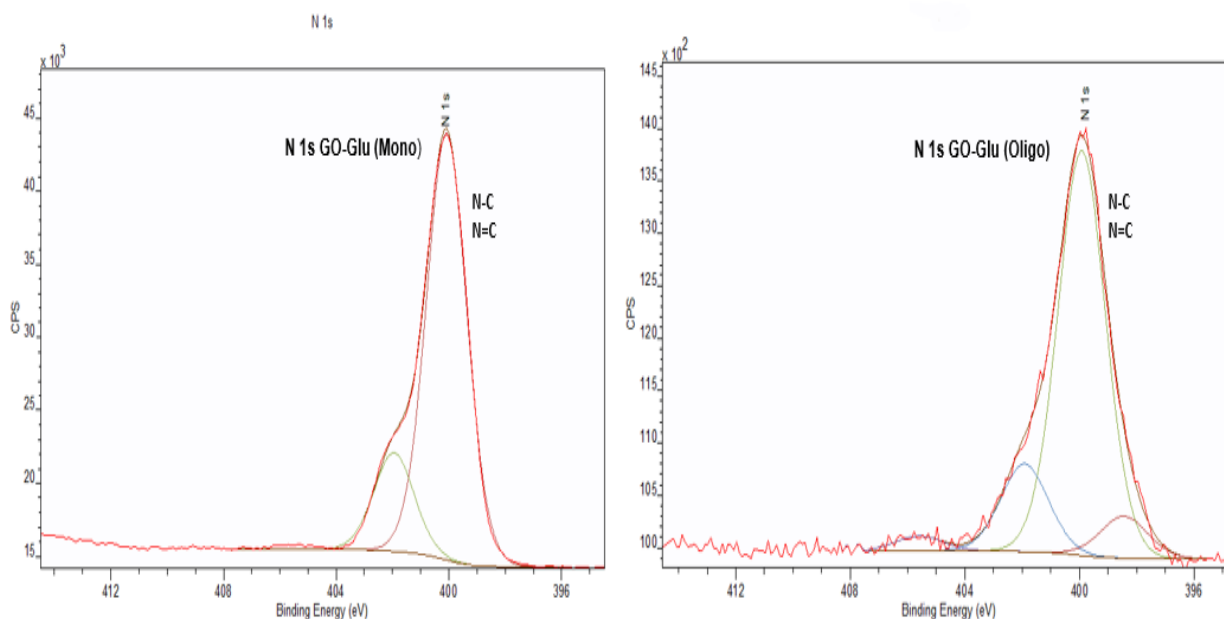


Figure 3.9: An illustration of functionalisation, presenting the deconvoluted XPS spectra of the N 1s of (b) GO–Glu (Mono) and (c) GO–Glu (Oligo).

XRD analysis additionally affords insights into functionalization through changes in d-spacing. Following functionalization, the distance between GO layers is expected to increase as amino acids occupy more surface space. Specifically, the oligomeric system is anticipated to exhibit the largest spacing due to addition of more amino acids on the GO surface and between the layers, as shown in figure 3.7. The XRD spectrum displayed broad diffraction peaks around  $2\theta = 26^\circ$ , indicating structural modifications to the GO material. The broadening of the peaks may suggest increased disorder or exfoliation in the GO layers, possibly due to the incorporation of glutamic acid. Furthermore, a noticeable shift in the peak from  $10^\circ$  to  $8.8^\circ$ , was observed post-functionalization, which could be attributed to an increased interlayer spacing, likely due to the attachment of carboxylic groups from glutamic acid. Moreover, a significant difference was noted between the monomeric and oligomeric approaches in terms of layer thickness produced (0.86 nm for

monomeric and 1.0 nm for oligomeric). Hence, the successful functionalization of GO samples using monomeric and oligomeric amino acids is confirmed.<sup>24</sup>

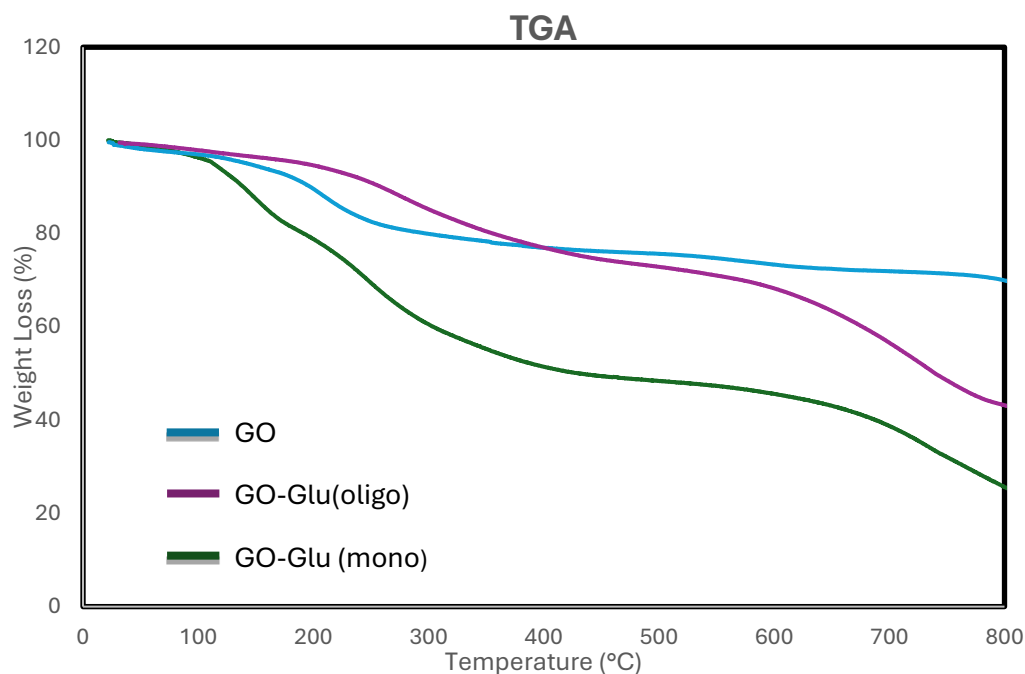


Figure 3.10: TGA of GO-Glu (Mono) and GO-Glu (Oligo) revealed different decomposition behaviors.

The thermogravimetric analysis (TGA) results of Graphene Oxide (GO) and its glutamic acid-stabilized variants exhibit distinct degradation patterns, which provide insights into the thermal stability and structural changes induced by functionalization. For the GO sample (represented by the blue curve), an initial weight loss between 100 °C and 200 °C is observed, corresponding to the loss of adsorbed water and labile oxygen-containing functional groups. This is typical for GO, where moisture and weakly bound functional groups are released at lower temperatures. A second, more significant degradation occurs between 200 °C and 400 °C, attributed to the decomposition of more stable oxygen-containing groups, such as carboxyl and epoxy groups, which are integral to the GO structure.

The GO sample stabilized with mono-glutamic acid demonstrates slightly better thermal stability compared to the unmodified GO. While the initial weight loss profile is similar, the degradation process is more gradual and extends over a broader temperature range. This extended thermal degradation, occurring between approximately 250°C and 500°C, is likely due to the decomposition of the organic mono-glutamic acid attached to the GO surface. The presence of glutamic acid adds thermal resilience by modifying the surface chemistry of the GO, thus altering its decomposition profile.

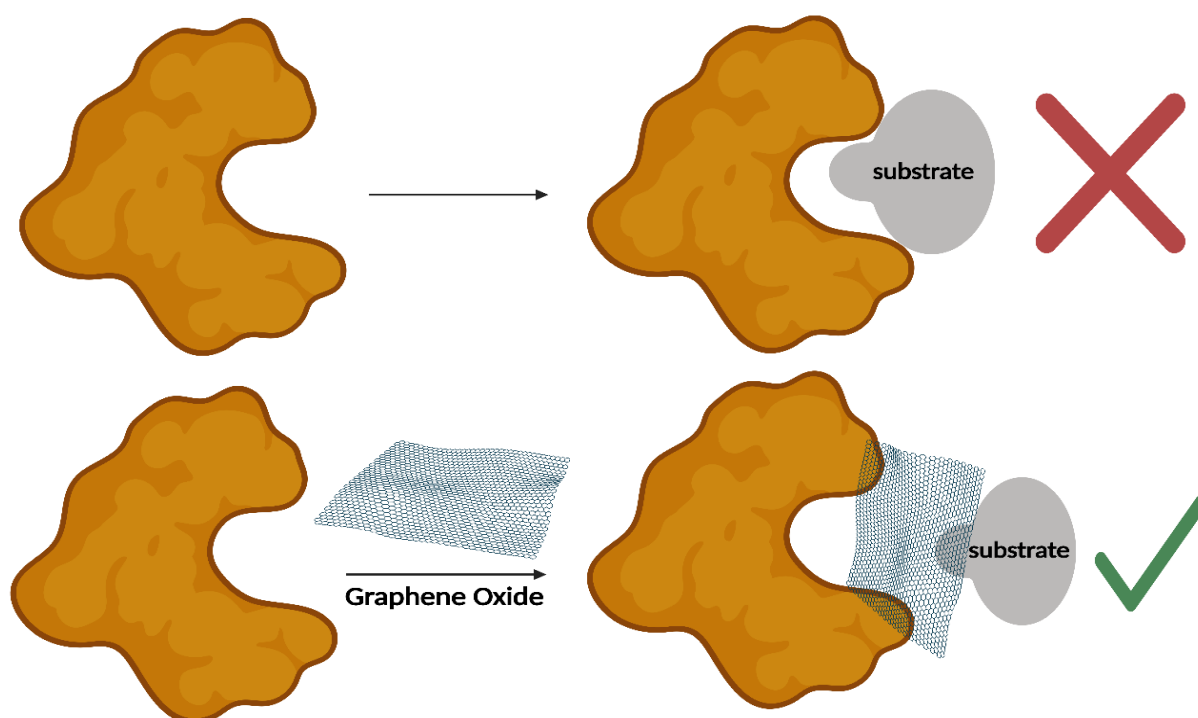
The GO sample stabilized with oligo-glutamic acid shows the highest thermal stability among the three samples. The TGA curve reveals a more gradual and slower weight loss, with a broad degradation profile occurring between 300°C and 600°C. This indicates that oligo-glutamic acid provides more extensive surface coverage and stronger interactions with the GO, resulting in enhanced thermal resistance. The increased molecular weight and multiple functional groups of the oligo-glutamic acid likely contribute to its ability to stabilize GO more effectively than the mono-glutamic acid. The stronger binding between GO and oligo-glutamic acid, coupled with its higher molecular mass, leads to a more robust thermal stability profile.

Overall, these results align with theoretical expectations, where the functionalization of GO with glutamic acid enhances its thermal stability. The oligo-glutamic acid, due to its greater molecular weight and increased binding capacity, provides the highest thermal resistance, while mono-glutamic acid offers moderate stabilization compared to unmodified GO. This trend highlights the effectiveness of surface functionalization in improving the thermal properties of GO, which is valuable for applications requiring enhanced material stability at elevated temperatures.



## Assay to measure relative binding between GO and glutamic acid functionalized GO systems using $\alpha$ -chymotrypsin:

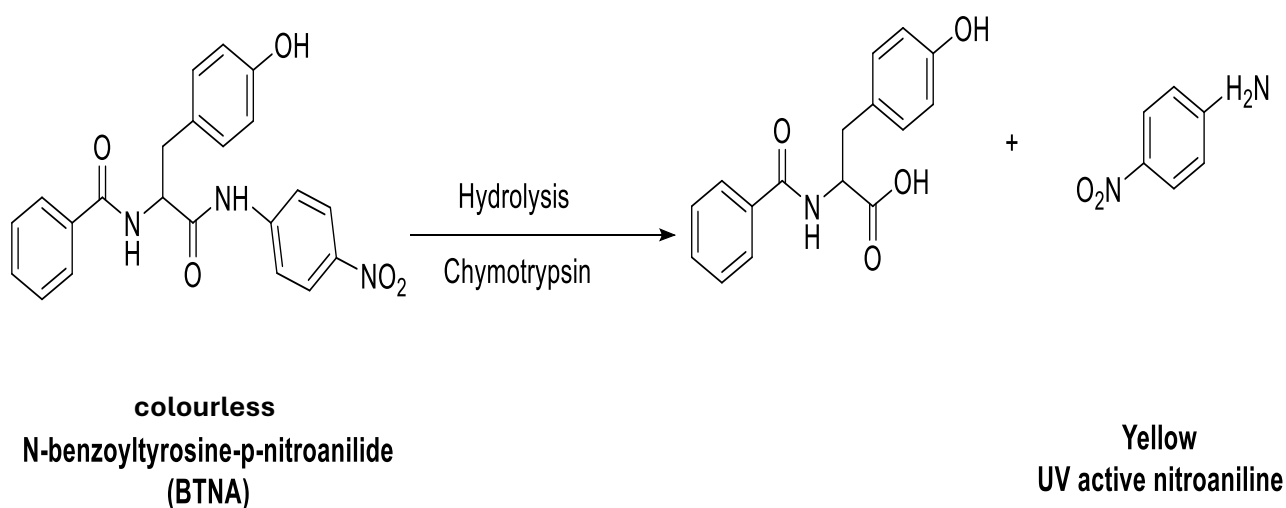
As outlined above, using non-protected glutamic acid generates an oligomeric, and is a simpler method can also offer the significant advantage of introducing additional carboxylates. Various protocols exist to measure binding between proteins and macromolecular ligands. For our experiments, we propose employing an enzyme inhibition assay to assess relative binding (scheme 3.7). This method has proven effective in comparing the binding abilities of related systems in previous studies. While direct binding affinities cannot be determined, the extent of inhibition directly correlates with the level of binding. Enzyme activity is directly influenced by the accessibility of the substrate to the enzyme's active site. If graphene oxide (GO) binds to the enzyme, it can obstruct the substrate's access to this critical region, thereby slowing down the catalytic reaction. The degree to which the reaction rate decreases is proportional to the binding affinity of the GO to the enzyme. In other words, stronger binding by the GO leads to a greater reduction in the reaction rate, serving as an indicator of the GO's binding capacity.<sup>31</sup>



Scheme 3.7: In the surface-bound inhibitor assay, the depiction on the left side of the image illustrates the enzyme's active site, where substrates can freely ingress and engage in catalytic reactions. Conversely, on the right side, a surface-binding inhibitor is introduced, which effectively hinders substrate access to the active site. This obstruction leads to the inhibition of catalysis, clearly demonstrating the inhibitory action of the inhibitor in this experimental setup.

Enzymes are biological catalysts that accelerate chemical reactions, often with high specificity. For instance, some enzymes hydrolyse amides, breaking down these bonds by adding water molecules. When the enzyme's active site is accessible, it efficiently catalyses this reaction. However, if graphene oxide (GO) binds to the enzyme, it can block the substrate's access to the active site, reducing the reaction rate. This decrease in rate is proportional to how well the GO binds to the enzyme, with stronger binding leading to a more significant slowdown.

The reaction, in the scheme 3.8, involves the enzymatic hydrolysis of a substrate N-benzoyl-L-tyrosine p-nitroanilide (BTNA), producing a yellow by-product, p-nitroaniline, which can be monitored using UV-Vis spectroscopy. Rate data can be obtained from concentration vs. time plots, with initial rates calculated from linear portions generated in the early part of these plots. The concentration of p-nitroaniline can be determined using its extinction coefficient ( $15960 \text{ M}^{-1}$  at 400 nm), which was derived using a Beer-Lambert analysis.<sup>32</sup>



Scheme 3.8: Illustrates an experiment where the enzyme  $\alpha$ -chymotrypsin hydrolysis the substrate N-benzoyl tyrosine p-nitroanilide (BTNA). This experiment is designed to investigate enzymatic reactions and their importance in biological practices.

In our initial experiment, a control reaction was conducted using just  $\alpha$ -chymotrypsin and the BTNA substrate, in phosphate buffer (pH 7.46, 0.01 M). The solution contained 0.56 mM BTNA and 1 mM  $\alpha$ -chymotrypsin. Data was collected at 30-second intervals over a 300-second period to determine the initial rate, which can be used as the control when estimating and

comparing relative binding abilities.<sup>32</sup> This  $\alpha$ -chymotrypsin control represents complete enzymatic activity without inhibition, resulting in 0% inhibition/binding. The plot is shown below in figure 3.11, and it was used to calculate an initial rate of  $1.8 \times 10^{-7} \text{ M sec}^{-1}$ .

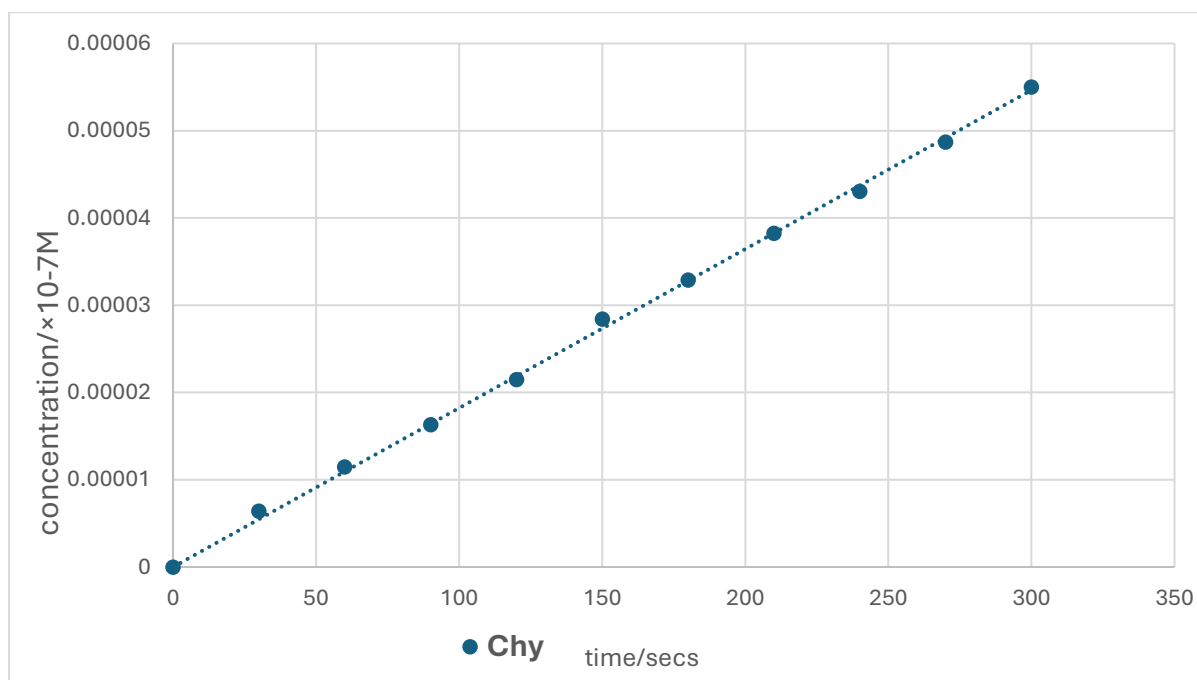


Figure 3.11: Rate plot depicting the enzymatic activity in just chymotrypsin over 300 seconds. an initial rate of  $1.8 \times 10^{-7} \text{ M sec}^{-1}$ .

Subsequently, after conducting the control experiments, we proceeded to investigate the binding capabilities of GO, GO-Glu-mono, and GO-Glu-oligo. These experiments followed the identical procedure as the control, with the addition of GO inhibitors at a concentration of  $25 \mu\text{g/mL}$ . The absorption results are shown below in table 3.2, along with the relative rates relative binding data in table 3.3. The initial rate plots are shown in figure 3.11.

Both table 3.2 and figure 3.12 present the initial rate plots and rate data with all values compared to chymotrypsin (Chy). The differentiation in reaction extent between Chy alone and in the presence of an inhibitor is highlighted. The data in table 3.3 clearly demonstrates that both GO-Glu mono and GO-Glu oligo have stronger inhibitory effects than GO by itself. This increased inhibition is due to the higher concentration of carboxylic acids in GO-Glu mono and GO-Glu oligo, which enhances the potential for negative charges. As a result, the binding affinity is improved, leading to higher inhibition levels. For example, at the specified concentrations, GO-Glu mono can bind up to 50% of the protein, while GO-Glu oligo can bind more than 60%. These significant inhibition levels underscore the greatly enhanced binding capabilities of the functionalized GO systems compared to GO alone, which can only bind 20% of the protein.

[sec]	Chy	GO	GO-Glu mono	GO-Glu oligo
0	0.00	0.00	0.00	0.00
30	6.43	4.12	3.95	1.99
60	11.52	8.27	6.86	4.64
90	16.36	12.57	9.27	6.70
120	21.55	16.94	12.57	7.82
150	28.52	21.38	14.83	10.16
180	33.02	25.79	17.36	12.35
210	38.38	30.28	19.91	13.83
240	43.23	34.96	21.81	16.87
270	48.88	39.82	23.76	19.25
300	55.23	45.40	26.31	20.43

Table 3.2: Details showing the para-nitroaniline absorption data versus time for the GO and glutamic acid functionalized GO systems.

0.56 mM BTNA, 1mM Chy and 25 mg/mL inhibitor			
Experiment	Initial rate- $\times 10^{-7}$ M	Extent of reaction-%	Relative binding-%
Chy	1.8	100	0
GO	1.51	84	16
GO-Glu-mono	0.87	48	52
GO-Glu-oligo	0.68	38	62

Table 3.3: Shows the data that relative binding correlates directly with the inhibition percentage. This percentage is calculated simply by the extent of reaction of chy % minus the extent of reaction of inhibition.

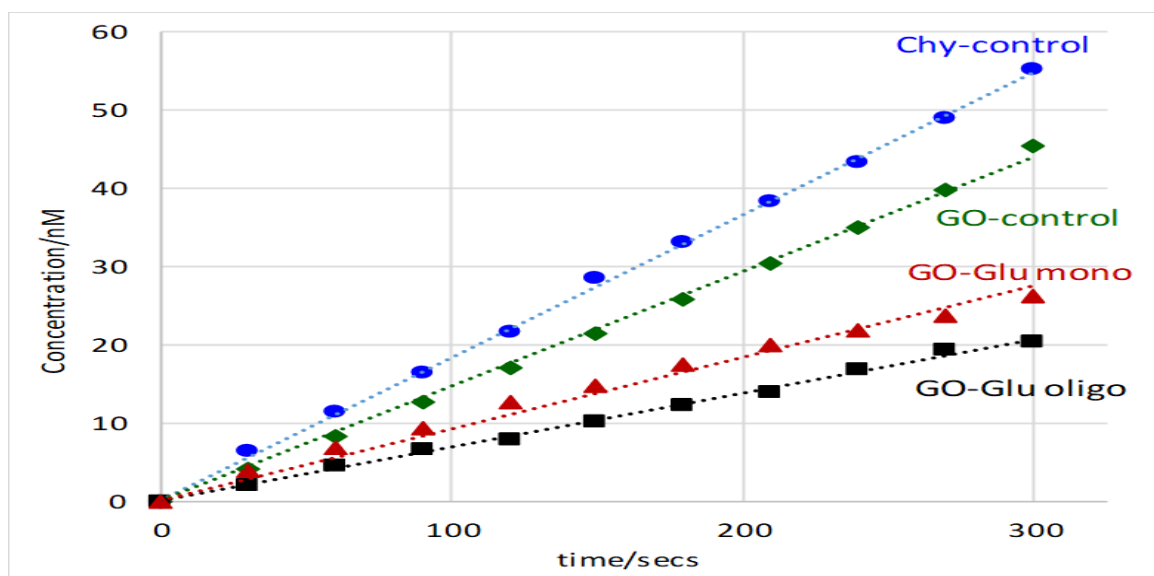


Figure 3.12: Rate plot depicting the enzymatic activity in the control sample, along with the inhibitory effects observed in samples containing GO, GO-Glu mono, and GO-Glu oligo. The plot illustrates the initial rates of reaction for each sample, highlighting the differences in inhibition levels due to the presence of GO and its functionalized variants.

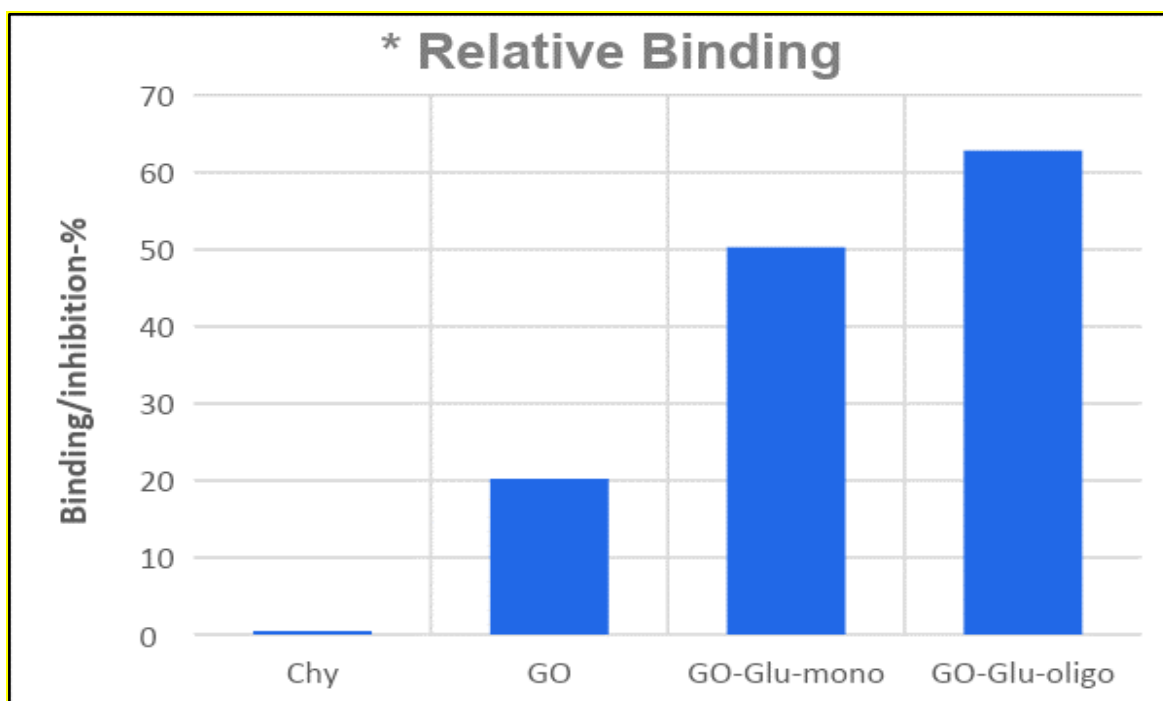


Figure 3.13: Effectively shows the relationship between relative binding and inhibition percentage for different graphene oxide systems, demonstrating that increased functionalization leads to improved performance. The bar chart provides a clear visual representation of how mono-functionalized and oligo-functionalized graphene oxide systems outperform unmodified graphene oxide, both in terms of binding capacity and inhibition effectiveness.

The data clearly shows that GO-Glu oligo had the highest inhibition rates, demonstrating a stronger binding affinity. Initial rates for all experiments were calculated at pH 7.46, and the fits were excellent, with R2 values exceeding 0.98. The data confirms that functionalized GO systems are more effective inhibitors than GO alone. Since inhibition is linked to binding, we



can infer that functionalized GO systems have a stronger attachment to the protein surface than unfunctionalized GO, leading to increased inhibition. GO-Glu oligo emerged as the most effective inhibitor, outperforming both the monomeric system and GO alone, with nearly four times better binding than GO alone. This is due to the fact that the monomeric glutamic acid system (GO-Glu mono) improves upon GO by significantly increasing the number of carboxyl groups (COOH), which enhances the binding affinity to target proteins. Each glutamic acid unit introduces additional COOH groups, doubling their number compared to GO alone. However, the oligomeric glutamic acid system (GO-Glu oligo) is even more effective because, although the addition of each glutamic acid unit does not double the COOH groups, it substantially increases their total number. This results in a much higher density of binding sites, leading to stronger and more effective interactions with the protein surface. The data clearly show that GO-Glu oligo has the highest inhibition rates and nearly four times better binding than GO alone, demonstrating its superior binding affinity and effectiveness as an inhibitor. In conclusion, the results confirm that a GO surface coated with an oligomeric layer of glutamic acid is the most effective at inhibiting chymotrypsin activity.

### Exploring selectivity by functionalizing GO with various amino acids:

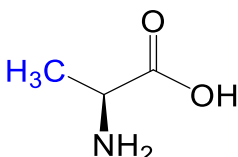
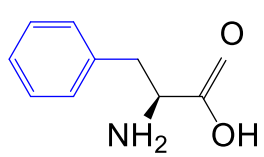
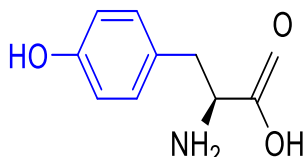
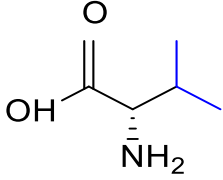
Having demonstrated that an increase in the number of CO<sub>2</sub>H groups results in increased binding affinity, we also wanted to test whether or not the functional groups on a range of various amino acids could influence binding affinity, particularly with respect to selectivity. Protein binding selectivity is determined by a number of factors, including the shape of the binding surface and the type and functionality present on the amino acids. In earlier experiments, we observed that GO Glu-oligo exhibited a very strong binding affinity for chymotrypsin, with over 60% of the enzyme bound at the concentrations used. This strong

binding was primarily due to the increase in electrostatic interactions. However, strong electrostatic binding alone does not guarantee selectivity when it comes to binding other proteins. To discover this, we simulated a protein's binding surface by incorporating various amino acids, each presenting different functional groups. To investigate this protein-mimicking approach, we chose a range of amino acids with different functional groups, as displayed in scheme 3.9. Tyrosine was selected for its aromatic group, which can facilitate additional  $\pi$ - $\pi$  interactions, and its phenolic OH group, which, after deprotonation to phenolate, can introduce an extra negative charge and support secondary hydrogen bonding. These features suggest that tyrosine might exhibit significant binding. We also included phenylalanine in our study, which is similar to tyrosine but lacks the phenolic OH group. By comparing the binding of tyrosine and phenylalanine, we can determine the specific role of the OH group and its impact on binding affinity. Additionally, we examined the glutamic acid system, which, as previously reviewed, be capable of offering a second carboxylic acid group to enhance the binding method. Lastly, we considered valine, an amino acid that contains only hydrophobic groups. This lack of functionality may not be able to contribute much to binding and could even hinder and reduce binding affinities. Nevertheless, even small contributions to binding affinity, could contribute to overall binding in a mixed amino acid system.

The goal at this stage is to evaluate relative binding in relation to single amino acids. If changes in binding are observed, it may be possible to introduce a degree of selectivity through functionalization and the use of mixed amino acid systems. We predicted that glutamic acid or tyrosine would display the strongest binding, as both possess functional groups that are likely to enhance this interaction. At this stage, we expected GO functionalized with glutamic acid to exhibit slightly better binding compared to the tyrosine derivative. Tyrosine should bind well, due to the number of different interactions possible, including electrostatic interactions from the CO<sub>2</sub>H and OH groups, p-p interactions between the aromatics, as well as additional

hydrogen bonding from the phenolic OH. Due to the absence of a phenolic OH group, we expected the phenylalanine system would have a noticeably lower binding affinity than the tyrosine-functionalized GO.

This order reflects the anticipated influence of each amino acid's functional groups on binding efficiency, with Glutamic Acid and Tyrosine having the most favorable interactions due to their additional functional groups, while Valine, lacking such groups, was expected to contribute the least to binding affinity.

Alanine	phenylalanine	Tyrosine	Valine
			

Scheme 3.9: Illustrates the proposed set of amino acids that are used for the functionalization of graphene oxide (GO), with the specific functional groups of each amino acid highlighted in blue. This scheme provides a clear visual representation of the chemical modifications aimed at improving the properties of GO by attaching functional amino acids to its surface, enhancing its selectivity.

## Assay to measure relative binding between amino acid functionalized GO and $\alpha$ -chymotrypsin:

The binding interactions were evaluated using the same inhibition assay previously outlined. This method was employed to measure how well each functionalized GO variant bound to the target protein. The results of these assessments are illustrated in the rate plots shown in figure 3.14. These plots provide a visual representation of the binding efficiency for each amino acid-functionalized GO system, allowing for a comparison of their relative affinities.

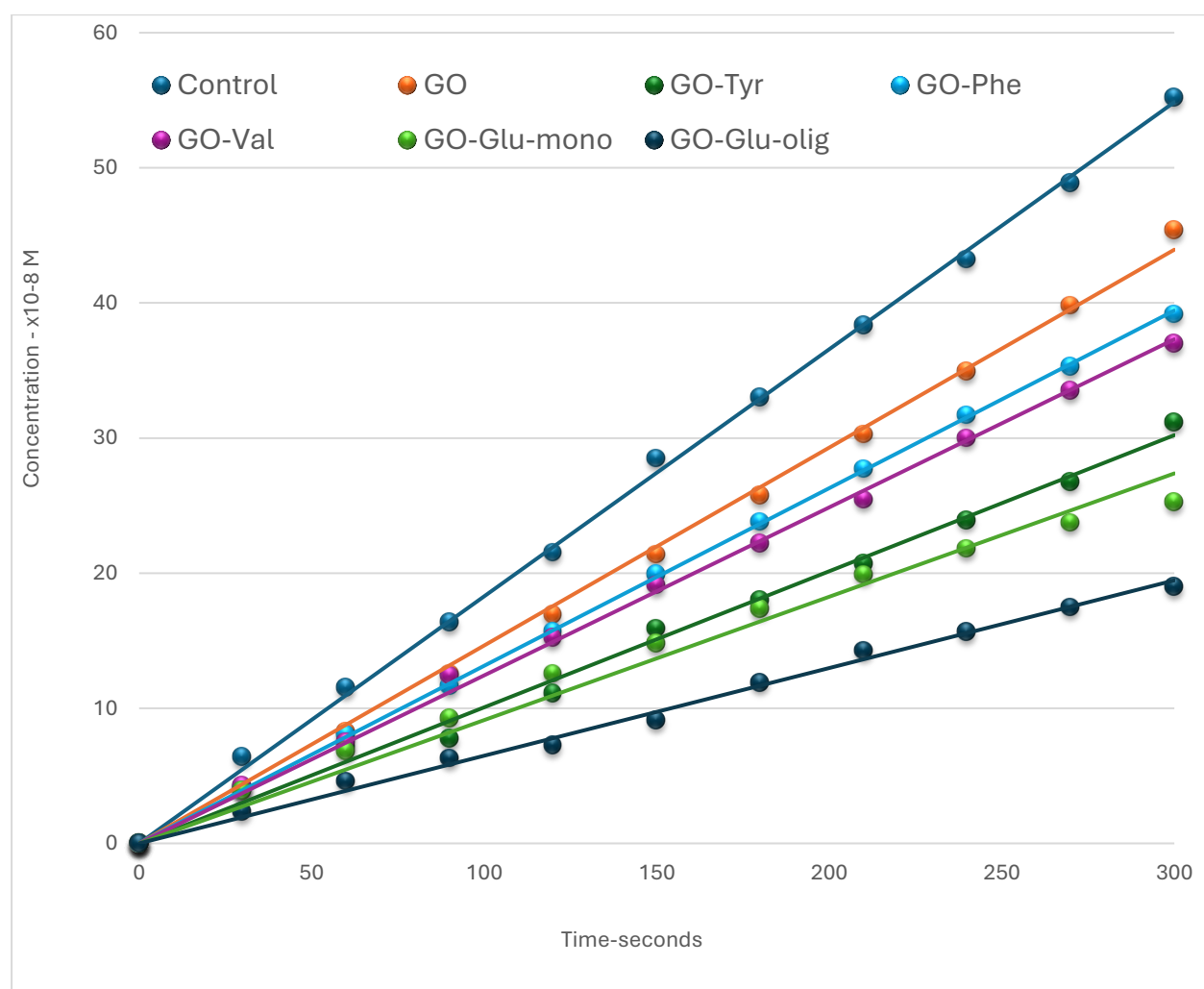


Figure 3.14: Initial rate plots (between concentration and time) for GO, the control, and the various chosen amino acids.

0.56 mM BTNA, 1mM Chy and 25 mg/mL inhibitor			
Experiment	Initial rate- $\times 10^{-7}$ M	Extent of reaction-%	Relative binding-%
Chy	1.8	100	0
GO	1.51	84	16
GO-phe	1.32	73	27
GO-Val	1.25	69	31
GO-Tyr	1.01	56	44
GO-Glu-mono	0.87	48	52
GO-Glu-oligo	0.68	38	62

Table 3.4: Shows the data that relative binding correlates directly with the inhibition percentage. This percentage is calculated simply by the extent of reaction of chy % minus the extent of reaction of Inhibition.

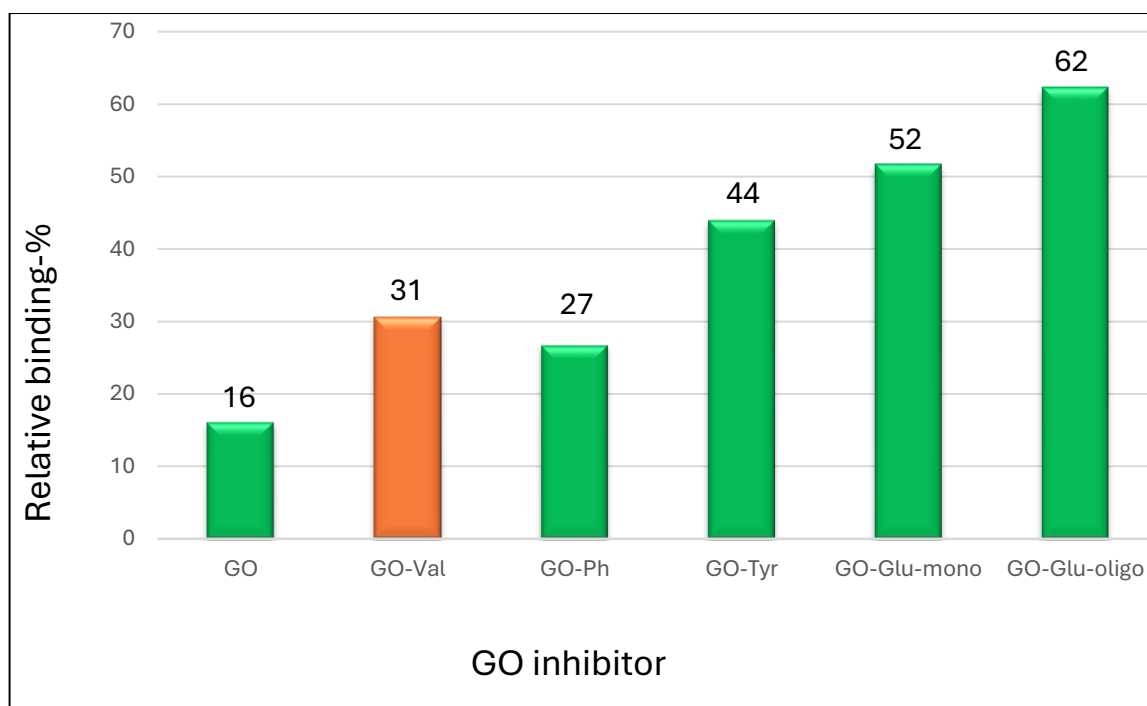


Figure 3.15: Graph showing relative binding between the amino acid functionalized GO and chymotrypsin. The results were consistent with expectations for most cases, except for Valine, which did not perform as anticipated.

The initial hypothesis of this study proposed that valine, due to its hydrophobic nature, would show weak interactions with graphene oxide (GO), as the chemical affinity between the hydrophobic valine and the largely hydrophilic GO surface was expected to be minimal. This assumption was based on the anticipated mismatch in the chemical properties of the two entities, which would likely lead to limited interaction. However, experimental results defied this expectation, revealing a stronger interaction between valine and GO than originally predicted. This unexpected result may be due to poor adsorption of valine onto the GO surface, which could be a consequence of its hydrophobicity hindering efficient interaction with the hydrophilic functional groups present on GO. Consequently, the low loading efficiency between valine and GO highlights the limitations imposed by valine's chemical nature.

Furthermore, SEM-EDX analysis provided additional insights into the nitrogen content of the two amino acids studied: glutamic acid and valine. Interestingly, glutamic acid exhibited a much higher nitrogen content than expected, with a ratio of 13, whereas valine showed a significantly lower nitrogen ratio of only 2, a stark contrast to the predicted ratio of 13 (as shown in table 1). This disparity further underscores the different binding capacities of the two amino acids when interacting with GO. Glutamic acid, with its carboxyl groups, was found to be a promising candidate for binding to GO, as its negatively charged carboxylate groups are well-suited to form electrostatic interactions with the positively charged regions of the GO surface. These electrostatic interactions contribute to the strong binding affinity between glutamic acid and GO, explaining its higher nitrogen content and greater overall attachment to the GO surface.

In contrast, phenylalanine (Phe), which contains an aromatic side chain, binds to GO through a different mechanism. The aromatic ring of Phe can interact with the graphene layers of GO via  $\pi$ - $\pi$  stacking interactions, where the delocalized electrons in the aromatic system of Phe align with those in the GO sheets. While this form of interaction provides additional binding capacity, it is generally weaker than the electrostatic interactions observed with glutamic acid. As a result, the overall binding affinity of Phe to GO is lower compared to glutamic acid. Moreover, oligomeric glutamic acid exhibits an even higher binding affinity than its monomeric counterpart. This increased affinity can be attributed to the presence of multiple carboxylate groups in the oligomeric form, allowing for a greater number of electrostatic interactions with the GO surface. This suggests that, in systems where multiple binding sites are available, the oligomeric form of glutamic acid offers enhanced stabilization and stronger interaction compared to individual monomeric amino acids. In summary, the binding properties of amino acids to GO depend heavily on their specific chemical structures and the functional groups they possess. Electrostatic interactions,  $\pi$ - $\pi$  stacking interactions, and the presence of

charged or polar groups are critical factors in determining the strength and effectiveness of these bindings. The study's findings reveal the nuanced ways in which amino acids, particularly glutamic acid and phenylalanine, interact with GO, offering insights into how their chemical properties influence their ability to stabilize and functionalize graphene-based materials.

## Conclusion:

The present study has underscored the significant potential of graphene oxide (GO) as a platform for binding proteins, a characteristic that holds immense promise for applications in disease treatment, particularly in addressing protein aggregation-related diseases such as Alzheimer's, diabetes, and thromboembolism. Graphene oxide's unique layered structure and abundance of oxygen-containing functional groups (e.g., hydroxyl, epoxy, and carboxyl groups) contribute to its capability to interact with proteins through various non-covalent interactions such as electrostatic forces, hydrogen bonding, and  $\pi$ - $\pi$  stacking. These intrinsic properties, combined with the ease of functionalizing its surface, provide a versatile approach to controlling its binding affinity and specificity for different proteins. The ability to manipulate these interactions opens up opportunities for tailoring GO for biomedical applications, including therapeutic interventions to prevent harmful protein aggregation.

The initial exploration of unfunctionalized GO's protein-binding capabilities demonstrated that its interaction with proteins is largely dominated by electrostatic forces, as the negative charge on GO interacts with positively charged amino acid residues on protein surfaces. While these interactions allowed for non-specific binding, unfunctionalized GO was found to lack the selectivity required for targeted protein interactions. This shortcoming led to the hypothesis



that functionalizing GO with specific amino acids, known for their roles in protein-protein interactions, could enhance both the strength and selectivity of binding. Such an approach would allow for the design of GO-based systems tailored to specific proteins, thereby providing a more effective tool for therapeutic applications.

One of the primary approaches explored in this study was the functionalization of GO with tyrosine, an amino acid known for its ability to engage in  $\pi$ - $\pi$  stacking interactions due to its aromatic ring structure. The initial hypothesis was that functionalizing GO with oligomeric tyrosine would result in stronger protein binding, given the potential for cooperative interactions between multiple tyrosine residues and the protein surface. However, the results, in table 3.4, were contrary to expectations. The strong  $\pi$ - $\pi$  interactions between tyrosine and the GO surface dominated, leading to a reduction in available binding sites for proteins. This phenomenon significantly reduced the overall binding efficiency of the oligomeric tyrosine-functionalized GO, highlighting the complexities of surface interactions and the need for careful consideration when designing functionalization strategies.

In contrast, functionalization with monomeric showed more promising results. Although  $\pi$ - $\pi$  interactions still played a role in binding, they were weaker compared to the oligomeric system, allowing more tyrosine molecules to interact with the protein. This finding suggests that while aromatic amino acids like tyrosine can enhance binding through  $\pi$ - $\pi$  stacking, careful control over the degree of functionalization is crucial to avoid hindering the desired protein interaction. This outcome also points to the potential limitations of using oligomeric systems in GO functionalization, as the cooperative effects that were expected to enhance binding can, in some cases, lead to unintended competition between the functional groups and the GO surface itself.

Given the challenges observed with tyrosine functionalization, the study shifted focus to glutamic acid, an amino acid lacking aromatic rings and thus unable to participate in  $\pi$ - $\pi$

stacking. This shift allowed the study to explore a functionalization route that relied more heavily on electrostatic interactions, specifically between the negatively charged carboxyl groups of glutamic acid and the positively charged regions of proteins. The results from this functionalization strategy were more in line with the original hypothesis. Glutamic acid, with its two carboxyl groups, provided an increase in available binding sites for electrostatic interactions, leading to enhanced binding affinity compared to both unfunctionalized GO and tyrosine-functionalized GO. Additionally, glutamic acid's inability to engage in  $\pi$ - $\pi$  stacking interactions allowed the carboxyl groups to remain available for protein binding, making it a more suitable candidate for increasing the binding efficiency of GO.

Further experiments compared the binding efficiency of monomeric and oligomeric glutamic acid-functionalized GO. The results indicated that oligomeric glutamic acid had a higher binding affinity due to the increased number of carboxylate groups available for electrostatic interactions. This finding aligns with the hypothesis that oligomeric systems can offer stronger binding capabilities through cooperative interactions, provided that these interactions do not compete with the GO surface, as seen in the case of tyrosine. The enhanced binding of glutamic acid-functionalized GO highlights the potential of using amino acids with charged or polar functional groups for selective protein binding, paving the way for the development of GO-based systems that can be customized for specific proteins.

In conclusion, the findings of this study provide valuable insights into the design and functionalization of GO for protein binding applications. The comparison between tyrosine and glutamic acid functionalization illustrates the importance of understanding the specific interactions between GO and the functionalizing agent to achieve the desired protein binding outcomes. While aromatic amino acids like tyrosine can offer strong binding through  $\pi$ - $\pi$  interactions, these interactions may reduce protein-binding efficiency if they dominate the

surface interactions with GO. On the other hand, amino acids like glutamic acid, which rely on electrostatic interactions, can provide a more efficient binding mechanism, especially when incorporated into oligomeric systems. These results underscore the potential for tailoring GO's surface properties to create highly specific and effective protein ligands, offering promising avenues for future research and applications in therapeutics and biomedical devices.

This study lays the groundwork for further exploration of GO functionalization with other amino acids and biomolecules to fine-tune its binding properties for various applications. Future research could investigate the combination of different functional groups or the incorporation of additional modifications to the GO surface to improve its biocompatibility, stability, and targeting efficiency. Additionally, the development of more advanced functionalization techniques could allow for greater control over the placement and density of functional groups on the GO surface, thereby optimizing its interactions with specific proteins. Overall, GO's unique properties, combined with the flexibility of functionalization, make it a promising material for the development of novel protein-binding systems and therapeutic agents.

## References

1. Novoselov, K.S., Geim, A.K., Morozov, S.V., Jiang, D.E., Zhang, Y., Dubonos, S.V., Grigorieva, I.V. and Firsov, A.A., 2004. *Electric Field Effect in Atomically Thin Carbon Films*. Science, 306(5696), pp.666–669.
2. Novoselov, K.S., Geim, A.K., Morozov, S.V., Dubonos, S.V., Zhang, Y. and Jiang, D., 2004. *Room-Temperature Electric Field Effect and Carrier-Type Inversion in Graphene Films*. arXiv preprint cond-mat/0410631.
3. Dreyer, D.R., Park, S., Bielawski, C.W. and Ruoff, R.S., 2010. *The Chemistry of Graphene Oxide*. Chemical Society Reviews, 39(1), pp.228–240.
4. Yang, X., Zhang, X., Ma, Y., Huang, Y., Wang, Y. and Chen, Y., 2009. *Superparamagnetic Graphene Oxide–Fe<sub>3</sub>O<sub>4</sub> Nanoparticles Hybrid for Controlled Targeted Drug Carriers*. Journal of Materials Chemistry, 19(18), pp.2710–2714.
5. Nair, R.R., Wu, H.A., Jayaram, P.N., Grigorieva, I.V. and Geim, A.K., 2012. *Unimpeded Permeation of Water Through Helium-Leak-Tight Graphene-Based Membranes*. Science, 335(6067), pp.442–444.
6. Brodie, B.C., 1859. *XIII. On the Atomic Weight of Graphite*. Philosophical Transactions of the Royal Society of London, (149), pp.249–259.
7. Hummers Jr, W.S. and Offeman, R.E., 1958. *Preparation of Graphitic Oxide*. Journal of the American Chemical Society, 80(6), pp.1339–1339.
8. Brodie, B.C., 1860. *XXIII.—Researches on the Atomic Weight of Graphite*. Quarterly Journal of the Chemical Society of London, 12(1), pp.261–268.

9. Gurzęda, B., Jeżowski, P., Boulanger, N. and Talyzin, A.V., *Oscillating Structural Transformations in the Electrochemical Synthesis of Graphene Oxide From Graphite*. *Angewandte Chemie International Edition*, p.e202411673.
10. Nanda, S.S., Papaefthymiou, G.C. and Yi, D.K., 2015. *Functionalization of Graphene Oxide and Its Biomedical Applications*. *Critical Reviews in Solid State and Materials Sciences*, 40(5), pp.291–315.
11. Wolf, E.L., 2014. *Applications of Graphene: An Overview*. Cham: Springer.
12. Zhu, Y., James, D.K. and Tour, J.M., 2012. *New Routes to Graphene, Graphene Oxide and Their Related Applications*. *Advanced Materials*, 24(36), pp.4924–4955.
13. Vogt, A.D., Pozzi, N., Chen, Z. and Di Cera, E., 2014. *Essential Role of Conformational Selection in Ligand Binding*. *Biophysical Chemistry*, 186, pp.13–21.
14. Koshland Jr, D.E., 1958. *Application of a Theory of Enzyme Specificity to Protein Synthesis*. *Proceedings of the National Academy of Sciences*, 44(2), pp.98–104.
15. Liu, Y., et al., 2012. *Interaction of Graphene Oxide with Proteins: The Influence of Hydrophobicity and Electrostatic Interactions*. *Journal of Colloid and Interface Science*, 376(1), pp.65–71.
16. Ghosh, R., Calero-Rubio, C., Saluja, A. and Roberts, C.J., 2016. *Relating Protein–Protein Interactions and Aggregation Rates from Low to High Concentrations*. *Journal of Pharmaceutical Sciences*, 105(3), pp.1086–1096.
17. Baker, D. and Sali, A., 2001. *Protein Structure Prediction and Structural Genomics*. *Science*, 294(5540), pp.93–96.

18. Yi, J., Choe, G., Park, J. and Lee, J.Y., 2020. *Graphene Oxide-Incorporated Hydrogels for Biomedical Applications*. Polymer Journal, 52(8), pp.823–837.
19. Perreault, F., De Faria, A.F. and Elimelech, M., 2015. *Environmental Applications of Graphene-Based Nanomaterials*. Chemical Society Reviews, 44(16), pp.5861–5896.
20. Wang, Y., Li, Z., Wang, J., Li, J. and Lin, Y., 2011. *Graphene and Graphene Oxide: Biofunctionalization and Applications in Biotechnology*. Trends in Biotechnology, 29(5), pp.205–212.
21. Aziz, A.A. and Twyman, L.J., 2019. *Synthesis of Oligomeric and Monomeric Functionalized Graphene Oxides and a Comparison of Their Abilities to Perform as Protein Ligands and Enzyme Inhibitors*. ACS Applied Materials & Interfaces, 11(48), pp.44941–44948.
22. Li, F., Ma, Y., Chen, L., Li, H., Zhou, H. and Chen, J., 2021. *In-Situ Polymerization of Polyurethane/Aniline Oligomer Functionalized Graphene Oxide Composite Coatings With Enhanced Mechanical, Tribological and Corrosion Protection Properties*. Chemical Engineering Journal, 425, p.130006.
23. Liu, L., Liu, C., Zhang, B. and Gao, L., 2022. *Detection of Chymotrypsin Using a Peptide Sensor Based on Graphene Oxide Modified with Sulfhydryl Groups and Gold Nanoparticles*. New Journal of Chemistry, 46(34), pp.16303–16308.
24. Gleissner, C., Landsiedel, J., Bechtold, T. and Pham, T., 2022. *Surface Activation of High-Performance Polymer Fibers: A Review*. Polymer Reviews, 62(4), pp.757–788.
25. Zou, X., Wei, S., Jasensky, J., Xiao, M., Wang, Q., Brooks III, C.L. and Chen, Z., 2017. *Molecular Interactions Between Graphene and Biological Molecules*. Journal of the American Chemical Society, 139(5), pp.1928–1936.

26. Ustunol, I.B., Gonzalez-Pech, N.I. and Grassian, V.H., 2019. *pH-Dependent Adsorption of  $\alpha$ -Amino Acids, Lysine, Glutamic Acid, Serine and Glycine, on TiO<sub>2</sub> Nanoparticle Surfaces*. Journal of Colloid and Interface Science, 554, pp.362–375.
27. Tan, J., Wang, F., Wang, Z., Lu, Q. and Deng, L., 2020. *An Enzyme-Free Fluorometric Nanoprobe for Chloramphenicol Based on Signal Amplification Using Graphene Oxide Sheets*. Microchimica Acta, 187, pp.1–7.
28. Cao, H., Huang, Y. and Liu, Z., 2016. *Interplay Between Binding Affinity and Kinetics in Protein–Protein Interactions*. Proteins: Structure, Function, and Bioinformatics, 84(7), pp.920–933.
29. Jilani, A., Othman, M.H.D., Ansari, M.O., Hussain, S.Z., Ismail, A.F., Khan, I.U. and Inamuddin, 2018. *Graphene and Its Derivatives: Synthesis, Modifications, and Applications in Wastewater Treatment*. Environmental Chemistry Letters, 16, pp.1301–1323.
30. Geim, A.K. and Grigorieva, I.V., 2013. *Van Der Waals Heterostructures*. Nature, 499(7459), pp.419–425.
31. James, D.K. and Tour, J.M., 2012. *The Chemical Synthesis of Graphene Nanoribbons—A Tutorial Review*. Macromolecular Chemistry and Physics, 213(10–11), pp.1033–1050.
32. Jing, Q., Liu, W., Pan, Y., Silberschmidt, V.V., Li, L. and Dong, Z., 2015. *Chemical Functionalization of Graphene Oxide for Improving Mechanical and Thermal Properties of Polyurethane Composites*. Materials & Design, 85, pp.808–814.

33. Thangamuthu, M., Hsieh, K.Y., Kumar, P.V. and Chen, G.Y., 2019. *Graphene- and Graphene Oxide-Based Nanocomposite Platforms for Electrochemical Biosensing Applications*. International Journal of Molecular Sciences, 20(12), p.2975.
34. Liu, X., Ma, R., Wang, X., Ma, Y., Yang, Y., Zhuang, L., Zhang, S., Jehan, R., Chen, J. and Wang, X., 2019. *Graphene Oxide-Based Materials for Efficient Removal of Heavy Metal Ions from Aqueous Solution: A Review*. Environmental Pollution, 252, pp.62–73.
35. Wang, S., Li, X., Liu, Y., Zhang, C., Tan, X., Zeng, G., Song, B. and Jiang, L., 2018. *Nitrogen-Containing Amino Compounds Functionalized Graphene Oxide: Synthesis, Characterization and Application for the Removal of Pollutants from Wastewater: A Review*. Journal of Hazardous Materials, 342, pp.177–191.
36. Li, J.H., Wang, S.S., Zhang, D.B., Ni, X.X. and Zhang, Q.Q., 2016. *Amino Acids Functionalized Graphene Oxide for Enhanced Hydrophilicity and Antifouling Property of Poly (Vinylidene Fluoride) Membranes*. Chinese Journal of Polymer Science, 34, pp.805–819.
37. Ye, N., Xie, Y., Shi, P., Gao, T. and Ma, J., 2014. *Synthesis of Magnetite/Graphene Oxide/Chitosan Composite and Its Application for Protein Adsorption*. Materials Science and Engineering: C, 45, pp.8–14.
38. Zhou, W., Zhuang, W., Ge, L., Wang, Z., Wu, J., Niu, H., Liu, D., Zhu, C., Chen, Y. and Ying, H., 2019. *Surface Functionalization of Graphene Oxide by Amino Acids for Thermomyces Lanuginosus Lipase Adsorption*. Journal of Colloid and Interface Science, 546, pp.211–220.



39. Vacchi, I.A., 2017. *Controlled Chemical Functionalization of Graphene Oxide* (Doctoral Dissertation, Université de Strasbourg).
40. Li, Y., Sadiq, F.A., Liu, T., Chen, J. and He, G., 2015. *Purification and Identification of Novel Peptides with Inhibitory Effect Against Angiotensin I-Converting Enzyme and Optimization of Process Conditions in Milk Fermented with the Yeast Kluyveromyces Marxianus*. Journal of Functional Foods, 16, pp.278–288.
41. De, M., Chou, S.S. and Dravid, V.P., 2011. *Graphene Oxide as an Enzyme Inhibitor: Modulation of Activity of  $\alpha$ -Chymotrypsin*. Journal of the American Chemical Society, 133(44), pp.17524–17527.

# Chapter 5

## Conclusion and Future Focuses

## Conclusion:

The primary aim of this research was to inhibit uncontrolled protein-protein interactions (PPIs), a process implicated in numerous diseases such as Alzheimer's, Parkinson's, certain cancers, and other neurodegenerative disorders. Protein-protein interactions are central to many biological processes, including signal transduction, cellular communication, and immune responses. However, when these interactions become dysregulated or uncontrolled, they can lead to the aggregation of proteins, which is a hallmark of many pathological conditions. For instance, in Alzheimer's disease, the aggregation of amyloid- $\beta$  peptides forms plaques in the brain, leading to neurodegeneration.

Traditional approaches to inhibiting PPIs have focused on small molecules, which act as inhibitors by disrupting the interaction between proteins. However, small molecules often face significant challenges, such as limited surface area and size, which restrict their ability to cover large protein interfaces effectively. As a result, they tend to exhibit weak binding affinities and lack the specificity needed for complex protein interactions. Consequently, there is a pressing need for novel approaches that can overcome these limitations and provide more effective therapeutic interventions.

This research explored a novel strategy by using dendrimer-stabilized iron oxide nanoparticles ( $\text{Fe}_3\text{O}_4$  MNPs) as inhibitors of PPIs. The highly branched and versatile structure of dendrimers makes them ideal candidates for nanoparticle systems. Their ability to be functionalized with various chemical groups allows for the customization of their surface properties, thereby enhancing their binding capabilities and stability. The goal was to develop a platform that could not only stabilize iron oxide nanoparticles but also improve their ability to bind target proteins selectively. This approach presents a promising alternative to traditional small-molecule inhibitors by offering a larger surface area for interactions and greater structural flexibility.

The first phase of the research focused on the synthesis of polyamidoamine (PAMAM) dendrimers, which were chosen for their unique dendritic structure. Dendrimers are hyperbranched macromolecules with a well-defined, tree-like architecture that grows in a stepwise fashion, leading to layers called generations. Each generation increases the size and number of terminal groups on the dendrimer surface, providing multiple binding sites for interactions with other molecules. The PAMAM dendrimers synthesized in this study ranged from generation 0.5 to generation 4.0, with each generation offering different levels of branching and surface area.

Initially, hydroxyl-terminated dendrimers were explored as potential stabilizers for  $\text{Fe}_3\text{O}_4$  MNPs. However, the results indicated that the neutral hydroxyl groups provided limited interaction with the charged surface of the iron oxide nanoparticles, leading to poor stabilization. The lack of electrostatic interactions meant that the dendrimers could not effectively prevent the aggregation of nanoparticles, resulting in large clusters that compromised the stability of the system. This was confirmed by dynamic light scattering (DLS) measurements, which showed a broad size distribution of the nanoparticles, indicating a high degree of aggregation.

To address this issue, the focus was shifted toward carboxyl-terminated PAMAM dendrimers. The introduction of carboxyl groups provided stronger electrostatic interactions with the iron oxide surface, which significantly improved the stabilization of the nanoparticles. The negatively charged carboxyl groups were able to form electrostatic bonds with the positively charged surface of the  $\text{Fe}_3\text{O}_4$  nanoparticles, preventing aggregation and ensuring better dispersion in aqueous environments. This was a crucial development, as stable nanoparticles are essential for biomedical applications, including drug delivery, biosensing, and therapeutic targeting.

Spectroscopic techniques such as nuclear magnetic resonance (NMR), Fourier-transform infrared spectroscopy (FTIR), TEM and mass spectrometry were employed to confirm the successful synthesis and functionalization of the dendrimers. These techniques provided detailed insights into the molecular structure of the dendrimers and the presence of the desired functional groups, verifying that the carboxyl-terminated PAMAM dendrimers were structurally sound and ready for further use in protein binding studies.

The next phase of the study involved using the functionalized dendrimers to stabilize  $\text{Fe}_3\text{O}_4$  MNPs. Stabilization of nanoparticles is a critical factor in determining their effectiveness in various applications. Nanoparticles have a natural tendency to aggregate due to van der Waals forces and magnetic interactions, which can significantly reduce their efficacy in biological systems. Aggregation not only increases the size of the nanoparticles but also reduces their surface area, making them less effective in binding to target proteins or delivering therapeutic agents.

By employing dendrimers of different generations, this study aimed to identify the optimal generation for stabilizing the nanoparticles. Among the generations tested, it was found that generation 2.5 (G2.5) carboxyl-terminated PAMAM dendrimers offered the best stabilization. G2.5 dendrimers had enough terminal groups to form a stable and uniform coating around the nanoparticles, preventing their aggregation without the excessive branching observed in higher-generation dendrimers like G3.5. This was an important finding, as excessive branching in higher generations can lead to challenges in achieving homogenous suspensions, which are necessary for consistent performance in biological systems.

The results of the stabilization experiments showed that G2.5 PAMAM dendrimers were able to effectively prevent the aggregation of  $\text{Fe}_3\text{O}_4$  MNPs, maintaining particle size stability and favorable dispersion properties. This made them ideal candidates for further functionalization

and protein-binding studies. The success of the stabilization process laid a strong foundation for the subsequent functionalization of the dendrimers with specific amino acids to enhance their protein-binding capabilities.

To further enhance the selectivity of protein-binding capabilities, stabilized magnetic nanoparticles with G2.5 carboxyl-terminated dendrimers were functionalized with specific amino acids. The goal of this functionalization was to leverage the non-covalent interactions that amino acids can form with proteins, such as hydrogen bonding,  $\pi$ - $\pi$  stacking, and hydrophobic effects. Four amino acids were selected for functionalization: Tyrosine, Phenylalanine, Alanine and Valine, each offering unique properties that could influence protein binding.

Tyrosine was chosen for its ability to engage in  $\pi$ - $\pi$  stacking interactions due to its aromatic ring structure and hydroxyl group. This made it a prime candidate for enhancing binding through both aromatic and hydrogen bonding interactions. Phenylalanine, which shares the aromatic ring structure but lacks the hydroxyl group, was selected to evaluate the impact of the hydroxyl group on binding affinity. Alanine was studied for its potential to introduce an additional carboxylic acid group, which may play a key role in enhancing binding interactions. This additional carboxyl group is expected to increase overall binding affinity by providing more sites for electrostatic interactions, hydrogen bonding, and other non-covalent forces, ultimately improving both the stability and specificity of the binding progression. Finally, valine, a hydrophobic amino acid, was included to study the role of hydrophobic interactions in protein binding.

The functionalization of the dendrimers with these amino acids was confirmed using NMR, FTIR and TEM analysis, which demonstrated the successful attachment of the amino acids to the dendrimer structure. The degree of functionalization was also quantified, with tyrosine-

functionalized dendrimers showing the highest degree of functionalization, with an average of five tyrosine groups attached to each dendrimer. This high degree of functionalization was expected to translate into stronger and more specific interactions with target proteins.

To assess the effectiveness of the functionalized dendrimers in binding to proteins, cytochrome-c was chosen as a model protein. It is selected for several reasons: its structure comprises three major and two minor helices folded into a globular shape, forming a heme pocket. It contains 104 amino acids and functions as an electron transporter in energy transduction by alternating between ferrous ( $\text{Fe}^{2+}$ ) and ferric ( $\text{Fe}^{3+}$ ) oxidation states. PAMAM dendrimers offer a suitable platform to complement the protein's interface, as the binding or interfacial area of cytochrome-c, known as the "hot spot," is typically about  $1100 \text{ \AA}^2$ . These interacting surfaces often exhibit a high charge density, with interactions mainly driven by polyvalent electrostatics. The interactions at the protein's active site can be optimized by targeting specific residues to harness non-covalent interactions.

The binding affinity of the functionalized dendrimers to cytochrome-c was measured by monitoring changes in UV absorbance, which provided a quantitative assessment of the binding interactions.

The results showed a clear generation- and amino acid-dependent effect on binding affinity. Tyrosine-functionalized dendrimers exhibited the highest binding affinity, achieving a binding efficiency of 53%. This high affinity was attributed to the ability of tyrosine to engage in multiple non-covalent interactions, including  $\pi$ - $\pi$  stacking and hydrogen bonding. These interactions allowed for a stronger and more specific interaction with the cytochrome-c surface. In contrast, phenylalanine-functionalized dendrimers showed a lower binding efficiency of 26%, suggesting that the absence of the hydroxyl group in phenylalanine reduced the overall interaction strength in addition to the lack of loading. Both Alanine- and Valine-functionalized

dendrimers exhibited moderate binding, ranging from 30% to 40%, likely driven by hydrophobic interactions. However, these interactions were weaker compared to those observed with tyrosine-functionalized dendrimers.

In parallel with the dendrimer studies, this research also explored the potential of graphene oxide (GO) as a platform for protein binding. GO's unique structure, characterized by its two-dimensional layers and abundance of oxygen-containing functional groups (e.g., hydroxyl, epoxy, and carboxyl groups), makes it a highly versatile material for interacting with proteins. These functional groups allow GO to engage in a variety of non-covalent interactions, including electrostatic forces, hydrogen bonding, and  $\pi$ - $\pi$  stacking, all of which are critical for protein binding.

Initial tests with unfunctionalized GO demonstrated that its interaction with proteins was dominated by electrostatic forces. The negatively charged surface of GO interacted with positively charged amino acid residues on protein surfaces, allowing for non-specific binding. However, this lack of specificity highlighted the need for functionalization to achieve targeted protein interactions.

To improve the specificity and strength of protein binding, GO was functionalized with amino acids, starting with tyrosine. The hypothesis was that tyrosine's aromatic ring would enable strong  $\pi$ - $\pi$  stacking interactions with proteins. However, the results revealed an unexpected outcome: oligomeric tyrosine-functionalized GO showed reduced binding efficiency compared to unfunctionalized GO. This was due to the strong  $\pi$ - $\pi$  interactions between tyrosine and the GO surface, which limited the availability of tyrosine molecules to interact with proteins.

Monomeric tyrosine-functionalized GO, in contrast, showed better binding efficiency. The weaker  $\pi$ - $\pi$  interactions in the monomeric system allowed more tyrosine molecules to interact with the protein, suggesting that controlling the degree of functionalization is critical for



optimizing binding interactions. This finding underscored the importance of balancing surface interactions when designing functionalized GO systems.

The focus then shifted to glutamic acid, an amino acid that lacks aromatic rings and is therefore incapable of engaging in  $\pi$ - $\pi$  stacking. Glutamic acid's two carboxyl groups provided increased binding sites for electrostatic interactions with proteins, leading to enhanced binding efficiency. Further experiments compared monomeric and oligomeric glutamic acid-functionalized GO, with oligomeric glutamic acid showing higher binding affinity due to the increased number of carboxylate groups available for interaction.

In conclusion, this study has demonstrated the potential of both dendrimer-stabilized iron oxide nanoparticles and functionalized graphene oxide as platforms for protein binding and inhibition of uncontrolled protein-protein interactions. The findings underscore the importance of selecting appropriate functional groups to enhance binding interactions, as well as the need to balance surface interactions to achieve the desired outcomes.

## Future Focuses:

The enhanced purification and functionalization of PAMAM dendrimer-stabilized magnetic nanoparticles (MNPs) using a mixed amino acids system represents a pivotal direction for future research. The primary goal is to improve the selectivity and binding affinity of these nanoparticles, enabling more precise interactions with target proteins such as cytochrome c. By optimizing purification techniques and incorporating a strategic combination of amino acids, researchers can significantly improve interaction specificity, leading to more efficient and targeted binding in various biomedical and industrial applications.

Achieving high-purity MNP solutions is critical for successful functionalization and binding studies. Currently, magnetic separation is the most commonly used method, but future work should focus on optimizing advanced techniques such as ultrafiltration and centrifugation to improve the purity of MNP solutions. Fine-tuning these methods can ensure that unbound proteins are thoroughly removed, and that nanoparticle aggregation is minimized, which is essential for consistent results. Ultrafiltration, in particular, holds promise for enhancing the removal of smaller proteins like cytochrome c. Using membranes with specific molecular weight cutoffs will allow for more selective purification, ensuring that only the target proteins and bound nanoparticles remain in the solution. This would improve the accuracy of binding measurements, which is essential for understanding the interaction dynamics between MNPs and target proteins.

Additionally, dual purification methods should be explored as a more refined approach to isolating MNPs and bound proteins. For instance, combining ultrafiltration with size exclusion chromatography (SEC) would enable selective retention of bound proteins while removing unbound cytochrome c and other impurities. This dual approach would not only enhance the reproducibility of binding experiments but also provide a more accurate assessment of

nanoparticle-protein interactions. Such improvements in purification methods would be especially important in applications where binding specificity and accuracy are critical, such as drug delivery and diagnostics.

Another critical aspect of future research lies in the functionalization of PAMAM dendrimers with a mixed amino acids system. Functionalizing MNPs with a combination of amino acids offers a powerful tool for enhancing selectivity and binding affinity, particularly for complex biological molecules like cytochrome c. By designing a multifunctional surface, researchers can take advantage of diverse non-covalent interactions, including hydrophobic forces, electrostatic interactions, and hydrogen bonding, to achieve highly specific binding. For example, a tailored combination of Tyrosine, Alanine, and Phenylalanine could create an optimal binding surface: Tyrosine enhances binding through  $\pi$ - $\pi$  interactions and hydrogen bonding due to its aromatic ring and hydroxyl group; Alanine provides a small, non-polar side chain that contributes to hydrophobic interactions without steric hindrance; and Phenylalanine promotes hydrophobic interactions and  $\pi$ - $\pi$  stacking with its additional aromatic ring, though it lacks hydroxyl groups for hydrogen bonding. Incorporating these amino acids at different ratios would allow researchers to fine-tune the MNPs' surface properties to match the target protein's binding site, enabling a synergistic effect that improves selectivity and affinity.

Future research should also explore the synergistic effects of mixed amino acids on binding affinity. Computational modeling, such as molecular dynamics simulations, can be employed to predict how different combinations of amino acids interact with target proteins. Such studies would provide insights into how binding affinity can be maximized by balancing hydrophobic, electrostatic, and hydrogen bonding interactions. Additionally, multimodal binding mechanisms should be investigated. By combining amino acids that promote different types of non-covalent interactions, researchers could design MNPs that exhibit stronger and more stable

binding. This approach has the potential to greatly improve the performance of MNPs in applications like biosensing, targeted drug delivery, and molecular imaging.

In conclusion, the purification and functionalization of PAMAM COOH G2.5 dendrimers for MNP systems offers numerous promising avenues for future exploration. Advanced purification techniques, such as ultrafiltration combined with size exclusion chromatography, can improve the purity of MNP solutions and ensure more accurate and reproducible binding studies. Meanwhile, innovative functionalization strategies involving mixed amino acids can greatly enhance the selectivity and binding affinity of MNPs to target proteins like cytochrome c. These advances will provide deeper insights into nanoparticle-protein interactions, enabling more precise control over binding mechanisms and opening the door to broader applications in biotechnology and nanomedicine.

Beyond the work with MNPs, future research could also explore the functionalization of graphene oxide (GO) and dendrimers with other amino acids and biomolecules to further fine-tune their binding properties for specific biomedical applications. GO's large surface area and chemical versatility make it an excellent candidate for such functionalization efforts. Combining GO with dendrimers could create a highly flexible platform for capturing a wide range of target molecules, from proteins to small drugs. Furthermore, the development of more advanced functionalization techniques could enable greater control over the placement and density of functional groups on both GO and dendrimer surfaces, optimizing their interactions with target proteins.

Overall, the unique properties of GO and dendrimers, combined with their flexibility in functionalization, position them as promising materials for developing novel protein-binding systems and therapeutic agents. This research not only enhances the understanding of binding mechanisms but also lays the groundwork for future innovations in treating diseases caused by

uncontrolled protein interactions. The ability to control these interactions could offer new avenues for therapeutic intervention and drug delivery, ultimately improving patient outcomes in various medical fields.

## Chapter 6

### Experimental Part:

Materials

and

Methods

## Solvents and Instrumentals:

All chemicals and reagents utilized in this experiment were obtained from commercial suppliers, such as Sigma Aldrich, and used as received without additional purification. Cytochrome c from equine heart (MW: 12,384 Da) and  $\alpha$ -chymotrypsin type-II from bovine pancreas (MW: 25 kDa) were also purchased from Sigma and employed without further purification.

## Instrumentation:

### Infrared (FTIR) spectroscopy

FTIR spectra were recorded using a Perkin-Elmer UATR infrared spectrometer over the wavenumber range of 4000–500  $\text{cm}^{-1}$ . The spectra were analyzed using Spectrum 100 software, with % transmittance and wavenumber ( $\text{cm}^{-1}$ ) applied as the scale parameters for the analysis.

### Nuclear Magnetic Resonance Spectroscopy (NMR)

All deuterated solvents were obtained from Sigma Aldrich. Nuclear magnetic resonance (NMR) spectra, including both  $^1\text{H}$  NMR and  $^{13}\text{C}$  NMR, were recorded at room temperature using a Bruker AMX-400 MHz spectrometer. The spectra were processed and analyzed using Topspin 4.0.7 and MestReNova software, with chemical shifts reported in parts per million (ppm).

### Mass Spectroscopy (MS)

Two analytical techniques were employed based on the molecular weight of the sample. Electrospray Ionization Mass Spectrometry (ESI-MS) was used for lower-generation samples

(generation 0.5), while Matrix-Assisted Laser Desorption Ionization Time-of-Flight (MALDI-TOF) spectrometry was utilized for higher-generation samples.

### The Raman spectroscopy

Raman spectra of the samples were collected over the range of 500 to 3500  $\text{cm}^{-1}$  using a Renishaw inVia Raman Microscope, equipped with a green laser operating at a wavelength of 514.5 nm and a laser power of 20 mW.

### X-ray photoelectron spectroscopy (XPS)

X-ray photoelectron spectroscopy (XPS) measurements were carried out using monochromatic Al-K $\alpha$  radiation ( $h\nu = 1486.69$  eV). The data was processed for curve fitting and atomic concentration calculations using CasaXPS version 2.3.16 software.

### Thermal conductivity analysis (TGA)

Thermogravimetric Analysis (TGA) was performed using a Perkin Elmer Pyris instrument over a temperature range of 25°C to 800°C under a controlled atmosphere of dry, flowing nitrogen. The resulting data was analyzed using Origin software.

### X-ray diffraction (XRD) patterns

X-ray diffraction (XRD) measurements were acquired using a Bruker D8 Advance diffractometer equipped with a copper target ( $\text{CuK}\alpha = 1.54178$  Å). The measurements were performed at a tube voltage of 40 kV and a tube current of 35 mA. XRD patterns were collected over a  $2\theta$  range of 5-100° with a scanning speed of 0.05°/min.



## Elemental Analysis

Elemental analysis was performed using a Vario MICRO Cube CHN/S analyzer, with solid samples utilized for the measurements.

## Scanning electron microscope

Scanning Electron Microscope (SEM) analysis was conducted using a JEOL-7001F instrument operating at 15 kV. Solid samples were utilized for both SEM and Energy-Dispersive X-ray (EDX) analysis. The samples were placed under vacuum and coated with a thin layer of gold prior to examination.

## Experiments:

### Synthesis of PAMAM dendrimers:

#### Synthesis of the methyl ester of PAMAM G 0.5 (4 OMe).

Ethylenediamine (EDA) (10 mL, 145 mmol) was dissolved in methanol (140 mL), and methyl acrylate (56.5 mL, 629 mmol) was added dropwise over the course of 30 minutes. The reaction mixture was stirred at room temperature for 24 hours. Excess solvent and unreacted methyl acrylate were removed, and the product was purified. The resulting product, generation 0.5 (G 0.5), was obtained as a yellow oil (55 g, 98% yield). FTIR ( $\nu_{\text{max}}/\text{cm}^{-1}$ ): 2951 (OCH<sub>3</sub> stretch), 1728 (C=O, ester), 1445 (CH<sub>2</sub> bend), 1173 (C-O), 1123, 1037 (C-N); <sup>1</sup>H NMR (400 MHz, MeOD):  $\delta$  3.78 (12H, s, OCH<sub>3</sub>), 2.76 (8H, t, J = 7.0 Hz, NCH<sub>2</sub>CH<sub>2</sub>CO), 2.56 (4H, s, CH<sub>2</sub>N), 2.49 (8H, t, J = 7.0 Hz, NCH<sub>2</sub>CH<sub>2</sub>CO); <sup>13</sup>C NMR (100 MHz, MeOD):  $\delta$  174 (C=O), 52.5, 51.5

(CH<sub>3</sub>), 48.8, 33.0 (CH<sub>2</sub>); Mass Spec (ES): m/z 409 (MH<sup>+</sup>), 426 (MNa<sup>+</sup>), ES-MS C<sub>18</sub>H<sub>32</sub>N<sub>2</sub>O<sub>8</sub> = 404 (calculated).

### Synthesis of the methyl ester of PAMAM G 1.0 (4NH<sub>2</sub>).

PAMAM G 0.5 (49.75 g, 0.13 mol) was dissolved in methanol (130 mL) and stirred, while ethylenediamine (EDA, 310.29 g, 5.15 mol) was added dropwise over a period of 45 minutes. The reaction mixture was then allowed to stir at room temperature for 70 hours. The excess methanol and EDA were removed at 45°C under reduced pressure. An azeotropic solution of toluene and methanol (1.0 L, 9:1 ratio) was used to purify the final product and further washed with methanol (100 mL). The purification process was performed several times to thoroughly remove any remaining EDA, followed by drying the product under vacuum. The final product, generation 1.0 (G 1.0), was achieved as a yellow oil (60 g, 95% yield).

FTIR (v<sub>max</sub>/cm<sup>-1</sup>): 3281 (N-H stretch), 2935 (C-H stretch), 1636 (C=O), 1557 (N-H bend), 1463, 1444 (C-H bend); <sup>1</sup>H NMR (400 MHz, MeOD): δ 3.29 (8H, t, J = 6.5 Hz, CONHCH<sub>2</sub>), 2.77 (8H, t, J = 7.0 Hz, CH<sub>2</sub>NCH<sub>2</sub>), 2.73 (8H, t, J = 6.5 Hz, CH<sub>2</sub>CH<sub>2</sub>NH<sub>2</sub>), 2.56 (4H, s, CH<sub>2</sub>N), 2.39 (8H, t, J = 7.0 Hz, CH<sub>2</sub>CONH); <sup>13</sup>C NMR (100 MHz, MeOD): δ 174.3 (C=O), 52.5, 50.6, 43.1, 41.1, 32.8 (CH<sub>2</sub>); Mass Spec (ES): m/z 517 (MH<sup>+</sup>), 539 (MNa<sup>+</sup>), ES-MS C<sub>22</sub>H<sub>48</sub>N<sub>10</sub>O<sub>4</sub> = 516 (calculated).

### Synthesis of the methyl ester of PAMAM G 1.5 (8OMe).

PAMAM G 1.0 (30.71 g, 59.45 mmol) was dissolved in methanol (110 mL) and stirred at 0 °C. Methyl acrylate (103.22 g, 1.18 mol) was then added dropwise over 50 minutes. The reaction mixture was allowed to continue at room temperature for 72 hours. Upon completion, the solvent was removed by concentration under reduced pressure at 45 °C. The final product, G 1.5, was obtained as a yellow oil (63 g, 89% yield) after drying. FTIR (v<sub>max</sub>/cm<sup>-1</sup>): 3313 (N-

H stretch), 2953 (C-H stretch), 2877, 1738 (C=O, ester), 1651 (C=O), 1538 (N-H), 1438 (CH<sub>2</sub> bend); <sup>1</sup>H NMR (400 MHz, MeOD): δ 3.68 (24H, s, OCH<sub>3</sub>), 3.26 (8H, t, J = 6.5 Hz, NHCH<sub>2</sub>), 2.85 (24H, t, J = 7.0 Hz, NCH<sub>2</sub>), 2.56 (12H, t, J = 6.5 Hz, CH<sub>2</sub>N), 2.47 (16H, t, J = 7.0 Hz, CH<sub>2</sub>CO), 2.43 (8H, t, J = 7.0 Hz, CH<sub>2</sub>CO); <sup>13</sup>C NMR (100 MHz, MeOD): δ 172.4 (C=O), 170.1 (C=O), 53.5, 52.3 (CH<sub>3</sub>), 51.9, 50.1, 48.7, 37.9, 34.1, 32.8 (CH<sub>2</sub>); Mass Spec (ES): m/z 1205 (M), 1228 (MNa<sup>+</sup>), ES-MS C<sub>54</sub>H<sub>96</sub>N<sub>10</sub>O<sub>20</sub> = 1205 (calculated).

### Synthesis of the methyl ester of PAMAM G 2.0 (8NH<sub>2</sub>).

PAMAM G 1.5 (40.75 g, 33.78 mmol) was dissolved in methanol (150 mL), and ethylenediamine (EDA, 329.2 g, 5.49 mol) was added dropwise over 45 minutes. The reaction mixture was allowed to stir at room temperature for 6 days. Purification was carried out using an azeotropic solvent mixture (2.0 L, 9:1 toluene) and subsequently washed with methanol (100 mL) until all excess EDA was removed. The final product, G 2.0, was obtained as a sticky yellow oil (48 g, 97% yield) after drying. FTIR (ν<sub>max</sub>/cm<sup>-1</sup>): 3287 (N-H stretch), 2939 (C-H stretch), 1645 (C=O, amide), 1562 (N-H); <sup>1</sup>H NMR (400 MHz, MeOD): δ 3.28 (24H, t, J = 6.0 Hz, NHCH<sub>2</sub>), 2.82 (24H, t, J = 7.0 Hz, NCH<sub>2</sub>), 2.75 (16H, t, J = 6.0 Hz, CH<sub>2</sub>NH<sub>2</sub>), 2.61 (12H, t, J = 7.0 Hz, CH<sub>2</sub>N), 2.34 (24H, t, J = 6.5 Hz, CH<sub>2</sub>CO); <sup>13</sup>C NMR (100 MHz, MeOD): δ 175.0 (C=O), 174.5 (C=O), 52.4, 51.5, 49.3, 42.0, 41.8, 37.5, 33.2, 31.9 (CH<sub>2</sub>); Mass Spec (ES): m/z 1430 (MH<sup>+</sup>), ES-MS C<sub>62</sub>H<sub>128</sub>N<sub>26</sub>O<sub>12</sub> = 1430 (calculated).

### Synthesis of the methyl ester of PAMAM G 2.5 (16OMe).

PAMAM G2.0 (29.19 g, 20.43 mmol) was dissolved in methanol (110 mL) and stirred while methyl acrylate (70.75 g, 0.83 mol) was added dropwise over 45 minutes. The reaction mixture was allowed to react at room temperature for 4 days. After completion, the excess methyl acrylate and solvent were removed at 45°C under reduced pressure. The product was further dried under high vacuum, yielding G2.5 (43 g, 72%) as a sticky yellow oil. FTIR (ν<sub>max</sub>/cm<sup>-1</sup>):

3298 (N-H stretch), 2952 (C-H stretch), 1735 (C=O, ester), 1645 (C=O, amide), 1553 (N-H, amide bend), 1430 (CH<sub>2</sub>); <sup>1</sup>H NMR (400 MHz, MeOD): δ 3.68 (48H, s, OCH<sub>3</sub>), 3.29 (24H, t, J = 6.5 Hz, NHCH<sub>2</sub>), 2.83 (24H, t, J = 7.0 Hz, NCH<sub>2</sub>), 2.78 (32H, t, J = 7.0 Hz, NCH<sub>2</sub>), 2.79 (12H, t, J = 7.0 Hz, NCH<sub>2</sub>), 2.59 (16H, t, J = 6.5 Hz, CH<sub>2</sub>N), 2.53 (32H, t, J = 7.0 Hz, CH<sub>2</sub>CO); <sup>13</sup>C NMR (100 MHz, MeOD): δ 173.5 (C=O), 172.0 (C=O), 172.5 (C=O), 53.5, 52.9, 51.9 (CH<sub>3</sub>), 50.1, 49.8, 49.7, 37.8, 37.5, 34.3, 33.4, 32.5 (CH<sub>2</sub>); Mass Spec (ES): m/z 2808 (MH<sup>+</sup>), ES-MS C<sub>126</sub>H<sub>224</sub>N<sub>26</sub>O<sub>44</sub> = 2807 (calculated).

### Synthesis of the methyl ester of PAMAM G 3.0 (16NH<sub>2</sub>).

PAMAM G 2.5 (24.79 g, 8.83 mmol) was dissolved in methanol (125 mL) and stirred, while ethylenediamine (EDA, 104.29 g, 1.75 mol) was added dropwise over 45 minutes. The reaction mixture was allowed to stir at room temperature for 10 days. The crude product was purified using an azeotropic mixture of toluene and methanol (2.0 L, 9:1) at 45°C to remove excess EDA. The final product was washed with methanol (90 mL), and the purification process was repeated until all EDA was completely removed. The resulting product, G 3.0, was obtained as a yellow oil (29 g, 97% yield) after drying. FTIR (ν<sub>max</sub>/cm<sup>-1</sup>): 3294 (N-H stretch), 3095 (C-H stretch), 1638 (C=O), 1563 (N-H), 1486 (CH<sub>2</sub>); <sup>1</sup>H NMR (400 MHz, MeOD): δ 3.29 (24H, t, J = 7.0 Hz, NHCH<sub>2</sub>), 2.83 (32H, t, J = 6.0 Hz, CH<sub>2</sub>N), 2.75 (56H, t, J = 7.0 Hz, CH<sub>2</sub>N), 2.58 (32H, t, J = 6.0 Hz, NCH<sub>2</sub>), 2.46 (56H, t, J = 7.0 Hz, CH<sub>2</sub>CO); <sup>13</sup>C NMR (100 MHz, MeOD): δ 175.5 (C=O), 174.8 (C=O), 173.9 (C=O), 51.2, 49.3, 41.4, 39.6, 37.2, 34.1 (CH<sub>2</sub>); Mass Spec (ES): m/z 3257 (MH<sup>+</sup>), ES-MS C<sub>142</sub>H<sub>288</sub>N<sub>58</sub>O<sub>28</sub> = 3256 (calculated).

### Synthesis of the methyl ester of PAMAM G 3.5 (32OMe)

PAMAM G 3.0 (24.99 g, 7.69 mmol) was dissolved in methanol (110 mL) and stirred, while methyl acrylate (51.62 g, 0.60 mol) was added dropwise over 45 minutes. The reaction mixture was allowed to proceed for 4 days at room temperature. After the reaction was complete, excess

methyl acrylate and solvent were removed at 45°C under reduced pressure. The product, G 3.5, was obtained as a sticky yellow oil (39 g, 84% yield). FTIR ( $\nu_{\text{max}}/\text{cm}^{-1}$ ): 3296 (N-H stretch), 2949 (C-H stretch), 2829, 1731 (C=O, ester), 1638 (C=O, amide), 1548 (N-H bend), 1445 ( $\text{CH}_2$ );  $^1\text{H}$  NMR (400 MHz, MeOD):  $\delta$  3.68 (96H, s,  $\text{OCH}_3$ ), 3.32 (24H, t,  $J = 5.0$  Hz,  $\text{NHCH}_2$ ), 2.87 (32H, t,  $J = 6.0$  Hz,  $\text{NCH}_2$ ), 2.79 (56H, t,  $J = 7.0$  Hz,  $\text{NCH}_2$ ), 2.66 (64H, t,  $J = 7.0$  Hz,  $\text{NCH}_2$ ), 2.59 (32H, t,  $J = 6.0$  Hz,  $\text{CH}_2\text{N}$ ), 2.53 (64H, t,  $J = 7.0$  Hz,  $\text{CH}_2\text{CO}$ ), 2.37 (56H, t,  $J = 7.0$  Hz,  $\text{CH}_2\text{CO}$ );  $^{13}\text{C}$  NMR (100 MHz, MeOD):  $\delta$  173.4 (C=O), 53.1, 52.4, 51.1, 49.5, 49.4 ( $\text{CH}_3$ ), 37.5, 35.9, 33.4, 31.8 ( $\text{CH}_2$ ); Mass Spec (ES):  $m/z$  6015 (M), ES-MS  $\text{C}_{270}\text{H}_{480}\text{N}_{58}\text{O}_{92} = 6011$  (calculated).

## Synthesis of hydroxyl-terminated PAMAM dendrimers:

### Synthesis of PAMAM dendrimer with 24 OH terminal groups

Tris(hydroxymethyl)aminomethane (1.75 g, 14.8 mmol) and anhydrous potassium carbonate (2.12 g, 15.20 mmol) were dissolved in dry DMSO (14 mL). PAMAM dendrimer generation 1.5 (2.04 g, 1.67 mmol) in dry DMSO (5 mL) was added to the stirred solution. The resulting mixture was stirred for two days at 50 °C under a nitrogen atmosphere. After completion, the mixture was filtered to remove any excess solid reagents, and the solvent was removed via vacuum distillation at 45 °C. The resulting viscous pale-yellow oil was dissolved in a minimal amount of water and subsequently precipitated using acetone. This precipitation step was repeated, and the product was dried overnight in a vacuum oven to yield the final product as a viscous pale-yellow oil (1.3 g, 65%).  $^1\text{H}$  NMR (400 MHz,  $\text{D}_2\text{O}$ ):  $\delta$  3.73 (s, 48H,  $\text{CH}_2\text{-OH}$ ), 3.28–3.11 (br m, 12H, NH), 2.71–2.61 (br m, 28H,  $\text{NCH}_2\text{CH}_2\text{C=O}$ ), 2.61–2.46 (br m,  $\text{NHCH}_2\text{CH}_2\text{N}$ ), 2.41–2.25 (br m, 28H,  $\text{NCH}_2\text{CH}_2\text{C=O} + \text{NCH}_2\text{CH}_2\text{N}$  (core));  $^{13}\text{C}$  NMR (100.61

MHz, D<sub>2</sub>O):  $\delta$  175.7, 173.8, 62.2, 60.7, 51.1, 50.2, 48.8, 36.3, 32.7, 32.4; FTIR (cm<sup>-1</sup>): 3175 (br, OH), 1695 (s, exterior C=O), 1633 (s, interior C=O); Mass Spec (ESI-MS): m/z 1918 (MH<sup>+</sup>), calculated 1916.

### Synthesis of PAMAM dendrimer with 48 OH terminal groups

PAMAM dendrimer generation 2.6 (1.10 g, 0.362 mmol) was dissolved in dry DMSO (5 mL) and added to a stirred solution of tris(hydroxymethyl)aminomethane (720 mg, 6.22 mmol) and anhydrous potassium carbonate (855 mg, 6.17 mmol) in dry DMSO (14 mL). The reaction mixture was stirred at 50 °C for three days under a nitrogen atmosphere. After the reaction, the solution was filtered to remove any solid residues, and the solvent was evaporated using vacuum distillation at 45 °C. The resulting viscous pale-yellow oil was dissolved in a minimal amount of water and precipitated using acetone. This precipitation step was repeated to ensure high purity. The final product was dried in a vacuum oven, yielding a viscous pale-yellow oil (0.58 g, 57%). <sup>1</sup>H NMR (400 MHz, D<sub>2</sub>O):  $\delta$  3.63 (s, 96H, CH<sub>2</sub>OH), 3.23–2.25 (broad multiplets, 164H, CH<sub>2</sub> + 28H, NH); <sup>13</sup>C NMR (100.61 MHz, D<sub>2</sub>O):  $\delta$  176.1, 173.8, 62.1, 60.8, 51.9, 48.9, 38.6, 37.3, 33.2; FTIR (cm<sup>-1</sup>): 3293 (br, OH), 1703 (s, exterior C=O), 1632 (s, interior C=O); Mass Spec (ESI-MS): m/z 4233 (MH<sup>+</sup>), calculated 4228.

### Synthesis of PAMAM carboxylate terminated PAMAM dendrimers from methyl ester PAMAM dendrimer:

The methyl ester-terminated PAMAM dendrimer was introduced into a methanol and water solution (12:1) containing an excess of NaOH (3 equivalents per methyl ester group). The mixture was stirred at room temperature for 12 hours and subsequently neutralized with NH<sub>4</sub>Cl. The resulting solution was first dried using rotary evaporation, followed by further drying under high vacuum with the addition

of a small amount of toluene. For larger dendrimers, extended reaction times were sometimes necessary, and purification was achieved through dialysis, with solvent removal by freeze-drying.

#### Generation 0.5 carboxylate PAMAM dendrimer (4 COOH)

$^1\text{H}$  NMR ( $\text{D}_2\text{O}$ , ppm): 3.61 (s, 4H), 3.33-3.39 (t, 8H), 2.63-2.68 (t, 8H),  $^{13}\text{C}$  NMR ( $\text{D}_2\text{O}$ , ppm): 178.2, 50.9, 47.5, 30.9, FTIR<sub>vmax</sub>, 3368(m), 1653(s), 1588(s)  $\text{cm}^{-1}$ . 63% yield.

#### Generation 1.5 carboxylate PAMAM dendrimer (8 COOH)

$^1\text{H}$  NMR ( $\text{D}_2\text{O}$ , ppm), 3.06-3.15 (t, 8H), 3.02 (m, 16H), 2.98 (t, 12H), 2.33-2.27 (t, 16H),  $^{13}\text{C}$  NMR ( $\text{D}_2\text{O}$ , ppm): 176.7, 51.5, 50.6, 36.7, 34.3, 30.2, FTIR<sub>vmax</sub>, 3371(m), 1695(s), 1586(s)  $\text{cm}^{-1}$ . 71% yield.

#### Generation 2.5 carboxylate PAMAM dendrimer (16 COOH)

$^1\text{H}$  NMR ( $\text{D}_2\text{O}$ , ppm), 3.48-3.63 (m, 24H), 3.33-3.36 (t, 56H), 3.04-3.20 (t, 28H), 2.55-2.60(t, 24H),  $^{13}\text{C}$  NMR ( $\text{D}_2\text{O}$ , ppm): 177.5, 173.7, 51.3, 50.6, 49.5, 33.4, 31.3, FTIR<sub>vmax</sub>, 3394(m), 1695(s), 1586(s)  $\text{cm}^{-1}$ . 73% yield.

#### Generation 3.5 carboxylate PAMAM dendrimer (32 COOH):

$^1\text{H}$  NMR ( $\text{D}_2\text{O}$ , ppm), 3.47-3.63 (m, 56H), 3.31-3.37 (t, 120H), 3.18-3.20 (m, 60H), 2.57-2.63 (t, 120H),  $^{13}\text{C}$  NMR ( $\text{D}_2\text{O}$ , ppm): 174.8, 172.5, 52.8, 50.7, 48.3, 30.1, 30.5. FTIR<sub>vmax</sub> 3335(m), 1652(s), 1588(s)  $\text{cm}^{-1}$ . 59% yield.

## Synthesis of functionalized generation 2.5 PAMAM dendrimers with Amino acid:

### Functionalization of PAMAM dendrimer with phenylalanine methyl ester

Starburst PAMAM dendrimer generation 1.5 (306 mg, 0.19 mmol) in a methanol solution was isolated by evaporation under a nitrogen stream, and the resulting solid residue was dissolved in water (3.75 mL) along with phenylalanine methyl ester hydrochloride (135 mg, 0.65 mmol). The pH of the solution was adjusted to 5.0 using 1 M hydrochloric acid. A solution of the coupling agent, 1-ethyl-3-(3-dimethylaminopropyl) carbodiimide hydrochloride (EDCI; 556 mg, 3.58 mmol), and NHS (3.58 mmol) in water (12.0 mL) was prepared and immediately added to the dendrimer solution. The reaction mixture was stirred at 25°C for 2 hours while maintaining the pH at 5.0. The resulting product was purified by dialysis and freeze-dried. <sup>1</sup>H NMR (DMSO-d<sub>6</sub>, ppm): 7.1–7.5 (br, 5H, C<sub>6</sub>H<sub>5</sub>), 2.18–3.55 (m, 2H, -CH<sub>2</sub>C<sub>6</sub>H<sub>5</sub>, 180H, -NCH<sub>2</sub>CH<sub>2</sub>CO, 12H, -NCH<sub>2</sub>CH<sub>2</sub>CH<sub>2</sub>N(CH<sub>3</sub>)<sub>2</sub>), 1.8–1.9 (q, 2H, -NCH<sub>2</sub>CH<sub>3</sub>), 0.86–1.3 (t, 3H, -NCH<sub>2</sub>CH<sub>3</sub>); <sup>13</sup>C NMR (DMSO-d<sub>6</sub>, ppm): 177.5, 135.3, 129.2, 128.8, 127.5, 55.8, 54.5, 52.7, 48.2, 37.5, 36.2, 34.5; FTIR (ν<sub>max</sub>, cm<sup>-1</sup>): 3345 (m), 2932 (s), 2855 (s), 1735 (s), 1655 (s), 1593 (s), 1458 (s), 1379 (m), 1030 (m); MS MALDI-TOF: m/z 4154 [MH<sup>+</sup>]; yield: 322 mg, 95%

### Functionalization of PAMAM dendrimer with Alanine methyl ester

<sup>1</sup>H NMR(DMSO-d<sub>6</sub>, ppm), 2.31-3.72 (180H, -NCH<sub>2</sub>CH<sub>2</sub>CO, 24H, -OCH<sub>3</sub>, 12H, -NCH<sub>2</sub>CH<sub>2</sub>CH<sub>2</sub>N(CH<sub>3</sub>)<sub>2</sub>), 1.75-1.85(q, 2H, -NCH<sub>2</sub>CH<sub>3</sub>), 1.3-1.5 (d, -CHCH<sub>3</sub>), 0.9-1.1 (t, 3H, -NCH<sub>2</sub>CH<sub>3</sub>), <sup>13</sup>C-NMR(DMSO-d<sub>6</sub> ,ppm) : 175.7, 173.6, 53.4, 51.4, 48.7, 48.7, 34.5, 30.4, 16.3, 15.3. Yield 72 mg.



## Functionalization of PAMAM dendrimer with valine methyl ester

$^1\text{H}$  NMR(DMSO- $d_6$ , ppm), 4.1-4.2(8H,  $\text{NHCHCOOCH}_3$ ), 2.03-3.75(180H,  $-\text{NCH}_2\text{CH}_2\text{CO}$ , 24H,  $-\text{OCH}_3$ , 12H,  $-\text{NCH}_2\text{CH}_2\text{CH}_2\text{N}(\text{CH}_3)_2$ ), 1.8-1.9(q, 2H,  $-\text{NCH}_2\text{CH}_3$ ), 1.0 (t, 3H,  $-\text{NCH}_2\text{CH}_3$ ), 0.9 (d, 8H,  $-\text{CH}(\text{CH}_3)_2$ ),  $^{13}\text{C}$ -NMR(DMSO- $d_6$ , ppm) :177., 171.0, 58.4, 53.2, 50.6, 34.5, 30.3, 29.7, 17.5, 16.8. FTIR $_{\text{vmax}}$  3371(m), 2923(s), 2854(s), 1746(s), 1672(s), 1576(w), 1463(s), 1376(w)  $\text{cm}^{-1}$ . MS MALDI – TOF, 3085, yield 112 mg.

## Functionalization of PAMAM dendrimer with tyrosine methyl ester

$^1\text{H}$  NMR (DMSO- $d_6$ , ppm): 7.1-7.3(br, 4H,  $\text{C}_6\text{H}_4$ ), 2.21-3.72(m, 2H,  $-\text{CH}_2\text{C}_6\text{H}_4$ , 180H,  $-\text{NCH}_2\text{CH}_2\text{CO}$ , 24H,  $-\text{OCH}_3$ , 12H,  $-\text{NCH}_2\text{CH}_2\text{CH}_2\text{N}(\text{CH}_3)_2$ ), 1.9(q, 2H,  $-\text{NCH}_2\text{CH}_3$ ), 1.1 (m, 3H,  $-\text{NCH}_2\text{CH}_3$ ),  $^{13}\text{C}$ -NMR (DMSO- $d_6$ , ppm) : 177.5, 170.9, 155.03, 130.6, 124.7, 115.3, 54.3, 53.1, 48.7, 35.4, 34.5, 31.2. FTIR $_{\text{vmax}}$  3328(m), 2935(s), 2852(s), 1735(s), 1654(w), 1570(m), 1457(s), 1386(s), 1035(s)  $\text{cm}^{-1}$ . MS MALDI – TOF, 4288  $\text{MH}^+$ , yield 215mg.

## General method for the Hydrolysis of PAMAM dendrimers

Each functionalized dendrimer, dissolved in 10 mL of methanol and 1 mL of distilled water, was combined with a stoichiometric amount of KOH and added to a 50 mL round-bottom flask equipped with a magnetic stir bar and reflux condenser. The mixture was heated at 30°C for 24 hours. After completion of the reaction, the solvent was removed using rotary evaporation.

## Hydrolysis of PAMAM with valine methyl ester

$^1\text{H}$ NMR ( $\text{D}_2\text{O}$ , ppm):3.76-3.84(d,8H,  $-\text{NHCHCOOH}$ ),1.85-3.35(br,180H,  $\text{NCH}_2\text{CH}_2\text{CO}$ ,  $-\text{NCH}_2\text{CH}_2\text{NH}$ ,  $-\text{NCH}_2\text{CH}_2\text{N}-$ ,  $-\text{CH}_2\text{COOH}$ ,  $\text{CH}_2\text{C}_6\text{H}_4$ ), 1.1-1.15 (d, 48H,  $\text{CH}(\text{CH}_3)_2$ ).  $^{13}\text{C}$ -NMR ( $\text{D}_2\text{O}$ , ppm): 177.3, 171.4, 53.3, 50.6, 34.5, 30.5, 29.8, 17.5, 16.7. FTIR $_{\text{vmax}}$  3455(m), 2925(s), 2855(s), 1746(s), 1675(s), 1576(w), 1463(s), 1370(m)  $\text{cm}^{-1}$ . MS MALDI – TOF, 3085.

Yield 77 mg.

### Hydrolysis of PAMAM with phenylalanine methyl ester

$^1\text{H}$ NMR ( $\text{D}_2\text{O}$ , ppm): 6.85-7.28(m, 5H, Ph), 3.35-3.48(m, 8H,  $-\text{NHCH}_2\text{COOH}$ ) 2.03-3.35(br, 180H,  $-\text{NCH}_2\text{CH}_2\text{CO}$ ,  $-\text{NCH}_2\text{CH}_2\text{NH}$ ,  $-\text{NCH}_2\text{CH}_2\text{N}$ -,  $-\text{CH}_2\text{COOH}$ ,  $\text{CH}_2\text{C}_6\text{H}_5$ ).  $^{13}\text{C}$ -NMR ( $\text{D}_2\text{O}$ , ppm): 177.6, 170.3, 135.3, 129.4, 128.8, 127.7, 54.8, 53.5, 37.5, 36.5, 34.5, 30.5. FTIR $_{\text{vmax}}$  3345(m), 2934(s), 2855(s), 1736(s), 1655(s), 1593(w), 1458(s), 1376(m), 1033(s)  $\text{cm}^{-1}$ . MS MALDI – TOF, 4045. Yield 65mg.

### Hydrolysis of PAMAM with Tyrosine methyl ester

$^1\text{H}$ NMR ( $\text{D}_2\text{O}$ , ppm): 6.68-7.15, (m, 4H, Ph), 4.3-4.38 (m, 8H,  $-\text{NHCH}_2\text{COOH}$ ), 2.15-3.48 (m, 8H,  $-\text{NHCH}_2\text{COOH}$ ) 2.85-3.25(br, 180H,  $-\text{NCH}_2\text{CH}_2\text{CO}$ ,  $-\text{NCH}_2\text{CH}_2\text{NH}$ ,  $-\text{NCH}_2\text{CH}_2\text{N}$ -,  $-\text{CH}_2\text{COOH}$ ,  $\text{CH}_2\text{C}_6\text{H}_4$ ),  $^{13}\text{C}$ -NMR ( $\text{D}_2\text{O}$ , ppm): 177.5, 170.3, 155.5, 130.6, 125.8, 115.9, 54.2, 53.2, 48.8, 35.5, 34.5, 31.5. FTIR $_{\text{vmax}}$  3328(m), 2935(s), 2856(s), 1735(s), 1655(m), 1578(w), 1458(s), 1380(m), 1035(m)  $\text{cm}^{-1}$ . MS MALDI – TOF, 4175.

Yield 125 mg.

### Synthesis of $\text{Fe}_3\text{O}_4$ NPs

The synthesis of  $\text{Fe}_3\text{O}_4$  nanoparticles was performed following a previously published procedure, utilizing controlled co-precipitation of Fe (II) and Fe (III) ions. A solution consisting of 25 mL of 1 M  $\text{FeCl}_3 \cdot 6\text{H}_2\text{O}$ , 0.5 M  $\text{FeCl}_2 \cdot 4\text{H}_2\text{O}$ , and 0.4 M HCl in water was prepared under vigorous stirring. The co-precipitation of  $\text{Fe}_3\text{O}_4$  NPs was conducted in a three-neck round-bottom flask. This mixture was added to 250 mL of 0.5 M NaOH, preheated to  $80^\circ\text{C}$  prior to the co-precipitation reaction. The reaction was carried out under a nitrogen atmosphere with continuous vigorous stirring. The resulting black powder was separated by sedimentation using

an external magnetic field and washed repeatedly with water until a stable ferrofluid was achieved. The particles were then redispersed in water.

### Stabilization of Fe<sub>3</sub>O<sub>4</sub> NPs using dendrimers

An aqueous solution (515 mL) containing 5 mg of Fe<sub>3</sub>O<sub>4</sub> nanoparticles (NPs) was combined with 1 mL of functionalized G3 PAMAM dendrimers (1 mg/mL in H<sub>2</sub>O) and shaken overnight. The mixture was then centrifuged at 6000 rpm for 10 minutes to remove any unadsorbed dendrimer material. The resulting particles were redissolved in water and dispersed through intense sonication. To purify the dendrimer-stabilized Fe<sub>3</sub>O<sub>4</sub> NPs, five cycles of centrifugation and dispersion were performed. Finally, the Fe<sub>3</sub>O<sub>4</sub> NPs were redissolved in water.

### Preparation for Cytochrome c (Cc) binding assay

#### The interactions between cytochrome c and PAMAM dendrimers

##### Preparation of cytochrome- c solution:

The molar mass of cytochrome c is approximately 12,384 g/mol. To prepare a  $1 \times 10^{-6}$  M solution of cytochrome c in 1 liter of water, the required mass is calculated using the formula:

Mass = molarity  $\times$  molar mass  $\times$  volume.

Thus, Mass =  $1 \times 10^{-6}$  M  $\times$  12,384 g/mol  $\times$  1 L = 0.012384 g.

Therefore, 0.012 grams of Cytochrome-c was carefully weighed and dissolved in 1.0 liter of distilled water to achieve the desired concentration.

##### Preparation of Phosphate buffer solution:

A buffer solution was prepared by dissolving 14.48 g of disodium hydrogen phosphate

( $\text{Na}_2\text{HPO}_4$ ) and 1.75 g of monosodium dihydrogen phosphate ( $\text{NaH}_2\text{PO}_4$ ) in 1.0 L of distilled water. The pH was adjusted to 7.46 using either HCl or NaOH, resulting in a buffer solution with a concentration of 0.1 M.

### Preparation of MNPs-Polymer Solution:

$1 \times 10^{-6}$  M stock solution of cytochrome-c was prepared in buffer (pH 7.3, 0.1M), and a UV spectrum recorded. The absorption of cytochrome-c's porphyrin Soret band, at 410 nm, was noted and would be used as the baseline/control value. Concentrated solutions of dendrimer-stabilized magnetic nanoparticles (MNPs) were then prepared such that the final concentrations were 167 mg/mL of MNPs, and 33 mg/mL of dendrimer. Subsequently, 50 mL of each MNP solution was then added to 3 mL of the cytochrome-c stock solution. This mixture was gently agitated, and the MNPs along with any bound protein were removed by magnetic separation. The remaining solution was analysed by UV, and the absorption of the remaining cytochrome-c's Soret band, at 410 nm, was measured and compared to the control sample.

### Assay of Cytochrome-c Activity

For each run a reading was taken for the cytochrome-c solution (3ml) by UV spectroscopy. The PAMAM solutions were then added in the following increments: MNP solution used contained 0.5 g of MNP and 0.1 g of dendrimer in 3 mL of buffer (0.1 M) and cytochrome-c concentration in the solution is  $1 \times 10^{-6}$  M (total amount in cuvette = 3.35ml). The fluorometer was set with a scan speed of 1200 nm/min and the emission was measured between 550 and 850 nm. The excitation wavelength was set at 410 nm. Data shown is the average from 3 runs with estimated error  $\pm 15\%$ .

## Synthesis of Graphene Oxide (GO)

Graphite particles (2.95 g, 1.0 eq) were added to a 1:9 mixture of concentrated  $\text{H}_3\text{PO}_4/\text{H}_2\text{SO}_4$  (40 mL/380 mL) along with 18.0 g (6.0 eq) of  $\text{KMnO}_4$ . The mixture was stirred and kept at 50 °C, followed by refluxing for 24 hours. Once the reaction cooled to room temperature, 500 mL of the mixture was poured onto ice, and 4 mL of 30%  $\text{H}_2\text{O}_2$  was added. The crude product was centrifuged at 4000 rpm for 35 minutes, and the supernatant was removed. The unrefined product was then washed multiple times with 400 mL of water. Next, a solution was prepared by mixing 400 mL of 30%  $\text{HCl}$  with 400 mL of ethanol, and the pH was adjusted to a stable level 7.4. To induce coagulation, 400 mL of diethyl ether was added, and the resulting mixture was filtered to obtain a suspension. The precipitate collected on the filter was vacuum-dried at room temperature for 24 hours, yielding 6.1 g of a dark brown solid product.

## Functionalized Graphene Oxide:

### Graphene oxide functionalized with methyl ester of tyrosine ( $\text{Tyr-OCH}_3$ )

Graphene oxide (GO) (0.3 g, 1 eq) was dispersed in 100 mL of deionized water using ultrasonic oscillation for 3 hours. To the mixture, triethylamine (4.11 g, 38.8 mmol), L-tyrosine methyl ester (2.9 g, 14 mmol), DMAP (3.17 g, 26.0 mmol), and  $\text{EDC}\cdot\text{HCl}$  (4.98 g, 26.0 mmol) were added in 10 equivalents. The reaction mixture was stirred and refluxed at 75 °C for 24 hours. After allowing the reaction to cool to room temperature, the crude product was washed three times with 100 mL of brine. The filtrate was centrifuged at 4000 rpm for 45 minutes, and the supernatant was

discarded. The precipitate was then washed with 2 L of a mixture of water and ethanol, followed by drying in a desiccator at 60 °C. A black solid (0.38 g) was obtained.

### Synthesis of Tyr-mono-deprotected Graphene Oxide

GO-Tyr-OMe (0.30 g, 1 eq) was dispersed in 100 mL of deionized water and subjected to ultrasonic treatment for 4 hours. The mixture was then combined with 18 mL of 2 M KOH and refluxed at 75 °C for 24 hours with continuous stirring. Once the reaction had cooled to room temperature, 15 mL of 2 M sulfuric acid was added, and the mixture underwent further sonication for 4 hours. The crude product was rinsed four times with 100 mL of brine solution and then dried using MgSO<sub>4</sub>. The material was filtered and dried at 60 °C, resulting in 0.29 g of a black solid product.

### Graphene Oxide – Valine -OCH<sub>3</sub>

Graphene oxide (GO) (0.30 g, 1 eq) was dispersed in 100 mL of deionized water and subjected to ultrasonic treatment for 3 hours. To the resulting dispersion, triethylamine (4.11 g, 39.11 mmol), DMAP (3.19 g, 25.8 mmol), L-valine methyl ester (2.18 g, 12.8 mmol), and EDC·HCl (5.5 g, 26.2 mmol) were added in 10 equivalents. The reaction mixture was stirred and refluxed at 75 °C for 24 hours, then allowed to cool to room temperature. The crude product was washed three times with 100 mL of brine solution, centrifuged at 4,000 rpm for 45 minutes, and the supernatant was decanted. The precipitate was then thoroughly washed with 2 L a mixture of water and ethanol, followed by drying at 60 °C. The final product, a black solid, was obtained with a yield of 0.39 g.

### Graphene Oxide modified with Valine through mono-deprotection

GO-Val-OMe (0.30 g, 1 eq) was dispersed in 100 mL of deionized water and sonicated for 5 hours. The mixture was then combined with 18 mL of 2 M KOH and refluxed at 75 °C for 22 hours with continuous stirring. After the reaction cooled to room temperature, 20 mL of 2 M sulfuric acid was added, followed by an additional 4 hours of sonication. The crude product was rinsed four times with 100 mL of brine solution and dried using MgSO<sub>4</sub>. The raw material was filtered and dried at 60 °C, yielding 0.39 g of a black solid product.

### Graphene Oxide – Phenylalanine -OCH<sub>3</sub>

Graphene oxide (GO) (0.25 g, 1 eq) was dispersed in 100 mL of deionized water and subjected to ultrasonic oscillation for 3 hours. Triethylamine (3.95 g, 39.0 mmol), DMAP (3.20 g, 26.2 mmol), L-phenylalanine methyl ester (3.10 g, 15 mmol), and EDC·HCl (5 g, 26.0 mmol) were then added to the mixture in 10 equivalents. The reaction mixture was stirred and refluxed at 75 °C for 22 hours. After cooling to room temperature, the crude product was rinsed three times with 100 mL of brine. The mixture was centrifuged at 4,000 rpm for 45 minutes, and the supernatant was decanted. The precipitate was further washed with 2 L of water and ethanol before being dried at 60 °C, yielding 0.39 g of a black solid.

### Graphene Oxide – Phenylalanine (Mono-Deprotection)

GO-Phy-OMe (0.30 g, 1 eq) was dispersed in 100 mL of deionized water and sonicated for 4 hours using ultrasonic oscillation. The mixture was then combined with 30 mL of 2 M KOH and refluxed at 75 °C for 24 hours with continuous stirring. After allowing the reaction to cool to room temperature, 18 mL of 2 M sulfuric acid was added, and the mixture was further sonicated for an

additional 4 hours. The crude product was rinsed four times with 100 mL of brine solution and desiccated using  $\text{MgSO}_4$ . The raw material was filtered and dried at  $60^\circ\text{C}$ . The final product, a black solid, was obtained with a yield of 0.22 g.

### Graphene Oxide – Glu - $\text{OCH}_3$

Graphene oxide (GO) (0.30 g, 1 equivalent) was dispersed in 100 mL of deionized water using ultrasonic oscillation for 3 hours. To this mixture, 10 equivalents of L-glutamic methyl ester (2.58 g, 13.1 mmol), DMAP (3.21 g, 25.8 mmol), triethylamine (4.12 g, 39.3 mmol), and EDC·HCl (5.11 g, 26.0 mmol) were added. The reaction mixture was stirred and refluxed at  $75^\circ\text{C}$  for 24 hours, after which it was allowed to cool to room temperature. The crude product was washed three times with 100 mL of brine. The filtrate was centrifuged at 4,000 rpm for 50 minutes, and the supernatant was decanted. The precipitate was then washed with a mixture of 2 L of water and ethanol, followed by drying at  $60^\circ\text{C}$ . The final product, a black solid, was obtained with a mass of 0.38 g.

### Graphene Oxide – Glutamic (Mono-Deprotection)

GO-Glu-OMe (0.3 g, 1 eq) was dispersed in 100 mL of deionized water and sonicated for 6 hours. The mixture was then combined with 18 mL of 2 M KOH and refluxed at  $75^\circ\text{C}$  for 24 hours with continuous stirring. After cooling to room temperature, 20 mL of 2 M sulfuric acid was added, followed by an additional 4 hours of ultrasonic oscillation. The crude product was rinsed four times with 100 mL of brine solution and dried using  $\text{MgSO}_4$ . The material was then filtered and dried at  $60^\circ\text{C}$ , yielding 0.29 g of a black substance.



## Graphene Oxide- Glutamic (Oligo)

A dispersion of GO (0.3 g, 1 equivalent) in 100 mL of deionized water was prepared and sonicated for 6 hours. The mixture was then combined with an excess amount of L-glutamic acid and DMAP (2.95 g, 26.4 mmol), followed by the addition of triethylamine (4.11 g, 39.4 mmol) and EDC·HCl (4.85 g, 25.8 mmol). The reaction mixture was stirred and refluxed at 75 °C for 24 hours. After the reaction was complete, the mixture was allowed to cool to room temperature and washed four times with 100 mL of brine per wash. The filtrate was centrifuged at 4000 rpm for 50 minutes, and the supernatant was removed. The precipitate was washed with a mixture of water and ethanol, and the final product was dried at 60 °C, yielding 0.28 g of a black solid.

## Inhibition of $\alpha$ -chymotrypsin using graphene oxide (GO):

### Experimental Procedure:

All samples were dissolved in a phosphate buffer solution at a pH of 7.4 and 25°C. Prior to the assay, GO concentrations were incubated with  $1.0 \times 10^{-7}$  M chymotrypsin (Chy) for 24 hours. In the control experiment, a cuvette containing 2 mL of chymotrypsin and 0.01 M phosphate buffer was supplemented with 0.50  $\mu$ M BTNA. The hydrolysis of the BTNA substrate was monitored by measuring the absorbance of 4-nitroaniline at 405 nm over 300 seconds.

### Assessment of chymotrypsin activity in presence of functionalised Graphene Oxide

Two solutions were prepared in this experimentation: Solution A, consisting of 25 mg of chymotrypsin dissolved in 1000 mL of buffer, and Solution B, containing 2.5 mg of graphene oxide dissolved in 100 mL of solvent. Solution A was incubated for 30 minutes to activate the

enzyme. Afterward, Solution B was added to Solution A, and the mixture was thoroughly stirred. Then, 50  $\mu\text{L}$  of a BTNA/methanol solution was introduced to initiate the reaction. The reaction was monitored for at 405 nm 300 seconds, observing any changes in color or turbidity. The goal of this experiment was to examine the inhibition of chymotrypsin in the presence of the BTNA/methanol solution.